Universidade Federal do Rio Grande – FURG

Instituto de Oceanografia

Programa de Pós-Graduação em Oceanologia

Variabilidade no Sistema frontal da Corrente Circumpolar Antártica e o seu impacto na Água Profunda Circumpolar

Brendon Yuri Damini

Tese apresentada ao Programa de Pós-Graduação em Oceanologia, como parte dos requisitos para a obtenção do Título de Doutor.

Orientador: *Prof. Dr.* Rodrigo Kerr

Universidade Federal do Rio Grande (FURG), Brasil.

Coorientador: *Prof. Dr.* Mauricio M. Mata

Universidade Federal do Rio Grande (FURG), Brasil.

Coorientador: *Prof. Dr.* Rob Hall

Scottish Association for Marine Science, UK

Rio Grande, RS, Brasil

Julho 2026

Variabilidade no Sistema frontal da Corrente Circumpolar Antártica e o seu impacto na Água Profunda Circumpolar

Tese apresentada ao Programa de Pós-Graduação em Oceanologia, como parte dos requisitos para a obtenção do Título de Doutor

por

Brendon Yuri Damini

Rio Grande, RS, Brasil

Julho 2026

© A cópia parcial e a citação de trechos desta tese são permitidas sobre a condição de que qualquer pessoa que a consulte reconheça os direitos autorais do autor. Nenhuma informação derivada direta ou indiretamente desta obra deve ser publicada sem o consentimento prévio e por escrito do autor.

D159v Damini, Brendon Yuri
Variabilidade no sistema frontal da corrente circumpolar Antártica e o seu impacto na água profunda circumpolar / Brendon Yuri Damini. – 2026.
243f.

Tese (Doutorado) – Universidade Federal do Rio Grande – Programa de Pós-Graduação em Oceanologia, 2026.

Orientador: Dr. Rodrigo Kerr
Coorientador: Dr. Mauricio M. Mata
Coorientador: Dr. Rob Hall

1. Oeste da Antártica. 2. Giro de Ross. 3. Aquecimento da água profunda circumpolar. 4. Corrente Circumpolar Antártica. I. Kerr, Rodrigo. II. Mata, Mauricio M. III. Hall, Rob. IV. Título

CDU 551.46

Catalogação na fonte: Bibliotecária Doris Santana CRB10/1806

“Sempre parece impossível até que seja feito”

Nelson Mandela

UNIVERSIDADE FEDERAL DO RIO GRANDE - FURG
IO – INSTITUTO DE OCEANOGRAFIA
PROGRAMA DE PÓS-GRADUAÇÃ0 EM OCEANOLOGIA
E-mail: ccpofqg@furg.br – home-page: www.ppgo.furg.br

ATA ESPECIAL DE DEFESA DE TESE DE DOUTORADO – 03/2026

Às oito horas do dia dezessete de julho do ano dois mil e vinte e seis, de forma Virtual: https://conferenciaweb.rnp.br/sala/rodrigo-rodrigo-kerr-duarte-pereira, reuniu-se a Comissão Examinadora da Tese de **DOUTORADO** intitulada: **"**VARIABILIDADE NO SISTEMA FRONTAL DA CORRENTE CIRCUMPOLAR ANTÁRTICA E O SEU IMPACTO NA ÁGUA PROFUNDA CIRCUMPOLAR**",** do **Acad. Brendon Yuri Damini.** A Comissão Examinadora foi composta pelos seguintes membros: Prof. Dr. Rodrigo Kerr Duarte Pereira – Orientador – (PPGO-IO/FURG); Prof. Dr. Mauricio M. Mata – Coorientador – (PPGO-IO/FURG); Prof. Dr. Rob Hall – Coorientador – (UEA-INGLATERRA); Dr. Marcos Tonelli – (IEAPM); Prof. Dra. Cláudia Klose Parise– (UFMA); Prof. Dr. Fabrício Sanguinetti Cruz de Oliveira– (PPGO-IO/FURG); Profa. Dra. Juliana Costi – (PPGO-IO/FURG) e Dr. Tiago S. Dotto – (PPGO-IO/FURG). Dando início à reunião, a Profa. Dra. Grasiela Lopes Leães Pinho, Coordenadora do PPGO, agradeceu a presença de todos e fez a apresentação da Comissão Examinadora. Logo após esclareceu que o candidato teria um tempo de 45 a 60 min para explanação do tema, e cada membro da Comissão Examinadora, um tempo máximo de 30 min para perguntas. A seguir, passou à palavra ao candidato que apresentou o tema e respondeu às perguntas formuladas. Após ampla explanação, a Comissão Examinadora reuniu-se em reservado para discussão do conceito a ser atribuído ao candidato. Foi estabelecido que as sugestões de todos os membros da Comissão Examinadora, que seguem em pareceres em anexo, foram aceitas pelo Orientador/Candidato para incorporação na versão final da Tese. Finalmente, a Comissão Examinadora considerou o candidato APROVADO**,** por unanimidade. Nada mais havendo a tratar, foi lavrada a presente ATA, por mim, Clabisnei Moura de Melo – Secretário PPGO, que após lida e aprovada, será assinada pela Comissão Examinadora, pelo Candidato e pela Coordenadora do Programa de Pós-Graduação em Oceanologia.

gov.br Documento assinado digitalmente
RODRIGO KERR DUARTE PEREIRA
Data: 17/07/2026 12:16:16-0300
Verifique em https://validar.iti.gov.br

Prof. Dr. Rodrigo Kerr Duarte Pereira

gov.br Documento assinado digitalmente
MAURICIO MAGALHAES MATA
Data: 20/07/2026 08:49:23-0300
Verifique em https://validar.iti.gov.br

Prof. Dr. Mauricio M. Mata

Prof. Dr. Rob Hall

gov.br Documento assinado digitalmente
FABRICIO SANGUINETTI CRUZ DE OLIVEIRA
Data: 18/07/2026 07:59:30-0300
Verifique em https://validar.iti.gov.br

Prof. Dr. Fabrício Sanguinetti Cruz de Oliveira

gov.br Documento assinado digitalmente
MARCOS HENRIQUE MARUCH TONELLI
Data: 17/07/2026 14:42:51-0300
Verifique em https://validar.iti.gov.br

Dr. Marcos Tonelli

Documento assinado digitalmente
gov.br
CLAUDIA KLOSE PARISE
Data: 17/07/2026 13:08:21-0300
Verifique em https://validar.iti.gov.br

Prof. Dra. Cláudia Klose Parise

Documento assinado digitalmente
gov.br
JULIANA COSTI
Data: 17/07/2026 14:48:22-0300
Verifique em https://validar.iti.gov.br

Profa. Dra. Juliana Costi

Documento assinado digitalmente
gov.br
TIAGO SEGABINAZZI DOTTO
Data: 20/07/2026 07:37:05-0300
Verifique em https://validar.iti.gov.br

Dr. Tiago S. Dotto

Documento assinado digitalmente
gov.br
BRENDON YURI DAMINI
Data: 20/07/2026 13:33:12-0300
Verifique em https://validar.iti.gov.br

Acad. Brendon Yuri Damini

Profª. Drª Grasiela Lopes Leães Pinho
Coordenadora PPGO

Documento assinado digitalmente
gov.br
GRASIELA LOPES LEAES PINHO
Data: 09/07/2026 08:22:03-0300
Verifique em https://validar.iti.gov.br

Índice

Agradecimentos **13**

Resumo **16**

Abstract **18**

Lista de figuras **20**

List of figures **22**

Lista de Acrônimos e Abreviações **32**

Prefácio **34**

Preface **35**

Hipótese **36**

Hypothesis **37**

Capítulo I: Introdução **38**

1.1 Objetivos **42**

1.1.1 Objetivo geral 43

1.1.2 Objetivos específicos 43

Capítulo II: Área de estudo **44**

2.1 Sistema frontal da Corrente Circumpolar Antártica **44**

2.2 Circulação do oceano Austral ao longo da região oeste da Antártica ... **46**

2.2.1 Mares de Amundsen e Bellingshausen 50

2.2.2 Península Antártica 53

Capítulo III: Dados e Métodos **56**

3.1 Conjunto de dados hidrográficos 56

3.2 Saída da reanálise GLORYS12v1 57

3.3 Equação de Estado Termodinâmica da Água do Mar (TEOS-10) 58

3.4 Aquecimento pós-década de 1990 da CDW ao longo do oeste da Antártica e seus mecanismos controladores..... 58

3.4.1 Definição da camada de CDW..... 59

3.4.2 Definição da SACCF 59

3.4.3 Validação da reanálise GLORYS12v1 na representação da variabilidade termohalina da CDW..... 60

3.4.4 Análise atmosférica..... 60

3.4.5 Alterações na temperatura conservativa da CDW devido aos deslocamentos meridionais da ACC 61

3.5 Variabilidade do Giro de Ross e seu papel na modulação das propriedades da CDW na região ao largo da plataforma continental no setor Amundsen–Bellingshausen (1993–2020)..... 63

3.5.1 Definição do Giro de Ross..... 63

3.5.3 Rotacional da tensão do cisalhamento total superficial oceânico.. 63

3.5.4 Fluxos de Flutuabilidade..... 64

3.5.5 Análises temporais e espaciais..... 65

3.6 Circulação de verão e transporte de massas d'água no estreito de Bransfield, Antártica: avaliação da resposta aos efeitos combinados do SAM e do ENSO 66

3.6.1 Método Dinâmico 66

3.6.2 Validação da reanálise GLORYS12v1 na representação da estrutura termohalina e da circulação do estreito de Bransfield 67

3.6.3 Cálculo do transporte de massa de água a partir da saída da GLORYS12v1..... 68

3.6.4 Conjunto de dados de altimetria por satélite..... 68

3.6.5 Análise atmosférica 69

Chapter I: Introduction 71

1.1 Objectives 75

1.1.1 Main objective 75

1.1.2 Specific objective 75

Chapter II: Study Area 77

2.1 Antarctic Circumpolar Current frontal system 77

2.2 The Southern Ocean Circulation Off West Antarctica 79

2.2.1 Amundsen and Bellingshausen Seas 82

2.2.2 Antarctica Peninsula 85

Chapter III: Data and Methods 89

3.1 Hydrographic Dataset 89

3.2 GLORYS12v1 reanalysis output 90

3.3 Thermodynamic Equation of State for Seawater (TEOS–10) 91

3.4 Post-1990s Warming of Circumpolar Deep Water Off West Antarctica and Its Drivers 91

3.4.1 CDW layer definition 92

3.4.2 SACCF definition 92

3.4.3 GLORYS12v1 reanalysis validation in the representation of CDW thermohaline variability 93

3.4.4 Atmospheric analysis 93

3.4.5 Changes in conservative temperature of CDW due to meridional ACC displacements 94

3.5 Gyre circulation variability preconditions the off-shelf ocean heat reservoir to the West Antarctic continental shelf 95

3.5.1 Definition of Ross Gyre 95

3.5.2 Ocean Stress Curl 96

3.5.3 Buoyancy Fluxes 96

3.5.4 Time-Series and composites 97

3.6 Summer circulation and water masses transport in Bransfield Strait, Antarctica: An evaluation of their response to combined effects of Southern Annular Mode and El Niño–Southern Oscillation 98

3.6.1 Dynamic Method 99

3.6.2 Validation of GLORYS12v1 reanalysis in representing the thermohaline structure and circulation of the Bransfield Strait 99

3.6.3 Water mass transport calculation by GLORYS12v1 output 100

3.6.4 Satellite altimetry dataset 100

3.6.5 Atmospheric analysis 101

Capítulo IV: Artigos 103

4.1 Aquecimento pós-década de 1990 da CDW ao longo do oeste da Antártica e seus mecanismos controladores 103

4.1.1 Introduction 103

4.1.2 Materials and Methods 105

4.1.3 Results and Discussion 116

4.1.4 Conclusions and outlook 131

4.1.5 Supplementary information 133

4.2 Variabilidade do Giro de Ross e seu papel na modulação das propriedades da CDW na região ao largo da plataforma continental no setor Amundsen–Bellingshausen (1993–2020) 137

4.2.1 Introduction 137

4.2.2 Materials and Methods 139

4.2.3 Results and Discussion 143

4.2.4 Concluding remarks 156

4.2.5 Supplementary information 157

4.3 Circulação de verão e transporte de massas d'água no estreito de Bransfield, Antártica: avaliação da resposta aos efeitos combinados do SAM e do ENSO 160

4.3.1 Introduction 160

4.3.2 Data and Methods 164

4.3.3 Results and Discussion 173

4.3.4 Summary and conclusions 196

4.3.5 Supplementary information 198

Capítulo V: Sumário e conclusões 206

5.1 Variabilidade interdecenal das propriedades termohalinas da CDW no verão ao longo do oeste da Antártica e forçantes associadas 206

5.2 Variabilidade interanual do Giro de Ross e seu papel na modulação das propriedades da CDW na região ao largo da plataforma continental no setor Amundsen–Bellingshausen 207

5.3 Circulação de verão e transporte de massas de água no estreito de Bransfield, Antártica 208

5.4 Considerações Finais 209

5.5 Impactos na sociedade 211

Capítulo VI: Agradecimentos 213

Chapter V: Summary and Conclusions 215

5.1 Interdecadal variability of CDW thermohaline properties in summer along West Antarctica and associated forcings 215

5.2 Interannual variability of the Ross Gyre and its role in modulating CDW properties in the off-shelf Amundsen–Bellingshausen sector 216

5.3 Summer circulation and water-mass transport in Bransfield Strait, Antarctica 218

5.4 Final Remarks..... 219

5.5 Social Impacts 221

Capítulo VII: Referências Bibliográficas 222

Agradecimentos

Essa tese eu dedico à minha família, que foi, sem dúvida, meu porto seguro em todos os momentos mais difíceis que enfrentei ao longo desta jornada acadêmica. Houve muitas ocasiões, desde a graduação, em que a desistência parecia bater à porta, e foi justamente esse apoio que me permitiu seguir em frente, superar as barreiras do caminho e chegar até aqui.

Gostaria de agradecer à Luísa, grande companheira durante todo esse processo maluco chamado doutorado. Sem dúvida, esta tese foi escrita a quatro mãos. Muito obrigado por todo o apoio, pela paciência, pelo carinho e por ter estado ao meu lado ao longo dessa caminhada. Te desejo todo o sucesso do mundo!

Um agradecimento especial a toda a minha rede de apoio, desde os amigos de infância até aqueles que fui encontrando ao longo da trajetória acadêmica. Cada um de vocês foi essencial nessa jornada. E um agradecimento mais do que especial ao Gohazinho, meu cãopanheiro, pela companhia nos dias leves e nos mais difíceis.

Um obrigado especial ao CHINA, que também esteve comigo em todo esse período louco do doutorado na busca do MMR perdido hahahhahhaha

E um agradecimento muito especial ao Andrei e ao Dionysio, grandes amigos que levo desde a graduação e que estiveram ao meu lado, me apoiando e me escutando em um dos momentos mais difíceis da minha vida.

Ao João e ao Juan, grandes amigos cassineiros, que foram minha rede de apoio ao me ajudarem a cuidar do Gohazinho em diversos momentos em que não estive presente.

Dedico também esta tese a um grande amigo, José de Souza (meu padrinho), cuja ajuda e apoio foram fundamentais ao longo dessa caminhada. Em momentos particularmente difíceis, sua presença me deu forças para continuar e chegar até aqui.

I would like to thank Rob, Karen, and everyone in room 3.16 at UEA. My time in Norwich was very special and contributed greatly to both my personal and professional growth.

Thank you very much for the warm welcome, the companionship, and all the exchanges we shared throughout that period.

I am also very grateful to the people at the National Oceanography Centre and the University of Southampton, especially Tiago Dotto and Alberto Naveira Garabato, for all the assistance, kindness, and support I received during my time in Southampton. The scientific discussions, the daily interactions, and the opportunity to follow your work more closely were extremely important for my academic development.

Um agradecimento especial à Ilana e ao pessoal do Laboratório de Oceanografia Física, Clima e Criosfera, que me receberam tão bem em São Paulo. Sou muito grato pela acolhida, pelas conversas, pelo ambiente de trabalho e por todo o apoio durante esse período, que foi muito importante para ampliar minha formação e minha visão científica.

Ao Rodrigo e ao Mauricio, agradeço por todas as reuniões, discussões e orientações ao longo deste trabalho. Tenho certeza de que grande parte do meu amadurecimento acadêmico durante esse período se deve à mentoria que recebi de vocês. Muito obrigado pela confiança, pela paciência e por tudo o que aprendi nesse processo.

Ainda no clima de agradecer ao pessoal do laboratório: um grande obrigado a todos do LEOC e à toda a equipe do *CARBON Team*. A convivência com vocês tornou essa caminhada muito mais leve, enriquecedora e especial.

Agradeço também a todos os professores do PPGO pelos ensinamentos e conhecimentos transmitidos ao longo do mestrado e do doutorado na FURG. Por fim, agradeço o apoio financeiro recebido durante meus estudos por meio das bolsas do CNPq, da CAPES e do INCT da Criosfera, fundamentais para a realização deste trabalho.

Agradeço também aos membros da banca (Cláudia Parise, Fabrício Sanguinetti, Tiago Dotto, Marcos Tonelli e Juliana Costi) que aceitaram o convite e contribuíram nessa minha última etapa de formação do doutorado.

Vindo de uma família de classe média baixa, onde enfrentei inúmeras dificuldades ao longo desta trajetória. Hoje, ao concluir este ciclo e defender essa tese, tenho a convicção de que o caminho até aqui foi construído com muito esforço e perseverança, mas também graças aos privilégios (não existe meritocracia) e oportunidades que surgiram por meio de pessoas que acreditaram em mim e me ofereceram apoio quando

eu mais precisei. Carrego por elas uma eterna gratidão. Com muito orgulho, torno-me o primeiro doutor da minha família.

Resumo

A Corrente Circumpolar Antártica (ACC) transporta grandes volumes de Água Profunda Circumpolar (CDW), uma massa de água relativamente quente e salina que constitui importante fonte de calor para as margens continentais antárticas. Nas últimas décadas, o aquecimento da CDW tem sido associado ao aumento da fusão basal das plataformas de gelo e à perda de massa da camada de gelo antártica. Entretanto, os mecanismos responsáveis pela redistribuição desse calor no oeste da Antártica e no norte da Península Antártica ainda não são completamente compreendidos. Esta tese investiga os processos que controlam a variabilidade termohalina da CDW e de massas de água derivadas dela em dois contextos oceanográficos: a borda sul da ACC nos mares de Amundsen e Bellingshausen e o estreito de Bransfield. Para isso, foram combinadas observações hidrográficas, altimetria por satélite, campos atmosféricos e a reanálise oceânica de alta resolução GLORYS12v1. No setor Amundsen–Bellingshausen, o aquecimento interdecenal da CDW ao largo da plataforma continental foi dominado por processos advectivos ao longo de isopicnais, associados ao fortalecimento do Giro de Ross e ao aumento das trocas de calor transversais à ACC. O deslocamento meridional da Frente Sul da ACC apresentou contribuição secundária. Em escalas sazonal e interanual, a intensidade e a extensão espacial do Giro de Ross estiveram fortemente relacionadas ao rotacional da tensão superficial oceânica, enquanto os fluxos de flutuabilidade exerceram papel menos relevante. Estados mais intensos do giro coincidiram com águas subsuperficiais mais quentes e salinas sobre o talude e ao largo dos mares de Amundsen e Bellingshausen. Contudo, essas anomalias não se propagaram uniformemente para a plataforma continental. No mar de Amundsen, observaram-se resfriamento, dessalinização e aprofundamento da termoclina, enquanto o mar de Bellingshausen apresentou aquecimento, salinificação e elevação da termoclina. Esses contrastes indicam que a transferência de calor para a plataforma depende de processos regionais, incluindo ventos costeiros, geometria batimétrica e estrutura frontal. No estreito de Bransfield, a circulação de verão e o transporte de águas com influência do mar de Bellingshausen responderam à variabilidade atmosférica de grande escala. Os efeitos combinados do Modo Anular Sul e do *El Niño*–Oscilação Sul modularam os ventos regionais, a posição

da Frente Sul da ACC e a intrusão de CDW, alterando a circulação e a distribuição das massas de água. Em conjunto, os resultados demonstram que a variabilidade de larga escala da ACC, do Giro de Ross e dos modos climáticos pré-condiciona a redistribuição de calor ao redor da Antártica, enquanto sua transferência efetiva para plataformas continentais, margens glaciais e bacias costeiras é regulada por mecanismos regionais e locais. Esses resultados contribuem para compreender como mudanças futuras nos ventos de oeste e na circulação do oceano Austral poderão modificar a intrusão de CDW e a estabilidade das geleiras e plataformas de gelo do oeste da Antártica.

Palavras-Chave: Oeste da Antártica; Giro de Ross; aquecimento da Água Profunda Circumpolar; Corrente Circumpolar Antártica.

Abstract

The Antarctic Circumpolar Current (ACC) transports large volumes of Circumpolar Deep Water (CDW), a relatively warm and saline water mass that represents an important source of heat to the Antarctic continental margins. Over recent decades, CDW warming has been associated with increased basal melting of ice shelves and mass loss from the Antarctic Ice Sheet. However, the mechanisms controlling the redistribution of this heat in West Antarctica and the northern Antarctic Peninsula remain incompletely understood. This thesis investigates the processes governing the thermohaline variability of CDW and CDW-derived water masses in two oceanographic settings: the southern boundary of the ACC in the Amundsen and Bellingshausen Seas and Bransfield Strait. To address this, hydrographic observations, satellite altimetry, atmospheric fields, and the high-resolution GLORYS12v1 ocean reanalysis were combined. In the Amundsen–Bellingshausen sector, interdecadal off-shelf CDW warming was primarily driven by advective processes along isopycnals, associated with the strengthening of the Ross Gyre and enhanced cross-ACC heat exchange. Meridional displacement of the Southern ACC Front made a secondary contribution. On seasonal and interannual timescales, the strength and spatial extent of the Ross Gyre were strongly related to ocean surface stress curl, whereas buoyancy fluxes played a less prominent role. Stronger gyre states coincided with warmer and saltier subsurface waters over the continental slope and in the off-shelf regions of the Amundsen and Bellingshausen Seas. However, these anomalies did not propagate uniformly onto the continental shelf. The Amundsen Sea shelf exhibited cooling, freshening, and thermocline deepening, whereas the Bellingshausen Sea shelf showed warming, salinification, and thermocline shoaling. These contrasting responses indicate that heat transfer onto the shelf depends on regional processes, including coastal winds, bathymetric geometry, and local frontal structure. In Bransfield Strait, summer circulation and the transport of Bellingshausen-influenced waters responded to large-scale atmospheric variability. The combined effects of the Southern Annular Mode and the El Niño–Southern Oscillation modulated regional winds, the position of the Southern ACC Front, and CDW intrusions, thereby altering the circulation and distribution of water

masses within the strait. Overall, the results demonstrate that large-scale variability in the ACC, the Ross Gyre, and climate modes preconditions heat redistribution around Antarctica, whereas its effective transfer to continental shelves, glacial margins, and coastal basins is regulated by regional and local mechanisms. These findings contribute to understanding how future changes in the westerly winds and Southern Ocean circulation may affect CDW intrusions and the stability of West Antarctic glaciers and ice shelves.

Keywords: West Antarctica; Ross Gyre; warming of Circumpolar Deep Water; Antarctic Circumpolar Current.

Lista de figuras

Figura 1: Esquema da circulação de revolvimento na perspectiva do oceano Austral. Esta região é o local mais proeminente do mundo onde águas profundas (roxo) ascendem à superfície, trocam calor e carbono com a atmosfera e, depois, retornam ao interior do oceano. Figura extraída de Meredith et al., [2022]..... 39
Figura 2: Posição média do sistema frontal da Corrente Circumpolar Antártica determinada por Orsi et al., [1995] a partir de dados hidrográficos históricos e com base em critérios de massas d'água (como um valor específico de temperatura em certa profundidade) para definir suas localizações. As frentes nomeadas são, de norte a sul: Frente Subtropical (STF), Frente Subantártica (SAF), Frente Polar (PF), Frente Sul da ACC (sACCF) e a Frente do Limite Sul (SBdy). O colorbar de fundo mostra a profundidade do oceano. Figura extraída de Chapman et al., [2020]..... 40
Figura 3: Vista vertical zonal (da superfície ao oceano profundo) dos fluxos meridionais das principais massas d'água que entram e saem do oceano Austral. As siglas derivadas do inglês são: Corrente Circumpolar Antártica (ACC), Água da Plataforma Continental (CSW), Água de Superfície Antártica (AASW), Água Modal Subantártica (SAMW), Água de Superfície Subantártica (SASW), Água de Superfície Subtropical (STSW), Água Intermediária Antártica (AIW), Água Profunda Circumpolar Superior (UCDW), Água Profunda Circumpolar Inferior (LCDW), Água de Fundo Antártica (AABW), Frente de Talude Antártica (ASF), Frente do Limite Sul (SB), Frente Sul da ACC (SACCF), Frente Polar (PF), Frente Subantártica (SAF) e Frente Subtropical (STF). As siglas ASC e ACC representam a corrente de talude e a corrente circumpolar respectivamente. Figura extraída de Yamazaki, 2022. 46
Figura 4: Médias de anomalias de pressão ao nível do mar (SLP; hPa) e anomalias de vento de superfície (m/s, setas). Os símbolos H e L indicam a localização dos centros maior (enfraquecimento) e menor (intensificação) SLP (do Amundsen Sea Low), respectivamente. Figura de Huguenin et al., [2024]..... 48
Figura 5: (a) Principais massas de água e seus fluxos ao longo e através do talude definidos por Thompson et al., [2018], sendo regime de plataforma fresca (Fresh shelf), plataforma quente (warm shelf) e plataforma densa (Dense shelf) painéis da esquerda à direita respectivamente. **(b)** Indica a localização geográfica desses regimes distintos. As siglas BS, AS e RS representam os mares de Bellingshausen, Amundsen e Ross, respectivamente. Figura modificada de Thompson et al., [2018]. 49
Figura 6: Representação esquemática das rotas de transporte nos mares de Amundsen (AS) e Bellingshausen (BS). As linhas cinzas tracejadas mostram a topografia dinâmica média de 2011–2016 [Armitage et al., 2018]. As cores das setas indicam a massa de água dominante que transporta o fluxo, sendo a azul (Água Superficial Antártica - ASW misturada com Água de inverno - WW) transportadas pela Corrente Costeira Antártica (ACoC), a vermelha (Água Circumpolar Profunda – CDW) e a roxa (WW). A seta roxa tracejada indica uma rota sugerida por Thompson et al., 2020 de WW e ASW para Amundsen Sea. Figura de Thompson et al., [2020]. 51
Figura 7: Região batimétrica do mar de Amundsen. As linhas pontilhadas mostram a divisão da região oeste do mar de Amundsen (WAS) representada pelo canal Dotson–

Getz e da região leste do mar de Amundsen (EAS) representada pelos canais Pine Island–Thwaites. Os retângulos azuis indicam o Dotson Shelf Break (DSB), o Inner Dotson Trough (DT), o canal Pine Island–Thwaites (PIT), o canal Pine Island–Thwaites Oeste (PITW) e o canal Pine Island–Thwaites Leste (PITE). São representadas as isóbatas de 500, 1000 e 3000 m. As plataformas de gelo locais estão identificadas: Abbot Ice Shelf (AIS), Cosgrove Ice Shelf (CIS), Pine Island Ice Shelf (PIIS), Thwaites Ice Shelf (TIS), Crosson Ice Shelf (Cr), Dotson Ice Shelf (DIS) e Getz Ice Shelf (GIS). Figura de Dotto et al., [2019]..... 52
Figura 8: Representação esquemática da circulação média na região da Península Antártica. As setas vermelhas (roxas) representam as rotas pelas quais a Transicionais do mar de Bellingshausen (TBW) e a Águas Transicionais do mar de Weddell (TWW) entram no Estreito de Bransfield. As linhas verde e amarela indicam, respectivamente, as posições médias da Frente Sul da Corrente Circumpolar Antártica (Southern Antarctic Circumpolar Current Front, SACCF) e do Limite Sul da Corrente Circumpolar Antártica (Southern Boundary, SB). Setas em azul-claro indicam o vórtice associado à bifurcação da Frente de Talude Antártica (Antarctic Slope Front bifurcation, ASFb). As setas laranja mostram a Corrente de Bransfield e sua recirculação ao redor das Ilhas Shetland do Sul (S.S.Is.). A linha preta representa a posição média da Frente de Talude Antártica (ASF). Os retângulos vermelhos em torno dos pontos magenta e pretos delimitam as seções hidrográficas das Seções 1 e 2 (**mais bem detalhado na seção de material e métodos**). A linha preta tracejada representa a Frente da Península (Peninsula Front, PF). As siglas correspondem a: Canal Antártico (AC), Corrente Costeira Antártica (ACoC), Ilha Joinville (J.Is.), Ilha D'Urville (D'U.Is.), Ilha Elefante (E.Is.), Ilha Clarence (C.Is.), Mar de Bellingshausen (BS), Passagem de Drake (DP), Mar de Weddell (WS), Bacia Ocidental (WB), Bacia Central (CB), Bacia Oriental (EB) e Estreito de Gerlache (GS). As linhas cinzas finas indicam as isóbatas de 0,10 km e 0,30 km fornecidas pelo IBCSO (www.scar.org/science/ibcso/ibcso/). O painel ampliado mostra a região de estudo. Figura extraída de Damini et al., [2025]..... 54

List of figures

Figure 1: Schematic of the overturning circulation from a Southern Ocean perspective. This region is the most prominent location globally where deep waters (purple) rise to the surface, exchange heat and carbon with the atmosphere, and then return to the ocean interior. Figure from Meredith et al., [2022]. 72
Figure 2: Mean position of the frontal system of the Antarctic Circumpolar Current as determined by Orsi et al., [1995] using historical hydrographic data and water-mass criteria (such as a specific temperature value at a given depth) to define their locations. The named fronts, from north to south, are: Subtropical Front (STF), Subantarctic Front (SAF), Polar Front (PF), southern ACC Front (sACCF), and the Southern Boundary (SBdy). The background colorbar shows ocean depth. Figure from Chapman et al., [2020]. 73
Figure 3: Zonal vertical view (from the surface to the deep ocean) of the meridional flows of the main water masses entering and leaving the Southern Ocean. The acronyms derived from English are: Antarctic Circumpolar Current (ACC), Continental Shelf Water (CSW), Antarctic Surface Water (AASW), Subantarctic Mode Water (SAMW), Subantarctic Surface Water (SASW), Subtropical Surface Water (STSW), Antarctic Intermediate Water (AIW), Upper Circumpolar Deep Water (UCDW), Lower Circumpolar Deep Water (LCDW), Antarctic Bottom Water (AABW), Antarctic Slope Front (ASF), Southern Boundary (SB), Southern ACC Front (SACCF), Polar Front (PF), Subantarctic Front (SAF), and Subtropical Front (STF). Figure from Yamazaki, [2022]. 78
Figure 4: Mean sea level pressure anomalies (SLP; hPa) and surface wind anomalies (m s^{-1}, arrows). The symbols H and L indicate the location of the major (weakening) and minor (intensification) SLP centers (of the Amundsen Sea Low), respectively. Figure from Huguenin et al., [2024]. 80
Figure 5: (a) Main water masses and along-slope and cross-slope flows defined by Thompson et al., [2018], namely the Fresh Shelf, Warm Shelf, and Dense Shelf regimes, shown from left to right, respectively. **(b)** Geographic locations of these distinct BS, AS and RS indicated the Bellinshausen, Amundsen and Ross Seas, respectively regimes. Figure from Thompson et al., [2018]. 82
Figure 6: Schematic representation of the transport pathways in the Amundsen and Bellingshausen Seas. The dashed gray lines show the mean dynamic topography for 2011–2016 (Armitage et al., 2018) at 5 cm intervals. The colors of the arrows indicate the dominant water mass carrying the flow: blue (Antarctic Surface Water – ASW mixed with Winter Water – WW), red (Circumpolar Deep Water – CDW), and purple (WW). The dashed purple arrow indicates a pathway of WW and ASW toward the Amundsen Sea suggested by Thompson et al., [2020]. The labels AS and BS indicate the Amundsen and Bellingshausen Seas, respectively. Figure from Thompson et al., [2020]..... 83
Figure 7: Amundsen Sea bathymetry region. Dotted lines show the definition of the Dotson–Getz trough and the Pine Island–Thwaites troughs. Blue rectangles indicate the Dotson Shelf Break (DSB), the Inner Dotson Trough (DT), the Pine Island–Thwaites Channel (PIT), the Pine Island–Thwaites West Channel (PITW), and the Pine Island–

Thwaites East Channel (PITE). The 500, 1000, and 3000 m isobaths are represented. Abbot Ice Shelf (AIS), Cosgrove Ice Shelf (CIS), Pine Island Ice Shelf (PIIS), Thwaites Ice Shelf (TIS), Crosson Ice Shelf (Cr), Dotson Ice Shelf (DIS), and Getz Ice Shelf (GIS). WAS and EAS indicates the regions West and East of Amundsen Sea, respectively. Figure from Dotto et al., [2019]. 85
Figure 8: Schematic representation of the mean circulation in the Antarctic Peninsula region. The red (purple) arrows represent the pathways through which Bellingshausen Transitional Water (TBW) and Weddell Transitional Water (TWW) enter Bransfield Strait. The green and yellow lines indicate the mean positions of the Southern Antarctic Circumpolar Current Front (SACCF) and the Southern Boundary (SB), respectively. Light-blue arrows indicate the eddy associated with the Antarctic Slope Front bifurcation (ASFb). The orange arrows show the Bransfield Current and its recirculation around the South Shetland Islands (S.S.Is.). The black line represents the mean position of the Antarctic Slope Front (ASF). The red rectangles surrounding the magenta and black dots delimit the hydrographic sections for Sections 1 and 2 (further detailed in the Materials and Methods section). The dashed black line represents the Peninsula Front (PF). The acronyms correspond to: Antarctic Channel (AC), Antarctic Coastal Current (ACoC), Joinville Island (J.Is.), D'Urville Island (D'U.Is.), Elephant Island (E.Is.), Clarence Island (C.Is.), Bellingshausen Sea (BS), Drake Passage (DP), Weddell Sea (WS), Western Basin (WB), Central Basin (CB), Eastern Basin (EB), and Gerlache Strait (GS). Thin gray lines indicate the 0.10 km and 0.30 km isobaths provided by IBCSO. The inset panel shows the study region. Figure modified from Damini *et al.,* [2025]. 87
Figure 9: The number of hydrographic profiles per decade used in this study. a Profiles categorised by: CTD dataset (blue), MEOP (grey), and Argo (red); and **b** total number of profiles per decade. 106
Figure 10: Decadal changes in the CDW layer properties, defined by neutral density (γ^n) of 27.93 and 28.03 kg m^{-3}. Difference between 2010s and 1990s in a Conservative Temperature (Θ, ºC) and b Absolute Salinity (S_A, g kg^{-1}) from GLORYS output. Blue and black lines indicate the mean positions of the Southern Antarctic Circumpolar Current Front during the 1990s and 2010s, respectively, based on GLORYS output. Thin grey contours represent the 500 m and 1,500 m isobaths from the R–Topo2 dataset [Schaffer et al., 2016]. 108
Figure 11: Meridional SACCF displacements. a Time–averaged position of the Southern Antarctic Circumpolar Current Front (SACCF) positions for the period 1990s–2010s, based on four different definitions: hydrographic measurements (blue line), satellite altimetry using Absolute Dynamic Topography (ADT; red line), GLORYS output (black line) definitions, and the climatological product from Orsi et al [1995] (purple dashed line). The Pearson correlation coefficient between the time–averaged (1990s–2010s) of the SACCF positions by satellite altimetry (red), hydrographic measurements (blue) and Orsi et al. 1995 (purple) with GLORYS output are indicated by r. **b** Decadal changes in the position of the Southern Antarctic Circumpolar Current Front (SACCF), as derived from GLORYS output (solid lines) and hydrographic measurements (dashed lines). Blue and black lines represent the mean SACCF position during the 1990s and 2010s, respectively. **c** Meridional displacement of the SACCF derived from ADT data. Amundsen Sea region is highlighted in red and Bellingshausen Sea region in purple. Also indicated are the average meridional displacement (in degrees latitude) for each region. Thin grey contours represent the 500 m and 1,500 m isobaths from the R–Topo2 dataset [Schaffer et al., 2016]. 110
Figure 12: Summer time-mean (1993-2020, jan-march) gradient of SSH (m per 100 km) off West Antarctica...... 113

Figure 13: Assessment of the contribution of the SACCF poleward displacement to the warming of CDW. a Climatology (1990s–2010s) of dynamic height (Φ) at 300 m relative to 1,800 m depth. **b** Change in Φ between 1990s and 2010s. Blue and black lines indicate the mean position of the Southern Antarctic Circumpolar Current Front (SACCF) during the 1990s and 2010s, respectively, as derived from GLORYS output. **c** Climatological change in Conservative Temperature (Θ, ºC) within the Circumpolar Deep Water (CDW) layer as a function of Φ. **d** Same as **c** but highlighting the Φ intervals used to compute the temperature gradient (dΘ/dΦ) by linear regression (black lines), with a correlation coefficient of the regression is r = 0.97. Thin grey contours represent the 500 m and 1,500 m isobaths from the R–Topo2 dataset [Schaffer et al., 2016]. 114
Figure 14: Decadal changes in the properties of the CDW layer, defined as the maximum Θ below 300 m. Difference between 2010s and 1990s in a Conservative Temperature (Θ, ºC) and b Absolute Salinity (S_A, g kg^{-1}) from hydrographic measurements and c-d from GLORYS output. Blue and black lines indicate the mean positions of the Southern Antarctic Circumpolar Current Front during the 1990s and 2010s, respectively, based on satellite altimetry (a–b) and GLORYS output (c–d). Thin grey contours represent the 500 m and 1,500 m isobaths from the R–Topo2 dataset [Schaffer et al., 2016]. The labels WAS, EAS, WBS, EBS denote the Western Amundsen Sea, Eastern Amundsen Sea, Western Belligshausen Sea, Eastern Bellingshausen Sea, respectively. 117
Figure 15: Evolution of CDW layer properties at the SACCF position. a Conservative Temperature (Θ, °C) anomalies relative to the 1993–2020 mean **b** Same as a, but for Absolute Salinity (S_A, g kg^{-1}) anomalies. 119
Figure 16: Decadal changes in the position of SACCF. **a** Hovmöller diagram of the displacement anomaly of SACCF (in km) relative to the period 1990-2020. Positive values show the Southern Antarctic Circumpolar Current Front – SACCF displacement poleward, while negative values show the SACCF displacement equatorward; **b** Meridional displacement of the SACCF derived from GLORYS output. The Amundsen Sea region is highlighted in red and Bellingshausen Sea region in purple. Also indicated is each region's average meridional displacement (in km); **c** Sea level pressure (SLP, Pa) anomaly for the 1990s, relative to the period 1990–2020; **d** same as **c** but for the 2010s. The black (yellow) solid lines indicate the summertime southern hemisphere maximum westerly position averaged for the 1990s (2010s). 121
Figure 17: Decadal changes in the wind stress curl. **a** Wind stress curl (N m^{-3}) anomaly for the 1990s, relative to the period 1990–2020; **b** same as **a** but for the 2010s. Positive anomalies indicate reduced Ekman upwelling, whereas negative anomalies denote enhanced Ekman upwelling. Black arrows mark the approximate positions of the Ross Gyre (RG) and the Weddell Gyre (WG). 123
Figure 18: Influence of the interdecadal poleward displacement of the SACCF on the conservative temperature of the CDW layer. The total conservative temperature (Θ, ºC) change between the 1990s and 2010s (**Figure 14c**) is decomposed into **a** the frontal displacement (ºC) and **b** the residual term. Blue and black lines indicate the mean position of the Southern Antarctic Circumpolar Current Front (SACCF) during the 1990s and 2010s, respectively, based on GLORYS output. Thin grey contours represent the 500 m and 1,500 m isobaths from the R–Topo2 dataset [Schaffer et al., 2016]. 123
Figure 19: Wind-driven shift in the vertical structure of CDW intruding onto West Antarctica continental shelf. **a** and **b** Decadal difference (2010s minus 1990s) in zonal and meridional wind speed anomalies (m s^{-1}) between two periods (i.e., 2010s minus 1990s), respectively. Thin grey contours represent the 500 m and 1,500 m isobaths from the R–Topo2 dataset [Schaffer et al., 2016]. The red arrows indicate CDW advection

through the ACC front and its intrusions onto the continental shelf by troughs. **c-h** Decadal difference of Conservative Temperature (Θ, °C) in sections across the Dotson-Getz Trough (DGT), Pine Island Eastern Trough (PIET), Pine Island Western Trough (PIWT), Latady Trough (LT), Belgica Trough (BT), and Marguerite Trough (MT). The locations of these sections are shown as black lines in panel (a). The dashed and solid lines indicate the mean neutral density contours (27.8, 27.9, 28.0, and 28.2kg·m^{-3}) for the 1990s and 2010s, respectively. The red arrows highlight the inflow of CDW (including eddy-driven pathways indicated by curved arrows) onto the continental shelf, while yellow arrows denote surface water transport. 127
Figure 20: Conservative temperature and absolute salinity differences between the hydrographic measurements and GLORYS output. Time-averaged (1990s-2010s) of a Conservative Temperature (Θ ºC) and b Absolute Salinity (S_A, g kg^{-1}). Areas with no data points within a 50 km radius of each grid point were masked in the hydrographic measurements. 130
Figure 21: West Antarctic study region and water-mass characteristics. (a) Map showing the major ocean circulation features, including the Ross Gyre (solid black contour), the Southern Antarctic Circumpolar Current Front (orange), and the cross-shelf sections in the Amundsen and Bellingshausen Seas (S1 and S2, respectively). The cross-gyre section (dashed black line) extends from the eastern boundary of the Ross Gyre towards the Bellingshausen Sea and was used to investigate the lateral redistribution of Circumpolar Deep Water (CDW). MBS denote the Marie Byrd Seamounts. Thin grey contours indicate the 500 and 1,500 m isobaths from the R-Topo2 dataset [Schaffer et al., 2016]. (b) Conservative temperature (Θ) - Absolute Salinity (SA) diagram from hydrographic observations, with the stations shown in the inset, and (c) same as (b), but derived from GLORYS12v1 data over the domain 65°S–79°S and 140°E–70°W. Colors indicate depth. Labels AASW, WW, CDW, AABW, and DSW denote Antarctic Surface Water, Winter Water, Circumpolar Deep Water, Antarctic Bottom Water, and Dense Shelf Water, respectively. Gray contours represent potential density (σ_θ; kg m^{-3}), while the red contours indicate σ_θ = 27.4 and 27.8 kg m^{-3}, which define the upper and lower boundaries of the CDW layer, respectively. 138
Figure 22: Seasonal variability of the Ross Gyre properties and atmospheric forcing during 1993–2020. (a) Gyre circulation strength, **(b)** gyre area, and **(c)** ocean surface stress curl (OSC). In panel **(a)**, bars show the seasonal mean gyre circulation strength for December–February (summer), March–May (autumn), June–August (winter), and September–November (spring), with error bars indicating the standard deviation of the values within each season. Shaded areas represent the monthly climatological standard deviation. The correlation coefficient (*r*) between gyre circulation strength and the variable shown in each panel is indicated. All correlations are significant at the 95% confidence level (*p-value* < 0.05). 145
Figure 23: Interannual variability of Ross Gyre properties from GLORYS12v1 (1993-2020): (a) Gyre circulation strength anomaly. The gray shaded area in **(a)** represents the standard deviation., **(b)** gyre area anomaly, and **(c)** ocean surface stress curl (OSC) anomaly. The correlation coefficient (*r*) between gyre circulation strength and each variable is indicated in the corresponding panel. All correlations are significant at the 95% confidence level ($p < 0.05$). Red and blue rectangles denote strong and weak gyre periods, respectively, defined as periods when gyre circulation strength anomalies exceed ±1 standard deviation relative to the detrended mean, and used for the composite analysis. 147
Figure 24: Subsurface thermohaline anomalies off West Antarctica associated with the Ross Gyre variability. (a) Conservative temperature (Θ) anomalies, during strong

Ross Gyre periods and the Ross Gyre boundary are evidenced by the solid black line. **(b)** Same as in **(a)**, but during weak Ross Gyre periods, the Ross Gyre boundary is shown as a dashed black line. **(c)** Difference (D) in Θ between strong and weak Ross Gyre periods. **(d)-(f)** Same as in **(a)-(c)**, respectively, but for absolute salinity, S_A. Blank areas in panels **(c)** and **(f)** indicate differences that are not significant according to the Monte Carlo permutation test. Thin gray contours represent the 500 and 1,500 m isobaths from the RTopo-2 dataset [Schaffer *et al.,* 2016]. 149
Figure 25: Atmospheric anomalies associated with Ross Gyre variability. (a) Sea level pressure (gray contours), the winds (black arrows) and ocean surface stress curl (OSC, shaded colors) anomalies (D) associated with strong Ross Gyre periods shown as a solid black line, **(b)** Same as in **(a)**, but for weak Ross Gyre periods shown as a dashed black line. Thin gray contours represent the 500 and 1,500 m isobaths from the RTopo-2 dataset [Schaffer *et al.,* 2016]. 150
Figure 26: Cross-gyre section's composite difference in subsurface conservative temperature (ΔΘ). Θ of strong Ross Gyre period minus Θ of weak Ross Gyre periods along the cross-gyre section extending from the eastern boundary of the Ross Gyre toward the Amundsen-Bellingshausen Seas (see **Figure 1a**). Solid black contours indicate potential density anomalies (σ_θ) for stronger Ross Gyre periods, while dashed black countours indicate weaker Ross Gyre periods. 151
Figure 27: Temporal subsurface thermohaline properties trends with grid cells masked where not significant and atmospheric conditions forcing trends over the West Antarctica region. (a) conservative temperature (Θ), **(b)** subsurface absolute salinity (S_A) and **(c)** ocean surface stress curl (OSC) trends over the West Antarctica region. The solid black line indicates the time-mean Ross Gyre position. Thin grey contours represent the 500 m and 1,500 m isobaths from the R–Topo2 dataset [Schaffer *et al.,* 2016]. 152
Figure 28: Variability of subsurface temperature and thermocline depth: (a, b) Hovmöller diagrams of subsurface conservative temperature anomalies (Θ) along cross-shelf sections 1 (Amundsen Sea) and 2 (Bellingshausen Sea), respectively (see **Figure 21a**). **(c)** Interannual variability of the mean thermocline depth along the continental shelf, including linear trends and corresponding *p-values* for each section. Shaded areas represent the standard deviation. 154
Figure 29: Schematic representation of the mean circulation at the Northern Antarctic Peninsula. The red (purple) arrows represent the pathways of the Circumpolar Deep Water (Dense Shelf Water) entering Bransfield Strait. The green and yellow lines indicate the mean locations of the Southern Antarctic Circumpolar Current Front (SACCF) and Southern Boundary of Antarctic Circumpolar Current (SB), respectively. Light blue arrows indicate Antarctic Slope Front bifurcation (ASFb) eddy. The orange arrows depict Bransfield Current and its recirculation around the South Shetland Islands (S.S.Is.). The black line represents the mean location of the Antarctic Slope Front (ASF). The red rectangles bounding the magenta and black dots depict hydrographic Sections 1 and 2, respectively. The black dashed line represents the Peninsula Front (PF). The acronyms stand for: Antarctic Channel (AC), Antarctic Coastal Current (ACoC), Joinville Island (J.Is.), D'Urville Island (D'U.Is.), Elephant Island (E. Is.), Clarence Island (C. Is.), Bellingshausen Sea (BS), Drake Passage (DP), Weddell Sea (WS), Western Basin (WB), Central Basin (CB), Eastern Basin (EB), and Gerlache Strait (GS). The thin gray lines indicate the 0.10 km and 0.30 km isobaths provided by https://www.scar.org/science/ibcso/ibcso/. The inset panel depicts the region study. Modified from Damini et al., [2022]. 161
Figure 30: Hydrographic CTD measurements positions across the two repetitive sections

over 2003–2019. 166
Figure 31: Time–averaged (2003–2019) of potential density anomaly ($\sigma\theta$ in kg m^{-3}) and Absolute Salinity (S_A g kg^{-1}) within Bransfield Strait system **(a)** and **(c)** for Section 1, between King George and D' Urville Island (D' U. Is.), and **(b)** and **(d)** for Section 2 between Elephant (E. Is.) and Joinvile Islands (J. Is.). 168
Figure 32: Time–averaged (2003–2019) of conservative temperature (Θ in ºC) within Bransfield Strait system for **(a)** Section 1, between King George and D' Urville Island, and **(b)** Section 2 between Elephant and Joinvile Islands. Scheme modified from Sangrà *et al.,* [2011] of the main components of the Bransfield Strait system along the section crossing of the strait (South Shetland Islands to Antarctic Peninsula) is depicted in **(c)**. The red ⊗ indicates a flow into the page (*i.e.,* northeastward flow), while the blue circle indicates a flow leaving the page (*i.e.,* southwestward flow). The acronyms stand for: Antarctic Coastal Current (ACoC), Bransfield Current (BC), Transitional Zonal Water with Bellingshausen influence (TBW), Transitional Zonal Water with Weddell influence (TWW), and Peninsula Front (PF). The topographic feature along the sections is shown in black and is based on IBCSO v1.0 data (https://www.scar.org/science/ibcso/ibcso/). 169
Figure 33: (a) Temporal evolution of the Southern Annular Mode-El Niño-Southern Oscillation (SEI) indices during austral summer periods (January–March) from 1979 to 2019. The red circles represent the SEI+ years, while the blue circles indicate the SEI– years. **(b)** The correlations between the normalized and detrended summer wind stress curl (WSC) over the northern Antarctic Peninsula and the summer SEI indices are presented, with the Spearman's correlation coefficient (r) and p-value (p) indicating the coefficient and statistical significance of the relationship, respectively. The summertime (January–march) composite maps of the anomaly of 10–m wind vector (black arrows), where **(c)** represents the average of yearly wind anomaly patterns during SEI + periods, and **(d)** represents the average of yearly wind anomaly patterns during SEI– periods. The yearly anomaly wind pattern was calculated from the time-average over the full period (1979-2019) minus each year's wind pattern. 172
Figure 34: Annual cross–section geostrophic velocities at Section 1, between King George and D' Urville Islands (D' U. Is). Positive velocities correspond to Bransfield Current, while negative values indicate Antarctic Coastal Current. The thin black lines indicate the 0 m s^{-1} isolines of velocity. The position of the Peninsula Front (PF) is indicated by the black line on each panel. Black dots indicate the locations of the geostrophic current profiles. Topographic features along the sections are shown in black and are based on IBCSO v1.0 data (https://www.scar.org/science/ibcso/ibcso/). 174
Figure 35: As **Figure 34** but for section 2, between Elephant (E. Is.) and Joinville Islands (J. Is). 175
Figure 36: Time–averaged (2003–2019) of vertical cross–sections **(a)** of geostrophic velocities estimate from hydrographic measurements for the summertime (January–March) at Section 1, between King George and D' Urville Islands (D' U. Is.), and **(b)** Section 2, between Elephant (E. Is.) and Joinville Islands (J. Is.). Positive cross–sections velocities correspond to the Bransfield Current (BC), while negative values indicate the Antarctic Coastal Current (ACoC). The standard deviations of the geostrophic velocity time–averaged based hydrographic measurements are shown in panels **(c)** and **(d)** for sections 1 and 2, respectively. Similarly, the time–average of vertical cross–sections of velocities derived from GLORYS12v1 reanalysis product for the same period (*i.e.,* January–March, 2003–2019) at **(e)** Section 1 and **(f)** Section 2. The corresponding standard deviations of the GLORYS's velocity time–averaged are shown in panels **(g)** and **(h)** for section 1 and 2, respectively. The red ⊗ indicates a flow into the page (*i.e.,*

northeastward flow), while the blue circle indicates a flow leaving the page (*i.e.,* southwestward flow). The thin black lines indicate the 0 isolines of velocity. The position of the Peninsula Front (PF) is indicated by the black line on each panel. The topographic feature along the sections is shown in black and is based on IBCSO v1.0 data (https://www.scar.org/science/ibcso/ibcso/). 177
Figure 37: Surface (~50 m) horizontal distribution of averaged conservative temperature – Θ showing the close match between the 0 cm s-1 isoline (blue) and 0.5 ºC isotherm (dark gray) depicting the Peninsula Front. The thick black lines represent the positions of hydrographic sections 1 (S1) and 2 (S2) analyzed in this study. The acronyms stand for D'Urville Island (D'U.Is.), Clarence Island (C. Is.), Elephant Island (E. Is.), and Joinville Island (J.Is.). 179
Figure 38: Time–averaged (January–March, 2003–2019) of relative vorticity (ζz; colour) and surface geostrophic velocity (vectors) in the Northern Antarctica Peninsula derived from altimetry. The black lines represent the mean position of the hydrographic Section 1 (S1) and Section 2 (S2) analyzed in this study. The yellow and purple arrows represent Bransfield Current and Antarctic Coastal Current, respectively. The black arrow depicts Antarctic Slope Front and ASFb eddy represents the Antarctic Slope Front bifurcation eddy. The acronyms stand for: D'Urville Island (D'U.Is.), Clarence Island (C. Is.), Elephant Island (E. Is.), and Joinville Island (J.Is.).The thin gray lines indicate the 500 m and 800 m isobaths based on IBCSO v1.0 data (https://www.scar.org/science/ibcso/ibcso/). 181
Figure 39: Time–averaged (January–March, 2003–2019) of the mean profile of **(a)** Θ and **(b)** S_A from the two sections by CTD dataset (in red) and GLORYS12v1 output (in blue), with the shaded area representing the standard deviation. 183
Figure 40: Summer–averaged (January–March) conservative temperature (Θ in ºC) – absolute salinity (S_A in g Kg^{-1}) diagrams up to 500 m depth for the two analyzed sections in the Bransfield Strait over the entire study period (2003–2019) for **(a)** GLORYS12v1 reanalysis and **(b)** CTD. The depth is indicated by the colours. The water masses indicated are: Transitional Zonal Water with Bellingshausen influence (TBW), Transitional Zonal Water with Weddell influence (TWW), and modifed Circumpolar Deep Water (mCDW). The boundaries of water masses indicated by black rectangles are based on [Huneke *et al.,*2016; Morozov *et al.,*2021; Gordey *et al.,*2024]. 184
Figure 41: Bathymetry of the Northern Antarctica Peninsula extracted from **(a)** IBCSO v1.0; and **(b)** GLORYS12v1. The thin gray lines indicate the 200 m, 500 m, 800 m, and 2000 m isobaths. The red (purple) arrows represent the pathways of the Circumpolar Deep Water (Dense Shelf Water, via Antarctic Coastal Current – ACoC) entering Bransfield Strait. The orange arrows depict Bransfield Current and its recirculation around the South Shetland Islands (S.S.Is.). Light blue arrows indicate the position of Antarctic Slope Front bifurcation (ASFb) eddy. The black line represents the mean location of Antarctic Slope Front (ASF). The acronyms stand for: D'Urville Island (D'U.Is.), Clarence Island (C. Is.), Elephant Island (E. Is.), and Joinville Island (J.Is.). 186
Figure 42: Time–mean of depth-integrated (50–500 m) velocity field (January–March, 2003–2019) with hydrographic properties averaged over the same depth range as the background field (colour) in the Northern Antarctic Peninsula, derived from GLORYS12v1 for **(a)** conservative temperature (Θ in ºC); **(b)** absolute salinity (S_A in g kg^{-1}) and **(c)** the current magnitude (cm s^{-1}) calculated as $u2 + v2$ where u and v are the zonal and meridional velocity components, respectively. The black lines indicate the mean of positions of hydrographic sections 1 (S1) and 2 (S2) analyzed in this study. The yellow arrows represent the Bransfield Current. The acronyms stand for D'Urville Island (D'U.Is.), Clarence Island (C. Is.), Elephant Island (E. Is.), and Joinville Island (J.Is.).

..... 188
Figure 43: Time–average of vertical cross–sections of velocities derived from GLORYS12v1 reanalysis product for the same period (*i.e.,* January–March, 2003–2019) at **(a)** Section 1 (between King George Island and D' Urville Island – D' U. Is.) and **(b)** Section 2 (between Elephant Island – E. I.s and Joinville Island..... 190
Figure 44: Surface horizontal distribution of time–averaged (January–March, 2003–2019) wind stress curl (colour–coded), with purple and red solid arrows representing the time-averaged volume transport (Sv) of Transitional Zonal Water with Weddell influence (TWW) and Transitional Zonal Water with Bellingshausen influence (TBW), respectively. The mean position of Sections 1 (S1) and 2 (S2) are depicted as black solid lines. Additionally, the length of the arrows indicates the magnitude of these transports. The grey vectors depict the wind stress. The acronyms stand for: D'Urville Island (D'U.Is.), Clarence Island (C. Is.), Elephant Island (E. Is.), and Joinville Island (J.Is.). 191
Figure 45: Surface horizontal distribution of averaged wind stress curl anomaly (colour–coded) of (a) SEI+ phase summers (i.e., 2006, 2008, 2009, 2011, 2012, 2013, 2014, 2015, and 2018) and (b) SEI– phase summers (i.e., 2010, 2016, and 2019). The purple and red solid arrows represent the time-averaged volume transport (Sv) of Transitional Zonal Water with Weddell influence (TWW) and Transitional Zonal Water with Bellingshausen influence (TBW), respectively, and their widths indicate the magnitude of these transports. The time-averaged of the TBW and TWW transports and the standard deviation of time-averaged are indicated by numbers. Southern Antarctic Circumpolar Current Front (SACCF) is represented by a black dashed line in both maps, while the mean position of Sections 1 (S1) and 2 (S2) are denoted by black solid lines. The acronyms stand for: D'Urville Island (D'U.Is.), Clarence Island (C. Is.), Elephant Island (E. Is.), and Joinville Island (J.Is.)..... 194

Supplementary Figure 1: Evolution of the conservative temperature (Θ, ºC) of CDW each decade from the hydrographic dataset and GLORYS output. Decadal average of Conservative temperature (Θ ºC) during **a** 1990s, **b** 2000s, and **c** 2010s from GLORYS output and **d**–**f** the same periods from hydrographic measurements. Blue and black lines indicate the mean position of the Southern Antarctic Circumpolar Current Front (SACCF) during the 1990s and 2010s, respectively, based on GLORYS output (panels on the left column) and satellite altimetry (panels on the right column). Thin grey contours represent the 500 m and 1,500 m isobaths from the R–Topo2 dataset [Schaffer et al., 2016]. ... 133
Supplementary Figure 2: As in the same **Supplementary Figure 1**, but to Absolute Salinity (S_A; g kg^{-1})..... 134
Supplementary Figure 3: Decadal displacement of SACCF and westerly wind. **a** The blue (black) solid lines represent the decadal average position of the SACCF in the 1990s (2010s). The shaded areas indicate the standard deviation of the decadal average positions. **b** Position of the westerly wind (defined as maximum of zonal wind speed between 30ºS and 70ºS) for ERA5. 135
Supplementary Figure 4: Decadal linear trends of CDW termohaline Properties for (a) Conservative temperature – Θ; ºC, and (b) Absolute Salinity – SA; g kg^{-1}..... 136
Supplementary Figure 5: Ross Gyre position and time series of gyre strength defined using the barotropic streamfunction. (a) Time-mean Ross Gyre boundary defined by the −8 Sv barotropic streamfunction closed contour (black) and all monthly −8 Sv closed contours (gray) during 1993–2020. **(b)** Ross Gyre strength time series computed using five different streamfunction contours. Although the absolute transport values vary with

the selected contour, all estimates remain highly correlated with the −8 Sv-based metric ($r > 0.9$). 157
Supplementary Figure 6: Correlation coefficient between the gyre strength, defined as the mean value of the barotropic streamfunction within the −8 Sverdrup contour, and ocean surface stress curl in each grid cell. The green contour indicates the mean gyre boundary. Blank areas denote regions where the correlation is not statistically significant. The black box marks the region of highest correlation, interpreted here as the area that most strongly forces the gyre. The ocean surface stress curl averaged over this region is shown in **Figures 23c and 24c**. 158
Supplementary Figure 7: Interannual and seasonal variability of Buoyancy fluxes. **(a)** Interannual buoyancy fluxes time-series averaged at the continental shelves off Ross Sea. Red and blue rectangles denote strong and weak gyre periods, respectively, defined as periods when gyre strength anomalies exceed ±1 standard deviation relative to the detrended mean, and used for the composite analysis. **(b)** Seasonal buoyancy fluxes time-series averaged at the continental shelves off Ross Sea. The correlation coefficient between gyre strength and buoyancy fluxes interannual and seasonal, corresponding panel. 158
Supplementary Figure 8: Composite difference (Δ) of the core of CDW layer depth between strong and weaker Ross Gyre periods. Positive (negative) anomalies indicate downwelling (upwelling) of the warm CDW layer during intensified gyre circulation. The solid black line shows Ross Gyre's time-mean position. Thin grey contours represent the 500 m and 1,500 m isobaths from the R-Topo2 dataset [Schaffer et al., 2016]. 159
Supplementary Figure 9: Hovmöller diagrams of subsurface thermohaline variability and thermocline depth along the Amundsen and Bellingshausen shelf sections: (a) Absolute Salinity, S_A (g kg^{-1}), along Section 1 in the Amundsen Sea; **(b)** same as in **(a)**, but along Section 2 in the Bellingshausen. 159
Supplementary Figure 10: Annual cross–section conservative temperature in Section 1 (Θ in ºC), between King George and D' Urville Islands. The thin black lines indicate the –0.5 and 0 isolines. The topographic feature along the sections is shown in black and is based on IBCSO v1.0 data (https://www.scar.org/science/ibcso/ibcso/). 198
Supplementary Figure 11: As **Supplementary Figure S10** but for section 2, between Elephant (E.Is.) and Joinville Islands. 199
Supplementary Figure 12: Annual cross–section absolute salinity in Section 1 (S_A in g kg^{-1}), between King George and D' Urville Islands. The thin black lines indicate the 34.3, 34.4 and 34.7 isolines. The topographic feature along the sections is shown in black and is based on IBCSO v1.0 data (https://www.scar.org/science/ibcso/ibcso/). 200
Supplementary Figure 13: As **Supplementary Figure 12** but for section 2, between Elephant (E. Is.) and Joinville Islands. 201
Supplementary Figure 14: Distribution of average Circumpolar Deep Water (CDW) thickness layer (colour) during **(a)** the entire study period (2003-2019), **(b)** positive Southern Annular Mode–El Niño–Southern Oscillation Index (SEI+) phases (i.e., 2008, 2009, 2011, 2013, 2014, 2015, and 2018) and **(c)** negative SEI (SEI–) phases (i.e., 2004, 2010, 2016, and 2019. Elephant and King George Islands are labelled as E. Is., and K.G. Is., respectively. 202
Supplementary Figure 15: Depth–averaged (50–500 m) of conservative temperature – Θ (colour–coded) and the depth–integrated (50–500 m) geostrophic velocity (vectors) of (a) SEI+ phase summers (i.e., 2006, 2008, 2009, 2011, 2012, 2013, 2014, 2015, and 2018) and (b) SEI–phase summers (i.e., 2010, 2016, and 2019). The acronyms stand for: D' Urville Island (D'U.Is.), Clarence Island (C. Is.), Elephant Island (E. Is.), and Joinville Island (J.Is.). 203

Supplementary Figure 16: (a) Time–series of Transitional Zonal Water with Bellingshausen influence (TBW) transports. The green circles represent the SEI+ years, while the blue circles indicate the SEI– years. Positive (negative) values indicate TBW inflow (outflow) to Bransfield Strait Panels **(b)** and **(c)** show the surface horizontal distribution of the wind stress curl anomaly (colour–coded) during positive SEI phase (i.e., 2012 and 2018, respectively), while panels **(d)** and **(f)** represent negative SEI phase (i.e., 2010 and 2016, respectively). The years were selected to represent a year of highest and lowest TBW intrusion for each SEI period (e.g., SEI+ and SEI–). 204
Supplementary Figure 17: Potential density anomaly ($\sigma\theta$, in kg m^{-3}), conservative temperature (Θ ºC) and absolute salinity (S_A g $kg^{-}1$) within the Bransfield Strait system at sections 1 (between Elephant Island – E. Is. and Joinville Islands – J. Is.) and 2 (between King George and D' Urville Island – D'U. Is.). Panels (a), (b), (e), (f), (i), and (j) represent the time-averaged conditions during SEI+ phase summers (2006, 2008, 2009, 2011, 2012, 2013, 2014, 2015, and 2018), while panels (c), (d), (g), (h), (k) and (i) represent the time-averaged conditions during SEI– phase summers (2010, 2016, and 2019)..... 205

Lista de Acrônimos e Abreviações

A

AASW – Água de Superfície Antártica (*Antarctic Surface Water)*

ACC – Corrente Circumpolar Antártica (*Antarctic Circumpolar Current*)

ACoC – Corrente Costeira Antártica (*Antarctic Coastal Current)*

***ADT* –** Topografia Absoluta Dinâmica *(Absolute dynamic Topography)*

ASC – Corrente de Talude Antártica (*Antarctic Slope Current*)

ASF – Frente do Talude (*Antarctic Slope Front*)

ASFb eddy – vórtice de Bifurcação da Frente de Talude Antártico (*Antarctica Slope Front bifurcation eddy*)

ASL – baixa do mar de Amundsen (*Amundsen Sea Low*)

B

BC – Corrente de Bransfield (*Bransfield Current)*

C

CO_2 – Dióxido de carbono (*Carbon Dioxide*)

CDW – Água Profunda Circumpolar (*Circumpolar Deep Water*)

CCHDO – *CLIVAR and Carbon Hydrographic Data Office*

D

DSW – Água Densas de plataforma (*Dense Shelf Water*)

E

ENSO – *El Niño*–Oscilação Sul (*El Niño–Southern Oscillation)*

G

GOAL – Grupo de Oceanografia de Altas Latitudes

GLORYS12v1 – *Global Ocean Reanalysis and Simulation*

I

IPCC – Painel Intergovernamental sobre Mudanças Climáticas (*Intergovernmental Panel on Climate Change*)

M

MEOP – *Marine Mammals Exploring the Ocean Pole to Pole*

P

PF – Frente da Península (*Peninsula Front*)

PROANTAR – Programa Antártico Brasileiro

S

SACCF – Frente Sul da Corrente Circumpolar Antártica (*Southern Antarctic Circumpolar Current Front*)

SAM – Modo Anular Sul (*Southern Annular Mode)*

***SB* –** *Limite Sul da Corrente Circumpolar Antártica (Southern Boundary of Antarctic Circumpolar Current)*

SSH – Altura da Superfície do Mar (*Sea Surface Height)*

SLP – Pressão ao nível do mar (*Sea Level Pressure*)

T

TWW – Água Transicional do mar de Weddell (*Transitional Zonal Water with Weddell influence)*

TBW – Água Transicional do mar de Bellingshausen (*Transitional Zonal Water with Bellingshausen influence)*

W

WW – Água de inverno (*Winter Water*)

WOD23 – *World Ocean Database 2023*

#

Θ – Temperatura Conservativa (Conservative Temperature)

σ – Densidade Potencial

$\mathbf{S_A}$ – Salinidade Absoluta (Absolute Salinity)

$\mathbf{S_p}$ – Salinidade prática (Pratical Salinity)

Ψ – Altura dinâmica (Dynamic Height)

$\boldsymbol{\mathcal{B}}$ – Fluxo de Flutuabilidade Superficial (Surface Buoyancy Fluxe)

Prefácio

Nas últimas décadas, o planeta tem passado por mudanças climáticas aceleradas impulsionadas pelo aumento exacerbado de gases de efeito estufa na atmosfera, como o dióxido de carbono. As concentrações atuais de dióxido de carbono ultrapassam 420 partes por milhão (ppm), um nível recorde que representa cerca de 50% acima das concentrações no período pré-industrial. Essa alta concentração de dióxido de carbono na atmosfera tem influenciado diretamente o aquecimento do sistema climático (como, por exemplo, os oceanos). Esse excesso de calor absorvido e armazenado pelos oceanos resulta na intensificação da frequência de eventos extremos, como as recentes crises hidrológicas no Brasil (enchentes em algumas regiões e secas em outras), e acelera o derretimento das regiões polares, ameaçando elevar o nível do mar em até 1 metro até 2100 (cenário que coloca em risco a existência de diversas cidades litorâneas). Nesse contexto de mudanças climáticas, o oceano Austral aparece como um protagonista, atuando como um responsável por armazenar vastas quantidades de calor e carbono através da formação de águas de fundo. Contudo, a estabilidade desse mecanismo é incerta. O aquecimento das águas profundas circumpolares, que ressurgem ao redor da Antártica, está acelerando o derretimento basal das plataformas de gelo. Esse processo cria um ciclo de retroalimentação que compromete a própria formação das águas de fundo e a ventilação do oceano profundo. Esta tese visa investigar os mecanismos influenciadores do aquecimento dessas águas profundas, a fim de trazer uma melhor compreensão desses processos. Entender tal dinâmica é crucial para aprimorar os modelos de estabilidade futura das plataformas de gelo da Antártica e, consequentemente, refinar as estimativas sobre a elevação global do nível do mar. Esta tese foi elaborada no formato de artigos, conforme as normas do Programa de Pós-Graduação em Oceanologia, estando os manuscritos correspondentes reunidos no **Capítulo IV**. Além disso, o texto foi redigido em português e inglês, com o objetivo de ampliar seu alcance e a acessibilidade das informações.

Preface

Over the past decades, the planet has undergone accelerated climate change driven by the sharp increase in greenhouse gases in the atmosphere, particularly carbon dioxide. Current atmospheric CO_2 concentrations now exceed 415 parts per million (ppm), a record level roughly 50% higher than pre-industrial values. This elevated concentration has directly intensified the warming of the climate system, including the oceans. The excess heat absorbed by the oceans, for instance, contributes to the increased frequency of extreme events, such as recent hydrological crises in Brazil (floods in some regions and droughts in others) and accelerates the melting of polar regions, which could raise global sea levels by up to 1 meter by 2100, putting numerous coastal cities at risk. Within this context of climate change, the Southern Ocean emerges as a key factor, responsible for storing vast amounts of heat and carbon through the formation of bottom waters. However, the stability of this mechanism is increasingly uncertain. The warming of circumpolar deep waters, which upwell around Antarctica, is accelerating the basal melting of ice shelves. This process establishes a feedback loop that undermines both the formation of bottom waters and the ventilation of the deep ocean. This thesis aims to investigate the mechanisms driving the warming of these deep waters, in order to improve our understanding of the underlying processes. Understanding this dynamic is crucial for improving models of future stability of Antarctic ice shelves, and consequently, refining estimates of global sea-level rise.

Hipótese

A variabilidade das propriedades termohalinas da Água Profunda Circumpolar na região oeste da Antártica é primariamente controlada pela modulação da posição do sistema frontal da Corrente Circumpolar Antártica impulsionada pelos ventos de oeste.

Hypothesis

The variability of the thermohaline properties of Circumpolar Deep Water in the western Antarctic region is primarily controlled by the modulation of the position of the frontal system of the Antarctic Circumpolar Current driven by westerly winds.

Capítulo I: Introdução

Nas últimas décadas, as avaliações globais do clima têm destacado o ritmo acelerado das mudanças climáticas antropogênicas e os seus impactos desproporcionais em altas latitudes. De acordo com o mais recente relatório do Painel Intergovernamental sobre Mudanças Climáticas [IPCC; sigla do inglês *Intergovernmental Panel on Climate Change*; IPCC, AR6], as concentrações atmosféricas de dióxido de carbono (CO_2) atingiram níveis sem precedentes em pelo menos 2 milhões de anos (~420 ppm em 2021), impulsionando o aumento das temperaturas globais, o aumento do conteúdo de calor armazenado nos oceanos e um declínio generalizado da criosfera.

O oceano Austral é responsável por absorver a maior parte do excesso de calor incorporado pelo oceano global (~75%) e também por reter cerca de 43% das emissões antropogênicas de carbono (ou seja, de origem humana). Portanto, atua como um regulador climático e retarda a manifestação completa do aquecimento global [IPCC AR6; Frölicher *et al.,* 2015; Gruber *et al.,* 2019; Friedlingstein *et al.,* 2020].

No interior da complexa circulação do oceano Austral encontra-se a mais intensa corrente oceânica do planeta, a Corrente Circumpolar Antártica [ACC, sigla do inglês *Antarctic Circumpolar Current*; *e.g.,* Rintoul & Sokolov, 2001; Mazloff *et al.,* 2010], formada, pela ausência de barreiras continentais ao seu fluxo zonal. Isso resulta em uma corrente dirigida pelos ventos de oeste, que flui para leste e circunda a Antártica [*e.g.,* Talley, 2011]. Além disso, a ACC conecta todas as principais bacias oceânicas (Atlântico, Índico e Pacífico; **Figura 1**), constituindo uma componente crucial da circulação meridional de revolvimento global. Essa conectividade entre bacias permite a troca de propriedades das massas de água e de sinais climáticos, sustentando teleconexões oceânicas em larga escala [*e.g.,* Peterson & White, 1998].

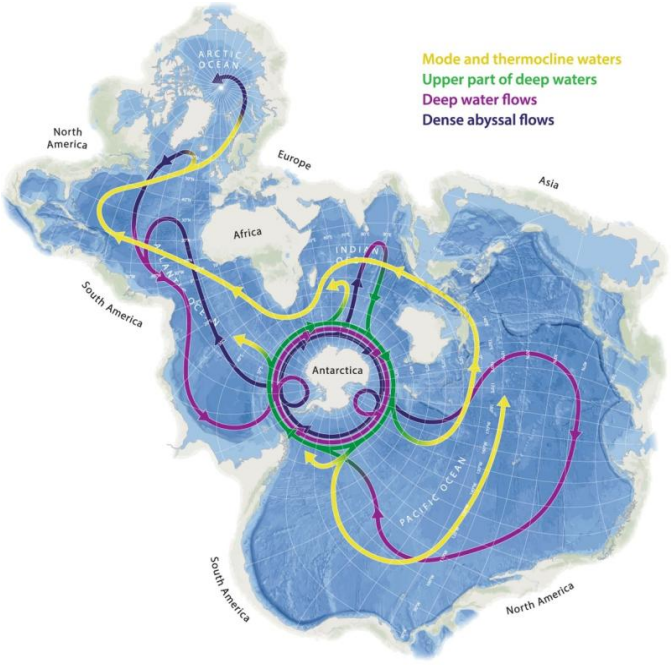


Figura 1: Esquema da circulação de revolvimento na perspectiva do oceano Austral. Esta região é o local mais proeminente do mundo onde águas profundas (roxo) ascendem à superfície, trocam calor e carbono com a atmosfera e, depois, retornam ao interior do oceano. Figura extraída de Meredith *et al.,* [2022].

O volume de transporte de água da ACC está concentrado em uma série de frentes bem definidas e separadas entre si por assinaturas distintas de temperatura e salinidade, e associadas a jatos de grande profundidade e à subducção ou ressurgência de diferentes massas de água (*i.e.,* a Frente Subtropical, a Frente Subantártica, a Frente Polar, a Frente Sul da ACC e a Frente do Limite Sul; Orsi *et al.,* 1995; **Figura 2**; **ver capítulo II para mais informações**). Aproximadamente 55% do transporte da ACC tem origem na Água Profunda Circumpolar (CDW, sigla do inglês *Circumpolar Deep Water*), quente e salina, que aflora próximo ao seu limite sul, tornando-se disponível para intrusão sobre a plataforma continental antártica, onde transfere calor oceânico para as cavidades sob as plataformas de gelo.

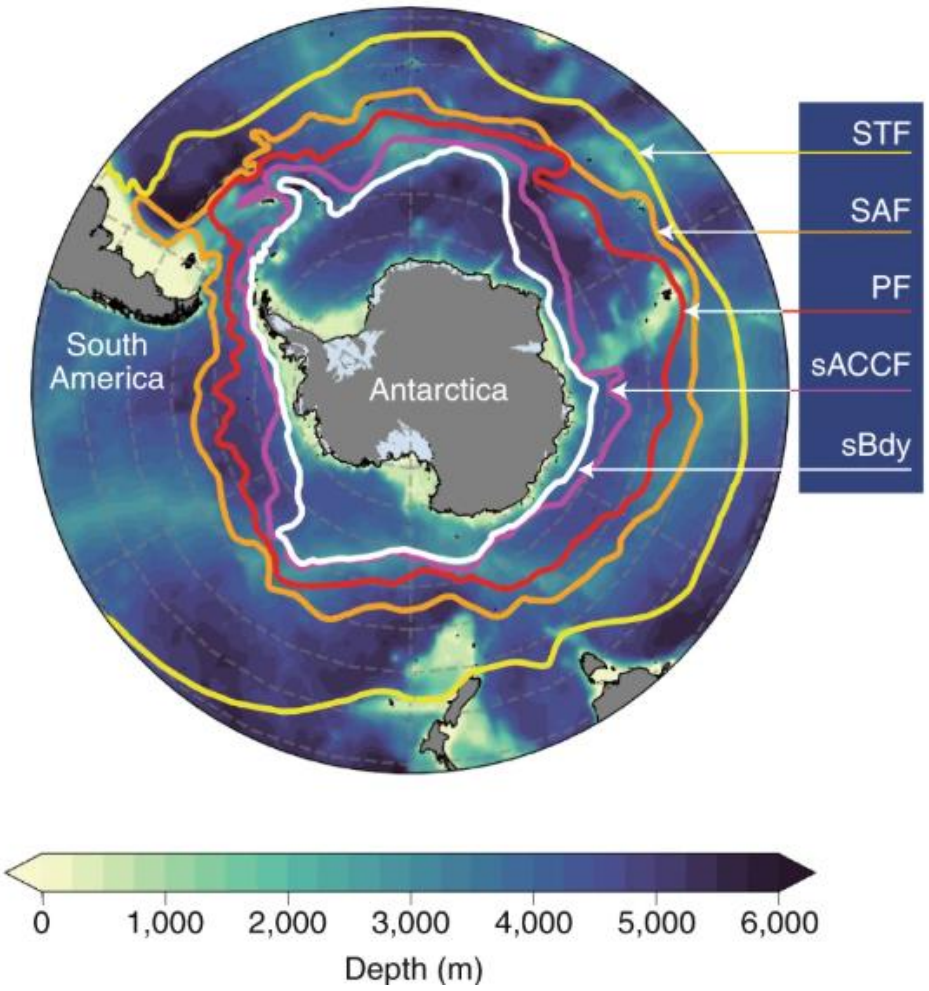


Figura 2: Posição média do sistema frontal da Corrente Circumpolar Antártica determinada por Orsi *et al.,* [1995] a partir de dados hidrográficos históricos e com base em critérios de massas d'água (como um valor específico de temperatura em certa profundidade) para definir suas localizações. As frentes nomeadas são, de norte a sul: Frente Subtropical (STF), Frente Subantártica (SAF), Frente Polar (PF), Frente Sul da ACC (sACCF) e a Frente do Limite Sul (SBdy). O colorbar de fundo mostra a profundidade do oceano. Figura extraída de Chapman *et al.,* [2020].

Diversos mecanismos são responsáveis pelo transporte da CDW para as plataformas continentais antárticas, tais como: (i) ressurgência ou sucção de Ekman induzido pelo vento na quebra da plataforma, modulado pelos ventos de oeste ao norte dessa região, que geram para norte na camada superficial e forçam a ascensão da CDW, permitindo sua penetração sobre a plataforma [*e.g.,* Kim *et al.,* 2017]; (ii) o escoamento através dos cânions submarinos, com extravasamento sobre a plataforma continental, controlado por variações nos ventos de leste, que modulam a corrente subsuperficial dirigida para oeste existente nessa região. A interação dessa corrente com a batimetria (especialmente com os cânions submarinos) direciona a CDW em direção à plataforma

continental [*e.g.,* Arneborg *et al.,* 2012; Walker *et al.,* 2013; Silvano *et al.,* 2022]; e (iii) a difusão associada a vórtices desprendidos da ACC devido à instabilidade baroclínica imposta pelos ventos de oeste [*e.g.,* Yamazaki *et al.,* 2021, 2023]. De modo geral, esses processos são influenciados pela variabilidade dos padrões de vento associados a modos climáticos de grande escala [*e.g.,* Modo Anular do Sul – SAM, *El Niño*/Oscilação Sul – ENSO e a Baixa do mar de Amundsen – ASL; Jenkins *et al.,* 2018; Dotto *et al.,* 2020].

Estudos recentes têm documentado um aquecimento significativo nas últimas décadas (~0,1 °C por década) nas camadas intermediárias e profundas do oceano Austral (na camada da CDW, abaixo de 200 m). Na região ao largo da plataforma continental do leste da Antártica, cerca de 60% desse aquecimento tem sido atribuído ao deslocamento para o polo do sistema frontal da ACC e de sua estrutura hidrográfica, o que substitui a CDW relativamente mais fria na borda sul da ACC por uma CDW mais quente proveniente de latitudes mais ao norte [Herraiz-Borreguero & Naveira Garabato, 2022]. Um segundo mecanismo-chave é o aumento do transporte de calor ao longo das superfícies isopicnais através da ACC [*e.g.,* via atividade de redemoinhos; Yamazaki *et al.,* 2021; Herraiz-Borreguero & Naveira Garabato, 2022]. Ambos os processos estão associados às mudanças das forçantes dos ventos ligadas à variabilidade climática em larga escala [Yamazaki *et al.,* 2021, 2023; Zu *et al.,* 2022]. Esse aquecimento oceânico progressivo tem implicado no aumento do derretimento basal das plataformas de gelo [Herraiz-Borreguero & Naveira Garabato, 2022; Rott *et al.,* 2018], resultando em mudanças significativas do nível do mar [Sheperd *et al.,* 2010] e na redução na formação de águas de fundo [Silvano *et al.,* 2018].

Embora esses mecanismos estejam relativamente bem estabelecidos para a região leste da Antártica, os fatores que controlam a variabilidade da CDW na região ao largo da plataforma continental da região oeste da Antártica (*i.e.,* mares de Amundsen e Bellingshausen e a Península Antártica) permanecem menos compreendidos [*e.g.,* Nakayama *et al.,* 2018]. Essa lacuna de conhecimento é particularmente preocupante, uma vez que os eventos mais rápidos de afinamento e colapso de plataformas de gelo observados na Antártica ocorreram ao longo da margem oeste do continente, impulsionados por intrusões de CDW através de vales batimétricos profundos [*e.g.,* Rignot *et al.,* 2019]. Assim, compreender em detalhe como a migração das frentes da ACC para o polo e as mudanças associadas aos ventos modulam o acesso da CDW à plataforma continental é essencial para prever a evolução futura da camada de gelo

antártica [*e.g.,* Gille *et al.,* 2016] e sua contribuição para a circulação meridional de revolvimento global e para o aumento do nível do mar [Morrison *et al.,* 2020].

Dessa forma, o foco desta tese é investigar as mudanças das propriedades termohalinas da CDW na região ao largo da plataforma continental do oeste da Antártica (*i.e.,* mares de Amundsen e Bellingshausen) entre as décadas de 1990 e 2010 (i.e.,1990-2020), destacando as variações interdecenais nas propriedades da CDW e buscando compreender os mecanismos que afetam essa variabilidade termohalina da CDW oceânica e suas possíveis consequências nas regiões sobre a plataforma continental. Para alcançar tal objetivo, foram utilizadas observações hidrográficas providas por diversos bancos de dados oceanográficos de livre acesso [*i.e., World Ocean Database 23*, *Thwaites-Amundsen Regional Survey and Network*, *Argo*; CLIVAR and *Carbon Hydrographic Data Office*; e *Marine Mammals Exploring the Ocean Pole to Pole consortium data*] e uma reanálise oceânica de alta resolução [*Global Ocean Reanalysis and Simulation;* GLORYS12v1; Jean–Michel *et al.,* 2021].

Além disso, essa tese busca examinar a variabilidade da intrusão dessa CDW modificada no estreito de Bransfield, localizado adjacente à Península Antártica, uma região considerada chave para o estudo dos impactos das mudanças climáticas devido ao seu ambiente transicional que conecta as águas do regime de plataforma fria do mar de Weddell ao regime oceânico relativamente mais quente do mar de Bellingshausen [Kerr *et al.,* 2018]. Essa é também a área mais estudada pelo Grupo de Oceanografia de Altas Latitudes (GOAL) desde os anos 2000 [Mata *et al.,* 2018]. Ao avançar o entendimento dos processos de circulação (*i.e.,* as regiões de entrada da CDW) nessa região, esta pesquisa visa subsidiar e informar futuros estudos físicos, biogeoquímicos e ecológicos conduzidos no âmbito do Programa Antártico Brasileiro (PROANTAR).

A seguir, apresentam-se os objetivos que orientam o desenvolvimento desta tese. O **Capítulo II** descreve a área de estudo com base em uma revisão bibliográfica detalhada, enquanto o **Capítulo III** apresenta a metodologia adotada para alcançar esses objetivos. Por fim, resultados e as discussões (que resultam nos manuscritos publicados ou submetidos) desta tese serão apresentados no **Capítulo IV** e posteriormente, no **Capítulo V**, um sumário das principais conclusões desta tese.

1.1 Objetivos

1.1.1 Objetivo geral

- Investigar a variabilidade temporal e espacial das propriedades termohalinas da CDW e avaliar os mecanismos que influenciam a sua intrusão na região oeste da Antártica.

1.1.2 Objetivos específicos

- Examinar a contribuição da posição do sistema frontal da ACC na variabilidade interdecenal, entre as décadas de 1990 (1991 – 2000) e 2010 (2011 – 2020), das propriedades termohalinas da CDW nos mares de Amundsen e Bellingshausen.

- Investigar o papel do Giro de Ross como modulador da variabilidade sazonal e interanual das propriedades da CDW nos mares de Amundsen e Bellingshausen.

- Investigar a influência do vento no transporte da CDW sobre a plataforma continental da Península Antártica e analisar a variabilidade interanual desse transporte durante o período de 2000 a 2020.

Capítulo II: Área de estudo

2.1 Sistema frontal da Corrente Circumpolar Antártica

A ACC é caracterizada por diversas frentes, as quais representam limites entre zonas com propriedades hidrográficas distintas de massas de água (**Figura 3**). As principais zonas delimitadas por essas frentes oceânicas são: (i) Zona Subantártica, localizada entre a Frente Subantártica e a Frente Polar; (ii) Zona da Frente Polar, situada entre a Frente Polar e a Frente Sul da ACC; e (iii) Zona Antártica, compreendida entre a Frente Sul da ACC (SACCF, sigla do inglês *Southern Antarctic Circumpolar Current Front*) e o continente. Na Zona Antártica, é possível distinguir ainda o regime subpolar, correspondente à região ao sul da Frente do Limite Sul, e a zona continental, caracterizada pela circulação e pelo transporte associados à Corrente de Talude Antártica (ASC, sigla do inglês *Antarctic Slope Current*).

A variabilidade sazonal e interanual no transporte, na extensão e na posição das frentes da ACC tem sido amplamente investigada nas últimas décadas por meio de diversas abordagens observacionais, incluindo propriedades de massas de água [*e.g.,* Orsi *et al.,* 1995; Kim & Orsi, 2014], contornos fixos de altura da superfície do mar (SSH sigla do inglês; *Sea Surface Height*) e/ou contornos fixos de Topografia Dinâmica Absoluta (ADT[1] sigla do inglês Absolute Dynamic Topography), gradientes de altura da superfície

[1] Topografia dinâmica absoluta (ADT): é um tipo específico de conjunto de dados de SSH. O ADT representa a altura total e instantânea da superfície do oceano acima do geoide, calculada como a soma das

do mar em relação ao geoide e posições médias de transporte [*e.g.,* Sokolov & Rintoul, 2007, 2009a,b; Billany *et al.,* 2010; Gille, 2014; Gille *et al.,* 2016; Schiavon *et al.,* 2025]. Alguns desses estudos revelaram que as frentes da ACC sofreram deslocamentos espacialmente heterogêneos, com algumas regiões apresentando pronunciado deslocamento em direção ao polo sul, enquanto outras permanecem relativamente estacionárias devido ao controle topográfico e aos efeitos de saturação de vórtices[2] [*e.g.,* Sokolov & Rintoul, 2009a, b; Yamazaki *et al.,* 2022; Herraiz-Borreguero & Naveira Garabato, 2022]. Por exemplo, Sokolov e Rintoul [2009b] usando contornos de SSH fixos para definir cada frente da ACC ao longo de 15 anos (1992–2007) relataram um deslocamento sentido ao polo Sul de ~0,6° de latitude (~60–70 km). No entanto, os autores alertaram que a latitude de contornos fixos de SSH reflete não apenas mudanças dinâmicas no escoamento geostrófico, mas também variações estéricas (*i.e.,* expansão ou contração do volume) do nível do mar associadas ao aquecimento, resfriamento nas camadas superiores do oceano (*e.g.,* efeitos termostéricos) de longo prazo cuja correção permanece um desafio.

Diante dessas incertezas, permanece em aberto e ativamente debatida na oceanografia polar a questão sobre o deslocamento ou não das frentes da ACC. Para minimizar a influência dos efeitos termostéricos, Gille, [2014] aplicou um índice de latitude de transporte (uma média latitudinal ponderada pelo transporte geostrófico) e constatou que a posição média circumpolar da ACC permaneceu amplamente estável nas décadas de 1990 e 2000. Contudo, a interpretação de médias circumpolares deve ser feito com cautela, uma vez que o sistema frontal da ACC não se comporta como uma estrutura única [Kim & Orsi, 2014]. Tendências regionais opostas podem, portanto, se anular mutuamente, levando a um sinal médio circumpolar suavizado que oculta as flutuações regionais. Nesse sentido, estudos mais recentes, que utilizam campos de temperatura subsuperficial para identificar a Frente do Limite Sul da ACC, observaram seu deslocamento para o polo em cerca de 150 km entre as décadas de 1990 e 2010, ao longo da região leste da Antártica [*e.g.,* Yamazaki *et al.,* 2022; Herraiz-Borreguero & Naveira Garabato, 2022]. Tal deslocamento para o sul intensificou o transporte de calor oceânico

Anomalias do Nível do Mar e da Topografia Dinâmica Média.
[2]Saturação de Vórtices: Em vez do fluxo médio acelerar ou da frente se mover, a energia extra do vento é imediatamente convertida para o campo de vórtices de mesoescala [Marshal & Radko, 2003].

em direção à região, potencialmente amplificando o derretimento basal e ameaçando a estabilidade de longo prazo da camada de gelo [*e.g.*, Herraiz-Borreguero & Naveira Garabato, 2022].

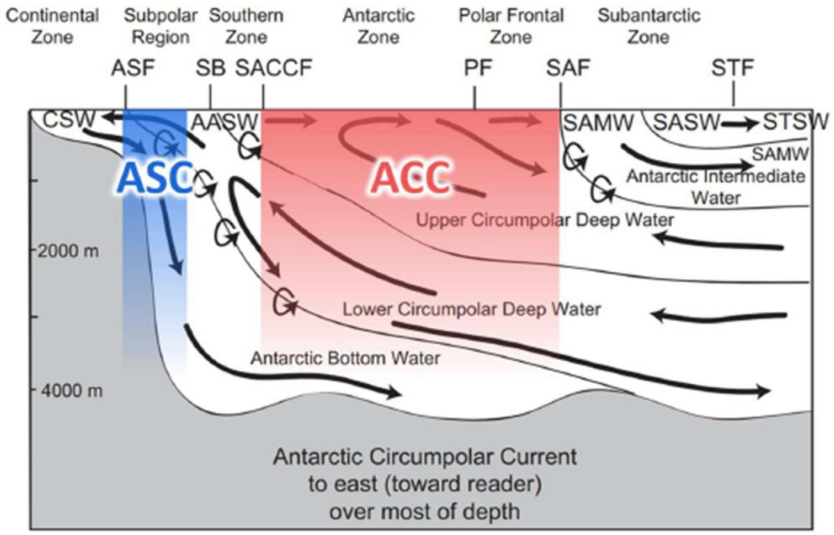


Figura 3: Vista vertical zonal (da superfície ao oceano profundo) dos fluxos meridionais das principais massas d'água que entram e saem do oceano Austral. As siglas derivadas do inglês são: Corrente Circumpolar Antártica (ACC), Água da Plataforma Continental (CSW), Água de Superfície Antártica (AASW), Água Modal Subantártica (SAMW), Água de Superfície Subantártica (SASW), Água de Superfície Subtropical (STSW), Água Intermediária Antártica (AIW), Água Profunda Circumpolar Superior (UCDW), Água Profunda Circumpolar Inferior (LCDW), Água de Fundo Antártica (AABW), Frente de Talude Antártica (ASF), Frente do Limite Sul (SB), Frente Sul da ACC (SACCF), Frente Polar (PF), Frente Subantártica (SAF) e Frente Subtropical (STF). As siglas ASC e ACC representam a corrente de talude e a corrente circumpolar respectivamente. Figura extraída de Yamazaki, 2022.

2.2 Circulação do oceano Austral ao longo da região oeste da Antártica

O setor oeste da Antártica situa-se no setor do oceano Pacífico do oceano Austral, abrangendo os mares de Amundsen e Bellingshausen e a Península Antártica, e é particularmente sensível às mudanças nos padrões regionais de vento, os quais são fortemente modulados pela circulação atmosférica de grande escala [Turner *et al.*, 2017; Dotto *et al.*, 2020; Damini *et al.*, 2022; Oelerich *et al.*, 2022]. O padrão regional de ventos é caracterizado por ventos de oeste ao norte do talude continental (em torno de 60°S) e ventos de leste sobre a plataforma continental (próximos de 70°S). Entretanto, na porção leste desse setor, entre o leste do mar de Bellingshausen e a Península Antártica, os ventos de leste estão praticamente ausentes, resultando em um regime de ventos costeiros mais

fraco.

A zona de transição entre esses sistemas de ventos opostos é conhecida como Divergência Antártica, uma região dinamicamente importante associada à intensa ressurgência de águas intermediárias e profundas (*e.g.,* CDW). Essa ressurgência é impulsionada pela circulação ciclônica de ventos (*i.e.,* rotacional negativo da tensão do cisalhamento do vento) gerada pela divergência entre os cinturões de ventos de oeste e de leste. A Divergência Antártica localiza-se tipicamente na borda sul da ACC, entre a SACCF e a Frente do Limite Sul.

Tal padrão de ventos regionais é altamente variável devido à influência da baixa do mar de Amundsen (ASL, sigla do inglês *Amundsen Sea Low*), um centro persistente de baixa pressão localizado entre os mares de Amundsen e Bellingshausen (**Figura 4**), que se desloca zonal e meridionalmente ao longo do ano [*e.g.,* Raphael *et al.,* 2016]. O aprofundamento (*i.e.,* fortalecimento) da ASL intensifica a circulação ciclônica de ventos sobre a região, promovendo o transporte de CDW em direção à região oeste da Antártica e, consequentemente, podendo aumentar o derretimento basal das plataformas de gelo [*e.g.,* Paolo *et al.,* 2018; Dotto *et al.,* 2020]. Outrossim, modos de variabilidade climática em larga escala, como o Modo Anular Sul (SAM, sigla do inglês *Southern Annular Mode)* e o *El Niño*–Oscilação Sul (ENSO, sigla do inglês *El Niño–Southern Oscillation*), modulam a intensidade e a posição da ASL e, portanto, influenciam o campo de ventos [Fogt *et al.,* 2012; Clem *et al.,* 2017].

O ENSO está relacionado a mudanças anômalas na temperatura do oceano tropical. Isso leva a mudanças no campo de pressão atmosférica e no padrão de ventos que se propagam por meio de ondas de Rossby atmosféricas para outras partes do globo, incluindo o oeste da Antártica (*e.g.,* Yuan, 2004). Durante a fase positiva (*El Niño*), ocorre uma anomalia positiva da pressão atmosférica sobre a Antártica (**Figura 4a**), enfraquecendo os ventos de oeste e deslocando a linha de nível do mar para oeste (em direção ao mar de Ross). Já durante a fase negativa (*La Niña*), ocorre uma anomalia negativa da pressão atmosférica sobre a Antártica (**Figura 4b**), fortalecendo os ventos de oeste e deslocando a linha de nível do mar para leste [em direção ao mar de Bellingshausen; Raphael *et al.,* 2016].

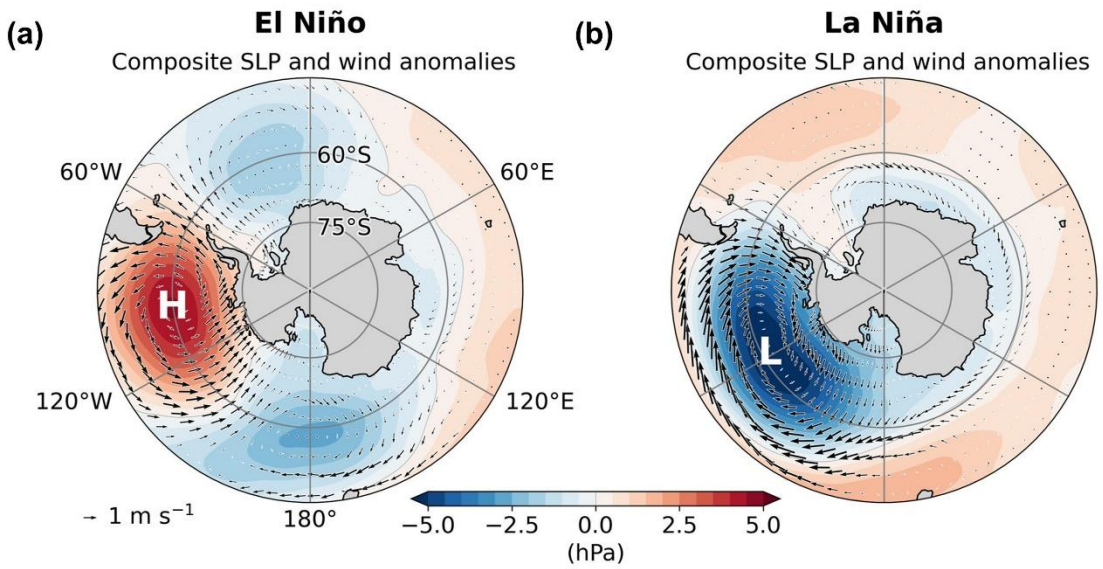


Figura 4: Médias de anomalias de pressão ao nível do mar (SLP; hPa) e anomalias de vento de superfície (m/s, setas). Os símbolos H e L indicam a localização dos centros maior (enfraquecimento) e menor (intensificação) SLP (do *Amundsen Sea Low*), respectivamente. Figura de Huguenin *et al.,* [2024].

Conforme mencionado anteriormente, a circulação ciclônica dos ventos sobre o oceano Austral promove a ressurgência da CDW na região oceânica adjacente à plataforma continental até o talude continental, onde ocorre o encontro com águas relativamente mais frias e densas da plataforma (*e.g.,* adjacentes às plataformas de gelo). O pronunciado gradiente transversal formado por esse encontro de águas com distintas características termohalinas dá origem ao sistema formado pela corrente do talude (ASC, sigla do inglês de *Antarctic Slope Current)* e pela frente do Talude (ASF, sigla do inglês de *Antarctic Slope Front).* A intensidade e a configuração desse sistema variam regionalmente ao longo da margem continental antártica (**Figura 5**). No setor oeste da Antártica, por exemplo, predomina um regime de plataforma quente, no qual os gradientes transversais de densidade tendem a ser menos acentuados, resultando em uma ASF menos definida e em uma ASC mais fraca e, em alguns trechos, descontínua. Nessas condições, a CDW pode penetrar mais facilmente na plataforma continental por meio de cânions submarinos profundos que conectam o oceano aberto às cavidades sob as plataformas de gelo. Em contraste, nos regimes de plataforma densa, como nos mares de Weddell e Ross, a ASC e a ASF são mais fortes e contínuas, atuando como uma barreira mais eficaz à intrusão de CDW sobre a plataforma e favorecendo a formação de águas frias e densas de plataforma [Thompson *et al.,* 2018].

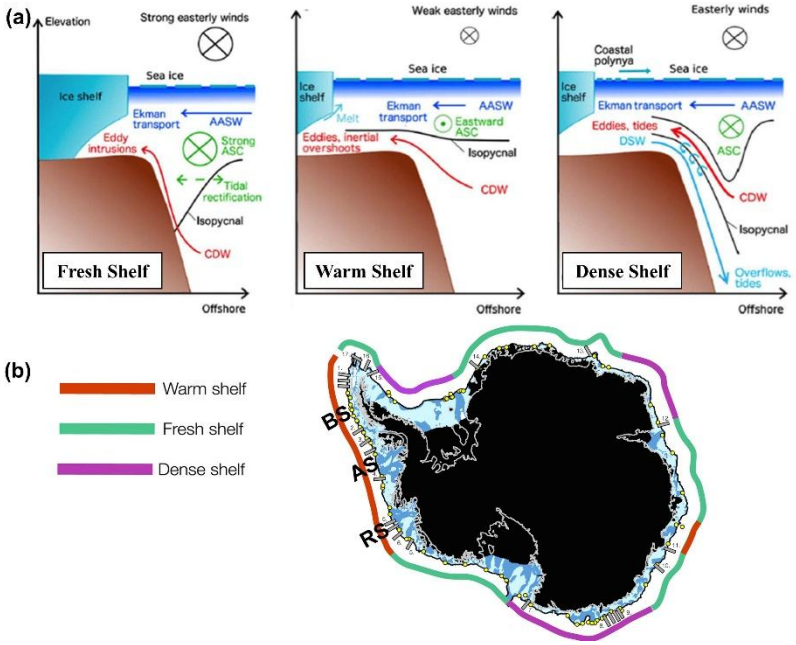


Figura 5: (a) Principais massas de água e seus fluxos ao longo e através do talude definidos por Thompson *et al.,* [2018], sendo regime de plataforma fresca (Fresh shelf), plataforma quente (*warm shelf)* e plataforma densa (*Dense shelf*) painéis da esquerda à direita respectivamente. **(b)** Indica a localização geográfica desses regimes distintos. As siglas BS, AS e RS representam os mares de Bellingshausen, Amundsen e Ross, respectivamente. Figura modificada de Thompson *et al.,* [2018].

Mais a oeste da região do mar de Amundsen, no mar de Ross, o padrão de ventos ciclônicos impulsiona a formação de um giro, comumente denominado Giro de Ross. Tal feição domina a circulação ao sul da ACC no setor oeste da Antártica. A posição do giro é limitada ao sul pelo talude continental e, ao norte/leste, pela Dorsal Pacífico–Antártica. Em seu flanco leste, a separação do fluxo do giro em relação à dorsal permite uma variabilidade muito maior. Estudos pretéritos sugerem que essa configuração favorece o transporte zonal de calor pela CDW em direção à região ao largo da plataforma continental dos mares de Amundsen e Bellingshausen [*e.g.,* Nakayama *et al.,* 2018], onde o calor pode ser posteriormente transferido para as plataformas de gelo [*e.g.,* Prend *et al.,* 2024]. Em contraste, o flanco oeste do giro segue o talude continental ao longo do mar de Ross, sendo responsável pelo escoamento sentido equador de águas densas de plataforma [*e.g.,* Dinniman *et al.,* 2011]. No entanto, apesar de seu papel fundamental, a escassez de observações *in situ* nessa vasta região coberta por gelo sazonalmente limita a compreensão da sua variabilidade e dos mecanismos que a controlam, além de sua influência sobre os mares de Amundsen e Bellingshausen. Assim, um dos objetivos desta

tese é elucidar essas questões relacionadas ao Giro de Ross (**ver capítulo 4.2**).

O oceano Austral é um sistema altamente dinâmico, e a região oeste da Antártica, devido à sua topografia complexa, apresenta características de circulação distintas entre as suas sub-regiões (*i.e.,* os mares de Amundsen e Bellingshausen e a Península Antártica). Assim, para oferecer uma compreensão mais abrangente dos processos dinâmicos que governam essa região e de sua influência sobre as intrusões de CDW, os principais padrões de circulação de cada sub-região serão descritos a seguir:

2.2.1 Mares de Amundsen e Bellingshausen

Os mares de Bellingshausen e Amundsen são oceanograficamente semelhantes, ambos sem limites geográficos bem definidos ao norte e oeste (**Figura 6**). Suas plataformas continentais são caracterizadas por cânions submarinos profundos que se estendem desde o talude continental até as plataformas de gelo.

A camada superior do oceano nessas regiões é composta principalmente por Água de Superfície Antártica (AASW, sigla em inglês de *Antarctic Surface Water*) e a Água de Inverno (WW, sigla do inglês *Winter Water*), formadas localmente por meio das interações ar-mar-gelo. A AASW se desenvolve no verão, quando o aquecimento superficial e o derretimento do gelo marinho produzem uma camada superior mais quente e menos salina. Em contraste, a WW se forma no inverno, quando o resfriamento intenso da superfície e a rejeição de salmoura durante a formação de gelo aumentam a densidade da água e aprofundam a camada de mistura. Abaixo dessas camadas se encontra a CDW, proveniente da região ao largo da plataforma continental e fornecida pela ACC. Suas intrusões sobre a plataforma continental são controladas por uma combinação de processos dinâmicos e termodinâmicos atuantes próximos ao talude e quebra de plataforma, os quais apresentam forte variabilidade espacial entre as regiões [*e.g.,* Webber *et al.,* 2017; Dotto *et al.,* 2019; Silvano *et al.,* 2022].

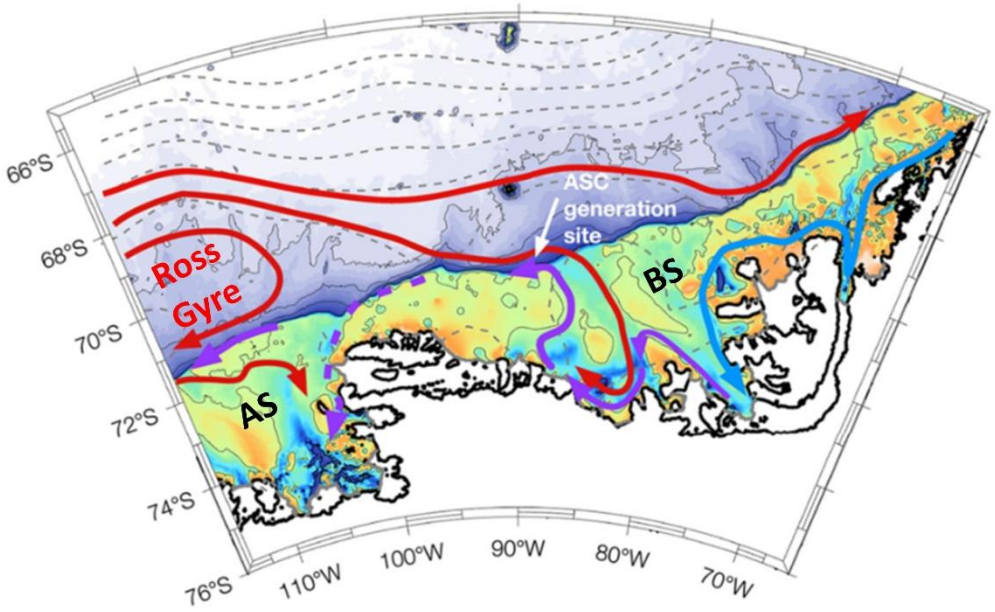


Figura 6: Representação esquemática das rotas de transporte nos mares de Amundsen (AS) e Bellingshausen (BS). As linhas cinzas tracejadas mostram a topografia dinâmica média de 2011–2016 [Armitage *et al.,* 2018]. As cores das setas indicam a massa de água dominante que transporta o fluxo, sendo a azul (Água Superficial Antártica - ASW misturada com Água de inverno - WW) transportadas pela Corrente Costeira Antártica (ACoC), a vermelha (Água Circumpolar Profunda – CDW) e a roxa (WW). A seta roxa tracejada indica uma rota sugerida por Thompson *et al.,* 2020 de WW e ASW para Amundsen Sea. Figura de Thompson *et al.,* [2020].

No mar de Bellingshausen, a ASC e a ASF estão ausentes ao longo da plataforma continental, permitindo que a CDW proveniente da região ao largo da plataforma continental flua quase sem restrições para a plataforma. A transporte transversal de CDW ocorre principalmente pelo cânion de Marguerite e através de vórtices desprendidos da ACC como resultado de processos de instabilidade baroclínica [Moffat *et al.,* 2009; Couto *et al.,* 2017]. Essa região também abriga a Corrente Costeira Antártica (ACoC, sigla do inglês *Antarctic Coastal Current*), que transporta AASW e WW para oeste, em direção ao mar de Amundsen [**Figura 6**; Thompson *et al.,* 2020; Schubert *et al.,* 2021]. Esse transporte influencia a profundidade da termoclina regional e contribui para a circulação da porção leste do mar de Amundsen [*e.g.,* Thompson *et al.,* 2020; Schubert *et al.,* 2021].

Em contraste, no mar de Amundsen, desenvolve-se uma corrente subsuperficial para leste ao longo da quebra da plataforma, resultante da baroclinicidade associada ao sistema composto por ASC e ASF [*e.g.,* Si *et al.,* 2023]. Essa corrente é mais pronunciada no setor oeste do mar de Amundsen (*i.e.,* na região do cânion *Dotson–Getz*; **Figura 7**),

onde a presença de um cânion mais profundo e aberto [*e.g.,* Cochran *et al.,* 2020] torna essa corrente de fundo uma das principais rotas de entrada da CDW na plataforma continental. Estudos numéricos recentes mostram que essa corrente pode ser intensificada por ventos de leste, os quais acentuam a inclinação do ASC e da ASF e aumentam a advecção de CDW sobre a plataforma continental [Silvano *et al.,* 2022].

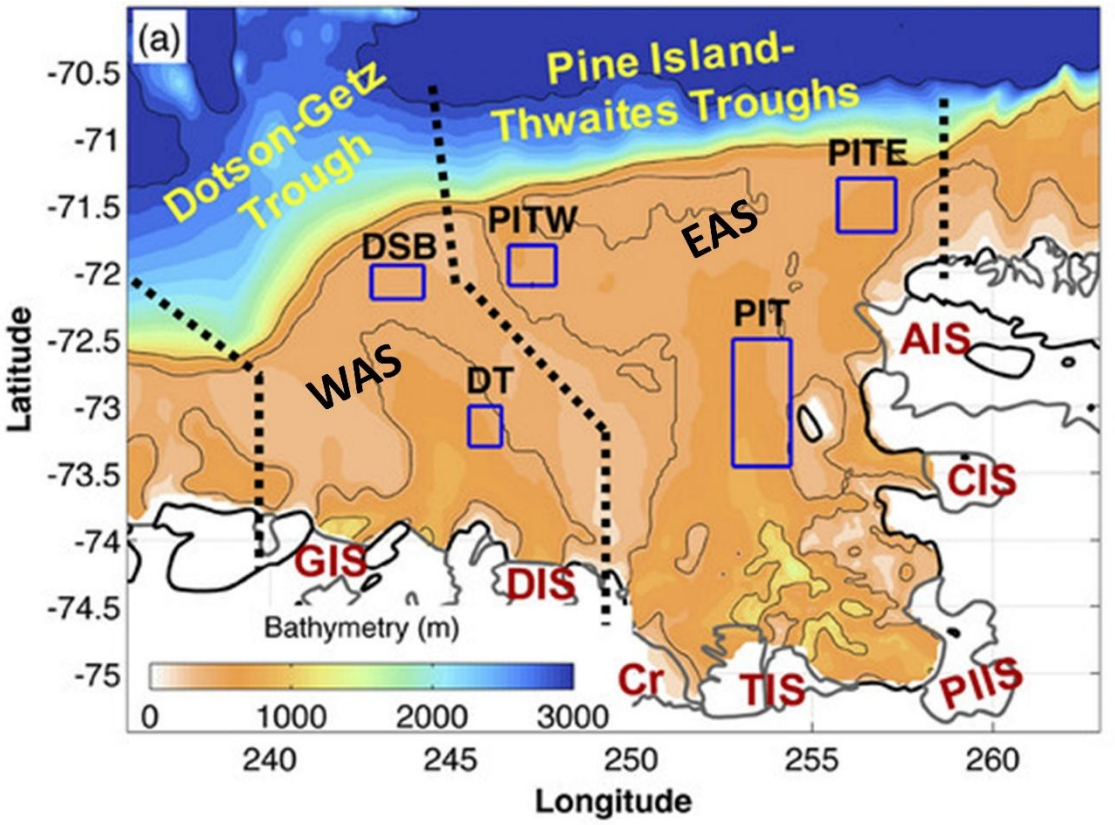


Figura 7: Região batimétrica do mar de Amundsen. As linhas pontilhadas mostram a divisão da região oeste do mar de Amundsen (WAS) representada pelo canal Dotson–Getz e da região leste do mar de Amundsen (EAS) representada pelos canais Pine Island–Thwaites. Os retângulos azuis indicam o Dotson Shelf Break (DSB), o Inner Dotson Trough (DT), o canal Pine Island–Thwaites (PIT), o canal Pine Island–Thwaites Oeste (PITW) e o canal Pine Island–Thwaites Leste (PITE). São representadas as isóbatas de 500, 1000 e 3000 m. As plataformas de gelo locais estão identificadas: Abbot Ice Shelf (AIS), Cosgrove Ice Shelf (CIS), Pine Island Ice Shelf (PIIS), Thwaites Ice Shelf (TIS), Crosson Ice Shelf (Cr), Dotson Ice Shelf (DIS) e Getz Ice Shelf (GIS). Figura de Dotto *et al.,* [2019].

No setor leste de Amundsen, no cânion de *Pine Island* (**Figura 7**), os cânions são mais rasos do que os do setor do cânion *Dotson–Getz*, o que restringe verticalmente o acesso da CDW. Como consequência, a intrusão de águas quentes torna-se altamente

dependente da profundidade da termoclina [*e.g.,* Webber *et al.,* 2017]. Nesse contexto, os mesmos ventos de leste promovem o transporte para o sul das águas superficiais, intensificando a convergência de Ekman e favorecendo o acúmulo de águas superficiais misturadas com água de degelo glacial [*e.g.,* Webber *et al.,* 2019; Huguenin *et al.,* 2024]. Esse acúmulo provoca a depressão das isopicnais e, consequentemente, restringe as intrusões de CDW sob a plataforma [Jacobs *et al.,* 2011; Nakayama *et al.,* 2013; Dutrieux *et al.,* 2014; Webber *et al.,* 2017; Dotto *et al.,* 2019].

2.2.2 Península Antártica

A Península Antártica é particularmente sensível às mudanças climáticas devido às profundas implicações que as variações nos fluxos de águas relativamente mais quentes provenientes do mar de Bellingshausen e das águas mais frias formadas no mar de Weddell exercem sobre a dinâmica das geleiras e a cobertura de gelo marinho nessa região [*e.g.,* Flexas *et al.,* 2022]. Nesta tese, parte do estudo será focada no estreito de Bransfield, localizado no setor norte da Península Antártica, uma região que atua como porta de entrada fundamental para a troca de massas de água entre os mares de Bellingshausen e Weddell.

A circulação do estreito de Bransfield é dominada por um giro ciclônico, responsável por transportar águas intermediárias misturadas com águas densas de plataforma (DSW, sigla do inglês *Dense Shelf Water*) formadas no mar de Weddell (*i.e.,* Águas Transicionais do mar de Weddell – TWW, sigla do inglês *Transitional Zonal Water with Weddell influence*) em direção ao sul, até as proximidades do mar de Bellingshausen [Sangrà *et al.,* 2011, 2017; Dotto *et al.,* 2016; van Caspel *et al.,* 2015, 2018; Ruiz Barlett *et al.,* 2018; Morrinson *et al.,* 2023]. Essas águas de plataforma são advectadas para dentro do estreito de Bransfield através do sistema acoplado entre a ACoC e a ASF [Fahrbach *et al.,* 1992; Gordon *et al.,* 2000; von Gyldenfeldt *et al.,* 2002; Heywood *et al.,* 2004; Thompson *et al.,* 2009; Collares *et al.,* 2018; Sangrà *et al.,* 2017]. Esse sistema de circulação transporta TWW ao sofrer uma bifurcação causada pelo choque com a cordilheira sul da Escócia do Sul, divide-se em três rotas distintas. A primeira consiste no transporte de TWW pela bacia leste, próxima à ilha Joinville; a segunda segue aproximadamente a isóbata de 1000 m em direção leste, ao longo da borda sul da Escócia do Sul; e a terceira está associada à ressurgência para a superfície, induzida pelo forte cisalhamento horizontal gerado pela elevação topográfica, formando um

vórtice estacionário na região [Heywood *et al.,* 2004; Thompson *et al.,* 2009; Damini *et al.,* 2022]. Além disso, alguns estudos indicam uma possível rota adicional da TWW através do canal Antártico, entre a ilha Joinville e a ponta da Península Antártica [Gordon *et al.,* 2000; Renner *et al.,* 2009; Thompson *et al.,* 2009; **Figura 8**]. Após a advecção para dentro do estreito de Bransfield, essas águas afundam devido à sua alta densidade por meio de cânions localizados na plataforma continental adjacente [*e.g.,* López *et al.,* 1999].

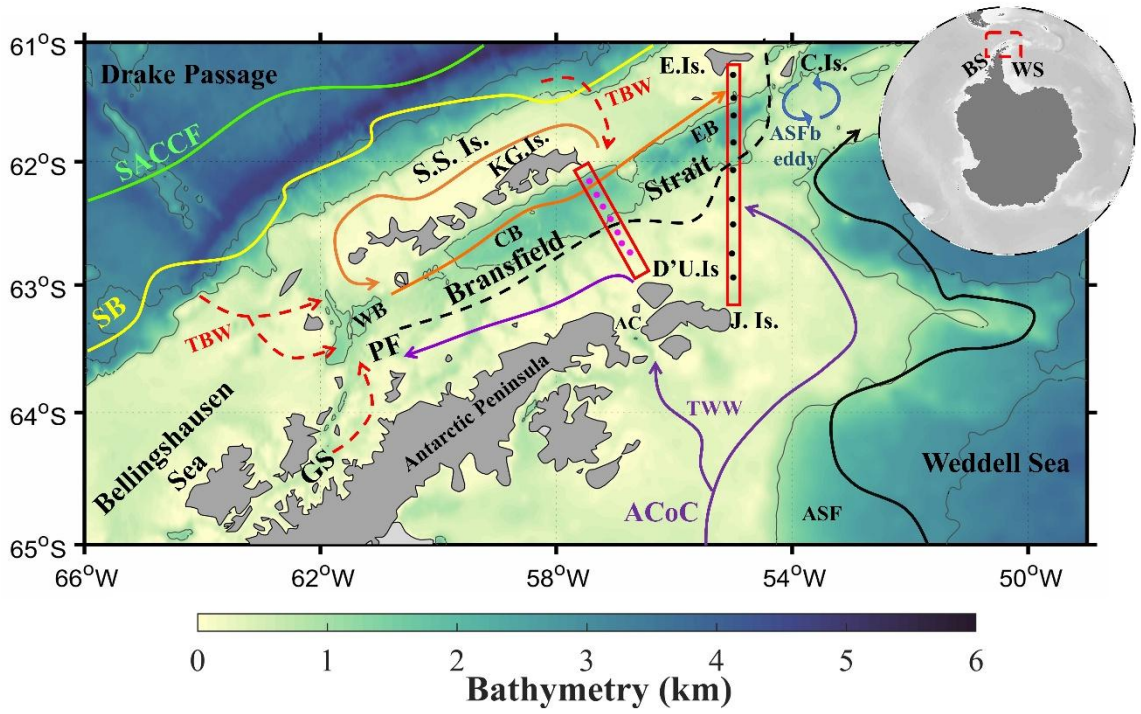


Figura 8: Representação esquemática da circulação média na região da Península Antártica. As setas vermelhas (roxas) representam as rotas pelas quais a Transicionais do mar de Bellingshausen (TBW) e a Águas Transicionais do mar de Weddell (TWW) entram no Estreito de Bransfield. As linhas verde e amarela indicam, respectivamente, as posições médias da Frente Sul da Corrente Circumpolar Antártica (Southern Antarctic Circumpolar Current Front, SACCF) e do Limite Sul da Corrente Circumpolar Antártica (Southern Boundary, SB). Setas em azul-claro indicam o vórtice associado à bifurcação da Frente de Talude Antártica (Antarctic Slope Front bifurcation, ASFb). As setas laranja mostram a Corrente de Bransfield e sua recirculação ao redor das Ilhas Shetland do Sul (S.S.Is.). A linha preta representa a posição média da Frente de Talude Antártica (ASF). Os retângulos vermelhos em torno dos pontos magenta e pretos delimitam as seções hidrográficas das Seções 1 e 2 (**mais bem detalhado na seção de material e métodos**). A linha preta tracejada representa a Frente da Península (Peninsula Front, PF). As siglas correspondem a: Canal Antártico (AC), Corrente Costeira Antártica (ACoC), Ilha Joinville (J.Is.), Ilha D'Urville (D'U.Is.), Ilha Elefante (E.Is.), Ilha Clarence (C.Is.), Mar de Bellingshausen (BS), Passagem de Drake (DP), Mar de Weddell (WS), Bacia Ocidental (WB), Bacia Central (CB), Bacia Oriental (EB) e Estreito de Gerlache (GS). As linhas cinzas finas indicam as isóbatas de 0,10 km e 0,30 km fornecidas pelo IBCSO

(www.scar.org/science/ibcso/ibcso/). O painel ampliado mostra a região de estudo. Figura extraída de Damini *et al.,* [2025].

A mistura entre as águas superficiais provenientes do mar de Bellingshausen e a CDW advectada pela ACC dá origem às Águas Transicionais do mar de Bellingshausen (TBW, sigla do inglês *Transitional Zonal Water with Bellingshausen influence*), que são subsequentemente transportadas para dentro do estreito de Bransfield através de passagens entre as ilhas Shetland do Sul e pelo estreito de Gerlache (setor sul da Península Antártica). Uma vez advectada para o interior do estreito, essa água é transportada por um jato baroclínico de mesoescala relativamente intenso, conhecido como Corrente de Bransfield (BC; sigla do inglês *Bransfield Current*). Essa corrente flui no sentido sudoeste–nordeste ao longo da quebra de plataforma das ilhas Shetland do Sul [**Figura 8**; Sangrà *et al.,* 2017]. A maior parcela do fluxo associado à BC é exportada para a bacia leste do estreito de Bransfield, entre as ilhas Rei George e Elefante; uma fração recircula entre as ilhas Shetland do Sul [*e.g.,* Sangrà *et al.,* 2017]; e o restante do fluxo entra na confluência Weddell–Scotia através do canal profundo existente entre as ilhas Elefante e Clarence [*e.g.,* López *et al.,* 1999].

O encontro dessas massas de água com as águas advectadas das plataformas continentais do mar de Weddell resulta na formação de uma frente de superfície que se estende até cerca de 100 m de profundidade, separando massas de água com características termohalinas distintas, a Frente da Península [PF; Tokarczyk, 1987; García *et al.,* 1994, 2002; Savidge & Amft, 2009; Sangrà *et al.,* 2011, 2017].Vale destacar que diversos estudos sugerem que a intensificação e o deslocamento para o sul dos ventos de oeste, sob a influência de eventos de SAM em sua fase positiva e de ENSO em sua fase negativa, promovem uma migração em direção ao polo da ACC e de seu sistema frontal. Esses processos, também investigados neste estudo, podem favorecer um maior influxo de TBW por meio de mecanismos turbulentos e advectivos na região da plataforma continental da Península Antártica [*e.g.,* Dotto *et al.,* 2016; Damini *et al.,* 2022; Ruiz Barlett *et al.,* 2018; Martinson & McKee, 2012; Couto *et al.,* 2017]. Tais mudanças na advecção dessas águas são fundamentais para serem monitoradas, pois modulam a dinâmica regional e influenciam diretamente o ecossistema local.

Capítulo III: Dados e Métodos

3.1 Conjunto de dados hidrográficos

Nesta tese, um abrangente conjunto de dados hidrográficos foi compilado contendo medições de pressão, temperatura e salinidade representativas da região oeste da Antártica (Latitude: 65°–79°S; Longitude: 140°E–070°W) entre 1990 e 2020. O banco de dados compila observações provenientes do World Ocean Database 2023 [WOD23; https://www.ncei.noaa.gov/products/world-ocean-database; Mishonov *et al.,* 2024], do Programa Argo (https://argo.ucsd.edu), do *CLIVAR and Carbon Hydrographic Data Office* (CCHDO; https://cchdo.ucsd.edu/), do *Marine Mammals Exploring the Ocean Pole to Pole* [MEOP; https://www.meop.net/; Roquet *et al.,* 2011] e do projeto *Thwaites–Amundsen Regional Survey and Network* (TARSAN; https://www.bodc.ac.uk/data/bodc_database/nodb/project/54319/). As observações do WOD23 e do TARSAN são obtidas por meio de sensores eletrônicos de condutividade–temperatura–profundidade, com acurácias típicas de 0,001 °C para temperatura e 0,002 para salinidade [Mishonov *et al.,* 2024]. Os perfis Argo reportam acurácias de 0,002 °C e 0,003, respectivamente [Cowley *et al.,* 2021; Riser *et al.,* 2015]. Apesar do conjunto de dados do MEOP (majoritariamente concentrado sobre a plataforma continental) apresentar acurácias inferiores a 0,02 °C e 0,03, respectivamente [Roquet *et al.,* 2011; Siegelman *et al.,* 2019], a variabilidade hidrográfica observada na região é substancialmente maior que esses níveis de incerteza, o que assegura a robustez dos sinais detectados.

Adicionalmente, para atender ao terceiro objetivo específico desta tese, a caracterização da variabilidade interanual do transporte e as trajetórias de intrusões da

CDW sobre a plataforma continental da Península Antártica, foi atribuída uma ênfase às observações hidrográficas provenientes dos projetos de pesquisa do grupo GOAL, realizadas durante os verões austrais de 2003 a 2019 (*i.e.,* pontos magenta e preto na **Figura 8**). A acurácia dos dados dos perfis de CTD realizados pelo GOAL é de ~0.001 °C e ~0.003 para temperatura e salinidade, respectivamente [Dotto *et al.,* 2021].

O controle de qualidade do conjunto de dados foi realizado mediante a remoção dos valores situados fora do intervalo de dois desvios-padrão para cada perfil. Os dados resultantes foram então interpolados verticalmente com resolução de 10 m, da superfície ao fundo, e posteriormente agrupados por década (i.e., 1990, 2000 e 2010). Apesar do grande volume de dados *in situ*, a uma descontinuidade espaço-temporal nas observações inviabiliza uma avaliação contínua das trocas de calor entre a região ao largo da plataforma continental e plataforma continental. Assim, para mitigar essa limitação, as análises *in situ* foram complementadas com a reanálise oceânica de alta resolução GLORYS12v1. Essa abordagem permite obter uma representação contínua da variabilidade das propriedades da CDW e de suas intrusões sobre a plataforma continental.

3.2 Saída da reanálise GLORYS12v1

A reanálise GLORYS12v1 (https://data.marine.copernicus.eu/product/) foi avaliada quanto à sua capacidade de reproduzir a variabilidade das propriedades termohalina por meio de comparação direta com dados hidrográficos referentes ao mesmo período e à mesma região geográfica. O GLORYS12v1 é uma reanálise física oceânica fornecida pelo *Copernicus Marine Environment Monitoring Service*, com resolução horizontal de 1/12º e 50 níveis verticais padrão, cobrindo o período de 1993 até o presente e com capacidade para resolver a mesoescala oceânica. Seus componentes baseiam-se no modelo oceânico *Nucleus for European Modelling of the Ocean* (NEMO), versão 3.1, acoplado ao modelo de gelo marinho Louvain-la-Neuve Ice Model, versão 2 (LIM2). Além disso, o GLORYS12v1 é inicializado com campos de temperatura e salinidade da climatologia mensal em grade ENACT/ENSEMBLES, versão 4.2.0 (EN4.2.0), e forçado pelas reanálises atmosféricas do ERA-Interim (https://www.ecmwf.int/en/forecasts/dataset/ecmwf-reanalysis-interim/) até 2018 e, posteriormente, pela ERA5 a partir de 2019 [Jean-Michel *et al.,* 2021]. Essa mudança no forçamento atmosférico não produziu alterações significativas nas saídas do

GLORYS12v1, exceto por uma menor redução no volume e na extensão do gelo marinho no Oceano Austral durante o verão austral [Jean-Michel *et al.,* 2021]. Avaliações independentes indicam que o GLORYS12v1 representa adequadamente os principais sinais de variabilidade climática interanual do oceano e do gelo marinho [Jean-Michel *et al.,* 2021].

3.3 Equação de Estado Termodinâmica da Água do Mar (TEOS-10)

Por mais de 30 anos, as equações da EOS-80 foram amplamente utilizadas pela comunidade oceanográfica. Contudo, nos últimos anos, diversas limitações foram apontadas a esse conjunto de equações, dentre elas: (i) a inconsistência termodinânica; (ii) a necessidade de um melhor entendimento das variações na composição do oceano e como essas podem afetar sua densidade; e, (iii) a necessidade de incorporar expressões exatas para entropia, entalpia e energia interna da água do mar para que possam então determinar com maior precisão os fluxos de calor na interface oceano-atmosfera.

Como resultado, a partir de 2010, a comunidade oceanográfica passou a adotar uma nova equação de estado baseada na formulação de Gibbs (função de salinidade absoluta; S_A – g kg^{-1}, temperatura conservativa; Θ – °C e pressão – decibar), que permite o cálculo direto de propriedades termodinâmicas, incluindo entropia, entalpia e entalpia potencial [McDougall & Barker, 2011]. A equação TEOS-10 enfatiza o papel central da entropia e da entalpia para representar com maior precisão os processos de advecção e difusão de calor, além de permitir quantificar o papel do oceano nas trocas térmicas com a atmosfera e a criosfera. Uma das principais alterações introduzidas pelo TEOS-10 é o uso da salinidade absoluta (S_A) em substituição à Salinidade Prática (S_P) em cálculos termodinâmicos, incorporando explicitamente íons de baixa condutividade elétrica não detectados por sensores de condutividade–temperatura–profundidade, mas que ainda influenciam a densidade. Nesse contexto, a S_A é superior à salinidade prática, pois as propriedades termodinâmicas da água do mar dependem diretamente da massa dos seus constituintes dissolvidos [McDougall & Barker, 2011]. Portanto, neste estudo, foi utilizada a equação da TEOS-10 para obter estimativas termohalinas mais precisas, a partir de observações hidrográficas e dos campos fornecidos pela reanálise GLORYS12v1.

3.4 Aquecimento pós-década de 1990 da CDW ao longo do oeste da

Antártica e seus mecanismos controladores

As propriedades termohalinas no verão austral (janeiro-março), obtidas a partir das medições hidrográficas e da reanálise GLORYS12v1, no setor compreendido entre 120°–70°W e 67,5°–74°S, foram agrupadas por década (*i.e.,* anos 1990, 2000 e 2010). Esse procedimento possibilitou investigar a evolução decenal das características da CDW, fornecendo evidências sobre mudanças termohalinas ao longo da Antártica Ocidental desde o início dos anos 1990, período em que a cobertura observacional passou a se tornar mais ampla, até as condições mais atuais representadas pela década de 2010.

Devido às lacunas espaciais significativas na amostragem hidrográfica, foi necessário o uso da interpolação para viabilizar o cálculo tanto das diferenças decenais quanto do campo médio referente a todo o período. Assim, as propriedades termohalinas foram interpoladas sobre uma grade regular de 0,25° por meio do método de Funções de Base Radial (RBF), utilizando ponderação linear. A interpolação por RBF foi escolhida por sua alta adaptabilidade às estruturas espaciais do banco de dados, característica fundamental para representar regiões com amostragem irregular e dados esparsos [Damini *et al.,* 2025; Yamazaki *et al.,* 2021]. Para garantir uma maior confiabilidade e robustez das análises, áreas da grade interpolada que não continham estações hidrográficas em um raio de 50 km foram mascaradas (~2 vezes o espaçamento da grade de interpolação).

3.4.1 Definição da camada de CDW

A camada de CDW foi definida como o máximo da Θ em profundidades superiores a 300 m, critério que exclui a influência direta de processos de superfície, como fluxos causados pela forçante de flutuabilidade (*i.e.,* movimentos verticais da coluna d'água causados por trocas de calor e fluxos de água doce). Esse método permite selecionar o núcleo da CDW, que ocupa profundidades intermediárias ao longo da SACCF e avança em direção à margem continental da região oeste da Antártica [*e.g.,* Schmidtko *et al.,* 2014; Orsi *et al.,* 1995].

3.4.2 Definição da SACCF

Conforme descrito anteriormente, a borda sul da ACC é identificada em seções hidrográficas como o setor em que a CDW atinge seu limite meridional mais ao sul e

aflora por ressurgência. Embora essa fronteira seja composta por duas frentes muito próximas (SACCF e a SB), ambas costumam estar separadas por apenas algumas dezenas de quilômetros e apresentam deslocamentos meridionais coerentes [Orsi *et al.,* 1995] e, por esse motivo, a SACCF foi utilizada para representar a variabilidade dessa borda sul da ACC. Assim, a posição da SACCF foi determinada como o ponto geográfico em que a isoterma de 1,8 °C, situada na camada núcleo da CDW, intercepta a isóbata de 500 m [Orsi et., 1995]. A SACCF foi definida utilizando dados de Θ obtidos tanto das observações hidrográficas interpoladas quanto da saída da reanálise GLORYS, para cada década analisada. Além disso, a SACCF também foi identificada usando o contorno de ADT de –1,10 m, calculado a partir da média sazonal de verão austral (janeiro a março) do conjunto de dados do Copernicus (0,25° × 0,25°, 1993–2020; https://data.marine.copernicus.eu/).

Para quantificar o deslocamento meridional da SACCF entre as décadas de 1990 e 2010, calculou-se inicialmente a posição média da frente para cada período. Em seguida, essas coordenadas foram interpoladas para uma grade longitudinal comum e regular, viabilizando o cálculo direto das variações latitudinais ao longo da extensão zonal da ACC. Esse procedimento assegura a comparabilidade espacial entre as décadas, permitindo avaliar o deslocamento de forma contínua, independentemente da distribuição original dos pontos de amostragem.

3.4.3 Validação da reanálise GLORYS12v1 na representação da variabilidade termohalina da CDW

Para garantir a robustez dos resultados, é essencial avaliar o desempenho da reanálise oceanográfica GLORYS12v1. Os resultados da GLORYS12v1 foram avaliados comparando quantitativamente e qualitativamente a sua capacidade de reproduzir a variabilidade decenal na camada da CDW observada com dados observacionais. Outrossim, a representação da SACCF foi validada pelo cálculo da correlação de Pearson entre a posição da frente na GLORYS e as posições definidas por medições hidrográficas observacionais, ADT e a climatologia histórica de Orsi *et al.,* [1995] https://data.aad.gov.au/metadata/records/antarctic_circumpolar_current_fronts/).

3.4.4 Análise atmosférica

Conjuntos de dados mensais de vento (componentes zonais e meridionais) e pressão ao nível do mar (SLP; sigla do inglês *Sea Level Pressure*) com média de verão (janeiro a março) foram analisados para investigar como as mudanças no campo atmosférico podem ter modulado a variabilidade das propriedades termohalinas da CDW (tanto na plataforma continental quanto nas regiões ao largo da plataforma continental). Os conjuntos de dados de vento e de SLP foram obtidos da reanálise ERA5 [Hersbach *et al.,* 2020] com uma resolução horizontal de 0,25º. Usando as médias de SLP e ventos zonais e meridionais de verão, foram calculadas as médias decenais das anomalias em relação à climatologia de 1990–2020. E, posteriormente, foram calculadas as mudanças decenais dessas anomalias (*i.e.,* anomalias da década de 2010 menos anomalias da década de 1990). Tal procedimento destaca as mudanças de longo prazo nas forçantes atmosféricas, enfatizando as alterações ocorridas na década de 2010.

O rotacional da tensão de cisalhamento do vento foi calculado seguindo Veny *et al.,* [2024], usando componentes zonais e meridionais do vento. As médias decenais foram calculadas para as décadas de 1990 e 2010, com anomalias definidas como desvios da climatologia de 1990–2020. O rotacional da tensão de cisalhamento do vento serve como um indicador do bombeamento de Ekman, fornecendo informações sobre os movimentos verticais da coluna d'água impulsionados pelo vento (*e.g.,* ressurgência de CDW).

Adicionalmente, investigou-se a relação entre o deslocamento da SACCF e as forçantes atmosféricas por meio da média de verão (janeiro-março) da componente zonal do vento. Neste contexto, adotou-se a metodologia proposta por Goyal *et al.,* [2021], na qual a posição dos ventos máximos de oeste é identificada pela latitude da velocidade zonal máxima do vento no verão (entre 30ºS e 70ºS) para cada longitude. Subsequentemente, foram calculadas as médias decenais a partir desses valores anuais (1993-2020). Com isso, foi possível avaliar se um deslocamento dos ventos de oeste ocorreu na região oeste Antártica e relacionar com as mudanças da SACCF [uma vez que a posição da ACC e suas frentes podem ser impulsionadas pela variabilidade dos padrões de vento da região; Meredith *et al.,* 2016].

3.4.5 Alterações na temperatura conservativa da CDW devido aos deslocamentos meridionais da ACC

Conforme mencionado anteriormente, as mudanças na temperatura da CDW vêm sendo reportadas em diversos estudos [*e.g.,* Herraiz-Borreguero & Naveira Garabato, 2022]. Para discernir os fatores que impulsionam as mudanças de temperatura associadas ao deslocamento de longo prazo do sistema frontal da ACC, a mudança total de temperatura foi decomposta em duas componentes usando a equação 1:

$$\Delta\Theta(x,y,z) = \Delta\Theta'(x,y,z) + \Delta front(x,y,z) \quad (1)$$

O lado esquerdo da equação 1 representa a mudança na Θ (ΔΘ), que é essencialmente a mudança no campo de Θ observada durante o período analisado. O primeiro termo do lado direito da equação 1 corresponde ao termo de transformação da massa de água. Este termo contabiliza as mudanças na Θ ao longo da SACCF associadas a fatores como o fluxo isopicnal (*i.e.,* fluxos causados pela forçante de flutuabilidade). O segundo componente do lado direito representa a mudança euleriana, que está ligada aos deslocamentos frontais (Δfront).

O termo ΔΘ foi quantificado diretamente a partir dos dados da reanálise GLORYS12v1. O cálculo consistiu na diferença entre as médias das décadas de 2010 e 1990 (*i.e.,* $\Delta\Theta = \Theta_{2010} - \Theta_{1990}$) para a camada da CDW. A seleção desses períodos baseou-se no objetivo de capturar as mudanças interdecenais nas propriedades da CDW. O termo referente ao deslocamento frontal (Δfront) foi calculado explicitamente pela equação 2, enquanto o termo de transformação da massa de água foi derivado como o resíduo da equação 1.

$$\Delta front = \Delta\Phi \times \frac{\partial\Theta}{\partial\Phi} \quad (2)$$

A mudança na altura dinâmica, representada por ΔΦ, foi avaliada da década de 1990 até a década de 2010, e a altura dinâmica (Φ) foi calculada a 300 m em relação a 1800 m para cada ponto na grade GLORYS ao norte da plataforma continental. Essa faixa de Φ foi escolhida seguindo Yamazaki *et al.* [2021], onde valores acima de 2000 dbar representam com precisão a posição das frentes barotrópicas da ACC [*e.g.,* Meijers *et al.,* 2011], enquanto temperaturas abaixo de 300 dbar são menos influenciadas por processos de pequena escala do que pela posição da frente. Nossos resultados não são sensíveis à definição precisa da altura dinâmica. As mudanças em Θ em relação a Ψ foram representadas por $\frac{\partial\Theta}{\partial\Phi}$ e serão determinadas empregando-se regressão linear por mínimos

quadrados em todos os dados de Θ e Φ disponíveis na camada de CDW.

3.5 Variabilidade do Giro de Ross e seu papel na modulação das propriedades da CDW na região ao largo da plataforma continental no setor Amundsen–Bellingshausen (1993–2020)

3.5.1 Definição do Giro de Ross

O limite do Giro de Ross foi definido conforme Roach & Speer [2019], que estabeleceram as bordas do giro como o contorno de −8 Sverdrup (Sv; 1 Sv = 10^6 m^3 s^{-1}) da função de corrente barotrópica, obtida pela integração vertical do campo de velocidade zonal do fundo à superfície, no sentido sul (a partir da costa). Esse contorno específico corresponde ao contorno fechado mais externo da média temporal da função de corrente que não apresenta extensões costeiras. Esse método fornece uma métrica consistente para monitorar mudanças na área do giro ao longo do tempo, permitindo identificar expansões ou contrações de seu limite. Além disso, seguindo Prend *et al.,* [2024], a intensidade da circulação do giro foi definida como o valor médio da função de corrente barotrópica dentro do contorno de −8 Sv.

3.5.3 Rotacional da tensão do cisalhamento total superficial oceânico

Para avaliar o papel da tensão superficial oceânica como possível forçante da circulação, a tensão superficial mensal foi calculada considerando as contribuições combinadas das tensões ar–oceano e gelo–oceano. O rotacional da tensão do cisalhamento total superficial oceânico em cada ponto de grade foi então obtido seguindo Dotto *et al.,* [2018]. Essa abordagem fornece uma representação física mais consistente do forçamento mecânico do que o uso exclusivo do rotacional da tensão do cisalhamento do vento. De fato, a variabilidade do vento, isoladamente, não explica completamente a dinâmica em regiões (*e.g.,* o Giro de Ross) onde a cobertura de gelo marinho modula a transferência de momento para o oceano [Meneghello *et al.,* 2018].

Adicionalmente, foi realizada a média espacial do rotacional da tensão do cisalhamento total superficial oceânico sobre a região de forçamento do giro (140–150°W, 67–70°S), definida como a área que apresenta a correlação linear mais forte com a variabilidade do Giro de Ross dentro dos limites climatológicos do giro [*e.g.,* Prend *et*

al., 2024]. Assim, através dessa média espacial, a série temporal representativa do rotacional da tensão do cisalhamento total superficial oceânico que atua como forçante mecânica que atua sobre o giro foi adquirida.

3.5.4 Fluxos de Flutuabilidade

Uma hipótese alternativa para a geração de circulação de grande escala em bacias oceânicas é que fluxos de flutuabilidade superficiais também possam atuar como mecanismo forçante. O forçamento de flutuabilidade superficial modifica a densidade das massas d'água, gerando uma velocidade vertical diabática através das isopicnais. Esse bombeamento termodinâmico pode contribuir para a injeção ou remoção de vorticidade potencial [Czaja & Hausmann, 2009], gerando circulações horizontais potencialmente comparáveis em magnitude às dos giros forçados pelo vento [Colin de Verdière, 1989]. Nesse contexto, os fluxos de flutuabilidade superficial são considerados aqui como um possível mecanismo forçante da variabilidade do Giro de Ross, seguindo a metodologia de Neme *et al.,* [2021]. Portanto, o fluxo de flutuabilidade superficial ($\mathcal{B}$; m^2s^{-3}) foi calculado através das equações 3, 4 e 5 a seguir:

$$\mathcal{B} = \mathcal{B}_{heat} + \mathcal{B}_{fresh}, \quad (3)$$

onde

$$\mathcal{B}_{heat} = \frac{-g\gamma Q_{net}}{c_w \rho}, \quad (4)$$

$$\mathcal{B}_{fresh} = g\beta F_w S_{A(sup)}, \quad (5)$$

ρ é a densidade superficial, g é a aceleração da gravidade (9,81 m s^{-2}), c_w é a capacidade térmica específica da água do mar (3.992 J kg^{-1} K^{-1}), γ é o coeficiente de expansão térmica, e β é o coeficiente de contração halina da água do mar derivado do TEOS-10 [McDougall & Barker, 2011]. $S_{A(sup)}$ é a salinidade absoluta superficial. Q_{net} representa o fluxo de calor líquido, calculado como a soma da radiação de onda longa líquida (QLW), soma de radiação de onda curta (QSW), soma do fluxo de calor latente (QLH) e soma de fluxo de calor sensível (QSH). F_w representa o fluxo líquido de água doce, definido como evaporação (E), escoamento continental (R), precipitação (P) e formação/derretimento de gelo marinho (isto é, P – E + R – F_{ice}). Os dados mensais de QLW, QSW, QLH, QSH, E, R e P foram obtidos do ERA5. F_{ice} representa o fluxo de

água doce associado à dinâmica de formação e derretimento do gelo marinho e foi estimado utilizando uma abordagem termodinâmica bulk, seguindo Hattermann *et al.*, [2021], na qual valores positivos de F_{ice} representam formação de gelo marinho (perda de água doce pelo oceano). Neste contexto, valores positivos de $\mathcal{B}$ representam ganho de flutuabilidade pelo oceano (redução da densidade por aquecimento e/ou aporte de água doce). Além disso, os maiores valores de $\mathcal{B}$ na região do mar de Ross ocorrem sobre a plataforma continental. Posteriormente, a média de $\mathcal{B}$ sobre a plataforma continental (definida por profundidades menores que 1000 m no mar de Ross; 160°E–150°W) foi realizada para a construção de uma série temporal representativa.

3.5.5 Análises temporais e espaciais

Os ciclos anuais climatológicos da intensidade do giro, do rotacional da tensão do cisalhamento total superficial oceânico, dos fluxos de flutuabilidade superficiais e da área do giro foram calculados para caracterizar a dinâmica sazonal. Para investigar a variabilidade interanual, foram calculadas anomalias em relação à climatologia média mensal de longo prazo para o período de janeiro de 1993 a dezembro de 2020. Todas as séries temporais foram então suavizadas com um filtro *Butterworth* passa-baixa de 12 meses, a fim de suprimir o ciclo sazonal e a variabilidade de alta frequência.

Posteriormente, coeficientes de correlação linear foram calculados entre as séries temporais de anomalias da intensidade da circulação do giro e as anomalias do rotacional da tensão do cisalhamento total superficial oceânico, dos fluxos de flutuabilidade superficiais e da área do giro. Essa análise foi empregada para identificar os processos dominantes associados à variabilidade da intensidade do giro em escalas sazonais e interanuais.

Campos médios de anomalias das propriedades termohalinas subsuperficiais (300–500 m) durante estados fortes e fracos do Giro de Ross foram analisados para investigar como essas propriedades variam nas regiões ao largo da plataforma continental e sobre a plataforma continental em associação às mudanças na intensidade do giro. Os períodos de giro forte foram definidos quando a série temporal suavizada da anomalia da intensidade do giro inferiores −1 desvio padrão, enquanto os períodos de giro fraco corresponderam a valores excederam a +1 desvio padrão. Para cada grupo, campos médios de anomalias de Θ e S_A foram calculados em relação à climatologia mensal de longo prazo. A significância estatística das diferenças entre os campos médios

condicionais de giro forte e fraco foi avaliada por meio de um teste de permutação de Monte Carlo com 1000 iterações, no qual os rótulos temporais associados aos estados forte e fraco do giro foram aleatoriamente reatribuídos para gerar uma distribuição nula das diferenças médias. Apenas anomalias que excederam o intervalo de confiança de 95% dessa distribuição foram consideradas estatisticamente significativas. Esses campos médios revelam os padrões termohalinos característicos associados a estados intensificados e enfraquecidos do Giro de Ross. Além disso, campos médios de anomalias da tensão superficial oceânica e da pressão ao nível do mar (1993–2020) também foram calculados para investigar os padrões atmosféricos associados aos eventos fortes e fracos do giro.

Por fim, tendências lineares espaciais na tensão superficial oceânica e nas propriedades termohalinas subsuperficiais foram analisadas a fim de avaliar se mudanças de longo prazo na intensidade do Giro de Ross estão associadas a transformações observadas nas massas d'água sobre a plataforma continental e na região ao largo da plataforma continental do oeste da Antártica.

3.6 Circulação de verão e transporte de massas d'água no estreito de Bransfield, Antártica: avaliação da resposta aos efeitos combinados do SAM e do ENSO

Com o objetivo de caracterizar a circulação local com foco na variabilidade interanual e nos caminhos de intrusões da CDW sobre a plataforma continental da Península Antártica, duas seções hidrográficas no estreito de Bransfield foram amostradas 17 vezes entre 2003 e 2019. Essas campanhas resultaram em perfis de condutividade-temperatura-profundidade com resolução vertical de 1 dbar (**Figura 8**). A seção 1 situa-se entre as ilhas King George e D'Urville (retângulo vermelho delimitando os pontos magenta na **Figura 8**), enquanto a seção 2 localiza-se entre as ilhas Elephant e Joinville (retângulo vermelho delimitando os pontos pretos na **Figura 8**). Através do método dinâmico pode-se obter as velocidades geostróficas entre as estações oceanográficas para cada seção analisada.

3.6.1 Método Dinâmico

O método dinâmico estima a componente baroclínica relativa da velocidade geostrófica, perpendicular a um transecto, a partir das diferenças horizontais de densidade

entre perfis hidrográficos. Como esse cálculo fornece apenas o cisalhamento vertical da velocidade em relação a um nível de referência, é necessário atribuir uma velocidade conhecida ou assumir velocidade nula nesse nível para determinar o campo de velocidade geostrófica ao longo de toda a coluna d'água. Quando uma velocidade de referência independente é utilizada, obtém-se a velocidade geostrófica absoluta, que pode incluir tanto a estrutura baroclínica quanto uma componente barotrópica.

Neste estudo, as velocidades geostróficas da seção transversal (seções 1 e 2) foram calculadas referindo-se o cisalhamento a um nível de não movimento a 500 m. Isso segue estudos regionais anteriores [*e.g.,* Grelowski *et al.,* 1986; Gomis *et al.,* 2002; Sangrà *et al.,* 2011, 2017]. A escolha de 500 m se justifica, pois, apenas pequenas porções das seções hidrográficas se estendem abaixo dessa profundidade. Além disso, as inclinações isopicnais abaixo de 500 m são geralmente fracas, sugerindo uma contribuição mínima das camadas mais profundas para o cisalhamento geostrófico integrado verticalmente, reduzindo assim a incerteza na definição do nível de referência. Adicionalmente, Mukhametyanov *et al.,* [2022] demonstraram que um nível de referência de 500 m no estreito de Bransfield captura mais da metade do transporte medido por um perfilador de corrente Doppler acústico, corroborando a adequação dessa profundidade.

As propriedades termohalinas (Θ e S_A) e as velocidades geostróficas foram interpoladas em uma grade de latitude de 0,05° abrangendo do primeiro ao último perfil de cada seção. Os dados foram interpolados em 2D usando uma função de base radial (RBF) com ponderação linear e um fator de suavização de 0,1. Essa interpolação facilitou o cálculo das médias temporais ao longo de todo o período, mitigando o impacto das lacunas de dados espaciais observadas em anos específicos.

3.6.2 Validação da reanálise GLORYS12v1 na representação da estrutura termohalina e da circulação do estreito de Bransfield

Considerando as lacunas espaciais e temporais no conjunto de dados observacionais, as médias de verão (janeiro-março) das propriedades termohalinas e o campo de velocidade completo (componentes barotrópicos e baroclínicos) da reanálise GLORYS12v1 foram utilizados para investigar a variabilidade interanual.

Para validar a GLORYS12v1, todas as medições hidrográficas de verão

disponíveis, de 2003 a 2019, foram interpoladas na grade do modelo. A validação envolveu a comparação dos perfis termohalinos médios para ambas as seções analisadas e a avaliação da capacidade do modelo de reproduzir as massas de água do estreito de Bransfield por meio de diagramas Θ/S_A.

3.6.3 Cálculo do transporte de massa de água a partir da saída da GLORYS12v1

Após a validação do GLORYS12v1, os transportes de volume das principais massas de água entre as duas seções foram calculados. Devido à orientação oblíqua do estreito de Bransfield em relação ao norte verdadeiro, a componente zonal da velocidade foi projetada em um sistema de coordenadas local rotacionado 60° no sentido horário a partir do norte geográfico [Gordey *et al.,* 2024]. Essa rotação alinhou o sistema de coordenadas com a orientação batimétrica local, isolando a componente da velocidade perpendicular às seções. O transporte de volume da massa de água em Sv foi obtido pela integração da componente da velocidade projetada vertical e horizontalmente dentro de camadas específicas da massa de água. As camadas foram definidas usando os critérios Θ e SA de estudos anteriores [*e.g.,* Huneke *et al.,* 2016; Morozov *et al.,* 2021; Gordey *et al.,* 2024]: TBW ($\Theta > 0$ °C e $S_A < 34{,}65$ g kg^{-1}) e TWW ($\Theta < -0{,}45$ °C e $S_A > 34{,}60$ g kg^{-1}).

Como a TBW se forma pela mistura entre a CDW e as águas superficiais/intermediárias de Bellingshausen, a contribuição da CDW para as camadas intermediárias e superficiais foi avaliada para investigar a variabilidade do transporte de TBW. A espessura média da camada de CDW, definida como a faixa de profundidade onde $\Theta > 0$ °C e $34{,}60$ g kg^{-1} $< S_A <$ $34{,}92$ g kg^{-1}, seguindo Damini *et al.,* [2022], foi calculada. Este método fornece informações sobre a penetração da CDW em profundidades intermediárias/superficiais e sua influência potencial na transformação regional das massas de água.

3.6.4 Conjunto de dados de altimetria por satélite

A circulação geostrófica superficial na área de estudo foi derivada do conjunto de dados *Global Ocean Gridded L4 Sea Surface Heights and Derived Variables Reprocessed* (https://doi.org/10.48670/moi-00145), acessível através do Serviço de

Monitoramento do Ambiente Marinho Copernicus (CMEMS; data.marine.copernicus.eu). As velocidades geostróficas superficiais derivadas deste conjunto de dados possuem uma resolução espacial de 0,25° e foram utilizadas para comparação com as velocidades geostróficas calculadas a partir da hidrografia. Adicionalmente, a vorticidade relativa[3] foi calculada como $\zeta z = \partial v/\partial x - \partial u/\partial y$ para verificar estruturas relevantes na circulação da região (e.g., vórtices), onde u e v são as componentes zonal e meridional do campo de velocidade da corrente, respectivamente.

3.6.5 Análise atmosférica

Como mencionado anteriormente, a posição da ACC, impulsionada pela variabilidade dos padrões de vento, desempenha um papel crucial na advecção da CDW para a Península Antártica (*i.e.,* o estreito de Bransfield), contribuindo para a formação da TBW, que é posteriormente transportada para o estreito de Bransfield. Nesse contexto, um dos objetivos desta tese é avaliar como os efeitos combinados do SAM com ENSO influenciam a advecção atmosférica e, consequentemente, no transporte de massas de água para dentro do estreito de Bransfield. Para quantificar esses efeitos combinados, foi utilizado o Índice ENSO-SAM de Verão (SEI; https://zenodo.org/records/7500163), que integra ambos os modos climáticos. Nesse contexto, valores positivos de SEI (> 0,50) correspondem a períodos de SAM positivo combinado com ENSO negativo, enquanto valores negativos de SEI (< −0,50) correspondem a SAM negativo combinado com ENSO positivo [Llanillo *et al.,* 2023].

Seguindo Veny *et al.,* [2024], a média do rotacional da tensão do cisalhamento do vento no verão (janeiro-março) e a velocidade vertical de Ekman foram calculadas a partir da velocidade média mensal do vento do *European Centre for Medium-Range Weather Forecasts* [ERA-Interim; https://www.ecmwf.int/en/forecasts/dataset/ecmwf-reanalysis-interim; Dee *et al.,* 2011], que possui uma resolução horizontal de 0,70 × 0,70° no período de 1979 a 2019 (resultado semelhante ao obtido com a nova versão ERA5). As anomalias do rotacional da tensão do cisalhamento do vento foram calculadas subtraindo-se a média

[3]Vorticidade relativa: A vorticidade relativa (ζ) quantifica a rotação horizontal do fluido em relação ao referencial da Terra. Mapas de vorticidade relativa permitem identificar regiões de alto cisalhamento e vórtices (e.g., o vórtice ASFb formado no estreito de Bransfield).

temporal de todo o período (janeiro-março de 2003-2019) da média de cada período do SEI analisado (*i.e.,* a fase positiva e a fase negativa do SEI). Assim, destacando as mudanças nas forçantes atmosféricas dos períodos analisados. Por fim, a relação dinâmica entre o forçamento atmosférico e a resposta oceânica local foi testada calculando-se as correlações de Spearman entre o rotacional da tensão de cisalhamento do vento normalizado e sem tendência sobre a estreito de Bransfield e o índice SEI para o período de 1979 a 2019 (*i.e.,* considerando a série histórica completa).

Chapter I: Introduction

Over the last decades, global climate assessments have emphasized the accelerating pace of anthropogenic climate change and its disproportionate impacts at high latitudes. According to the latest IPCC report [IPCC AR6], atmospheric carbon dioxide (CO_2) concentrations have reached levels unprecedented in at least the last 2 million years (~ 420 ppm in 2021), driving record global temperatures, increased ocean heat content, and widespread cryospheric decline.

It accounts for absorbing the majority of the excess heat taken up by the global ocean (~75%) and is also responsible for absorbing around 43% of anthropogenic carbon emissions (*i.e.,* human-derived). Therefore, acting as a climate regulator and delaying the full expression of global warming [IPCC AR6; Frölicher *et al.,* 2015; Gruber *et al.,* 2019; Friedlingstein *et al.,* 2020]. Within the complex Southern Ocean circulation, there is the world's strongest ocean current, the Antarctic Circumpolar Current [ACC; *e.g.,* Rintoul & Sokolov 2001; Mazloff *et al.,*2010], formed in part by the lack of continental landmass in its zonal flow. This results in a large wind–driven eastward current that surrounds Antarctica [Talley, 2011]. Within the complex Southern Ocean circulation, there is the world's strongest ocean current, the Antarctic Circumpolar Current [ACC; *e.g.,* Rintoul & Sokolov 2001; Mazloff *et al.,*2010], formed in part by the lack of continental landmass in its zonal flow. This results in a large wind–driven eastward current that surrounds Antarctica [Talley, 2011]. Additionally, the ACC connects all major ocean basins (*i.e.,* Atlantic, Indian and Pacific basins; **Figure 1**), forming a critical component of the global overturning circulation. This inter-basin connectivity enables the exchange of water mass properties and climate signals, supporting large-scale oceanic teleconnections [*e.g.,* Peterson & White, 1998].

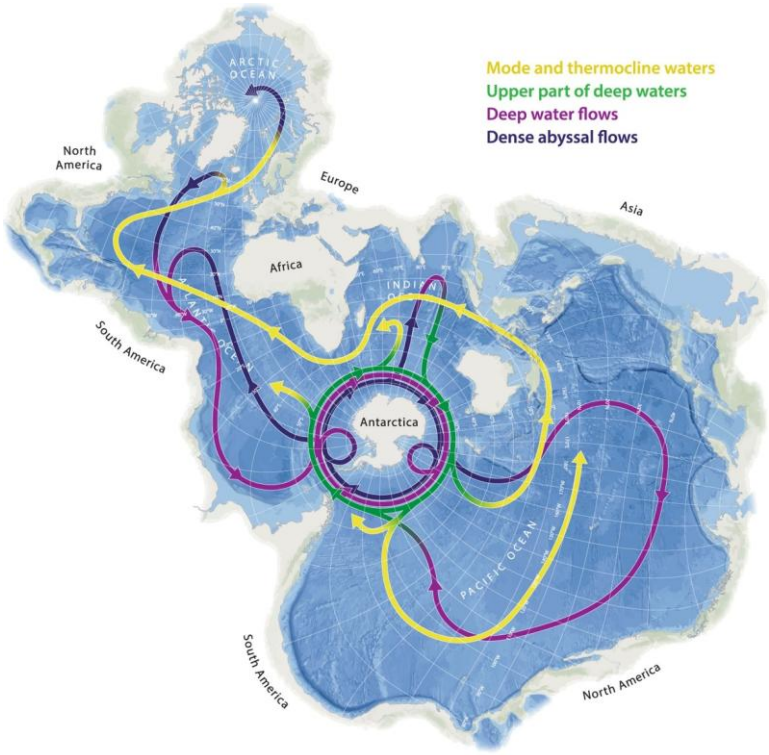


Figure 1: Schematic of the overturning circulation from a Southern Ocean perspective. This region is the most prominent location globally where deep waters (purple) rise to the surface, exchange heat and carbon with the atmosphere, and then return to the ocean interior. Figure from Meredith *et al.,* [2022].

The volume of water transport of ACC is concentrated in a series of well–separated fronts with distinct temperature and salinity signatures and are associated with deep–reaching jets and subduction or upwelling of different water masses (*i.e.,* the Subtropical Front, the Subantarctic Front, the Polar Front, the Southern ACC Front – SACCF and the Southern Boundary Front – SB; Orsi *et al.,* 1995; **Figure 2**; **please see chapter II to more information**). Around 55% of ACC transport originates from warm, saline Circumpolar Deep Water (CDW), which shoals near the southern boundary, making it available for intrusion onto the Antarctic continental shelf, where it delivers ocean heat to ice-shelf cavities.

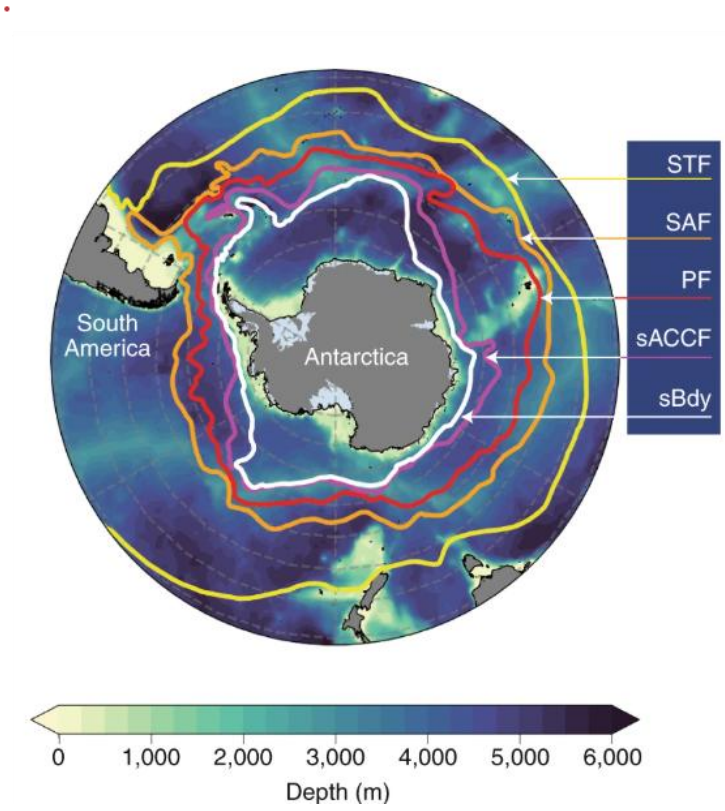


Figure 2: Mean position of the frontal system of the Antarctic Circumpolar Current as determined by Orsi *et al.,* [1995] using historical hydrographic data and water-mass criteria (such as a specific temperature value at a given depth) to define their locations. The named fronts, from north to south, are: Subtropical Front (STF), Subantarctic Front (SAF), Polar Front (PF), southern ACC Front (sACCF), and the Southern Boundary (SBdy). The background colorbar shows ocean depth. Figure from Chapman *et al.,* [2020].

There are several mechanisms responsible for the transport of CDW onto Antarctic continental shelves, such as (i) wind-induced upwelling (*e.g.,* Ekman suction) at the shelf break, modulated by westerlies north of the break, which generates off-shore Ekman transport in the surface layer and forces CDW to rise and invade the shelf [*e.g.,* Kim *et al.,* 2017]; (ii) flow into the canyons with overflow onto the continental shelf controlled by easterly winds, which forces the westward undercurrent present there. The interaction of this undercurrent with the bathymetry (especially submarine canyons) directs the CDW towards the continental shelf [*e.g.,* Arneborg *et al.,* 2012; Walker *et al.,* 2013; Silvano *et al.,* 2022]; and (iii) diffusion by eddies shed from ACC through baroclinic instability imposed by the westerlies [*e.g.,* Yamazaki *et al.,* 2021, 2023]. Overall, these processes are influenced by wind patterns variability linked to climate modes [*e.g.,* Southern Annular Mode – SAM, El Niño/Southern Oscillation – ENSO, and the Amundsen Sea Low – ASL; Jenkins *et al.,*2018; Dotto *et al.,*2020].

Recent studies have documented significant warming in recent decades (~0.1 °C per decade) of the intermediate and deep layers of the Southern Ocean (at the CDW layer below 200 m). Off East Antarctica, around 60% of this warming has been attributed to a poleward shift of the ACC frontal system and its hydrographic structure, which replaces relatively cooler CDW at the southern edge of the ACC with warmer CDW from farther north [Herraiz-Borreguero & Naveira Garabato, 2022]. A second key mechanism is enhanced isopycnal heat transport cross-ACC [*e.g.,* via eddy activity; Yamazaki *et al.,* 2021; Herraiz-Borreguero & Naveira Garabato, 2022]. Both processes are linked to changes in wind forcing associated with large-scale climate variability [Yamazaki *et al.,* 2021, 2023; Zu *et al.,* 2022]. This progressive ocean warming has been implicated in the increased basal melting of ice shelves [Herraiz-Borreguero & Naveira Garabato, 2022; Rott *et al.,* 2018], resulting in significant changes in sea level [Sheperd *et al.,* 2010] and the formation of bottom waters [Silvano *et al.,* 2018].

While these mechanisms are relatively well established for East Antarctica, the drivers of off-shelf CDW variability in West Antarctica (Amundsen, Bellingshausen Seas, and the western Antarctic Peninsula) remain less well understood [*e.g.,* Nakayama *et al.,* 2018]. This knowledge gap is particularly concerning, as the most rapid ice shelf thinning and collapse observed in Antarctica has occurred along the West Antarctic margin, driven by intrusions of CDW through deep bathymetric troughs [*e.g.,* Rignot *et al.,* 2019]. A detailed understanding of how the poleward migration of ACC fronts and associated wind-driven changes modulate CDW access to the continental shelf is, therefore, essential for predicting future Antarctic Ice Sheet evolution [*e.g.,* Gille *et al.,* 2016] and its contribution to global overturning circulation and sea-level rise [Morrison *et al.,* 2020].

Therefore, the focus of this thesis study changes of CDW off West of Antarctica (*i.e.,* Amundsen, Bellingshausen Seas) between the 1990s and 2010s (i.e.,1990-2020) and seeking to understand the mechanisms that affect this thermohaline variability of the off-shelf CDW and possible consequences in the continental shelf regions. For this, we used hydrographic observations provided by several open-access oceanographic databases [*i.e.,* World Ocean Database 23, Thwaites-Amundsen Regional Survey and Network; Argo; Carbon Hydrographic Data Office; and Marine Mammals Exploring the Ocean Pole to Pole consortium data] and a high–resolution ocean reanalysis [GLORYS12v1; Jean–Michel *et al.,* 2021].

Additionally, a dedicated component of this thesis examines the variability of this modified CDW intrusion into the Bransfield Strait, located adjacent to the Antarctic Peninsula. A region considered a key area for studying the impacts of climate change due to its transitional environment connecting waters from the cold shelf regime of the Weddell Sea with the relatively warm oceanic regime of the Bellingshausen Sea [Kerr *et al.,* 2018], and most studied by the Brazilian High Latitude Oceanography Group (GOAL) since the 2000s [Mata *et al.,* 2018]. By advancing the understanding of circulation processes (*i.e.,* CDW pathways) in this area, this research aims to support and inform future physical, biogeochemical, and ecological studies carried out under the Brazilian Antarctic Program (PROANTAR).

Next, we present the objectives that guide the development of this thesis. **Chapter II** describes the area of study based on a detailed literature review, while **Chapter III** presents the methodology adopted to achieve these objectives. Finally, the results and discussions (resulting in published or submitted manuscripts) of this thesis will be presented in **Chapter IV**, and subsequently, in **Chapter V**, a summary of the main considerations of this thesis will be provided.

1.1 Objectives

1.1.1 Main objective

- To investigate the thermohaline properties of the CDW and assess the mechanisms that influence the intrusion of this water into the West Antarctic region.

1.1.2 Specific objective

- To examine the contribution of the position of the ACC frontal system to the interdecadal variability (between the 1990s and 2010s) of the thermohaline properties of the CDW in the Amundsen and Bellingshausen Seas.

- To investigate the role of the Ross Gyre as a modulator of the seasonal and interannual variability of the CDW properties in the Amundsen and Bellingshausen Seas.

- To investigate the influence of wind on the transport of the CDW over the continental shelf of the Antarctic Peninsula and analyze the interannual variability of this transport during the period from 2000 to 2020.

Chapter II: Study Area

2.1 Antarctic Circumpolar Current frontal system

The ACC is characterized by several fronts representing boundaries between zones with distinct water mass properties (**Figure 3**). The main zones delimited by the oceanic fronts are: (i) Subantarctic Zone between the SAF and PF, (ii) Polar Front Zone between the PF and SACCF, and (iii) Antarctic Zone between the SACCF and the continent. Within the AZ, one can further distinguish between the subpolar regime, the region south of the SB, and the continental zone marked by circulation and transport associated with the Antarctic Slope Current (ASC).

The seasonal to interannual variability in the transport, extent, and position of the ACC fronts has been extensively examined over the past decades using a range of observational and diagnostic approaches, including water mass properties [*e.g.,* Orsi *et al.,* 1995; Kim & Orsi, 2014], fixed sea surface height (SSH) contours and/or fixed Absolute Dynamic Topography (ADT[4]) fixed contours, SSH gradients, and mean transport positions [*e.g.,* Sokolov and Rintoul, 2007, 2009a,b; Billany *et al.,* 2010; Gille, 2014; Gille *et al.,* 2016; Schiavon *et al.,* 2025]. Collectively, these studies reveal that the ACC fronts have undergone spatially heterogeneous displacements, with some regions exhibiting pronounced poleward displacement while others remain relatively stationary

[4] Absolute dynamic topography (ADT): is a specific type of SSH dataset. ADT represents the total and instantaneous height of the ocean surface above the geoid, calculated as the sum of Sea Level Anomalies and Mean Dynamic Topography.

due to topographic steering and eddy saturation effects[5] [*e.g.,* Sokolov and Rintoul, 2009 a,b; Yamazaki *et al.,* 2022; Herraiz-Borreguero & Naveira Garabato, 2022]. For instance, Sokolov and Rintoul [2009b], using fixed SSH contours to define each front of the ACC over 15 years (1992–2007), reported a south pole-toward shift of ~0.6° latitude (~60–70 km). However, they warned that the latitude of fixed SSH contours reflects not only dynamical shifts in geostrophic flow, but also steric sea-level variations driven by long-term upper-ocean warming, cooling (*i.e.,* thermosteric effects), which, correcting this, remains a challenge. remains challenging.

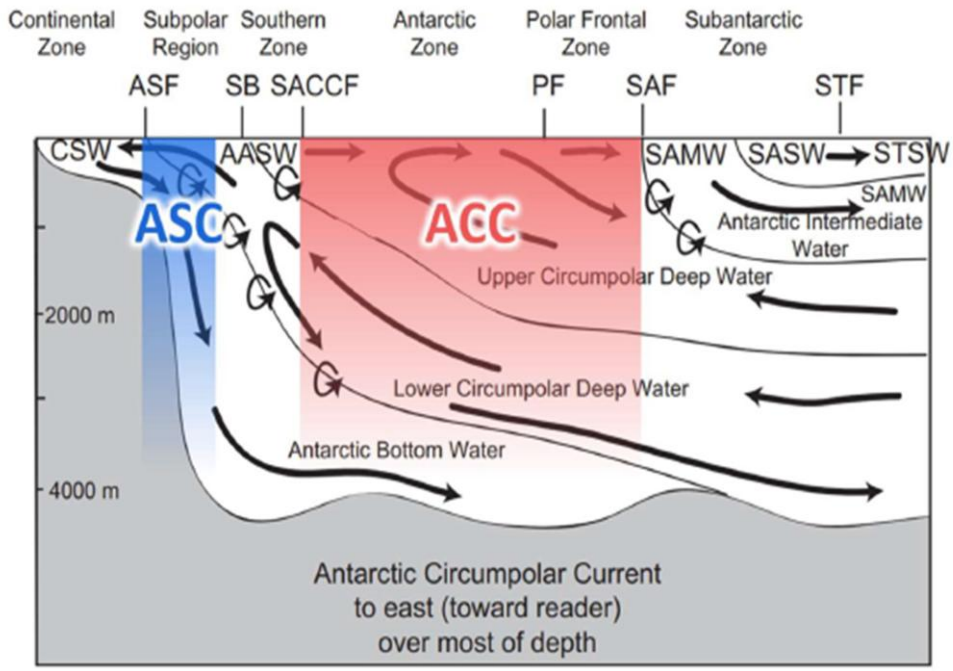


Figure 3: Zonal vertical view (from the surface to the deep ocean) of the meridional flows of the main water masses entering and leaving the Southern Ocean. The acronyms derived from English are: Antarctic Circumpolar Current (ACC), Continental Shelf Water (CSW), Antarctic Surface Water (AASW), Subantarctic Mode Water (SAMW), Subantarctic Surface Water (SASW), Subtropical Surface Water (STSW), Antarctic Intermediate Water (AIW), Upper Circumpolar Deep Water (UCDW), Lower Circumpolar Deep Water (LCDW), Antarctic Bottom Water (AABW), Antarctic Slope Front (ASF), Southern Boundary (SB), Southern ACC Front (SACCF), Polar Front (PF), Subantarctic Front (SAF), and Subtropical Front (STF). Figure from Yamazaki, [2022].

[5]Eddy saturation: Instead of the mean flow accelerating or the front displacement, the extra energy from the wind is immediately converted into the mesoscale eddy field [Marshal & Radko, 2003].

Given these uncertainties, whether or not the ACC fronts are displacing remains an open and actively debated question in polar oceanography. To minimize the influence of thermosteric effects, Gille, [2014] applied a transport latitude index (a latitudinal average weighted by geostrophic transport) and found that the circumpolar-mean position of the ACC has remained largely stable between 1990s e 2000s. However, interpreting circumpolar averages can be misleading, as the ACC frontal system does not behave as a single feature [Kim & Orsi, 2014]. Opposing regional trends can therefore cancel each other out, leading to a smoothed (or weakened) circumpolar average signal that conceals regional fluctuations. In this sense, more recent studies using subsurface temperature fields to identify the Southern Boundary Front of ACC observed its poleward displacement of ~150 km between the 1990s and 2010s off East Antarctica [*e.g.,* Yamazaki *et al.,* 2022; Herraiz-Borreguero & Naveira Garabato, 2022]. Such a poleward shift may enhance oceanic heat transport toward East Antarctica, potentially amplifying basal melting and threatening the long-term stability of the ice sheet [Herraiz-Borreguero & Naveira Garabato, 2022].

2.2 The Southern Ocean Circulation Off West Antarctica

The West Antarctica sector lies within the Pacific Ocean sector of the Southern Ocean (encompassing the Amundsen and Bellingshausen Seas and the Antarctic Peninsula) and is particularly sensitive to changes in regional wind patterns, which are strongly modulated by large-scale atmospheric circulation [Turner *et al.,* 2017; Dotto et a., 2020; Damini *et al.,* 2022; Oelerich *et al.,* 2022]. The regional wind pattern is characterized by westerlies north to continental slope (around 50 ºS), and easterlies over the continental shelf (around 70°S). However, in eastern portion of this sector (*i.e.,* from the eastern Bellingshausen Sea to the Antarctic Peninsula), where easterlies are practically absent, resulting in a weaker coastal wind regime. The transition zone between the opposing wind systems is known as the Antarctic Divergence, a dynamically important region associated with the strong upwelling of intermediate and deep waters (*e.g.,* CDW). This upwelling is driven by the input of cyclonic wind circulation (*i.e.,* negative wind stress curl) produced by that divergence of the westerlies and easterlies belts. The Antarctic Divergence is typically found at the southern Antarctic Circumpolar Current edge, between the boundaries of the SAACF and the SBDY.

Moreover, these regional winds pattern are highly variable due to the influence of

the Amundsen Sea Low (ASL), a persistent centre of low pressure located between the Amundsen-Bellingshausen Seas (**Figure 4**) that shifts zonally and meridionally through the year [*e.g.,* Raphael *et al.,* 2016]. The deepening of ASL (*i.e.,* strengthened) leads to intensified cyclonic wind circulation over the region, which supplies CDW off West Antarctica and consequently might increase basal melting of the Ice Shelves [*e.g.,* Paolo *et al.,* 2018; Dotto *et al.,* 2020]. Large-scale modes of climate variability, such as the Southern Annular Mode (SAM) and the El Niño Southern Oscillation (ENSO), modulate the strength and position of ASL and therefore influence the regional wind field over the region [Fogt *et al.,* 2012; Clem *et al.,* 2017].

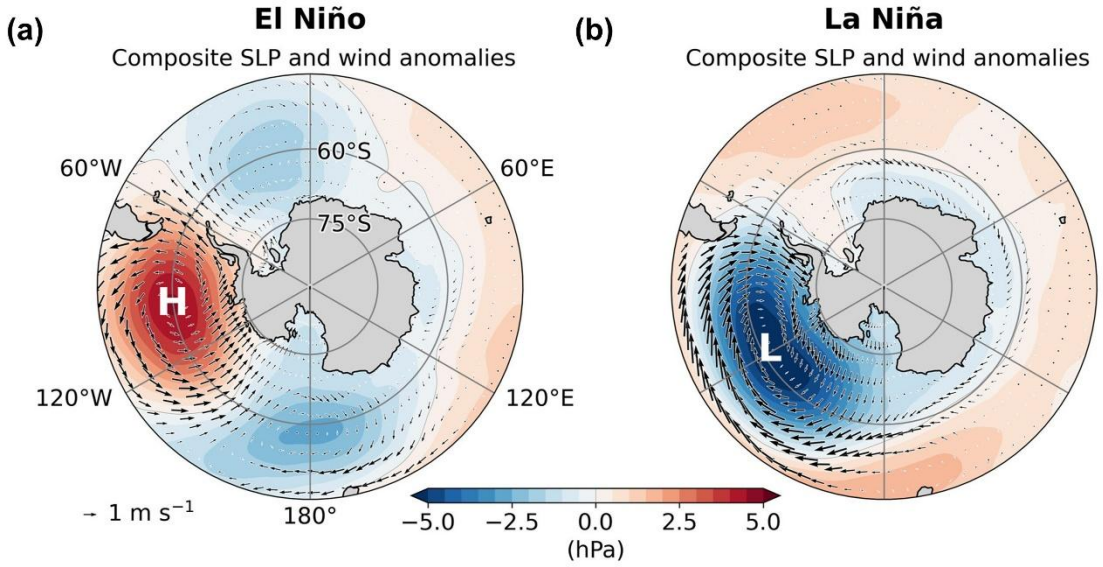


Figure 4: Mean sea level pressure anomalies (SLP; hPa) and surface wind anomalies (m s^{-1}, arrows). The symbols H and L indicate the location of the major (weakening) and minor (intensification) SLP centers (of the Amundsen Sea Low), respectively. Figure from Huguenin *et al.,* [2024].

The SAM is the dominant mode of atmospheric variability in the high southern latitudes, and it characterized by the difference of pressure and mass between Antarctica and mid-latitudes [*e.g.,* Marshall, 2003]. During its positive phase, a negative sea level pressure anomaly occurs over Antarctica, strengthening the westerlies and shifting the ASL eastward (toward the Bellingshausen Sea). On the other hand, during the negative phase, positive sea level pressure anomaly occurs at mid latitudes weaken the westerlies and leading to a westward displacement of ASL (toward Ross Sea).

ENSO is related to anomalous changes in the temperature of the tropical ocean. This leads to changes in the atmospheric pressure field and in the wind pattern that

propagates through planetary Rossby waves to other parts of the globe, including towards West Antarctica (*e.g.,* Yuan 2004). During its positive phase (El Niño), a positive sea level pressure anomaly occurs over Antarctica (**Figure 4a**), weakening the westerlies and ASL westward (toward Ross Sea). While, during the negative phase (La Niña), a negative sea level pressure anomaly occurs over Antarctica (**Figure 4b**), strengthening the westerlies and shifting the ASL eastward [toward Bellingshausen Sea; Raphael *et al.,* 2016].

As mentioned before, the cyclonic winds circulation over the Southern Ocean promotes the upwelling of the CDW in the oceanic region adjacent to the continental shelf (off-shelf) up to the continental slope, where it meets the relatively colder and denser waters of the shelf (*e.g.,* adjacent to ice shelves). The pronounced gradient formed by this encounter of waters with distinct thermohaline characteristics forms a system composed by Antarctic Slope Current (ASC) and Antarctic Slope Front (ASF). This system varies in intensity and configuration regionally along the Antarctic continental margin (**Figure 5**). For instance, the West Antarctic is characterized by a warm-shelf regime, in which transverse density gradients tend to be less pronounced, resulting in the ASC and ASF tends to be relatively weak or even discontinuous. In this regime, the CDW can flow more easily through submarine troughs that connect the continental shelf to the open ocean, in contrast to dense-shelf regimes such as those in the Weddell and Ross Seas, where the presence of the ASC and ASF acts as a dynamic barrier. This front inhibits the on-shelf intrusion of CDW and favors the formation of dense, cold shelf waters [Thompson *et al.,* 2018].

The cyclonic wind pattern of West Antarctica drives the formation of a gyre, commonly called the Ross Gyre, which dominates the circulation south of the ACC in the western Pacific sector of the Southern Ocean. The position of the gyre is bounded to the south by the continental slope and to the north-east by the Pacific–Antarctic Ridge. On its eastern flank, the separation of the gyre's flow from the ridge allows much greater variability. Previous studies suggest that this configuration permits zonal heat transport by CDW toward the off-shelf of the Amundsen and Bellingshausen Seas [*e.g.,* Nakayama *et al.,* 2018], where it can be further delivered to the ice shelves [*e.g.,* Prend *et al.,* 2024]. In contrast, the western flank of the gyre follows the continental slope along the Ross Sea. This branch is responsible for transporting dense shelf waters equatorward [*e.g.,* Dinniman *et al.,* 2011]. However, despite its fundamental role, the scarcity of in situ

observations in this vast region seasonally covered by ice limits the understanding of its variability and the mechanisms that control it, as well as its influence on the Amundsen and Bellingshausen Seas. Thus, one of the objectives of this thesis is to elucidate these questions related to the Ross Gyre (**see Chapter 4.2**).

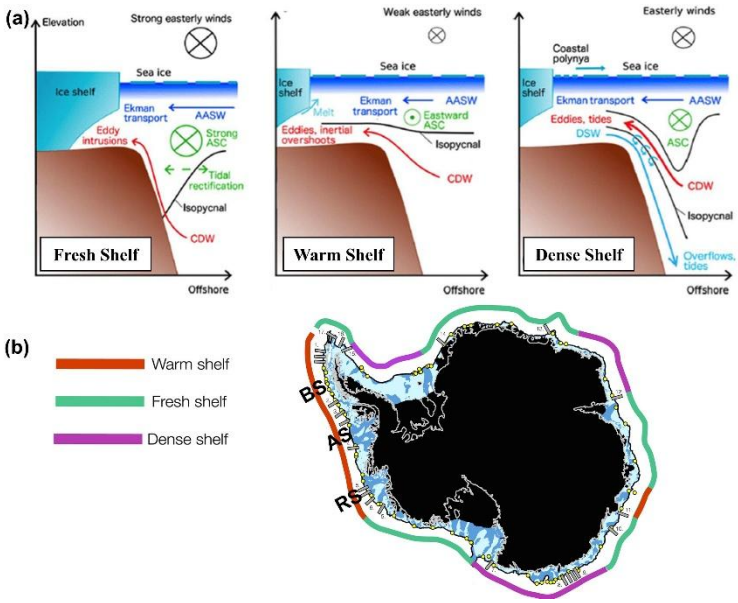


Figure 5: (a) Main water masses and along-slope and cross-slope flows defined by Thompson *et al.,* [2018], namely the Fresh Shelf, Warm Shelf, and Dense Shelf regimes, shown from left to right, respectively. **(b)** Geographic locations of these distinct BS, AS and RS indicated the Bellinshausen, Amundsen and Ross Seas, respectively regimes. Figure from Thompson *et al.,* [2018].

The Southern Ocean is a highly dynamic system, and the western Antarctic region, owing to its complex topography, exhibits distinct circulation characteristics across its subregions (*i.e.,* the Amundsen and Bellingshausen Seas and the Antarctic Peninsula). To provide a more comprehensive understanding of the dynamical processes governing this region and their influence on CDW intrusions, the main circulation patterns of each subregion will be described below.

2.2.1 Amundsen and Bellingshausen Seas

The Bellingshausen and Amundsen Seas are oceanographically similar, both lacking well-defined northern and western boundaries (**Figure 6**). Their continental shelves are characterized by deep submarine troughs that incise the seafloor, extending from the shelf break toward the ice shelves.

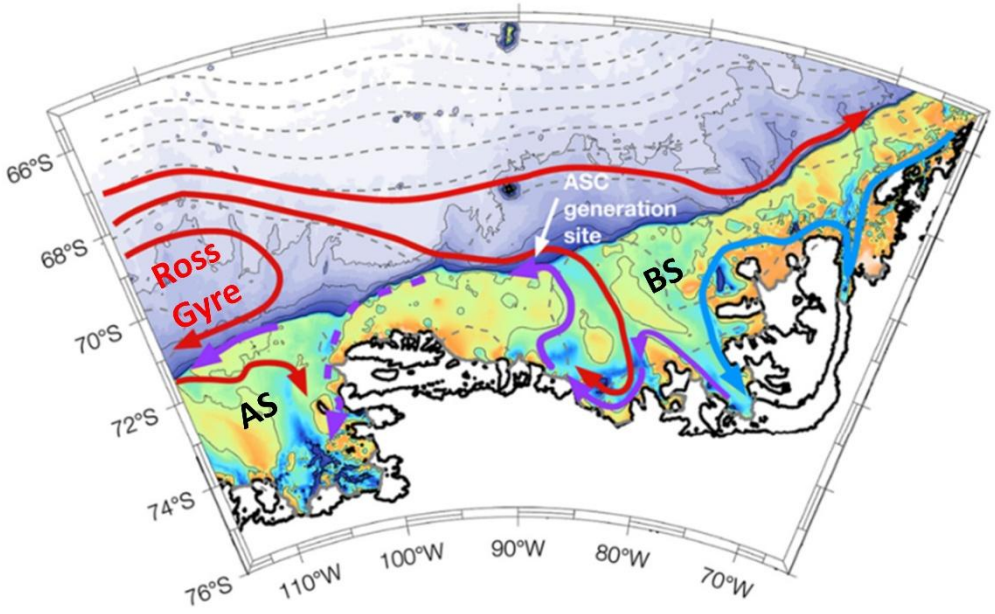


Figure 6: Schematic representation of the transport pathways in the Amundsen and Bellingshausen Seas. The dashed gray lines show the mean dynamic topography for 2011–2016 (Armitage *et al.,* 2018) at 5 cm intervals. The colors of the arrows indicate the dominant water mass carrying the flow: blue (Antarctic Surface Water – ASW mixed with Winter Water – WW), red (Circumpolar Deep Water – CDW), and purple (WW). The dashed purple arrow indicates a pathway of WW and ASW toward the Amundsen Sea suggested by Thompson *et al.,* [2020]. The labels AS and BS indicate the Amundsen and Bellingshausen Seas, respectively. Figure from Thompson *et al.,* [2020].

The upper ocean in these regions is composed by Antarctic Surface Water (AASW) and Winter Water (WW), that are formed locally through air–sea–ice interactions. The AASW develops during summer, when surface warming and sea-ice melt produce a warmer and fresher upper layer. In contrast, the WW forms in winter as intense surface cooling and brine rejection during sea-ice formation increase water density, deepening the mixed layer. Beneath these layers lies CDW, supplied from offshore by the ACC. Its intrusions onto the continental shelf are controlled by a combination of dynamic and thermodynamic processes operating near the shelf break, which exhibit pronounced spatial variability across these regions [*e.g.,* Webber *et al.,* 2017; Dotto *et al.,* 2019; Silvano *et al.,* 2022].

In the Bellingshausen Sea, the ASC and ASF are absent along the continental shelf, allowing off-shelf CDW to flow onto the shelf almost unrestricted. Cross-shelf exchange primarily occurs through the Marguerite Trough and via coherent eddies shed from the ACC as a result of baroclinic instability [Moffat *et al.,* 2009; Couto *et al.,* 2017].

This region also hosts an ACoC, which transports AASW and WW westward toward the Amundsen Sea [*e.g.,* Thompson *et al.,* 2020; Schubert *et al.,* 2021]. This advection influences the depth of the regional thermocline and contributes to the circulation of the eastern Amundsen Sea [*e.g.,* Thompson *et al.,* 2020; Schubert *et al.,* 2021].

In contrast, in the Amundsen Sea, an eastward subsurface current develops along the shelf break due to baroclinicity associated with the ASC and ASF [*e.g.,* Si *et al.,* 2024]. This current is more pronounced in the western Amundsen Sea (*i.e.,* Dotson–Getz Troughs; **Figure 7**), where the presence of a deeper and more open trough [*e.g.,* Cochran *et al.,* 2020] makes this undercurrent one of the main pathways for CDW inflow. A recent numerical study shows that this undercurrent can be intensified by easterlies winds, which steepen the ASC and ASF and enhance CDW advection onto the continental shelf [*e.g.,* Silvano *et al.,* 2022].

In the eastern Amundsen (Pine Island Trough; **Figure 7**), the troughs are shallower than those in the Dotson–Getz Troughs, vertically restricting CDW access. Consequently, the penetration of warm water becomes critically dependent on the depth of the thermocline [*e.g.,* Webber *et al.,* 2017]. In this context, the same easterlies winds drive a southward transport of surface waters, enhancing Ekman convergence and promoting the accumulation of surface waters mixed with glacial meltwater [*e.g.,* Webber *et al.,* 2019; Huguenin *et al.,* 2024]. This accumulation depresses isopycnals and consequently suppresses CDW intrusions onto the shelf [Jacobs *et al.,* 2011; Nakayama *et al.,* 2013; Dutrieux *et al.,* 2014; Webber *et al.,* 2017; Dotto *et al.,* 2019].

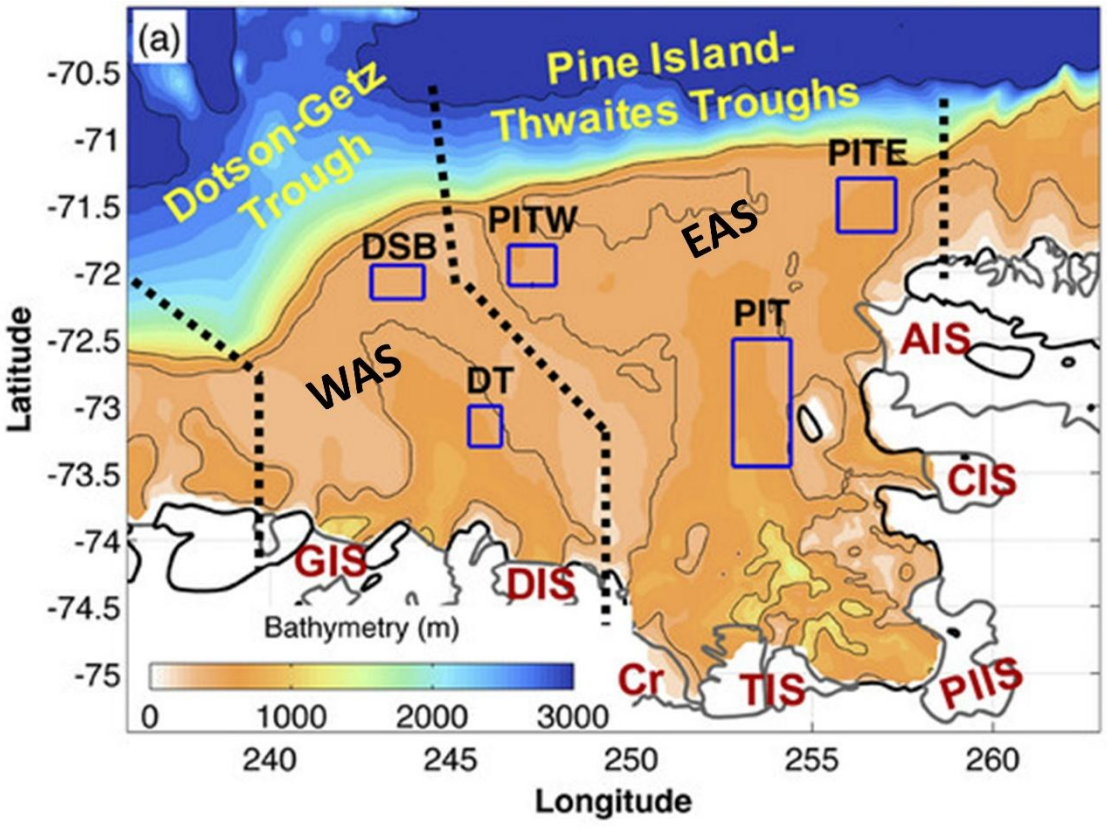


Figure 7: Amundsen Sea bathymetry region. Dotted lines show the definition of the Dotson–Getz trough and the Pine Island–Thwaites troughs. Blue rectangles indicate the Dotson Shelf Break (DSB), the Inner Dotson Trough (DT), the Pine Island–Thwaites Channel (PIT), the Pine Island–Thwaites West Channel (PITW), and the Pine Island–Thwaites East Channel (PITE). The 500, 1000, and 3000 m isobaths are represented. Abbot Ice Shelf (AIS), Cosgrove Ice Shelf (CIS), Pine Island Ice Shelf (PIIS), Thwaites Ice Shelf (TIS), Crosson Ice Shelf (Cr), Dotson Ice Shelf (DIS), and Getz Ice Shelf (GIS). WAS and EAS indicates the regions West and East of Amundsen Sea, respectively. Figure from Dotto *et al.,* [2019].

2.2.2 Antarctica Peninsula

The Antarctica Peninsula is particularly sensitive to climate change due to the profound implications that variations in the inflow of relatively warmer waters from the Bellingshausen Sea and colder waters formed in the Weddell Sea have for glacier dynamics and sea ice cover in this region [*e.g.,* Flexas *et al.,* 2022]. In this thesis, part of the study will focus on the Bransfield Strait, located in the northern sector of the Antarctica Peninsula, a region that acts as a key gateway for water mass exchange between the Bellingshausen and Weddell Seas.

The circulation in the Bransfield Strait is dominated by a cyclonic gyre that transports intermediate waters mixed with Dense Shelf Water (DSW) formed in the

Weddell Sea (*i.e.,* Transitional Weddell Water – TWW) southward, toward the vicinity of the Bellingshausen Sea [Sangrà *et al.,* 2011, 2017; Dotto *et al.,* 2016; van Caspel *et al.,* 2015, 2018; Ruiz Barlett *et al.,* 2018; Morrinson *et al.,* 2023]. These shelf waters are advected into the Bransfield Strait through the coupled system formed by the Antarctic Coastal Current (ACoC) and the Antarctic Slope Front (ASF) [Fahrbach *et al.,* 1992; Gordon *et al.,* 2000; von Gyldenfeldt *et al.,* 2002; Heywood *et al.,* 2004; Thompson *et al.,* 2009; Collares *et al.,* 2018; Sangrà *et al.,* 2017]. Upon encountering the South Scotia Ridge, this circulation system bifurcates into three distinct TWW pathways: the first transports water through the eastern Bransfield Strait near Joinville Island; the second follows the 1000 m isobath eastward along the southern flank of the South Scotia Ridge; and the third forms a quasi-stationary eddy generated by strong horizontal shear and associated topographically induced upwelling [Heywood *et al.,* 2004; Thompson *et al.,* 2009; Damini *et al.,* 2022]. In addition, some studies suggest another TWW advection pathway through the Antarctic Sound, between Joinville Island and the tip of the Antarctic Peninsula [Gordon *et al.,* 2000; Renner *et al.,* 2009; Thompson *et al.,* 2009; **Figure 8**]. Once advected into the Bransfield Strait, these dense waters sink through submarine canyons located on the adjacent continental shelf [*e.g.,* López *et al.,* 1999].

The mixing between surface waters from the Bellingshausen Sea and CDW advected by the ACC forming the Transitional Bellingshausen Water (TBW), which is subsequently transported into the Bransfield Strait through passages between the South Shetland Islands and via the Gerlache Strait (southern sector of the Antarctic Peninsula). Once advected into the strait, this water mass is transported by a relatively intense mesoscale baroclinic jet known as the Bransfield Current (BC), which flows southwest–northeast along the shelf break of the South Shetland Islands [**Figure 8**; Sangrà *et al.,* 2017]. Most of the flow associated with the BC is exported to the eastern of Bransfield Strait between King George and Elephant Islands; part of it recirculates between the South Shetland Islands [*e.g.,* Sangrà *et al.,* 2017]; and the remaining fraction flows into the Weddell–Scotia Confluence through the deep channel located between Elephant and Clarence Islands [*e.g.,* López *et al.,* 1999]. Additionally, the encounter of these water masses with those advected from the Weddell Sea continental shelf results in the formation of a surface front extending down to about 100 m depth, which separates water masses with distinct thermohaline properties, known as the Peninsula Front (PF) [Tokarczyk, 1987; García *et al.,* 1994, 2002; Savidge and Amft, 2009; Sangrà *et al.,* 2011,

2017].

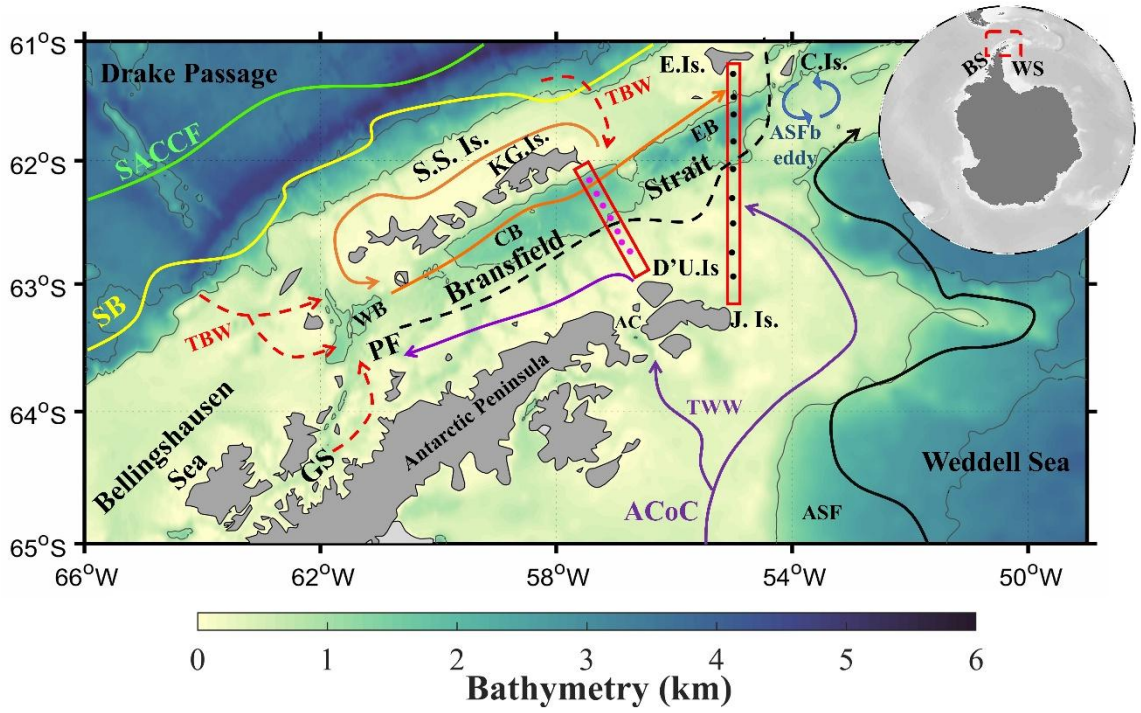


Figure 8: Schematic representation of the mean circulation in the Antarctic Peninsula region. The red (purple) arrows represent the pathways through which Bellingshausen Transitional Water (TBW) and Weddell Transitional Water (TWW) enter Bransfield Strait. The green and yellow lines indicate the mean positions of the Southern Antarctic Circumpolar Current Front (SACCF) and the Southern Boundary (SB), respectively. Light-blue arrows indicate the eddy associated with the Antarctic Slope Front bifurcation (ASFb). The orange arrows show the Bransfield Current and its recirculation around the South Shetland Islands (S.S.Is.). The black line represents the mean position of the Antarctic Slope Front (ASF). The red rectangles surrounding the magenta and black dots delimit the hydrographic sections for Sections 1 and 2 (further detailed in the Materials and Methods section). The dashed black line represents the Peninsula Front (PF). The acronyms correspond to: Antarctic Channel (AC), Antarctic Coastal Current (ACoC), Joinville Island (J.Is.), D'Urville Island (D'U.Is.), Elephant Island (E.Is.), Clarence Island (C.Is.), Bellingshausen Sea (BS), Drake Passage (DP), Weddell Sea (WS), Western Basin (WB), Central Basin (CB), Eastern Basin (EB), and Gerlache Strait (GS). Thin gray lines indicate the 0.10 km and 0.30 km isobaths provided by IBCSO. The inset panel shows the study region. Figure modified from Damini *et al.,* [2025].

It is worth noting that several studies suggest that the intensification and southward shift of the westerly winds, driven by positive phases of the SAM and negative phases of the ENSO, promote a poleward displacement of the ACC and its frontal system. This displacement, also investigated in this study, may enhance the inflow of TBW through turbulent and advective mechanisms over the continental shelf of the Antarctic

Peninsula [*e.g.,* Dotto *et al.,* 2016; Damini *et al.,* 2022; Ruiz Barlett *et al.,* 2018; Martinson and McKee, 2012; Couto *et al.,* 2017]. Monitoring such changes in water mass advection is crucial, as they modulate the regional circulation and directly influence the local ecosystem [*e.g.,* Kerr *et al.,* 2018].

Chapter III: Data and Methods

3.1 Hydrographic Dataset

In this study, we compiled a comprehensive hydrographic dataset consisting of pressure, temperature and salinity measurements spanning West Antarctica (Latitude: 65°–79°S; Longitude: 140°E–070°W) from 1990 to 2020. The dataset integrates observations from the World Ocean Database 2023 (WOD23; https://www.ncei.noaa.gov/products/world-ocean-database; Mishonov *et al.,* 2024), the Argo Program (https://argo.ucsd.edu/about/), the CLIVAR and Carbon Hydrographic Data Office (CCHDO; https://argo.ucsd.edu/about/), the Marine Mammals Exploring the Ocean Pole to Pole (MEOP; http://www.meop.net; Roquet *et al.,* 2011), and Thwaites-Amundsen Regional Survey and Network (TARSAN; https://www.bodc.ac.uk/data/bodc_database/nodb/project/54319/). WOD18 and TARSAN observations rely on electronic conductivity–temperature–depth (CTD) sensors with typical accuracies of 0.001 °C for temperature and 0.002 for salinity [Mishonov *et al.,* 2024]. Argo profiles report accuracies of 0.002 °C and 0.003, respectively [Cowley *et al.,* 2021; Riser *et al.,* 2015]. Although the MEOP dataset, primarily concentrated along the continental shelf, has lower accuracies of 0.02 °C and 0.03 [Roquet *et al.,* 2011; Siegelman *et al.,* 2019], the hydrographic variability in this region substantially exceeds these uncertainty levels, ensuring that the detected signals remain robust.

To address the third specific objective of this thesis, the characterization of interannual transport variability and the intrusion pathways of the CDW onto the continental shelf of the Antarctic Peninsula, emphasis was placed on hydrographic

observations from the GOAL project, carried out during the austral summers from 2003 to 2019 (*i.e.,* magenta and black dots in **Figure 8**). The accuracy of the CTD profile data obtained by GOAL is ~0.001 ºC and ~0.003 for temperature and salinity, respectively [Dotto *et al.,* 2021].

Furthermore, statistical quality control was performed on the dataset, where spurious values outside the range of two standard deviations in each profile were removed. After that, the dataset was vertically binned in 10 m windows from the surface to the bottom and subsequently grouped by decade (*i.e.,* 1990s, 2000s, and 2010s).

However, despite the large volume of in situ data, there is a spatial and temporal gap in the observations that makes a continuous assessment of ocean exchanges between the off-shelf and continental-shelf domains. Thus, to mitigate this limitation, the in situ analyses were complemented with the high-resolution ocean reanalysis from GLORYS12v1. This approach allows for a continuous representation of the variability of the CDW properties and their intrusions onto the continental shelf.

3.2 GLORYS12v1 reanalysis output

GLORYS12v1 (https://data.marine.copernicus.eu/product/), provided by the Copernicus Marine Environment Service, is a global eddy-resolving physical ocean and sea ice reanalysis with 1/12º horizontal resolution and 50 standard vertical levels, that covers the period from 1993 to the present. The model component is based on the Nucleus for European Modelling of the Ocean (NEMO) version3.1, coupled to the louvain-La-Neuve sea ice Model version 2 [LIM2]. GLORYS12v1 is initialized with temperature and salinity fields from the ENACT/ENSEMBLES versio 4.2.0 (EN4.2.0) monthly gridded climatology, and is atmospherically forced by ERA-Interim (https://www.ecmwf.int/en/forecasts/dataset/ecmwf-reanalysis-interim/) until 2018 and subsequently ERA version 5 (ERA5) from 2019 to the present [Jean-Michel *et al.,* 2021]. The switch in atmospheric forcing led to no significant changes at outputs of GLORYS12v1 except for a lower reduction in sea ice volume and extent in the Southern Ocean during austral summer [Jean-Michel et al. 2021]. Quality assessments have shown that GLORYS effectively captures the main interannual climate variability signals for the ocean and sea ice [Jean-Michel et al. 2021].

3.3 Thermodynamic Equation of State for Seawater (TEOS–10)

For more than 30 years, the EOS-80 equations have served the oceanographic community. However, in recent years, several limitations have been pointed out, including: (i) the EOS-80 equations are not thermodynamically consistent with each other; (ii) the need for a better understanding of variations in ocean composition and how these can affect its density; and (iii) the need for the use of exact expressions for entropy, enthalpy, and internal energy of seawater, which were not provided by EOS-80, that can then determine with greater precision the heat fluxes across the ocean-atmosphere interfaces.

As a result, beginning in 2010, the community adopted a new equation of state based on the Gibbs formulation (a function of absolute salinity; S_A – g kg^{-1}, conservative temperature; Θ – °C e pressure – decibar), allowing thermodynamic properties such as entropy, enthalpy, and potential enthalpy to be calculated directly [McDougall & Barker, 2011]. TEOS-10 emphasizes the importance of entropy and enthalpy for a more accurate representation of heat advection and diffusion, and for quantifying the ocean's role in heat exchange with the atmosphere and cryosphere. A major change introduced by TEOS-10 is the use of Absolute Salinity (S_A) instead of Practical Salinity in all thermodynamic calculations, thereby explicitly accounting for dissolved ions that have low electrical conductivity but still influence density. In this sense, SA is preferable to Practical Salinity because seawater thermodynamic properties depend directly on the mass of dissolved constituents [McDougall & Barker, 2011]. Therefore, in this study, the TEOS-10 equation was used to obtain more precise thermohaline estimates from hydrographic observations and fields provided by the GLORYS12v1 reanalysis.

3.4 Post-1990s Warming of Circumpolar Deep Water Off West Antarctica and Its Drivers

Summertime (January-March) thermohaline properties from hydrographic measurements and the GLORYS12v1 reanalysis spanning 120°–70°W and 67.5°–74°S were grouped by decade (1990s, 2000s, and 2010s). This grouping allowed for the analysis of the decadal evolution of CDW properties, providing insight into changes off West Antarctica from the early 1990s, when observational coverage began improving, to the present-day conditions represented by the 2010s.

Due to significant spatial gaps in hydrographic sampling, interpolation was necessary to enable the calculation of both decadal differences and the mean field for the entire period. Thus, thermohaline properties were interpolated onto a regular 0.25° grid using the Radial Basis Function (RBF) interpolation[6], employing linear weighting. RBF interpolation was chosen for its high adaptability to the spatial structures of the database, a fundamental characteristic for representing regions with irregular sampling and sparse data [Damini *et al.,* 2025; Yamazaki *et al.,* 2021]. To ensure robustness, grid cells lacking hydrographic measurements within a 50-km radius (~2 times the grid spacing) were masked out.

3.4.1 CDW layer definition

The CDW layer was defined as the maximum of Θ below 300 m, a criterion that excludes the direct influence of surface processes such as buoyancy forcing (*i.e.,* vertical movements of the water column caused by heat exchange and freshwater flows). This method selects the CDW core [*e.g.,* Schmidtko *et al.,* 2014], which occupies intermediate depths and intrudes onto the West Antarctic continental margin along the SACCF [*e.g.,* Orsi *et al.,* 1995].

3.4.2 SACCF definition

As described before, the southern edge of the ACC is identified in hydrographic sections as the region where CDW reaches its southernmost extent and upwells. While this boundary technically comprises two closely spaced fronts (*i.e.,* SACCF and the Southern Boundary [Orsi *et al.,* 1995]) they are typically separated by only a few tens of kilometres and exhibit coherent meridional migrations. Therefore, SACCF was used to represent the variability of the southern edge of the ACC. Thus, SACCF position was determined using the Θ field from both interpolated hydrographic observations and GLORYS output for each decade, following Orsi *et al.,* [1995]. Specifically, the front was defined as the location where the 1.8ºC isotherm within the CDW layer intersects the

[6]Radial basis function interpolation (RBF): The RBF approach has emerged as a powerful mathematical tool for the interpolation and approximation of complex functions across various scientific and engineering domains. Unlike traditional mesh-based methods, RBF offers a meshless framework that can handle scattered data points and complex geometries without requiring structured grids [Hillier *et al.,* 2014].

500 m isobath. To assess the consistency of this hydrographic definition with satellite altimetry, the SACCF was also identified using the –1.10m of ADT contour from the summertime-mean (January–March) Copernicus dataset (0.25º x 0.25º, 1993–2020; https://data.marine.copernicus.eu/).

To quantify the meridional displacement of SACCF, we first calculated the decadal-mean SACCF position (latitude and longitude) for the 1990s and 2010s. These positions were then interpolated onto a common longitude grid to enable a direct comparison of latitudinal shifts along the entire zonal extent. This procedure ensures spatial comparability between decades, allowing for continuous assessment of the shift, regardless of the original distribution of sampling points.

3.4.3 GLORYS12v1 reanalysis validation in the representation of CDW thermohaline variability

To ensure the robustness of the results, it is essential to evaluate the performance of the GLORYS12v1 oceanographic reanalysis. The GLORYS12v1 results were evaluated by quantitatively and qualitatively comparing its ability to reproduce the decadal variability in the observed CDW layer with observational data. Furthermore, the representation of the SACCF was validated by calculating the Pearson correlation between the front's position in GLORYS and those defined by hydrographic measurements, ADT, and the historical climatology of Orsi *et al.,* [1995] (https://data.aad.gov.au/metadata/records/antarctic_circumpolar_current_fronts/).

3.4.4 Atmospheric analysis

Summertime-mean (January–March) monthly wind (zonal and meridional winds components) and sea-level pressure (SLP) datasets were analyzed to investigate how climate-driven changes in atmospheric forcing may have modulated CDW variability across both the continental shelf and off-shelf regions. Datasets were obtained from the ERA5 reanalysis [Hersbach *et al.,* 2020], which provides a horizontal resolution of 0.25º and is considered one of the most accurate representations of atmospheric conditions over Antarctica [Dong *et al.,* 2020]. Using summertime means of SLP and zonal and meridional winds, decadal averages of anomalies relative to the 1990–2020 climatology were computed, alongside decadal changes in these anomalies (*i.e.,* 2010s anomalies

minus 1990s anomalies). This procedure highlights long-term changes in atmospheric forcing, emphasizing the changes that occurred in the 2010s.

Wind stress curl was computed following Veny *et al.,* [2024] using zonal and meridional wind components. Decadal averages were calculated for the 1990s and 2010s, with anomalies defined as deviations from the 1990–2020 climatology. Wind stress curl serves as a proxy for Ekman pumping, providing insight into wind-driven vertical motions, including the upwelling of interior water masses such as CDW.

Additionally, the relationship between the displacement of the SACCF and atmospheric forcing was investigated using the summer average (January-March) of the zonal component of the wind. In this context, the methodology proposed by Goyal *et al.,* [2021] was adopted, in which the position of the maximum westerly jet is identified by the latitude of the maximum zonal wind speed in summer (between 30ºS and 70ºS) for each longitude. Subsequently, decadal averages were calculated from these annual values (1993-2020). This made it possible to assess whether a displacement of westerly winds occurred in the western Antarctic region and to relate it to changes in the SACCF [since the position of the ACC and its fronts can be driven by the variability of wind patterns in the region; Meredith *et al.,* 2016].

3.4.5 Changes in conservative temperature of CDW due to meridional ACC displacements

As mentioned earlier, changes in CDW temperature have been reported in several studies [*e.g.,* Herraiz-Borreguero & Naveira Garabato, 2022]. To discern the drivers of temperature changes associated with the long-term displacement of the ACC frontal system, the total change was decomposed into two components using equation 1:

$$\Delta\Theta(x,y,z) = \Delta\Theta'(x,y,z) + \Delta front(x,y,z), z = CDW\ layer \quad (1)$$

The left-hand side of equation 1 represents the change in conservative temperature (ΔΘ), which is essentially the observed isopycnal change. The first term on the right-hand side of equation 1 corresponds to the water mass transformation term. This term accounts for changes in Θ along the SACCF associated with factors such as isopycnal flux (*i.e.,* flows caused by buoyancy force). The second component on the right-hand side represents the Eulerian change, which is linked to frontal shifts (Δfront).

The $\Delta\Theta$ (x, y, z) will be quantified directly based on GLORYS12v1 output reanalysis. The quantification process entails subtracting the mean Θ in the CDW layer from the decadal means of the 1990s and 2010s (*i.e.,* $\Delta\Theta = \Theta_{2010} - \Theta_{1990}$). These two periods were chosen based on the available dataset and looking to highlight the interdecadal changes in CDW properties. The frontal shift term was explicitly calculated (Δfront) as follows in equation 2, whereas the water transformation term was derived as the residual of equation 1.

$$\Delta front = \Delta\Psi \times \frac{\partial\Theta}{\partial\Psi} \quad (2)$$

The change in dynamic height, represented by $\Delta\Psi$, will be assessed from the 1990s to the 2010s, and the dynamic height (Ψ) will be computed at 300 m relative to 1800 m for each point on the GLORYS grid north of the continental shelf. This Φ range was chosen following Yamazaki *et al.,* [2021], where values above 2,000 dbar accurately represent the position of the ACC barotropic fronts [*e.g.,* Meijers *et al.,* 2011], while temperatures below 300 dbar are less influenced by small-scale processes than by the position of the front. Our results are insensitive to the precise definition of dynamic height. The changes in Θ concerning Ψ were represented by $\partial\Theta/\partial\Psi$ and will be determined by employing least–squared linear regression on all available Θ and Ψ data in CDW layer.

3.5 Gyre circulation variability preconditions the off-shelf ocean heat reservoir to the West Antarctic continental shelf

3.5.1 Definition of Ross Gyre

The boundary of the Ross Gyre was defined following Roach & Speer [2019], who identified the gyre edges as the −8 Sverdrup (Sv; 1 Sv = 10^6 m^3 s^{-1}) contour of the barotropic streamfunction[7], obtained by vertically integrating the zonal velocity field from the ocean bottom to the surface in the northward direction (from the coast). This

[7] The barotropic streamfunction is a scalar field that represents the vertically integrated horizontal volume transport of the ocean. It provides a two-dimensional description of the depth-averaged circulation. While it removes information about vertical shear (baroclinic structure), it retains the full contribution of all depth-dependent motions to the integrated transport.

specific contour corresponds to the outermost closed contour in the time-mean streamfunction that does not include coastal extensions. This method provides a consistent metric for monitoring changes in gyre area over time, allowing identification of expansions or contractions of its boundary. In addition, following Prend *et al.,* [2024], the strength of the gyre circulation was defined as the mean value of the barotropic streamfunction within the −8 Sv contour.

3.5.2 Ocean Stress Curl

To assess the role of ocean surface stress as a potential driver of circulation, the monthly ocean surface stress was calculated by considering the combined contributions of air–ocean and ice–ocean stresses. The total ocean surface stress curl at each grid point was then computed following Dotto *et al.,* [2018] using data by ERA5 from January–December, 1993–2020. This approach provides a more physically consistent representation of mechanical forcing than the use of wind stress curl alone. Indeed, wind variability by itself does not fully explain circulation dynamics in regions (*e.g.,* the Ross Gyre) where sea ice cover modulates momentum transfer to the ocean [Meneghello *et al.,* 2018].

Additionally, the ocean surface stress curl was spatially averaged over the gyre forcing region (130–150°W, 67–70°S), defined as the area exhibiting the strongest linear correlation with Ross Gyre variability within the climatological gyre boundaries [*e.g.,* Prend *et al.,* 2024]. Through this spatial averaging, a representative time series of the ocean surface stress curl acting as mechanical forcing on the gyre was obtained.

3.5.3 Buoyancy Fluxes

An alternative hypothesis for the generation of large-scale circulation in ocean basins is that surface buoyancy fluxes may also act as a forcing mechanism. Surface buoyancy forcing modifies water mass density, generating a diabatic vertical velocity across isopycnals. This thermodynamic pumping can contribute to the injection or removal of potential vorticity [Czaja & Hausmann, 2009], generating horizontal circulations potentially comparable in magnitude to wind-driven gyres [Colin de Verdière, 1989]. In this context, surface buoyancy fluxes are considered here as a possible forcing mechanism for Ross Gyre variability, following the theoretical framework of

Neme *et al.,* [2021]. Therefore, the surface buoyancy flux ($\mathcal{B}$; m^2s^{-3}) is defined as:

$$\mathcal{B} = \mathcal{B}_{heat} + \mathcal{B}_{fresh}, \quad (3)$$

where

$$\mathcal{B}_{heat} = \frac{-g\gamma Q_{net}}{c_w \rho}, \quad (4)$$

$$\mathcal{B}_{fresh} = g\beta F_w S_{A(sup)}, \quad (5)$$

ρ is surface density, g is the acceleration due to gravity (9.81 ms^{-2}), c_w the specific heat capacity of seawater (3,992 J Kg^{-1} K^{-1}), γ is the thermal expansion coefficient, β the haline contraction coefficient of seawater derived from TEOS-10 [McDougall & Barker, 2011], $S_{A(sup)}$ is the surface absolute salinity. Q_{net} is the heat fluxes, calculated as the sum of the net of longwave radiation (QLW), shortwave radiation (QSW), latent heat flux (QLH), and sensible heat flux (QSH).F_w represents the net freshwater fluxes, defined as evaporation (E), runoff (R), precipitation (P), and sea ice formation/melt (*i.e.,* P – E + R – F_{ice}). Monthly QLW, QSW, QLH, QSH, E, R and P data are obtained from ERA5. The freshwater flux associated with sea ice formation and melting dynamics (*i.e.,* F_{ice}) was estimated using a bulk thermodynamic approach following Hattermann *et al.,* [2021], where positive F_{ice} represents sea ice formation (freshwater loss). In this convention, positive $\mathcal{B}$ represent a gain of buoyancy by the ocean (decreased density via warming or freshening). In addition, the largest $\mathcal{B}$ in the Ross Sea region are found over the continental shelf, so $\mathcal{B}$ is averaged at the continental shelves (defined by depths shallower than 1,000 m over the Ross Sea; 160ºE–150ºW) to build a time series.

3.5.4 Time-Series and composites

Climatological annual cycles of gyre strength, ocean surface stress curl, surface buoyancy fluxes, and gyre area were calculated to characterize seasonal dynamics. To investigate interannual variability, anomalies were computed relative to the long-term monthly mean climatology for the period January 1993 to December 2020. All time series were then smoothed using a 12-month low-pass Butterworth filter in order to suppress the seasonal cycle and high-frequency variability.

Subsequently, linear correlation coefficients were calculated between time series

of gyre circulation strength anomalies and anomalies in ocean surface stress curl, surface buoyancy fluxes, and gyre area. This analysis was used to identify the dominant processes associated with gyre strength variability on seasonal and interannual timescales.

Mean anomaly fields of subsurface thermohaline properties (300–500 m) during strong and weak Ross Gyre states were analyzed to investigate how these properties vary in off-shelf regions and over the continental shelf in association with changes in gyre strength. Strong gyre periods were defined when the smoothed gyre strength anomaly time series exceeded +1 standard deviation, while weak gyre periods corresponded to values below −1 standard deviation. For each group, mean anomaly fields of Conservative Temperature and Absolute Salinity were computed relative to the long-term monthly climatology.

The statistical significance of differences between the strong and weak gyre composite mean fields was assessed using a Monte Carlo permutation test with 1000 iterations, in which the temporal labels associated with strong and weak gyre states were randomly reassigned to generate a null distribution of mean differences. Only anomalies exceeding the 95% confidence interval of this distribution were considered statistically significant. These mean fields reveal the characteristic thermohaline patterns associated with intensified and weakened Ross Gyre states. In addition, mean anomaly fields of ocean surface stress and sea level pressure (obtained by ERA5 from 1993–2020) were also computed to investigate atmospheric patterns associated with strong and weak gyre events.

Finally, spatial linear trends in ocean surface stress and subsurface thermohaline properties were analyzed to assess whether long-term changes in Ross Gyre strength are associated with observed transformations in water masses over the continental shelf and in the off-shelf region of West Antarctica.

3.6 Summer circulation and water masses transport in Bransfield Strait, Antarctica: An evaluation of their response to combined effects of Southern Annular Mode and El Niño–Southern Oscillation

To characterize the local circulation focusing on interannual variability and the intrusion pathways of the CDW over the continental shelf of the Antarctic Peninsula, two

hydrographic sections in the Bransfield Strait were surveyed 17 times between 2003 and 2019. These surveys resulted in conductivity-temperature-depth profiles with a vertical resolution of 1 dbar (**Figure 8**). Section 1 extended between King George and D'Urville Islands (red rectangle bounding magenta dots in **Figure 8**), while section 2 was situated between Elephant and Joinville Islands (red rectangle bounding black dots in **Figure 8**). Using the dynamic method, geostrophic velocities can be obtained between oceanographic stations for each analyzed section.

3.6.1 Dynamic Method

The dynamic method estimates the relative geostrophic velocity component perpendicular to a transect based on density differences between vertical profiles. To convert relative velocities into absolute baroclinic geostrophic velocities, a reference level with known velocity is required.

In this study, cross-section geostrophic velocities (Sections 1 and 2) were computed by referencing the shear to a level of no motion at 500 m. This follows previous regional studies [*e.g.,* Grelowski *et al.,* 1986; Gomis *et al.,* 2002; Sangrà *et al.,* 2011, 2017]. The choice of 500 m is justified as only small portions of the hydrographic sections extend below this depth. Furthermore, isopycnal slopes below 500 m are generally weak, suggesting minimal contribution from deeper layers to the vertically integrated geostrophic shear, thereby reducing uncertainty in reference level definition. Additionally, Mukhametyanov *et al.,* [2022] demonstrated that a 500 m reference level captures over half of the transport measured by acoustic Doppler current profiler, supporting the suitability of this depth.

Hydrographic properties (Θ and S_A) and geostrophic velocities were gridded onto a 0.05° latitude grid spanning from the first to the last profile of each section. Data were 2-D interpolated using a RBF with linear weighting and a smoothing factor of 0.1. The RBF method was selected for its adaptability to irregular spatial structures. This interpolation facilitated the calculation of time-averages over the entire period, mitigating the impact of spatial data gaps observed in specific years.

3.6.2 Validation of GLORYS12v1 reanalysis in representing the thermohaline structure and circulation of the Bransfield Strait

Given the spatial and temporal gaps in the observational dataset, summertime (January-March) averages of thermohaline properties and the full velocity field (barotropic and baroclinic components) from the GLORYS12v1 reanalysis were utilized to investigate interannual variability.

To validate GLORYS12v1, all available summertime hydrographic measurements from 2003 to 2019 were interpolated onto the model grid. Validation involved comparing mean thermohaline profiles for both analyzed sections and assessing the model's capacity to reproduce Bransfield Strait water masses via Θ/S_A diagrams.

3.6.3 Water mass transport calculation by GLORYS12v1 output

Following validation, volume transports of the main water masses across the two sections were calculated. Due to the oblique orientation of the Bransfield Strait relative to true north, the zonal velocity component was projected onto a local coordinate system rotated 60° clockwise from geographic north [Gordey *et al.,* 2024]. This rotation aligned the coordinate system with the local bathymetric orientation, isolating the velocity component perpendicular to the sections. Water mass volume transport in Sv was obtained by integrating the projected velocity component vertically and horizontally within specific water mass layers. The layers were defined using Θ and S_A criteria from previous studies [*e.g.,* Huneke *et al.,* 2016; Morozov *et al.,* 2021; Gordey *et al.,* 2024]: TBW ($\Theta > 0$ °C and SA < 34.65 g kg^{-1}), and TWW ($\Theta < -0.45$ °C and SA > 34.60 g kg^{-1}).

Since TBW forms through mixing between Circumpolar Deep Water (CDW) and Bellingshausen surface/intermediate waters, CDW contribution to intermediate and surface layers was assessed to investigate TBW transport variability. The average thickness of the CDW layer, defined as the depth range where $\Theta > 0$°C and 34.60 g kg^{-1} < SA < 34.92 g kg^{-1}, following Damini *et al.,* [2022], was calculated. This method provides insight into CDW penetration intermediate/surface depths and its potential influence on regional water-mass transformation.

3.6.4 Satellite altimetry dataset

The surface geostrophic circulation in the study area is derived from the Global Ocean Gridded L4 Sea Surface Heights and Derived Variables Reprocessed dataset

(https://doi.org/10.48670/moi-00145), accessible through the Copernicus Marine Environment Monitoring Service (CMEMS; data.marine.copernicus.eu). The surface geostrophic velocities derived from this dataset have a spatial resolution of 0.25° and were used for comparison with geostrophic velocities calculated from hydrography. Additionally, relative vorticity[8] was calculated $\zeta z = \partial v/\partial x - \partial u/\partial y$, where u and v are zonal and meridional components of the current velocity field, respectively.

3.6.5 Atmospheric analysis

As mentioned before, the wind pattern variability-driven ACC position and consequently, plays a critical role in advecting the CDW onto the Peninsula of Antarctica (*i.e.,* Bransfield Strait), contributing to the formation of TBW, which is subsequently transported into Bransfield Strait. Given this context, one of the objectives of this thesis is to assess how the combined effects of summer SAM and ENSO influence the wind field over the Antarctic Peninsula and, in turn, the circulation in the Bransfield Strait. To quantify these combined effects, the Summer ENSO–SAM Index (SEI; https://zenodo.org/records/7500163), which integrates both climate modes, was used. In this context, positive SEI values (> 0.50) correspond to periods of positive SAM combined with negative ENSO, while negative SEI values (< −0.50) correspond to negative SAM combined with positive ENSO [Llanillo *et al.,* 2023].

Following Veny *et al.,* [2024], the average of the summertime (January-March) wind stress curl and Ekman vertical velocity were calculated from monthly averaged wind velocity from the European Centre for Medium-Range Weather Forecast Reanalysis-Interim [ERA-Interim; https://www.ecmwf.int/en/forecasts/dataset/ecmwf-reanalysis-interim; Dee *et al.,* 2011], which has a horizontal resolution of 0.70 × 0.70° over the period 1979 to 2019 (that results is the same using the new version ERA5). Anomalies of wind stress curl were calculated by subtracting the time-average over the full period (January-March 2003-2019) from the average of each SEI period analyzed (*i.e.,* the positive phase of SEI and the negative phase of SEI). Thus, highlighting the changes in

[8] Relative vorticity: Relative vorticity (ζ) quantifies the horizontal rotation of the fluid relative to the Earth's frame of reference. Maps of relative vorticity allow us the identify of high-shear regions and eddies (e.g., ASFbeddy in Bransfield Strait).

atmospheric forcing during the periods analyzed. Finally, the dynamical link between atmospheric forcing and local ocean response was tested by computing Spearman correlations between the normalized and detrended wind stress curl over the northern Antarctic Peninsula and the SEI index for the period 1979-2019 (*i.e.,* considering the complete historical series).

Capítulo IV: Artigos

4.1 Aquecimento pós-década de 1990 da CDW ao longo do oeste da Antártica e seus mecanismos controladores

O manuscrito, de autoria de Brendon Yuri Damini, Tiago S. Dotto, Karen J. Heywood, Alberto C. Naveira Garabato, Rob A. Hall, Mauricio M. Mata e Rodrigo Kerr, é intitulado "*Post-1990s warming of Circumpolar Deep Water off West Antarctica and its drivers*", foi publicado no periódico *Journal Geophysical Research: Oceans* (Damini *et al.,* 2026 – disponível em https://doi.org/10.1029/2025JC023856). Em síntese, o estudo demonstra que a CDW ao largo da plataforma continental aqueceu significativamente desde a década de 1990 na região oeste da Antártica e que aproximadamente 90% desse aquecimento pode ser atribuído ao incremento do transporte zonal de calor associado à intensificação do Giro de Ross e ao aumento da transferência de calor em direção ao sul, cruzando a ACC. Esses processos estiveram associados ao fortalecimento e ao deslocamento para o sul dos ventos de oeste sobre o oceano Austral, sugerindo uma ligação de causa e efeito entre a variabilidade atmosférica de grande escala e o aquecimento da CDW *off–shelf*. Além disso, os resultados indicam que, caso essas tendências persistam ao longo do século XXI, o reservatório de calor ao norte da plataforma continental poderá continuar a se intensificar, aumentando o aporte de calor ao largo da plataforma continental às plataformas de gelo ao oeste da Antártica e, consequentemente, o risco à sua estabilidade. As seções principais do manuscrito serão apresentadas a seguir.

4.1.1 Introduction

The Antarctic Ice Sheet has been losing mass at an accelerated rate since at least the 1970s and now accounts for approximately 15% of global sea-level rise [*e.g.,* Frederikse *et al.,* 2020]. The most rapid loss and disintegration of ice shelves in recent decades have been observed along the West Antarctic margins [*e.g.,* Rignot *et al.,* 2019]. This retreat has primarily been driven by enhanced intrusions of relatively warm Circumpolar Deep Water (CDW) via submarine glacial troughs [*e.g.,* Dutrieux *et al.,* 2014]. In the Antarctic subpolar zone, off-shelf CDW circulates within the intermediate layers of the Antarctic Circumpolar Current (ACC), particularly near its southern edge, close to the Southern ACC Front (SACCF) and the Southern Boundary front [*e.g.,* Orsi *et al.,* 1995].

Recent studies indicate that the CDW layer off-shelf has warmed over the past few decades [Sallée, 2018; Schmidtko *et al.,* 2014]. In East Antarctica (115°-150°E), this warming is mainly attributed to poleward displacement of ACC fronts and their hydrographic structure driven by intensifying westerly winds [Herraiz-Borreguero & Naveira Garabato, 2022; Yamazaki *et al.,* 2021]. Additionally, enhanced isopycnal transfer of CDW across the ACC, facilitated by both Ekman processes and eddy activity, may further contribute to this warming [Herraiz-Borreguero & Naveira Garabato, 2022; Yamazaki *et al.,* 2021, 2023; Zu *et al.,* 2022]. This off-shelf CDW warming has enhanced oceanic heat delivery to ice shelves, likely contributing to the recent acceleration of ice-mass loss in East Antarctica [Herraiz-Borreguero & Naveira Garabato, 2022].

In West Antarctica, the supply of CDW to the shelf break region has been proposed to occur primarily via isopycnal heat transport. Such transport may be affected by: (i) lateral heat transfer within the SACCF, associated with the Ross Gyre's eastward extension; this has been illustrated by modelling studies, which indicate that expansion of the gyre's eastern limb under increased cyclonic wind stress curl can enhance poleward heat transport toward the West Antarctic shelf break [Castagno *et al.,* 2017; Nakayama *et al.,* 2018; Gómez-Valdivia *et al.,* 2023; Prend *et al.,* 2024]; and (ii) cross-ACC isopycnal exchanges, driven by mesoscale eddy activity [*e.g.,* Marshall & Speer, 2012; Thompson & Naveira Garabato, 2014].

Both (i) and (ii) are expected to respond dynamically to the documented ongoing poleward intensification of the westerly winds over the Southern Ocean, which would result in a strengthening of both transport processes [*e.g.,* Prend *et al.,* 2024; Marshall &

Speer, 2012].

Although previous studies have discussed the potential links between these processes and changes in the thermohaline properties of CDW off West Antarctica [*e.g.,* Marshall & Speer, 2012; Prend *et al.,* 2024], the processes' relative contributions have not been quantified with observations, and neither has that from meridional displacements of ACC fronts. Here, we investigate interdecadal changes (1990s-2010s) in CDW properties in both the off-shelf and continental shelf regions around West Antarctica (120°-70°W; 67.5°-74°S) using hydrographic observations and a high-resolution ocean reanalysis. We identify a warming of the CDW off West Antarctica in both datasets and quantitatively elucidate its drivers. Our analysis indicates that the observed off-shelf CDW warming has been mainly driven by a lateral heat transfer linked to a stronger Ross Gyre and to enhanced cross-ACC isopycnal heat transport. A poleward expansion of the southern edge of the ACC's hydrographic structure made a secondary contribution to the warming. All drivers are associated with a poleward shift and intensification of the westerly winds. Despite this overall off-shelf warming, the continental shelf exhibits spatial heterogeneity in its hydrographic response, reflecting the influence of regional wind patterns at the shelf break [*e.g.,* Huguenin *et al.,* 2024] and thermodynamic processes (*i.e.,* vertical convection driven by surface heat loss) on the highly variable shelf [Oelerich *et al.,* 2022].

4.1.2 Materials and Methods

4.1.2.1 Hydrographic and GLORYS12v1 dataset

The dataset used here encompasses hydrographic measurements of temperature and salinity from: World Ocean Database 2023 (https://www.ncei.noaa.gov/products/world-ocean-database); Thwaites-Amundsen Regional Survey and Network (TARSAN; https://www.bodc.ac.uk/data/bodc_database/nodb/project/54319/); Argo (https://argo.ucsd.edu); the CLIVAR and Carbon Hydrographic Data Office (https://cchdo.ucsd.edu/); and the Marine Mammals Exploring the Ocean Pole to Pole consortium (MEOP; https://www.meop.net/, spanning 1990-2020; **Figure 9**). The hydrographic measurements of temperature and salinity were collected by electronic conductivity-temperature-depth (CTD) sensors with temperature and salinity accuracies

of 0.001ºC and 0.002, respectively [Mishonov *et al.*, 2023]. For Argo profiles, accuracies are 0.002ºC and 0.0035 [Cowley *et al.*, 2021; Riser *et al.*, 2015], while the MEOP dataset, predominantly concentrated along the continental shelf, reports accuracies of 0.02ºC and 0.03 for temperature and salinity, respectively [Roquet *et al.*, 2011; Sielgelman *et al.*, 2019]. Importantly, the temperature and salinity changes observed along the continental shelf exceed the MEOP dataset's accuracy thresholds (0.02°C for temperature and 0.03 for salinity), supporting the robustness of our findings. For each hydrographic station, spurious hydrographic data greater than two standard deviations from the mean value of each profile were removed.

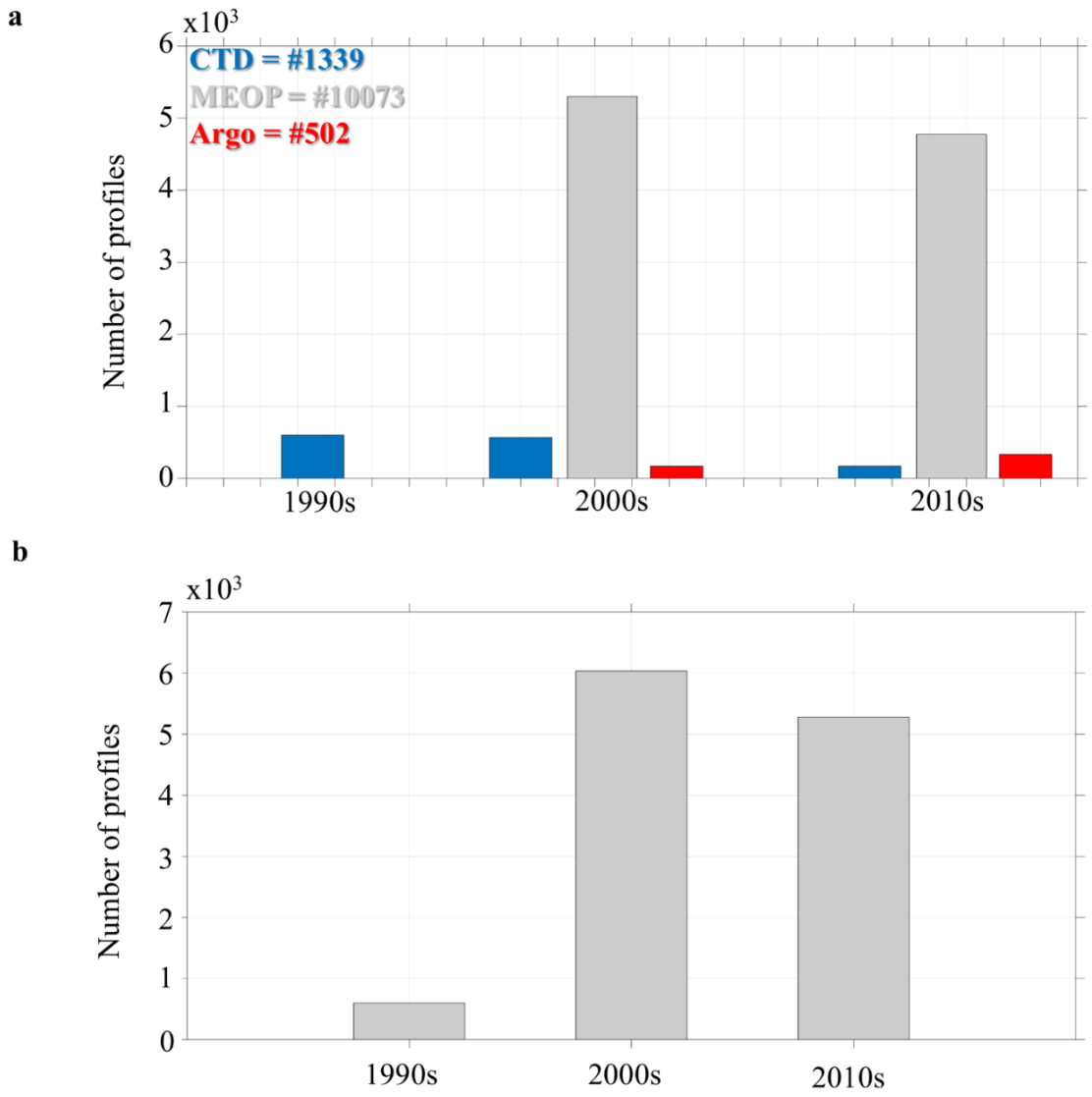


Figure 9: The number of hydrographic profiles per decade used in this study. a Profiles categorised by: CTD dataset (blue), MEOP (grey), and Argo (red); and **b** total number of profiles per decade.

Hydrographic properties spanning 120°-70°W and 67.5°-74°S were grouped by

decade (1990s, 2000s, and 2010s) and interpolated onto a 0.25° grid using radial basis function interpolation with a linear weighting. The radial basis function interpolation method was chosen for its flexibility in adapting to the spatial structure of the data, making it particularly effective for irregular or sparse datasets [Damini *et al.,* 2025; Yamazaki *et al.,* 2021]. Since we have spatial data gaps, we decided to apply an interpolation method to calculate the difference between the decades and the time-average over the entire period. Additionally, we opted to mask areas with no data points within a 50 km radius (~2 times the grid spacing), ensuring greater robustness for our analyses.

We assessed the ability of GLobal Ocean Reanalysis and Simulation (GLORYS) to reproduce thermohaline variability by examining whether similar patterns are evident in hydrographic data for the same period and the same region. For this, we again analysed hydrographic properties (*i.e.,* temperature and salinity) grouped by decades (the 1990s, 2000s and 2010s). GLORYS is a global eddy-resolving physical ocean and sea ice reanalysis with 1/12º horizontal resolution and 50 standard vertical levels. It covers the period from 1993 to the present, is based on the Nucleus for European Modelling of the Ocean platform (NEMO), and is atmospherically forced with ERA-Interim (https://www.ecmwf.int/en/forecasts/dataset/ecmwf-reanalysis-interim/). Quality assessments have shown that GLORYS effectively captures the main interannual climate variability signals for the ocean and sea ice [Jean-Michel et al. 2021].

4.1.2.2 CDW layer definition

We calculated conservative temperature – Θ, ºC, and absolute salinity – S_A, g kg^{-1}, using the International Thermodynamic Equation of Seawater – 2010 (TEOS-10) [McDougall & Barker, 2011] from hydrographic measurements and GLORYS. The CDW layer was defined as the maximum Θ below 300 m, thereby excluding the influence of surface processes such as buoyancy forcing. This criterion identifies the CDW core [**Supplementary Figures 1 and 2**; *e.g.,* Schmidtko *et al.,* 2014], which occupies intermediate layers along the SACCF around West Antarctica [*e.g.,* Orsi *et al.,* 1995]. In the study region, the CDW layer typically occurs within a density range of $\gamma^n \approx 27.93$–28.03 kg m^{-3} [Yamazaki *et al.,* 2024]. Similar results are obtained when temperature variability is evaluated directly along these neutral density surfaces (**Figure 10**).

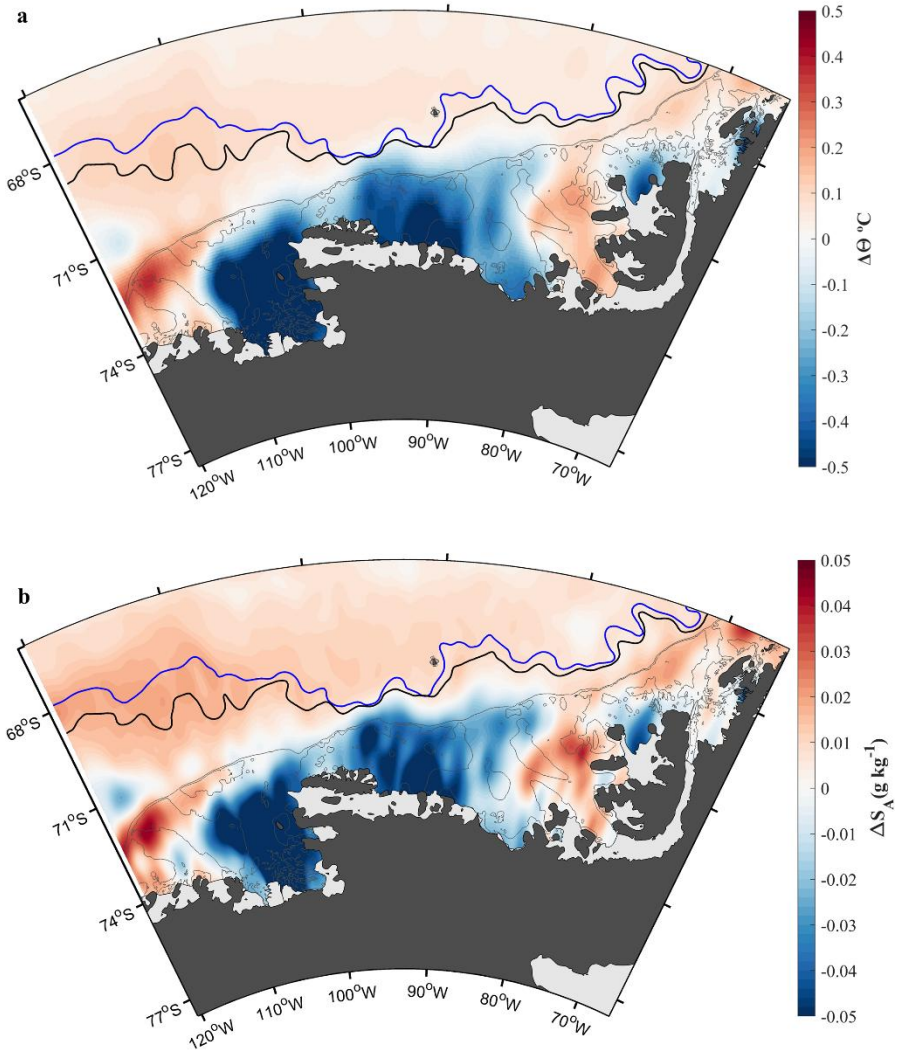


Figure 10: Decadal changes in the CDW layer properties, defined by neutral density (γ^n) of 27.93 and 28.03 kg m^{-3}. Difference between 2010s and 1990s in a Conservative Temperature (Θ, ºC) and b Absolute Salinity (S_A, g kg^{-1}) from GLORYS output. Blue and black lines indicate the mean positions of the Southern Antarctic Circumpolar Current Front during the 1990s and 2010s, respectively, based on GLORYS output. Thin grey contours represent the 500 m and 1,500 m isobaths from the R–Topo2 dataset [Schaffer *et al.,* 2016].

4.1.2.3 SACCF definition

The southern edge of the Antarctic Circumpolar Current can be identified in hydrographic sections across the Southern Ocean as the zone where CDW reaches its southernmost extent and upwells [Orsi *et al.,* 1995]. This boundary is commonly described as comprising two distinct hydrographic fronts: the SACCF and the Southern Boundary [Orsi *et al.,* 1995; Chapman *et al.,* 2020]. However, as noted by Orsi et al. [1995], these two fronts are often separated by only a few tens of kilometres and tend to migrate meridionally in a coherent fashion. Accordingly, for this study, we treat the

SACCF-Southern Boundary system as a single, unified feature and trace it in terms of the SACCF.

Historically, ACC fronts in this region have been defined based on hydrographic water-mass properties [*e.g.,* Orsi *et al.,* 1995]. In this study, we follow this hydrographic definition and identify the SACCF as the location where the 1.8°C isotherm within CDW intersects 500 m depth, using both interpolated hydrographic observations and GLORYS12v1 output for each decade. Additionally, because ACC fronts are associated with strong geostrophic flows, their positions are expected to correspond to gradients in Absolute Dynamic Topography (ADT), representing sea surface height relative to the geoid [Kim & Orsi, 2014; Sokolov & Rintoul, 2009a, b]. To evaluate the consistency of our SACCF defined from the 1.8°C isotherm with satellite observations, we additionally analyzed summer-mean (January–March; to minimize the noise in SACCF definition due to sea ice cover) ADT fields provided by Copernicus with a spatial resolution of 0.25° × 0.25° spanning 1993 to 2020.

Our analysis revealed a close match between the hydrographic, GLORYS output definition and the ADT = −1.10 m contour (**Figure 11a**). In addition, we found a consistent close match between the SACCF positions derived from our hydrographic, GLORYS, and satellite altimetry definitions and the dataset of ACC positions from Orsi et al. [1995]. Furthermore, the time-averaged (1990-2020) SACCF positions derived from GLORYS output show a significant correlation (r) with p-*value* < 0.05 with those from hydrographic measurements, satellite altimetry and dataset of ACC positions from Orsi et al. [1995] (r = 0.94, r = 0.96 and r = 0.70, respectively; **Figure 11a**), reaffirming the reliability of our findings.

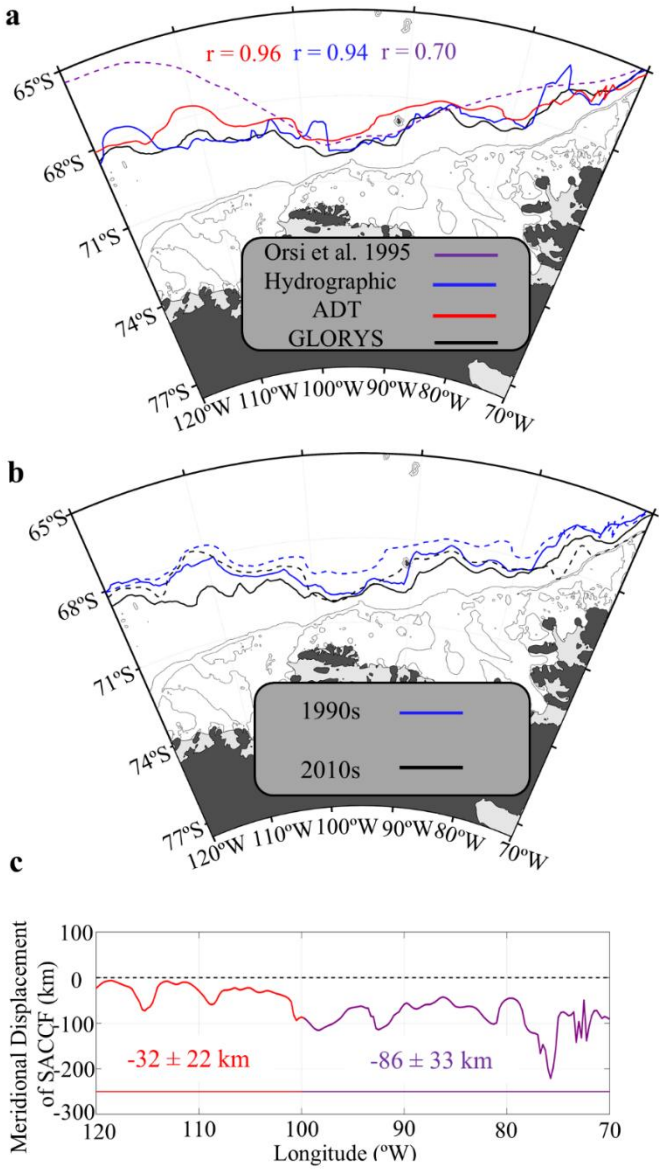


Figure 11: Meridional SACCF displacements. a Time–averaged position of the Southern Antarctic Circumpolar Current Front (SACCF) positions for the period 1990s–2010s, based on four different definitions: hydrographic measurements (blue line), satellite altimetry using Absolute Dynamic Topography (ADT; red line), GLORYS output (black line) definitions, and the climatological product from Orsi et al [1995] (purple dashed line). The Pearson correlation coefficient between the time–averaged (1990s–2010s) of the SACCF positions by satellite altimetry (red), hydrographic measurements (blue) and Orsi et al. 1995 (purple) with GLORYS output are indicated by r. **b** Decadal changes in the position of the Southern Antarctic Circumpolar Current Front (SACCF), as derived from GLORYS output (solid lines) and hydrographic measurements (dashed lines). Blue and black lines represent the mean SACCF position during the 1990s and 2010s, respectively. **c** Meridional displacement of the SACCF derived from ADT data. Amundsen Sea region is highlighted in red and Bellingshausen Sea region in purple. Also indicated are the average meridional displacement (in degrees latitude) for each region. Thin grey contours represent the 500 m and 1,500 m isobaths from the R–Topo2 dataset [Schaffer *et al.*, 2016].

To analyze the meridional displacement of the SACCF between the 1990s and 2010s, we first calculated the average SACCF position (latitude and longitude) for each decade. These data were then aligned onto a common longitude grid, enabling a direct comparison of latitudinal displacements. Additionally, to ensure that the interdecadal poleward SACCF displacement is robust against interannual variability, we performed a sensitivity analysis using sliding 10-year windows for both the historical (1993–2004) and modern (2009–2020) periods. The poleward shift remains statistically consistent across all temporal permutations (**Table 1**).

Table 1. Sensitivity of the interdecadal SACCF meridional displacement under varying decadal definitions. The difference between the largest and smallest displacements found here was 7.6 for the Amundsen region and 10.4 for the Bellingshausen region.

	Amundsen Sea Shift (km)	**Bellingshausen Sea Shift (km)**
2009–2018 minus1993–2002	-68.2±35.6	-36.5±24.1
2010–2019 minus 1993–2002	-73.5±34.0	-33.7±24.5
2011–2020 minus1993–2002	-73.6±34.2	-30.4±22.6
2009–2018 minus 1994–2003	-70.4±36.3	-37.7±25.2
2010–2019 minus 1994–2003	-75.6±34.6	-34.8±25.0
2011–2020 minus 1994–2003	-75.8±34.5	-31.6±22.6
2009–2018 minus 1995–2004	-67.1±33.8	-40.8±26.6
2010–2019 minus 1995–2004	-72.3±32.1	-37.9±26.4
2011–2020 minus 1995–2004	-72.5±32.2	-34.6±24.1
Time-mean and temporal std	-72.1±3.0	-35.3±3.3

Because the SACCF definition used here is based on fixed values of isotherm and ADT, its position may be influenced by long-term thermodynamic changes of the CDW layer. and long-term steric changes of the water column [Chapman *et al.,* 2020]. Previous studies using alternative dynamical diagnostics based on meridional gradients of ADT [Kim & Orsi, 2014], did not yield a unique and spatially continuous frontal position, likely due to strong frontal meandering and mesoscale variability [**Figure 12**; Chapman, 2014], resulting in a weak meridional ADT-gradient signature for the SACCF [Schiavon *et al.,* 2025]. Consequently, we retain the hydrographic definition to maintain consistency with recent literature [Yamazaki *et al.,* 2021; Herraiz-Borreguero & Naveira Garabato, 2022], explicitly acknowledging its inherent inability to fully decouple kinematic frontal displacements from the thermodynamic changes of the CDW layer.

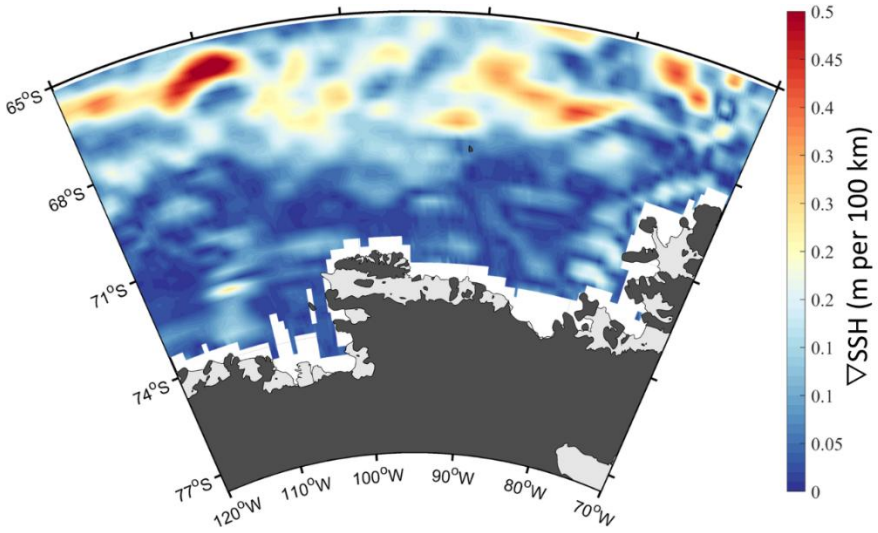


Figure 12: Summer time-mean (1993-2020, jan-march) gradient of SSH (m per 100 km) off West Antarctica.

4.1.2.4 Calculation of dynamic height from hydrographic profiles

Following Yamazaki et al. [2021], the dynamic height (Φ) was calculated by vertically integrating specific volume from 300 decibars (dbar) to 1,800 dbar for each point on the GLORYS grid north of the continental shelf (**Figure 13a**). This range of Φ was chosen because values above 2,000 dbar accurately represent the position of the equivalent barotropic ACC fronts [*e.g.,* Meijers *et al.,* 2011], while temperatures above 300 dbar are more influenced by small-scale processes than by the frontal position [*e.g.,*

mixing processes in the mixed layer; Yamazaki *et al.,* 2021].

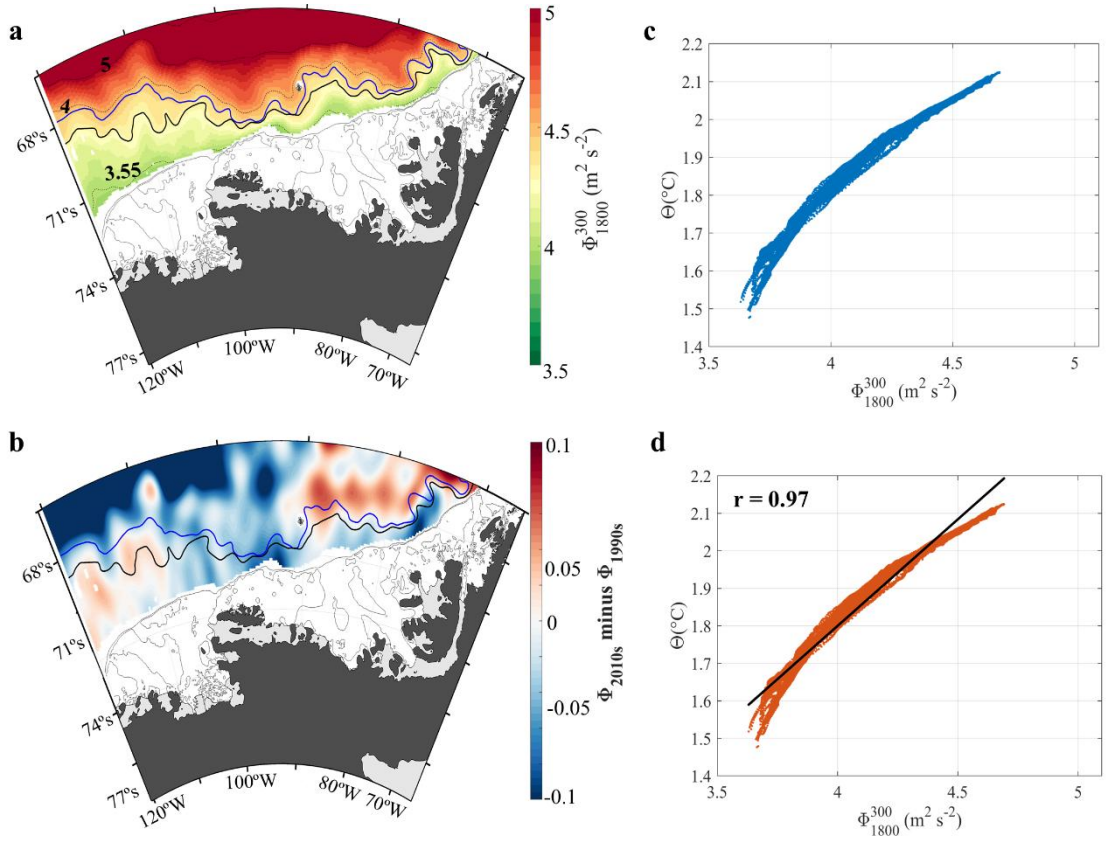


Figure 13: Assessment of the contribution of the SACCF poleward displacement to the warming of CDW. a Climatology (1990s–2010s) of dynamic height (Φ) at 300 m relative to 1,800 m depth. **b** Change in Φ between 1990s and 2010s. Blue and black lines indicate the mean position of the Southern Antarctic Circumpolar Current Front (SACCF) during the 1990s and 2010s, respectively, as derived from GLORYS output. **c** Climatological change in Conservative Temperature (Θ, ºC) within the Circumpolar Deep Water (CDW) layer as a function of Φ. **d** Same as **c** but highlighting the Φ intervals used to compute the temperature gradient (dΘ/dΦ) by linear regression (black lines), with a correlation coefficient of the regression is r = 0.97. Thin grey contours represent the 500 m and 1,500 m isobaths from the R–Topo2 dataset [Schaffer *et al.,* 2016].

4.1.2.5 Changes in conservative temperature of CDW due to meridional ACC displacements

Here, the CDW layer changes are explained by two main mechanisms. To this end, we decompose the changes into two components to elucidate their underlying causes in geographical space. In Equation 1, ΔΘ(x,y) represents the changes in conservative temperature along the geostrophic contour of the equivalent barotropic ACC front, reflecting decadal changes in conservative temperature within the CDW layer. The first

term on the right-hand side, ΔΘfront (hereafter referred to as the frontal shift), accounts for conservative temperature changes associated with the meridional displacements of dynamic height, representing the Eulerian response to frontal displacements. In other words, this term considers the barotropic effect induced by the southern expansion of the southern edge of the ACC's hydrographic structure on temperature changes throughout the CDW layer. The second term, ΔΘ'(x,y), is computed here as the residual of Equation 1. This term corresponds to the along-streamline changes, *i.e.,* the temperature change occurring along the geostrophic contour of the equivalent barotropic SACCF, driven by baroclinic processes, such as *e.g.,* eddy activity and lateral heat advection along isopycnals.

$$\Delta\Theta(x,y) = \Delta\Theta_{front}(x,y) + \Delta\Theta'(x,y). \quad (1)$$

ΔΘ(x,y) was quantified directly from GLORYS output, subtracting the 2010s time-average conservative temperature in the CDW layer field from that of the 1990s, thus highlighting the interdecadal change in CDW properties. ΔΘfront was calculated as follows:

$$\Delta\Theta_{front}(x,y) = \Delta\Phi(x,y) \times \frac{\partial\Theta}{\partial\Phi}, \quad (2)$$

where ΔΦ(x,y) was obtained by subtracting the 1990s time-average dynamic height field (see Calculation of dynamic height) from that of the 2010s (**Figure 13b**). Additionally, we applied a low-pass spatial filter to the decadal climatologies of dynamic height of ~3 times the meridional grid spacing to attenuate spatial scales smaller than 50 km. This filtering removes eddy-like features or artefact residuals that are irrelevant to the frontal position. ∂Θ/∂Φ is determined by fitting a least-squares linear relationship between conservative temperature of the CDW layer climatology and the climatological dynamic height (**Figure 13c–d**). Sensitivity tests using alternative depth ranges (*e.g.,* Φ400 dbar to 1,800 dbar and Φ300 to 1,500 dbar) showed similar results. The strong correlation between dynamic height and CDW temperature variability remained consistent across all definitions ($r = 0.97, p < 0.01$; **Figure 13d**). This confirms that the analysis is not sensitive to the exact depth ranges selected. We highlighted that the above method for assessing the influence of the SACCF's poleward displacement on CDW warming cannot be applied in regions that encompass the continental slope and continental shelf, where circulation features such as the Antarctic Slope Current and the Amundsen Sea

undercurrent may introduce strong non-equivalent barotropic structure.

4.1.2.6 Ancillary data sets

The summertime (January-March) monthly wind and sea level pressure (SLP) datasets were analyzed to investigate how climate-driven changes in atmospheric forcing may have influenced the CDW layer variability in both the continental shelf and off-shelf regions of Antarctica. These datasets were obtained from the ERA5 reanalysis [Hersbach *et al.,* 2020], which features a horizontal resolution of 0.25° and is considered to provide one of the most accurate representations of climate conditions over Antarctica [Dong *et al.,* 2020]. Using summertime means of sea level pressure, and zonal and meridional winds, we calculated decadal averages of their anomalies relative to the 1990-2020 climatology, as well as decadal changes of these anomalies (i.e. anomalies of the 2010s minus anomalies of the 1990s). This approach offers a first-order assessment of the prevailing atmospheric conditions around West Antarctica for each period. We also examined decadal anomalies of wind stress curl [calculated following Veny *et al.,* 2024] relative to the 1990-2020 climatology. That analysis indicated the wind-driven upwelling of subsurface water masses, including CDW. In addition, we tracked the latitudinal position of the southern hemisphere maximum westerly jet following Goyal et al. [2021], which identifies the latitude of maximum summertime zonal wind speed between 30°S and 70°S and averages these peak latitudes across all longitudes for each decade.

4.1.3 Results and Discussion

4.1.3.1 Interdecadal off-shelf CDW layer warming off West Antarctica

Hydrographic measurements off-shelf around the SACCF (defined by −1.10 m contour of ADT, and validated by hydrographic measurements using 1.8 ºC isotherm within the CDW layer intersects 500 m depth and the ACC frontal position from Orsi *et al.,* [1995]) reveal a widespread significant CDW layer warming of ~0.10 ± 0.05 °C; (**Figure 14a**) and salinification of ~0.02 ± 0.01 g kg^{-1} (**Figure 14b**) between the 1990s and 2010s. For both properties, the reported uncertainty represents the standard deviation of the area-averaged values. These warmer and saltier signals generally align with the results reported by Zu et al. [2022], who documented increased temperature and salinity of CDW along East Antarctica from 2006 to 2020. This suggests a potentially circumpolar

change of the CDW.

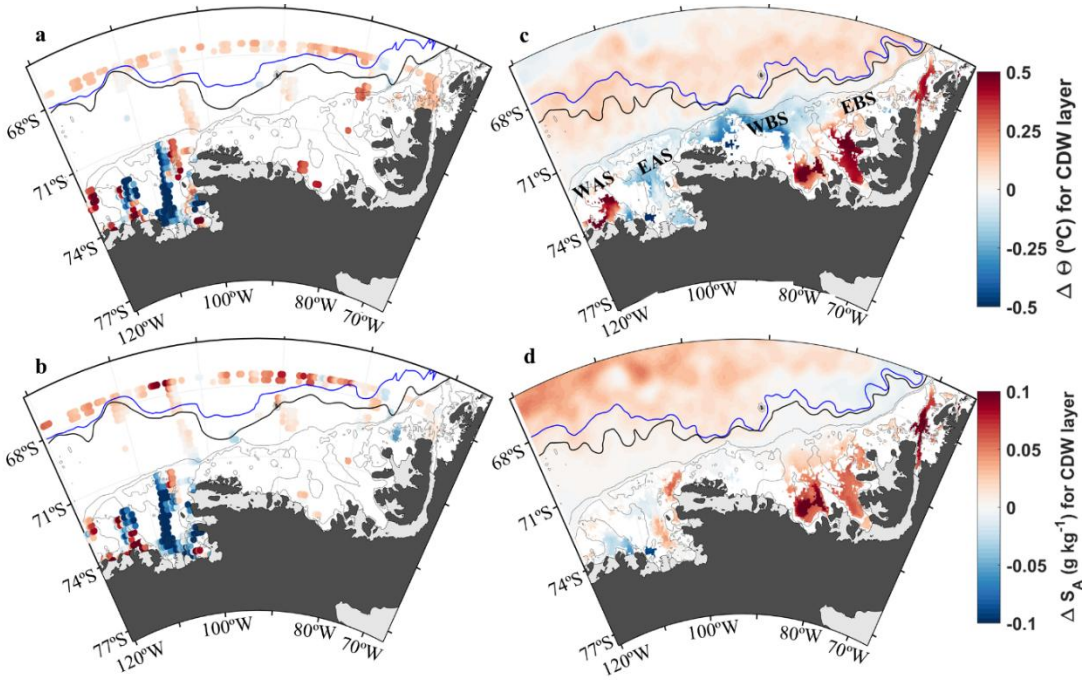


Figure 14: Decadal changes in the properties of the CDW layer, defined as the maximum Θ below 300 m. Difference between 2010s and 1990s in a Conservative Temperature (Θ, ºC) and b Absolute Salinity (S_A, g kg^{-1}) from hydrographic measurements and c-d from GLORYS output. Blue and black lines indicate the mean positions of the Southern Antarctic Circumpolar Current Front during the 1990s and 2010s, respectively, based on satellite altimetry (a–b) and GLORYS output (c–d). Thin grey contours represent the 500 m and 1,500 m isobaths from the R–Topo2 dataset [Schaffer *et al.,* 2016]. The labels WAS, EAS, WBS, EBS denote the Western Amundsen Sea, Eastern Amundsen Sea, Western Belligshausen Sea, Eastern Bellingshausen Sea, respectively.

The sparseness of hydrographic observations, particularly before the Argo period, which began in the 2000s, hampers any evaluation of the dynamic links between off-shelf and continental shelf signals. Therefore, we used the high-resolution GLORYS reanalysis to explore the CDW variability in more detail. Here, we divided the series into conventional decades; i.e. 1990s represent the period of 1993-2000, 2000s represent the period of 2001-2010, and 2010s represent the period of 2011-2020. A Hovmöller analysis over the off-shelf region (**Figure 15**) revealed that this choice highlights the interdecadal change in CDW properties, with warming and salinification becoming particularly pronounced after 2010. This timing mirrors the off-shelf CDW warming reported by Herraiz-Borreguero & Naveira Garabato [2022], and coincides with a transition toward a warmer continental shelf regime in areas of East Antarctica, where warm modified CDW

became more widespread after ~2010 [Ribeiro *et al.,* 2023]. Therefore, such interdecadal warming may increase the availability of heat that can potentially access the continental shelf through troughs.

GLORYS also shows a significantly warmer (~0.1 ± 0.02 °C) and saltier (~0.02 ± 0.01 g kg^{-1}) off-shelf CDW layer around the SACCF (defined by 1.8 ºC at depths > 500 m in the GLORYS reanalysis, and validated by hydrographic measurements, ADT, and the ACC frontal position from Orsi *et al.,* [1995]) during the 2010s relative to the 1990s, in agreement with the sparse observations (**Figure 14c–d**). The decadal variations of conservative temperature in the off-shelf CDW layer between the 2010s and 2000s (~0.06 ± 0.02 °C) and between the 2000s and 1990s (~0.03 ± 0.01 °C) suggest a gradual and consistent off-shelf warming. Despite pronounced interannual variability (**Figure 15**), the long-term evolution of CDW temperature is well approximated by a linear trend from 1993 to 2020. In this sense, we found a significant off-shelf CDW warming at the SACCF of ~0.05 °C per decade over the full study period (**Supplementary Figure 4**). This estimate, although slightly smaller, is qualitatively consistent with the warming trend of ~0.1 °C per decade reported by Schmidtko et al. [2014] for West Antarctica during 1975–2012. Moreover, our findings align with previous studies that suggested a circumpolar warming of up to ~0.2 °C per decade since the 1970s in waters below 200 m [*e.g.,* Auger *et al.,* 2021; Böning *et al.,* 2008; Gille, 2002, 2008; Sallée, 2018]. The CDW warming identified here may result from two distinct mechanisms, both of which may be enhanced by an intensification and poleward displacement of the westerly winds. Below, we will assess these candidate mechanisms in more detail.

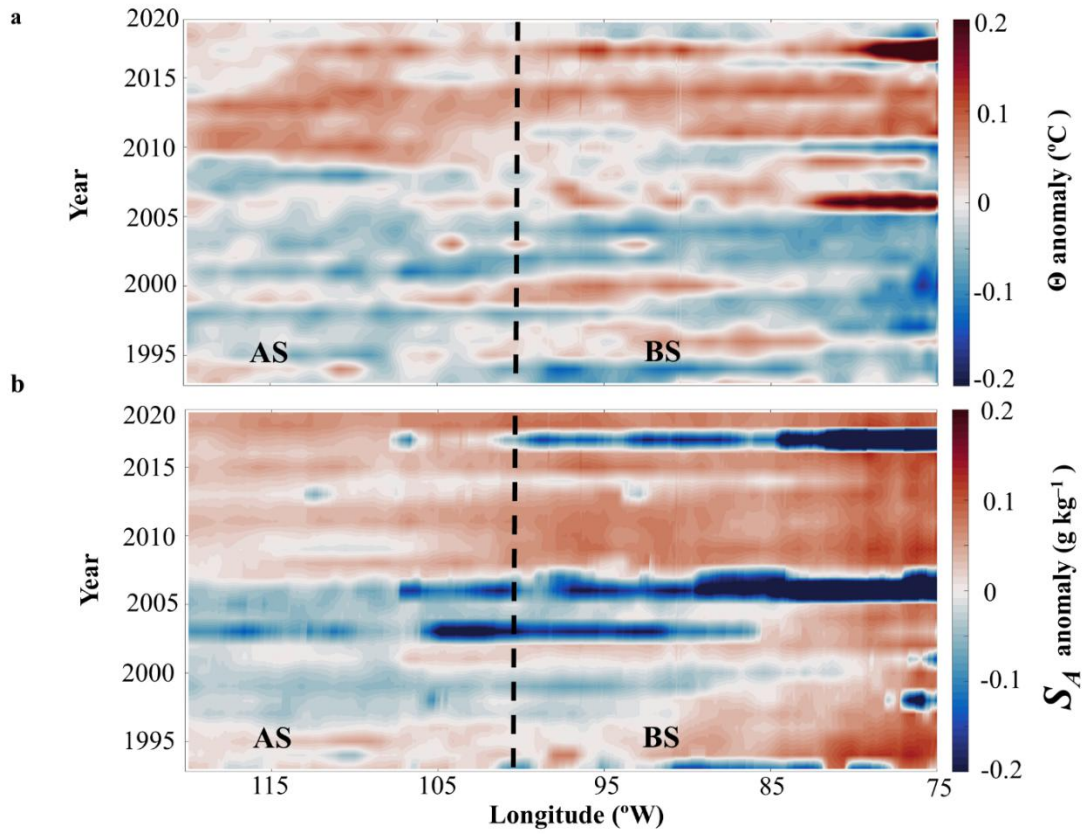


Figure 15: Evolution of CDW layer properties at the SACCF position. a Conservative Temperature (Θ, °C) anomalies relative to the 1993–2020 mean **b** Same as a, but for Absolute Salinity (S_A, g kg^{-1}) anomalies.

4.1.3.2 Potential mechanisms driving off-shelf CDW layer warming

The first mechanism considers the ACC frontal displacement, which represents a poleward expansion of the southern edge of the ACC's hydrographic structure [Gille, 2002; Herraiz–Borreguero & Naveira Garabato, 2022; Meijers *et al.,* 2011; Orsi *et al.,* 1995; Yamazaki *et al.,* 2021]. Although previous studies suggested that the circumpolar-mean position of the ACC has remained broadly stable over recent decades [*e.g.,* Gille, 2014], such averages may mask substantial regional variability. The ACC does not respond uniformly to atmospheric forcing across longitudes and cannot be treated as a single coherent dynamical feature [Kim & Orsi, 2014]. Here, we provide evidence for a regional poleward displacement of the SACCF in the West Antarctic sector during the 2010s, supported by both GLORYS output (**Figure 16a–b and Supplementary Figure 3a**), hydrographic measurements, and satellite altimetry (**Figure 11b–c**). This displacement is consistent with recent studies documenting regional migrations of ACC fronts [Herraiz-Borreguero & Naveira Garabato, 2022; Park *et al.,* 2019; Yamazaki *et al.,*

2021]. The quantitative discrepancy between GLORYS and satellite altimetry may reflect the relatively coarse horizontal resolution of altimetry (0.25° × 0.25°), which cannot fully resolve mesoscale processes with horizontal scales of ~10 km [*e.g.,* eddy–mean flow interactions; McKee *et al.,* 2019] that influence decadal frontal variability. Furthermore, a Hovmöller analysis between 120ºW and 70ºW of the summer-averaged SACCF position based on the GLORYS output definition captures a clear long-term poleward displacement, with an average of 26.13 ± 17.29 km since 2009-2010. It highlights high interannual variability in the SACCF position over the region (**Figure 16**). However, because the CDW layer also warmed significantly during the study period, we cannot exclude a thermodynamic contribution to the apparent displacement of the SACCF and therefore interpret this signal cautiously. In this sense, further studies using complementary dynamical diagnostics will be needed to better separate dynamical frontal migration from long-term ocean thermodynamic changes.

We analyzed the Southern Hemisphere maximum westerly winds' position and sea level pressure (SLP) to assess possible mechanisms that contribute to the poleward displacement of the SACCF. The decadal position of the Southern Hemisphere maximum westerly winds exhibited a poleward shift during the 2010s (**Figure 16c–d** and **Supplementary Figure 3b**). Concurrently, a significant decline in SLP anomaly around West Antarctica between the 1990s and the 2010s was observed (**Figure 16c–d**), which indicates a deepening and intensification of the Amundsen Sea Low — ASL [a persistent low-pressure system that strongly modulates wind fields in this region; Raphael *et al.,* 2016; Turner *et al.,* 2017]. This deepening and intensification of the ASL during the 2010s is associated with a strengthening of westerly winds driven by an increased meridional SLP gradient between the mid-latitudes and the polar region [Clem & Fogt, 2015; Hosking *et al.,* 2013; Raphael *et al.,* 2016]. As the ACC is primarily wind-driven, the position of its fronts is closely linked to the structure and variability of the wind field [*e.g.,* Meredith, 2016]. Hence, it is expected that the observed intensification and poleward migration of westerly winds in the 2010s may be the mechanism responsible for the observed southward expansion of ACC fronts around West Antarctica. This result aligns with previous studies showing that variability in the westerly winds can modulate ocean circulation and frontal positions around Antarctica [*e.g.,* Herraiz-Borreguero & Naveira Garabato, 2022; Mizobata *et al.,* 2025]. In particular, Herraiz-Borreguero & Naveira Garabato [2022] showed that poleward displacement of SACCF by ~100-200 km

in East Antarctica was largely aligned with variability in the westerly winds.

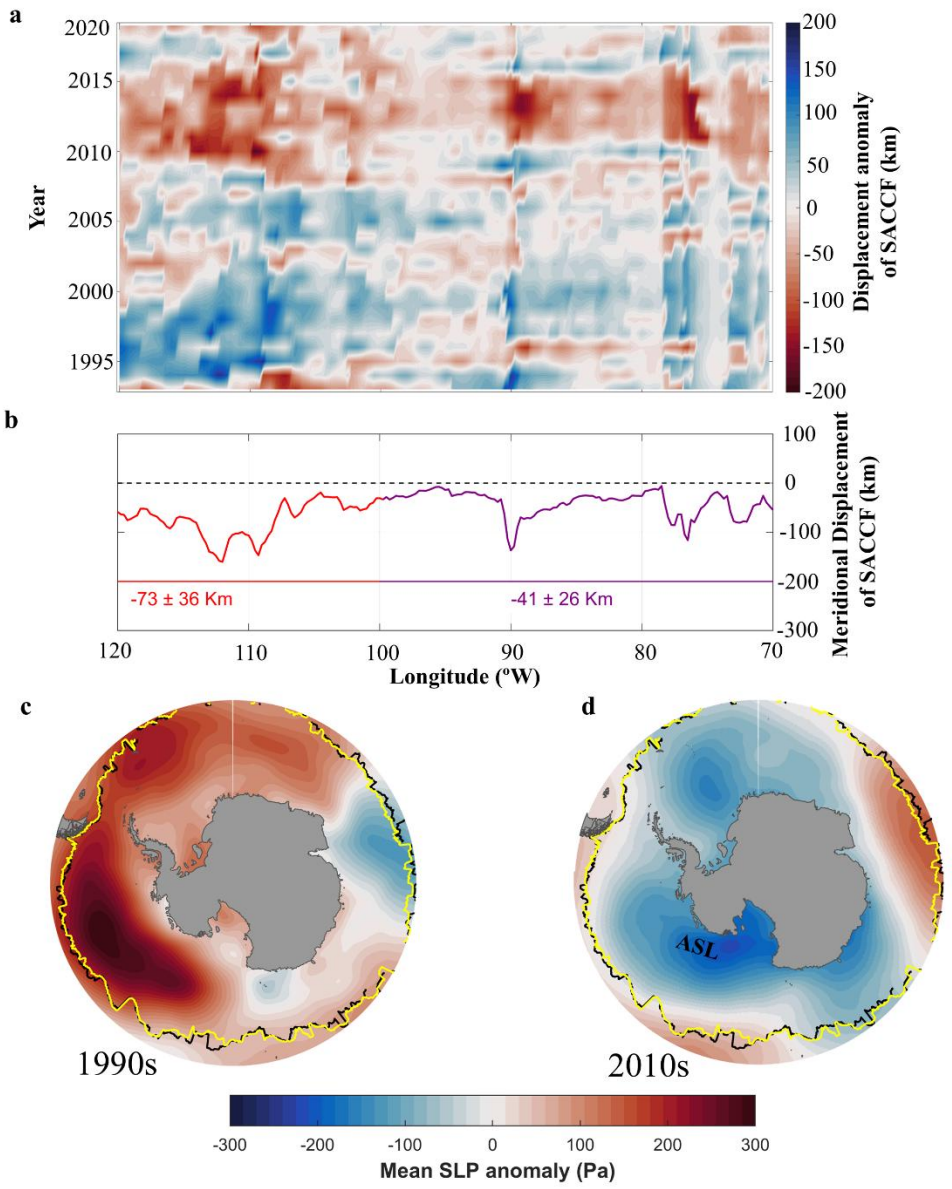


Figure 16: Decadal changes in the position of SACCF. **a** Hovmöller diagram of the displacement anomaly of SACCF (in km) relative to the period 1990-2020. Positive values show the Southern Antarctic Circumpolar Current Front – SACCF displacement poleward, while negative values show the SACCF displacement equatorward; **b** Meridional displacement of the SACCF derived from GLORYS output. The Amundsen Sea region is highlighted in red and Bellingshausen Sea region in purple. Also indicated is each region's average meridional displacement (in km); **c** Sea level pressure (SLP, Pa) anomaly for the 1990s, relative to the period 1990–2020; **d** same as **c** but for the 2010s. The black (yellow) solid lines indicate the summertime southern hemisphere maximum westerly position averaged for the 1990s (2010s).

Because surface forcing weakens below 300 m, the increase in off-shelf CDW heat content along the SACCF must arise from advective processes at intermediate

depths. We suggest that this CDW warming results from a wind-driven circulation response that enhances both cross-ACC isopycnal exchange [*e.g.,* John Marshall & David Speer, 2012; Yamazaki *et al.,* 2023] and lateral isopycnal heat transport associated with a strengthening of the Ross Gyre [Nakayama *et al.,* 2018; Gómez-Valdivia *et al.,* 2023; Prend *et al.,* 2024]. Firstly, intensified westerly winds during the 2010s, indicated by the deepening and intensification of the ASL (**Figure 16b**), can enhance baroclinic instability along the ACC, potentially increasing mesoscale eddy activity [Zhang *et al.,* 2021]. This interpretation is consistent with the significant positive trend in eddy kinetic energy (9.7 ± 7.5 $cm^2\ s^{-2}$) observed across the Pacific sector of the ACC (150°E–60°W) between 1993 and 2018 [Zhang *et al.,* 2021]. Enhanced eddy activity in this sector may facilitate cross-frontal exchange by advecting CDW poleward and diffusively redistributing heat along isopycnals through eddy stirring [*e.g.,* Dufour *et al.,* 2015; Ferrari & Nikurashin, 2010; Yamazaki *et al.,* 2023]. On the other hand, intensified westerlies strengthen the negative wind-stress curl over the Ross Gyre region (**Figure 17**), consistent with enhanced cyclonic vorticity input to the ocean [Dotto *et al.,* 2018]. Through geostrophic adjustment, this forcing intensifies and expands the Ross Gyre circulation [Nakayama *et al.,* 2018; Gómez-Valdivia *et al.,* 2023; Prend *et al.,* 2024]. Changes in gyre strength are closely tied to shifts in the position and extent of its eastern limb, which acts as a conduit transporting CDW poleward toward the continental slope [*e.g.,* Nakayama *et al.,* 2018]. An intensified gyre therefore increases southward heat transport along this boundary, enhancing the supply of CDW at intermediate depths that is subsequently advected laterally along isopycnals toward West Antarctica.

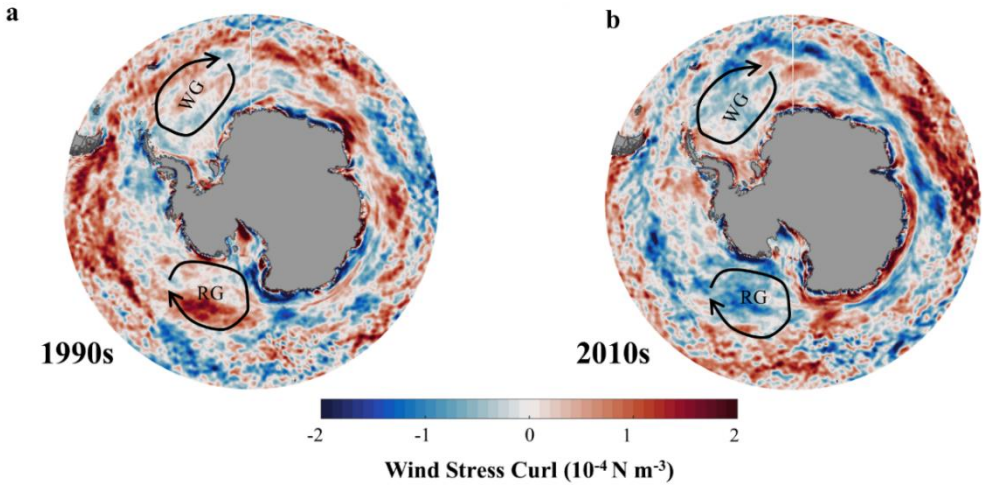


Figure 17: Decadal changes in the wind stress curl. **a** Wind stress curl (N m^{-3}) anomaly for the 1990s, relative to the period 1990–2020; **b** same as **a** but for the 2010s. Positive anomalies indicate reduced Ekman upwelling, whereas negative anomalies denote enhanced Ekman upwelling. Black arrows mark the approximate positions of the Ross Gyre (RG) and the Weddell Gyre (WG).

The relative contributions of these mechanisms to the observed off-shelf CDW warming along the SACCF were evaluated using a decomposition of isopycnal temperature changes. Our results indicate that frontal displacement contributes approximately 0.01 °C (~10%; **Figure 18a**), consistent with a modest increase in dynamic height of up to 0.1 m^2 s^{-2} (**Figure 13b**). However, this contribution varies regionally, and in some locations frontal movement is associated with local cooling (**Figures 14c and 15a**), indicating that frontal displacement alone cannot explain the overall warming signal.

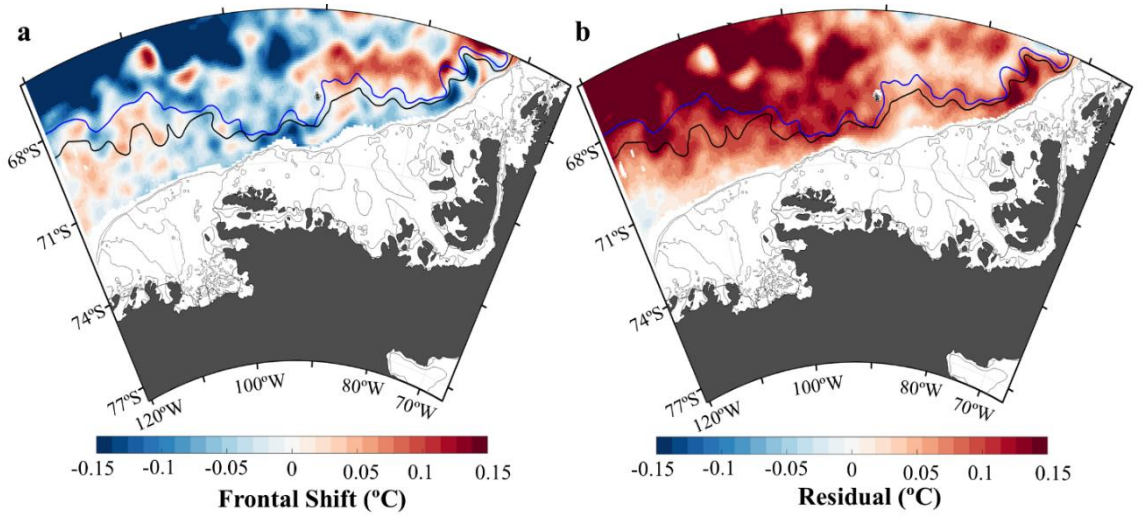


Figure 18: Influence of the interdecadal poleward displacement of the SACCF on the conservative temperature of the CDW layer. The total conservative temperature (Θ, ºC) change between the 1990s and 2010s (**Figure 14c**) is decomposed into **a** the frontal displacement (ºC) and **b** the residual term. Blue and black lines indicate the mean position of the Southern Antarctic Circumpolar Current Front (SACCF) during the 1990s and 2010s, respectively, based on GLORYS output. Thin grey contours represent the 500 m and 1,500 m isobaths from the R–Topo2 dataset [Schaffer *et al.,* 2016].

Instead, the dominant contribution to the observed warming arises from processes captured within the residual term (~0.09 °C; ~90%; **Figure 18b**). In our decomposition of the conservative temperature of CDW, this term accounts for water mass property changes occurring along the core of CDW, independently of frontal displacement. Here, we interpret this dominant CDW warming as being indicative of enhanced lateral heat

transport associated with Ross Gyre strengthening and increased meridional heat transport by cross-ACC exchanges. This contrasts with results from East Antarctica (80–60°E), where CDW warming has been more strongly linked to poleward displacement of the ACC fronts [Yamazaki *et al.,* 2021; Herraiz-Borreguero & Naveira Garabato, 2022]. This difference likely reflects distinct circulation regimes. Although regional gyres exist in East Antarctica (*e.g.,* the Prydz Bay Gyre), their spatial extent and transport are more regionally confined compared to the basin-scale Ross Gyre [*e.g.,* Yamazaki *et al.,* 2020]. Because lateral heat redistribution depends on both the strength and meridional extent of the circulation, smaller and more localized gyres might be expected to exert a more limited influence on large-scale isopycnal heat transfer. In contrast, the Ross Gyre spans a broader sector of the Pacific Southern Ocean and provides a more extensive pathway for lateral isopycnal heat transport toward West Antarctica [*e.g.,* Nakayama *et al.,* 2018]. This interpretation is also consistent with the regional pattern of eddy kinetic energy change reported by Zhang et al. [2021], who found no coherent circumpolar increase in eddy kinetic energy but identified a significant increase downstream of the Campbell Plateau. Such regional enhancement may favor stronger cross-ACC isopycnal exchange in the Pacific sector, thereby contributing to lateral heat transport toward West Antarctica. This difference in circulation regimes may help explain why CDW variability in West Antarctica appears more influenced by Ross Gyre variability, whereas in East Antarctica it has been more closely linked to meridional displacements of ACC fronts.

Taken together, these results highlight the likely sensitivity of off-shelf CDW warming to wind-driven circulation changes. Because both SACCF displacement and isopycnal heat transport are linked to variability in the westerly winds, their relative contributions in future will depend on how continued wind intensification modulates gyre circulation, frontal structure, and mesoscale eddy activity. Climate projections indicate that sustained off-shelf warming in West Antarctica under intensified westerlies is probable, largely associated with Ross Gyre strengthening [Gómez-Valdivia *et al.,* 2023]. However, whether the fractional contribution of frontal displacement increases or remains secondary will require further scrutiny.

4.1.3.3 Long-term variability of CDW layer on the continental shelf

Having quantified the (likely wind-driven) warming of the off-shelf CDW layer, it is important to determine whether this enhanced heat reservoir can access the

continental shelf. The presence of warmer off-shelf CDW does not necessarily lead to increased CDW intrusions, as highly dynamic shelf break processes and local thermodynamic forcing act as modulators [*e.g.,* Couto *et al.,* 2017; Dotto *et al.,* 2019; Huguenin *et al.,* 2024; Silvano *et al.,* 2022; Oelerich *et al.,* 2022; Webber *et al.,* 2017]. Although the mechanisms controlling CDW intrusions (*e.g.,* local wind forcing and thermodynamic processes) are partly understood, their regional response to the atmospheric conditions of the 2010s remains unclear. In this section, we examine how interdecadal changes in shelf-break processes during the 2010s, primarily driven by ASL variability, modulated CDW intrusions and the regional expression of the off-shelf warming signal across the continental shelf of West Antarctica.

Despite overall warming of the off-shelf CDW around West Antarctica between the 1990s and the 2010s, the continental shelf exhibits pronounced spatial heterogeneity (**Figure 14c**). These spatial variations reflect the highly dynamic shelf break processes (*e.g.,* local wind forcing at the shelf break) and thermodynamic processes within the continental shelf region (*e.g.,* convection driven by surface heat loss and sea ice production), both of which are key to driving CDW thermohaline variability at the continental shelf [Azaneu *et al.,* 2023; Dotto *et al.,* 2019, 2020; Nakayama *et al.,* 2018; Oelerich *et al.,* 2022; Webber *et al.,* 2017].

A similar regional dependence of CDW intrusions has also been documented in East Antarctica. There, the delivery of CDW onto the continental shelf is strongly modulated by local dynamical mechanisms, including isopycnal shoaling in regions such as Vincennes Bay [Ribeiro *et al.,* 2025], variability in the Antarctic Slope Current, and wind-driven processes such as Ekman divergence poleward of the wind stress curl maximum [Greene *et al.,* 2017; Nakayama *et al.,* 2018; Kusahara *et al.,* 2023]. These studies emphasize that, although the large-scale circulation sets the off-shelf CDW heat reservoir around Antarctica, the actual intrusion of CDW onto the continental shelf is primarily controlled by regional oceanographic and atmospheric conditions.

Here, we found across the Amundsen Sea continental shelf, distinct hydrographic regimes emerge between the western and eastern basins, shaped by local bathymetry and the physical processes that regulate CDW intrusions at the shelf break. In the western basin, the CDW layer experienced a significant warming (area averaged ~0.10 ± 0.06 °C; **Figure 14c**) between the decades of the 1990s and 2010s. These changes are likely linked

to the presence of a deeper, more open trough [*e.g.,* Cochran *et al.,* 2020] that enables strong CDW inflow modulated by the Amundsen Sea undercurrent [*e.g.,* Dotto *et al.,* 2019]. On interannual and decadal timescales, this undercurrent responds to zonal wind variability over the shelf break [Silvano *et al.,* 2022]. During the 2010s, a westward wind anomaly along the shelf break (**Figure 19a**), associated with a deeper and more intense ASL [Raphael *et al.,* 2016; **Figure 16d**], steepened the Antarctic Slope Front by depressing isopycnals across the continental shelf (**Figure 19c**). This process strengthened the undercurrent, thereby facilitating greater CDW inflow (**Figure 19c**), which is consistent with the mechanism proposed by Silvano et al. [2022].

In contrast, the eastern Amundsen Sea basin experienced CDW cooling (area averaged ~ −0.11 ± 0.07 °C; **Figure 14c**) between the 1990s and 2010s. Here, the troughs are shallower than the Dotson-Getz trough, vertically restricting CDW access. Consequently, the intrusion of warm water is critically dependent on the depth of the thermocline [*e.g.,* Webber *et al.,* 2017]. We suggest that enhanced wintertime coastal-polynya activity in the eastern Amundsen Sea during the 2010s may have increased the production and retention of Winter Water observed in the following summer. The larger intermediate-depth reservoir of Winter Water strengthened stratification near the shelf break, deepened the summer thermocline, and depressed isopycnals, ultimately limiting the access of CDW-contained oceanic heat and contributing to regional cooling [*e.g.,* O'Connor *et al.,* 2025]. An additional contributor to the observed cooling is the persistence of westward summertime wind anomalies along the continental shelf break (**Figure 19a**). These anomalies intensify surface-layer Ekman transport, reinforcing shelf-break convergence and promoting water mass accumulation in the upper ocean. This, combined with enhanced mixing between Winter Water and glacial meltwater [Huguenin *et al.,* 2024; Webber *et al.,* 2019], drives further isopycnal deepening and reduces the capacity of shelf-break processes to transport CDW onto the continental shelf via submarine troughs [Dotto *et al.,* 2019; Dutrieux *et al.,* 2014; Jacobs *et al.,* 2011; Nakayama *et al.,* 2013; Webber *et al.,* 2017]. This is evident in both Pine Island troughs (eastern and western troughs; **Figure 19d–e**).

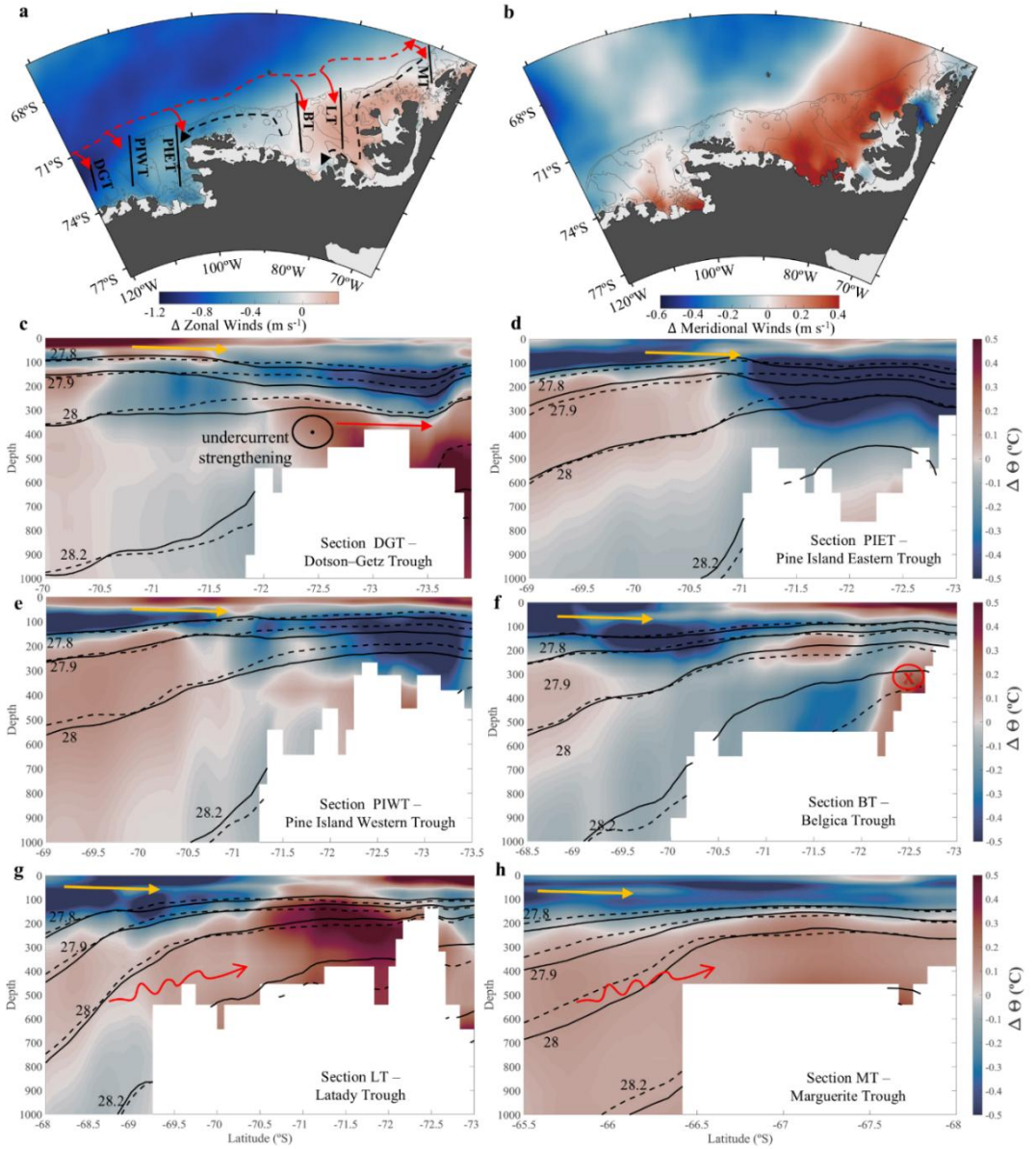


Figure 19: Wind-driven shift in the vertical structure of CDW intruding onto West Antarctica continental shelf. **a** and **b** Decadal difference (2010s minus 1990s) in zonal and meridional wind speed anomalies (m s^{-1}) between two periods (*i.e.,* 2010s minus 1990s), respectively. Thin grey contours represent the 500 m and 1,500 m isobaths from the R–Topo2 dataset [Schaffer *et al.,* 2016]. The red arrows indicate CDW advection through the ACC front and its intrusions onto the continental shelf by troughs. **c-h** Decadal difference of Conservative Temperature (Θ, °C) in sections across the Dotson-Getz Trough (DGT), Pine Island Eastern Trough (PIET), Pine Island Western Trough (PIWT), Latady Trough (LT), Belgica Trough (BT), and Marguerite Trough (MT). The locations of these sections are shown as black lines in panel (a). The dashed and solid lines indicate the mean neutral density contours (27.8, 27.9, 28.0, and 28.2kg·m^{-3}) for the 1990s and 2010s, respectively. The red arrows highlight the inflow of CDW (including eddy-driven pathways indicated by curved arrows) onto the continental shelf, while yellow arrows denote surface water transport.

Across the Bellingshausen Sea continental shelf, decadal differences in CDW layer properties also exhibit a pronounced contrast between eastern and western basins, likely reflecting the influence of the ASL on shelf break dynamics and thermodynamic processes. In the western basin, we observed cooling (area averaged ~ –0.10 ± 0.07 °C; **Figure 14c**) associated with a westward wind anomaly at the shelf break (Figure 6a), consistent with the influence of a deeper and more intense ASL. This atmospheric state promotes enhanced on-shelf Ekman transport of cold surface waters, which reduces CDW inflow [*e.g.,* Huguenin *et al.,* 2024], as evidenced along the Belgica trough section (**Figure 19f**). Simultaneously, over the continental shelf, intensified northward and westward winds (**Figure 19a–b**) acted to reduce sea-ice concentration, favouring increased heat loss and convective processes, which combined lead to gradual cooling of continental shelf waters, as previously suggested by Oelerich et al. [2022].

Conversely, in the eastern Bellingshausen Sea basin, we observed CDW warming (area averaged ~ 0.17 ± 0.10 ºC; **Figure 14c**). Here, the influence of the ASL was weaker (**Figure 16d**), characterised by stronger northward wind anomalies and reduced westward wind anomalies (**Figure 19a–b**), conditions typically expected to restrict CDW intrusions due to enhanced off-shelf Ekman transport of cold surface waters [*e.g.,* Huguenin *et al.,* 2024]. We therefore suggest that CDW warming observed in this region was most likely associated with enhanced CDW transfer by mesoscale eddy activity [Couto *et al.,* 2017; Martinson & McKee, 2012; Moffat *et al.,* 2009], likely facilitated by the closer proximity of the SACCF to the continental shelf break (**Figure 14**). Such dynamics are particularly evident in the Latady and Marguerite troughs (**Figure 19g–h**), where the enhanced CDW inflow can subsequently be advected westward, delivering heat to the Belgica trough (**Figure 19f**). These conditions appear to offset the local thermodynamic cooling processes also observed at the western Belligshausen Sea continental shelf basin. Such processes would typically cool the deeper water column, but here they are counteracted by the stronger inflow of warm CDW. Furthermore, the increased access of warmed CDW delivers heat to ice shelves and potentially intensifies basal melting, which would lead to enhanced local meltwater input in this region [*e.g.,* Sheehan *et al.,* 2023]. This meltwater is likely subsequently transported by the Antarctic Coastal Current westward along the continental shelf, contributing freshwater to adjacent regions such as the western Bellingshausen and eastern Amundsen Seas [Chretien *et al.,* 2021; Schubert *et al.,* 2021; Thompson *et al.,* 2020].

4.1.3.4 Key limitations

Overall, hydrographic observations and the GLORYS output reanalysis show good qualitative agreement in representing the thermohaline structure of the off-shelf CDW (**Supplementary Figures 1 and 2**). Quantitatively, differences between the two datasets reach up to ~0.1 °C in temperature and 0.15 g kg^{-1} in salinity (**Figure 20**). Despite these differences, the overall consistency indicates that GLORYS output captures the large-scale interdecadal variability of the off-shelf CDW reasonably well.

For clarity, we group the analysis into decades. Although the choice of temporal boundaries is somewhat arbitrary, the observed changes in CDW properties are consistent with a broader linear warming trend throughout the study period (**Supplementary Figure 4**). The decadal averages, therefore, serve mainly as a practical way to illustrate longer-term variability rather than implying discrete shifts between time periods. We also note that the number of hydrographic profiles available varies between decades because observations in this region are sparse and irregular in time, with particularly limited coverage during the 1990s. This uneven sampling introduces some uncertainty when comparing decadal averages.

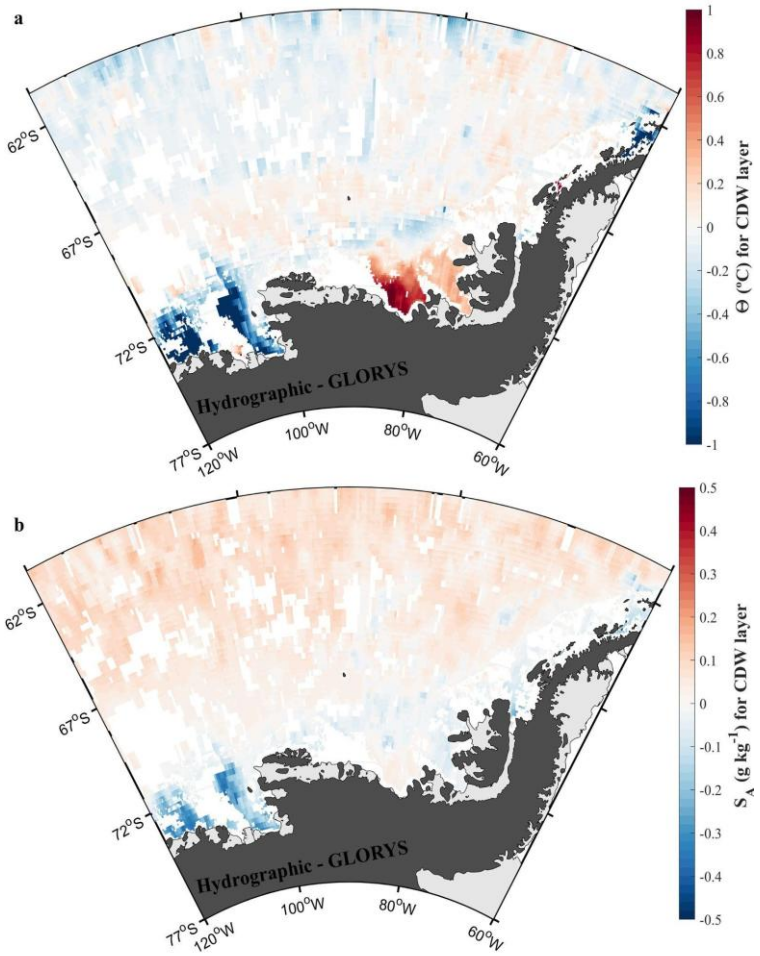


Figure 20: Conservative temperature and absolute salinity differences between the hydrographic measurements and GLORYS output. Time-averaged (1990s-2010s) of a Conservative Temperature (Θ ºC) and b Absolute Salinity (S_A, g kg^{-1}). Areas with no data points within a 50 km radius of each grid point were masked in the hydrographic measurements.

We highlighted that larger discrepancies appear over the continental shelf. Although GLORYS output reproduces the general pattern of interdecadal differences seen in hydrographic observations across much of the West Antarctic continental shelf (**Figure 14**), differences between observations and the reanalysis can reach ~1.3 °C in temperature and 0.3 g kg^{-1} in salinity (**Figure 20**). Several factors likely contribute to these differences. First, observational coverage over the continental shelf remains sparse and uneven through time, which increases uncertainty in decadal estimates. Second, the horizontal resolution of GLORYS output (~8 km) does not fully resolve mesoscale dynamics in this region. Because the first baroclinic Rossby radius is about 4 km, resolving mesoscale eddies would require grid spacing closer to ~1 km [Nøst *et al.,* 2011; Hattermann *et al.,* 2014; Thompson *et al.,* 2014]. These unresolved eddies play an

important role in cross-shelf exchanges and may affect how CDW pathways toward the continental shelf are represented. Third, inaccuracies in bathymetry (particularly in the representation of submarine glacial troughs) that may lead to circulation pathways that differ from those in reality [Oelerich *et al.,* 2022], even though these troughs strongly guide CDW intrusions onto the shelf. For these reasons, caution is needed when interpreting interdecadal variability of CDW properties on the continental shelf, including the influence of local wind forcing and on-shelf thermodynamic processes. Future studies that combine higher-resolution regional modeling with improved observational coverage will be important to resolve these processes better.

4.1.4 Conclusions and outlook

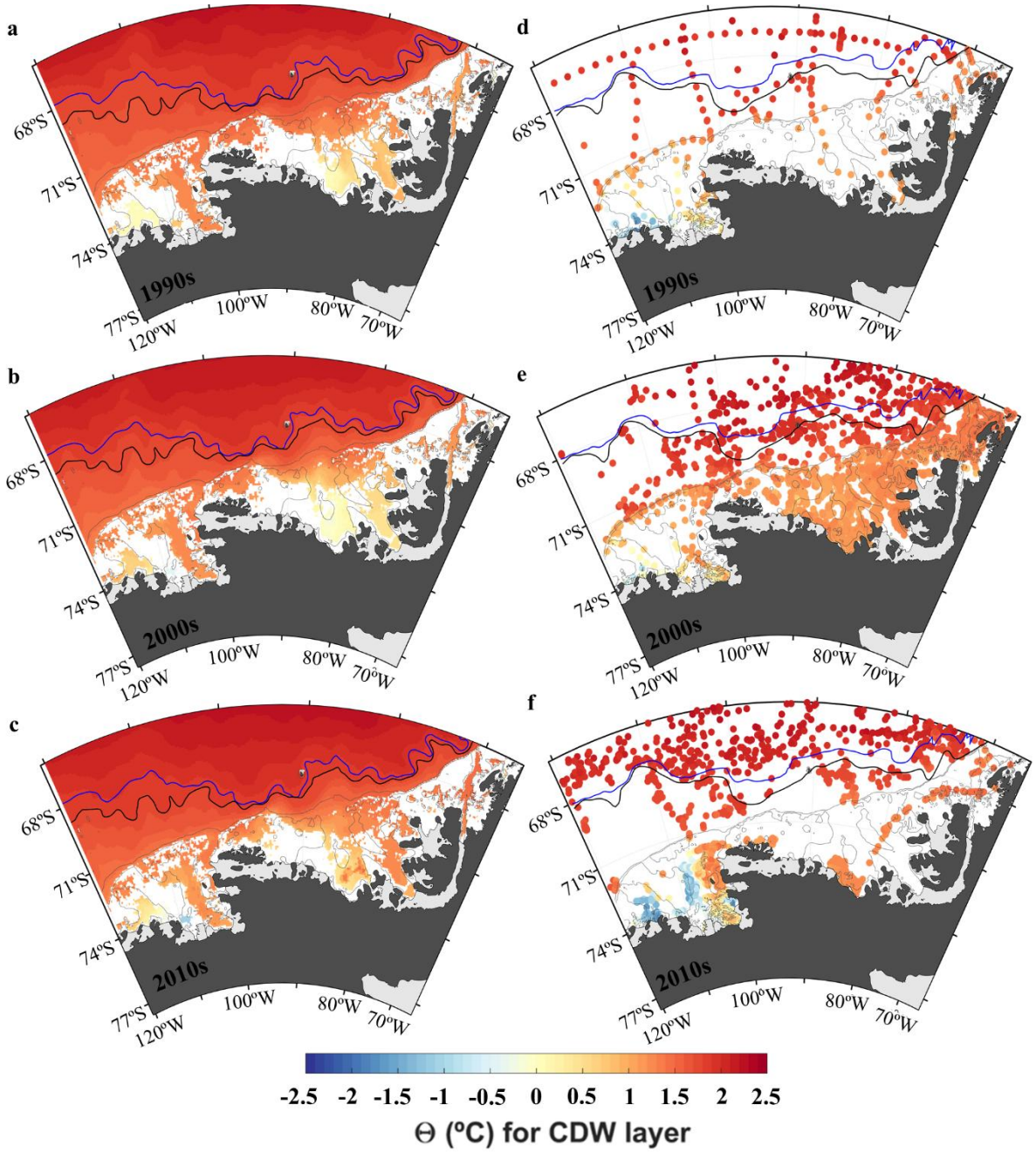
Based on hydrographic measurements and reanalysis output, we show that an interdecadal warming and salinification of the off-shelf CDW layer in West Antarctica occurred between the 1990s and 2010s, most likely driven by wind-forced circulation changes. Specifically, the poleward shift and intensification of the westerly winds strengthened the Ross Gyre, predictably enhancing lateral heat transport along isopycnals in the SACCF region and cross-ACC isopycnal exchange. These advective processes account for approximately 90% of the observed CDW warming. Although we also identified an interdecadal poleward displacement of the SACCF around West Antarctica, our results indicate that this frontal shift contributed only about 10% and therefore played a secondary role.

While we observe an increase in the contribution of warmer, saltier CDW along the off–shelf region, GLORYS outputs suggest that intrusion of this water onto the adjacent continental shelf may have been inhibited in some areas (i.e. eastern Amundsen and western Bellingshausen Seas) due to a westward wind anomaly there, potentially linked to a deepened and intensified ASL. In contrast, due to the specific conditions of each region (i.e. the extent of the influence of the Amundsen undercurrent and of eddy activity near the SACCF), this warmed CDW can penetrate onto the continental shelf of the western Amundsen and eastern Bellingshausen Seas, leading to a warming and salinification of those areas. Additionally, thermodynamic processes associated with the sea-ice production and surface heat loss on the continental shelf might also have contributed to changes in CDW layer properties. Thus, our results evidence the importance of the localized processes over the shelf break and continental shelf (*e.g.,*

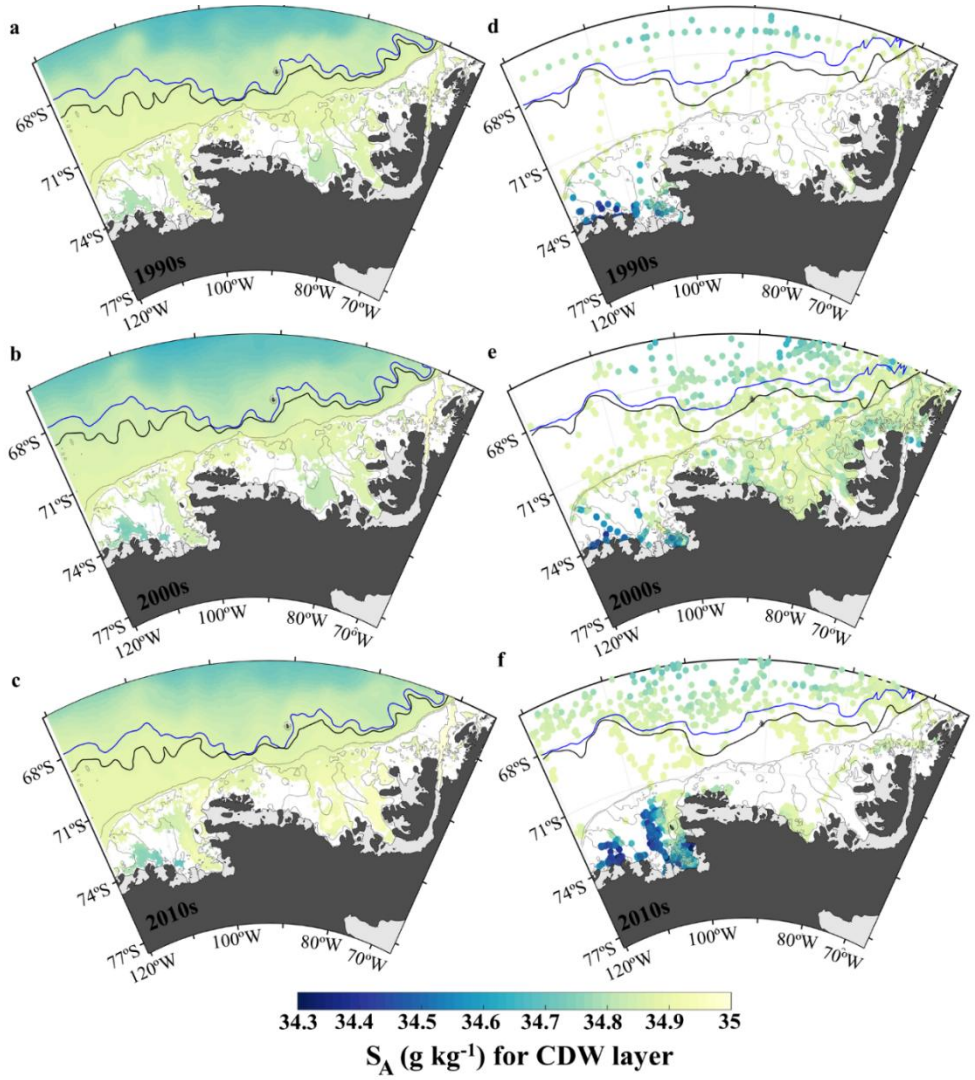
local wind forcing and thermodynamic processes) in regulating the extent to which CDW changes offshore may affect the shelf regions. These findings highlight the complex interplay between large-scale atmospheric forcing, ACC frontal dynamics, and regional oceanographic processes in shaping the evolution of CDW properties around West Antarctica.

Ongoing atmospheric trends are toward an intensified and poleward displacement of the Southern Hemisphere westerlies [*e.g.,* Marshall, 2003], which are expected to modulate the large-scale ocean circulation [*e.g.,* the Ross Gyre strength and eastward expansion; Dotto *et al.,* 2018]. As documented here, such changes can lead to off-shelf CDW warming, which could, in the long-term, enhance the intrusion of this warmer water onto the continental shelf in some regions of West Antarctica and, in turn, compromise the stability of the ice sheet in those areas, with implications for global sea-level rise. Therefore, ongoing monitoring and the use of high-resolution ocean-ice models are vital to better understand the mechanistic linkages between large-scale climatic changes over the ACC and Ross Gyre, variations in the cross-shelf transfer of CDW, and coastal ocean-ice interactions in this climatically sensitive region.

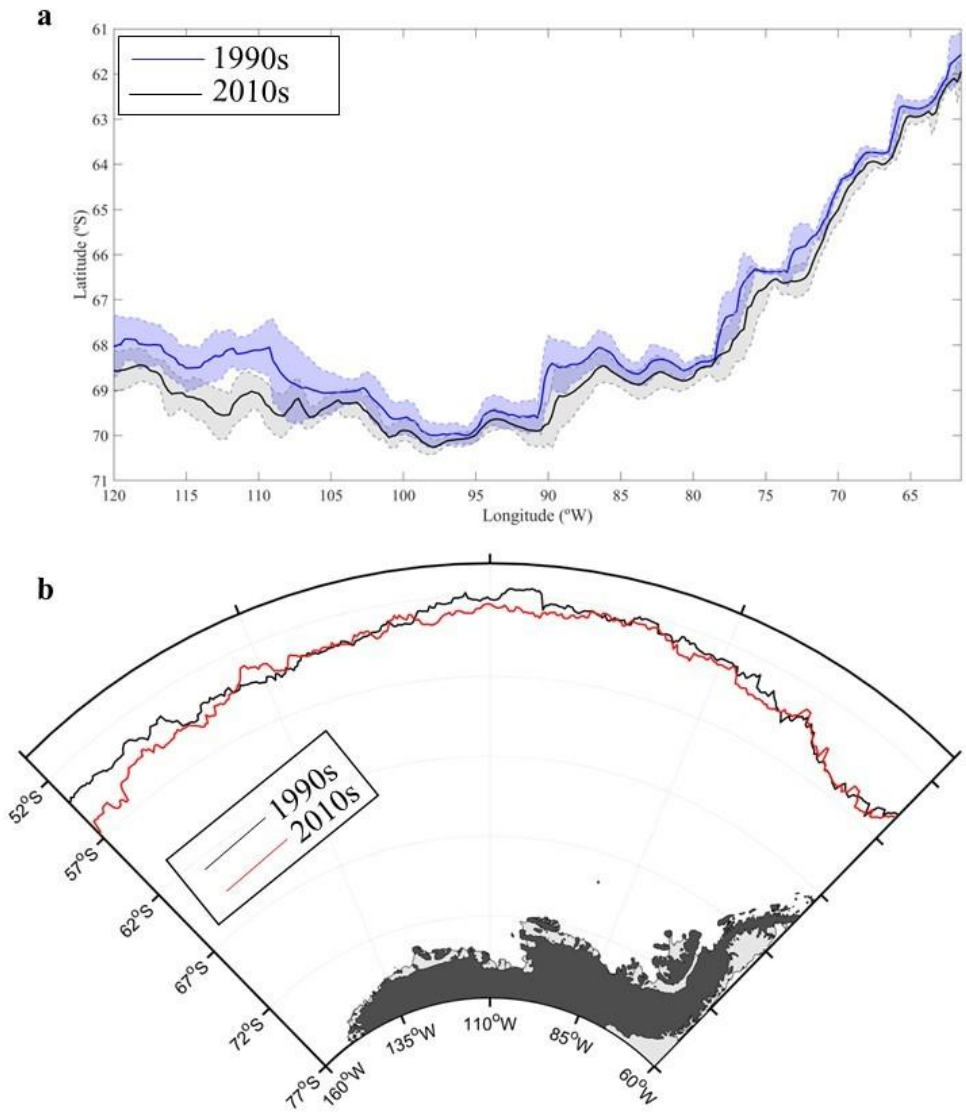
4.1.5 Supplementary information



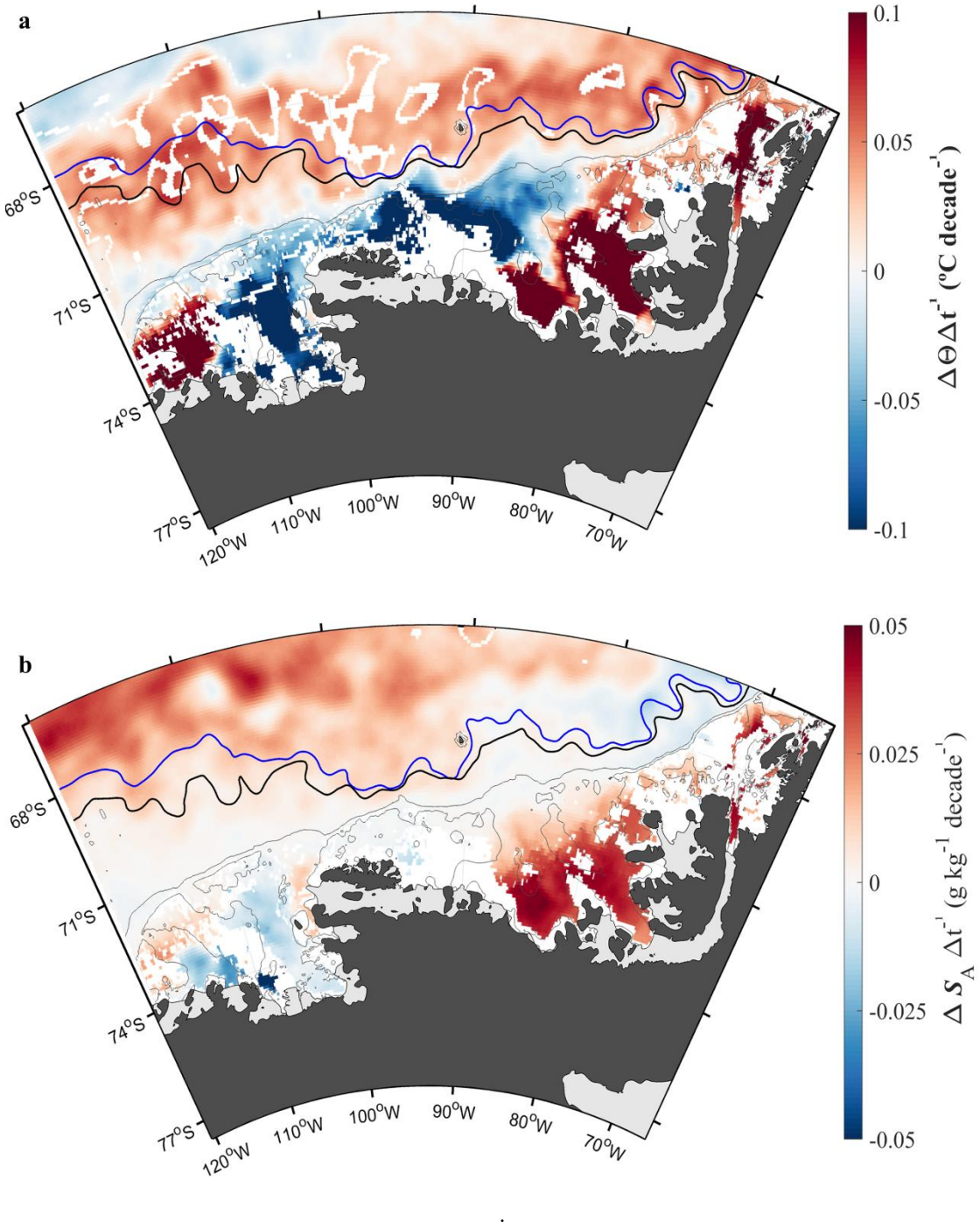
Supplementary Figure 1: Evolution of the conservative temperature (Θ, ºC) of CDW each decade from the hydrographic dataset and GLORYS output. Decadal average of Conservative temperature (Θ ºC) during **a** 1990s, **b** 2000s, and **c** 2010s from GLORYS output and **d**–**f** the same periods from hydrographic measurements. Blue and black lines indicate the mean position of the Southern Antarctic Circumpolar Current Front (SACCF) during the 1990s and 2010s, respectively, based on GLORYS output (panels on the left column) and satellite altimetry (panels on the right column). Thin grey contours represent the 500 m and 1,500 m isobaths from the R–Topo2 dataset [Schaffer *et al.,* 2016].



Supplementary Figure 2: As in the same **Supplementary Figure 1**, but to Absolute Salinity (S_A; g kg^{-1}).



Supplementary Figure 3: Decadal displacement of SACCF and westerly wind. **a** The blue (black) solid lines represent the decadal average position of the SACCF in the 1990s (2010s). The shaded areas indicate the standard deviation of the decadal average positions. **b** Position of the westerly wind (defined as maximum of zonal wind speed between 30ºS and 70ºS) for ERA5.



Supplementary Figure 4: Decadal linear trends of CDW termohaline Properties for (a) Conservative temperature – Θ; ºC, and (b) Absolute Salinity – SA; g kg^{-1}.

4.2 Variabilidade do Giro de Ross e seu papel na modulação das propriedades da CDW na região ao largo da plataforma continental no setor Amundsen–Bellingshausen (1993–2020)

O manuscrito, de autoria de Brendon Y. Damini, Tiago S. Dotto, Marina Noro, Ilana Wainer, Mauricio M. Mata e Rodrigo Kerr, é intitulado "*Ross Gyre circulation variability preconditions the off-shelf ocean heat reservoir to the West Antarctic continental shelf*" e está em revisão no periódico *Progress in Oceanography*. Em síntese, o estudo demonstra que a variabilidade sazonal e interanual do Giro de Ross modula de forma significativa o reservatório de calor e sal ao largo da plataforma continental na região de Amundsen-Bellingshausen associado a intrusões de CDW entre 1993 e 2020. Os resultados indicam que estados mais intensos do giro, associados principalmente a variações do rotacional da tensão do cisalhamento total superficial oceânico, coincidem com águas subsuperficiais mais quentes e salinas sobre o talude e na região ao largo da plataforma continental, consistentes com uma intensificação do reservatório regional de CDW. Em contraste, essa variabilidade ao largo da plataforma continental não se traduz em uma resposta síncrona e uniforme sobre a plataforma continental: enquanto a plataforma do mar de Amundsen apresenta resfriamento, refrescamento e aprofundamento das isopicnais, a do mar de Bellingshausen mostra aquecimento, salinificação e soerguimento das isopicnais. Assim, o estudo sugere que o Giro de Ross atua principalmente como um mecanismo de precondicionamento do calor disponível ao largo da plataforma, ao passo que a transferência efetiva desse calor para a plataforma continental é fortemente mediada por processos regionais na quebra de plataforma e por forçantes atmosféricas locais. As seções principais do manuscrito são apresentadas a seguir.

4.2.1 Introduction

The West Antarctic Ice Sheet has experienced rapid mass loss in recent decades [Rignot *et al.,* 2019], largely driven by enhanced basal melting associated with the oceanic heat supplied by the Circumpolar Deep Water (CDW) that accesses the cavities of the ice shelves through submarine glacial troughs [*e.g.,* Jenkins *et al.,* 2016; Naughten *et al.,* 2022; Wåhlin *et al.,* 2013]. In the Pacific sector of the Southern Ocean, this heat

supply is influenced by the large-scale circulation of the Ross Gyre (**Figure 21a**), which redistributes CDW laterally toward the Amundsen-Bellingshausen Seas [Nakayama *et al.,* 2018; Prend *et al.,* 2024]. Recent studies further suggest that a strengthening of the gyre enhances lateral heat advection along the southern boundary of the Antarctic Circumpolar Current (ACC), contributing to the recent warming of the off-shelf CDW reservoir in the West Antarctica [Damini *et al.,* under review].

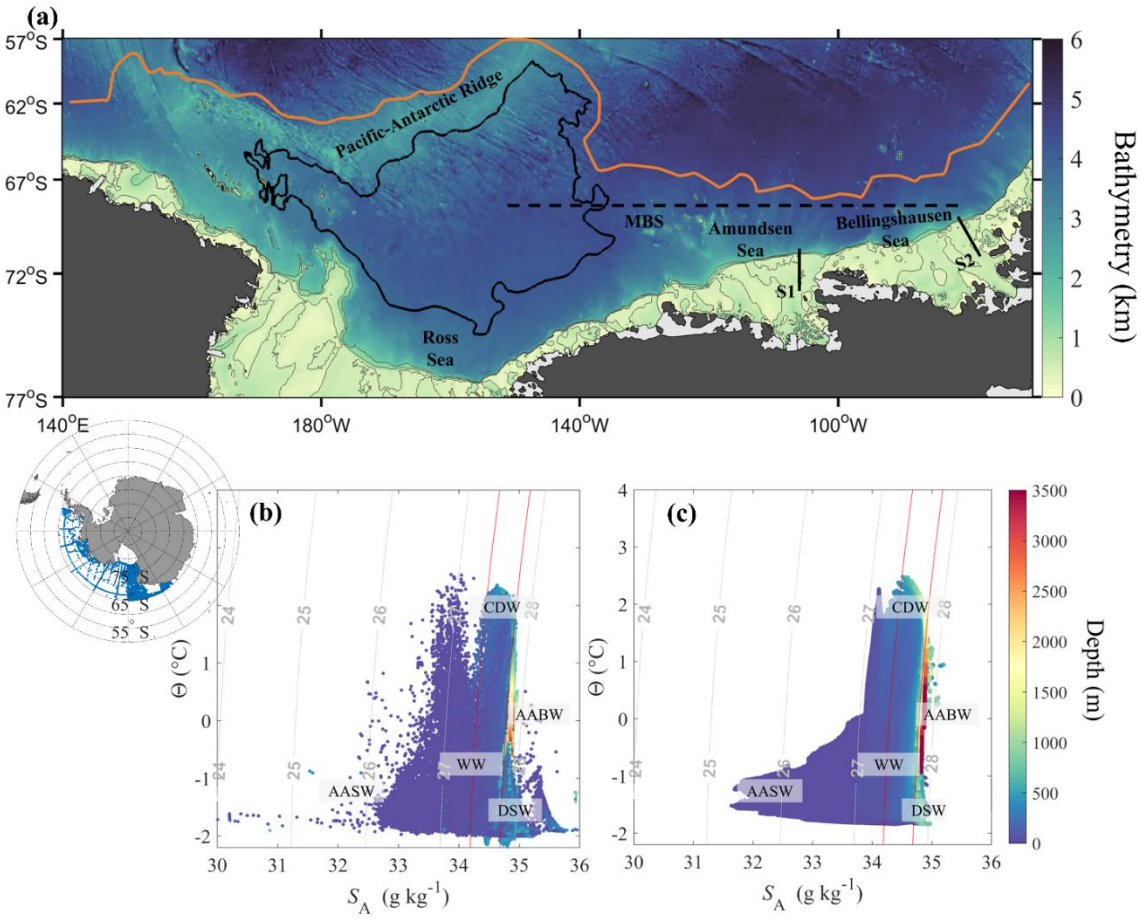


Figure 21*:* West Antarctic study region and water-mass characteristics. (a) Map showing the major ocean circulation features, including the Ross Gyre (solid black contour), the Southern Antarctic Circumpolar Current Front (orange), and the cross-shelf sections in the Amundsen and Bellingshausen Seas (S1 and S2, respectively). The cross-gyre section (dashed black line) extends from the eastern boundary of the Ross Gyre towards the Bellingshausen Sea and was used to investigate the lateral redistribution of Circumpolar Deep Water (CDW). MBS denote the Marie Byrd Seamounts. Thin grey contours indicate the 500 and 1,500 m isobaths from the R-Topo2 dataset [Schaffer *et al.,* 2016]. (b) Conservative temperature (Θ) - Absolute Salinity (SA) diagram from hydrographic observations, with the stations shown in the inset, and (c) same as (b), but derived from GLORYS12v1 data over the domain 65°S–79°S and 140°E–70°W. Colors indicate depth. Labels AASW, WW, CDW, AABW, and DSW denote Antarctic Surface Water, Winter Water, Circumpolar Deep Water, Antarctic Bottom Water, and Dense Shelf Water, respectively.

Gray contours represent potential density (σ_θ; kg m^{-3}), while the red contours indicate σ_θ = 27.4 and 27.8 kg m^{-3}, which define the upper and lower boundaries of the CDW layer, respectively.

4.2.2 Materials and Methods

4.2.2.1 GLORYS12v1 and hydrography

GLORYS12v1, provided by the Copernicus Marine Environment Service, is a global eddy-resolving physical ocean and sea ice reanalysis with 1/12° horizontal resolution and 50 standard vertical levels that covers the period from 1993 to the present. The model component is based on the Nucleus for European Modelling of the Ocean – NEMO [Madec & the NEMO Team, 2008] version 3.1, coupled to the Louvain-La-Neuve sea ice model version 2 [Lellouche *et al.,* 2018; Drévillon *et al.,* 2022]. GLORYS12v1 is initialized with temperature and salinity fields from the EN4.2.0 monthly gridded climatology [Good *et al.,* 2013]. It is atmospherically forced by ERA-Interim until 2018 and ERA5 from 2019 to the present. The switch in atmospheric forcing led to no significant changes in the outputs of GLORYS12v1 except for a lower reduction in sea ice volume and extent in the Southern Ocean during austral summer [Jean-Michel et al. 2021]. Quality assessments have shown that GLORYS effectively captures the main interannual climate variability signals for the ocean and sea ice [Jean-Michel et al. 2021].

The reanalysis temperature and salinity were evaluated against hydrographic observations in the Ross Gyre region from the World Ocean Database 2023, Argo, the CLIVAR and Carbon Hydrographic Data Office, and the Marine Mammals Exploring the Ocean Pole to Pole consortium data (MEOP) between 1993 and 2020 (inset in **Figure 21**). We calculated conservative temperature (Θ in ºC) and absolute salinity (S_A in g kg^{-1}) using the International Thermodynamic Equation of Seawater 2010 [McDougall & Barker, 2011] from hydrographic measurements and GLORYS12v1 outputs. Then, to assess the ability of GLORYS12v1 to reproduce local water masses, we compared the Θ-S_A diagram derived from GLORYS12v1 and the hydrographic climatology.

4.2.2.2 Ross Gyre definition

We defined the Ross Gyre boundary as the −8 Sv (1 Sv = 10^6 m^3 s^{-1}) contour of the time-mean barotropic streamfunction. In GLORYS12v1, this contour represents the outermost closed streamfunction contour without coastal extensions (**Supplementary Figure 5a**), consistent with the Ross Gyre definition of Roach & Speer [2019]. This

choice isolates the off-shelf recirculating gyre from continental shelf flows, providing a physically consistent and reproducible metric for tracking changes in gyre area over time. Following Prend et al. [2024], we defined the gyre circulation strength as the mean barotropic streamfunction within this contour. To assess the robustness of this choice, we performed a sensitivity test using four different streamfunction contours (−6 Sv, −7 Sv, −9 Sv and −10 Sv). The resulting estimates of gyre circulation strength were all highly and significantly correlated with the metric based on the −8 Sv contour ($r > 0.9$; **Supplementary Figure 5b**). Additionally, according to this Ross Gyre definition, more negative values indicate stronger Ross Gyre circulation.

4.2.2.3 Ancillary data sets

To assess the role of momentum flux over the ocean's surface as a possible driver of circulation, we computed the monthly total ocean surface stress (OSC) as the sum of the ice–ocean stress ($\alpha\vec{\tau}_{ice-water}$) and air–ocean stress ($\vec{\tau}_{air-water}$) components. The total OSC (Eqs. 1–3) in each grid cell is as follows:

$$\vec{\tau} = \vec{\tau}_{ice-ocean} + (1-\alpha)\vec{\tau}_{air-ocean}; \quad (1)$$

where $\vec{\tau}_{ice-ocean}$ is:

$$\vec{\tau}_{ice-ocean} = \rho_{ocean} C_{Iw} |\vec{U}_{ice}| \vec{U}_{ice}; \quad (2)$$

and $\vec{\tau}_{air-ocean}$ is:

$$\vec{\tau}_{air-occean} = \rho_{air} C_d |\vec{U}_{air}| \vec{U}_{air}; \quad (3)$$

α is sea ice concentration (%) obtained from the GLORYS12v1 output, ρ_{air} is 1.25 kg/m^3, ρ_{water} is mean seawater density of 1,028 kg/m^3, C_d and C_{Iw} are the air–ocean and ice–ocean drag coefficients, set to 1.25×10^{-3} and 5.50×10^{-3}, respectively [Dotto *et al.*, 2018]. $\vec{U}_{ice}$ and $\vec{U}_{air}$ represent the sea-ice drift velocity (m s^{-1}) from GLORYS12v1 and the wind velocity (m s^{-1}) from ERA5 reanalysis, respectively. Furthermore, the ocean surface stress was averaged over the gyre-forcing region (130–150°W, 67–70°S), defined as the area of strongest linear correlation within the Ross Gyre boundaries [*e.g.,* Prend *et al.,* 2024; **Supplementary Figure 6**]. This averaging provides a representative time series of the surface stress forcing acting on the gyre.

4.2.2.4 Buoyancy Flux calculation

To assess whether the Ross Gyre variability is also influenced by buoyancy forcing, we calculated the surface buoyancy flux over the continental shelf. Surface buoyancy forcing can contribute to the input or removal of potential vorticity (Czaja & Hausmann, 2009), driving horizontal circulations comparable to wind-driven gyres (Colin de Verdière, 1989). In the Ross Sea sector, buoyancy-driven steric changes over the shelf can alter the large-scale pressure field, with anomalies potentially transmitted along the boundary through barotropic adjustment. Following Neme et al. (2021), the surface buoyancy flux ($\mathcal{B}$; $m^2\ s^{-3}$; Eqs. 4–6):

$$\mathcal{B} = \mathcal{B}_{heat} + \mathcal{B}_{fresh} \tag{4}$$

where

$$\mathcal{B}_{heat} = \frac{-g\gamma Q_{net}}{c_w \rho} \tag{5}$$

$$\mathcal{B}_{fresh} = g\beta F_w S_{A(sup)} \tag{6}$$

and ρ is surface density, g is the acceleration due to gravity (9.81 ms^{-2}), c_w the specific heat capacity of seawater (3,992 J kg^{-1} K^{-1}), γ is the thermal expansion coefficient, β the haline contraction coefficient of seawater derived from TEOS-10 (McDougall & Barker, 2011), $S_{A(sup)}$ is the surface absolute salinity. Q_{net} is the heat fluxes, calculated as the sum of the net of longwave radiation (QLW), shortwave radiation (QSW), latent heat flux (QLH), and sensible heat flux (QSH). F_w represents the net freshwater fluxes, defined as evaporation (E), runoff (R), precipitation (P), and sea ice formation/melt (*i.e.,* P – E + R – F_{ice}). Monthly QLW, QSW, QLH, QSH, E, R and P data are obtained from ERA5. The freshwater flux associated with sea ice formation and melting dynamics (*i.e.,* F_{ice}) was estimated using a bulk thermodynamic approach following Hattermann et al. (2021), where positive F_{ice} represents sea ice formation (freshwater loss). In this convention, positive $\mathcal{B}$ represents the gain of buoyancy by the ocean (decreased density via warming or freshening). In addition, the largest $\mathcal{B}$ in the Ross Sea region is found over the continental shelf, so $\mathcal{B}$ is averaged at the continental shelves (defined by depths shallower than 1,000 m over the Ross Sea; 160ºE–150ºW) to build the time series.

4.2.2.5 Ross Gyre parameters

We computed the climatological seasonal cycles of the Ross Gyre circulation strength (Sv), gyre area (km^2), OSC ($N\ m^{-3}$), and surface buoyancy flux ($m^2\ s^{-3}$) to characterize the mean seasonal variability of the system. To investigate interannual variability, monthly anomalies were calculated relative to the long-term annual mean (1993–2020). The anomaly time series of Ross Gyre parameters (*i.e.,* gyre circulation strength, gyre area, OSC and surface buoyancy flux) were then smoothed using a zero-phase low-pass Butterworth filter with a cutoff period of 12 months. Linear Pearson correlation coefficients were calculated for both the climatological seasonal cycles and the filtered anomaly time series to assess the relationship between Ross Gyre circulation strength and the area, OSC, and surface buoyancy flux across seasonal and interannual timescales. Statistical significance was assessed from the corresponding p-values, and correlations were considered significant at the 95% confidence level (*p-value* < 0.05).

4.2.2.6 Cross-shelf and cross-gyre analyses of CDW variability in the West Antarctica

We selected two cross-shelf sections (S1 and S2 in **Figure 21a**) across the Amundsen and Bellingshausen continental shelves to assess the availability of CDW-derived heat to the shelf by analyzing Θ and S_A fields. Here, we calculated the averaged thermocline depth over the continental shelf portion along both sections following O'Connor et al. [2025], using the 0.5 °C isotherm to obtain a time series.

Furthermore, to investigate the potential role of the Ross Gyre dynamics in modulating subsurface thermohaline variability under changes in OSC over the West Antarctica, we analyzed a cross-gyre vertical section extending from the eastern boundary of the Ross Gyre towards the Bellingshausen Sea (**Figure 21a**). This analysis was used to examine the spatial structure of subsurface Θ anomalies and their possible relationship with lateral heat redistribution under intensified gyre circulation. In addition, we computed the mean thickness of CDW core depth, defined here as the depth of maximum temperature [Damini *et al.,* under review], to investigate whether changes in subsurface water properties over the off-shelf region were accompanied by vertical displacements consistent with enhanced Ekman-driven upwelling associated with intensified cyclonic OSC over the region.

4.2.2.7 The influence of the Ross Gyre dynamics variability at off-shelf and continental shelf regions off West Antarctica

We conducted composite analyses for strong and weak Ross Gyre circulation anomaly periods to examine how subsurface waters [300–400 m; layer mainly occupied by CDW; Nakayama *et al.,* 2018] conservative temperature and absolute salinity vary over off-shelf and continental shelf regions in relation to changes in the gyre. Following Dotto et al. [2018], the strong-gyre circulation composites were defined as periods when the smoothed gyre-strength circulation anomaly time series exceeded −1 standard deviation (consisting of 40 months) and weak-gyre circulation composites consisting of +1 standard deviation (consisting of 58 months). In both cases, anomalies of the composites were calculated relative to the long-term mean gyre circulation strength (consisting of 336 months). Additionally, the Monte Carlo test indicates that the reported temperature and salinity contrasts exceed the 95% confidence bounds derived from random reassignment across large portions of the off-shelf region. Because the selected months may retain some temporal persistence, this test is interpreted here as an empirical robustness check of the composite patterns rather than as a strict test of fully independent realizations. In addition, we computed anomaly composites of OSC and sea level pressure (monthly outputs from ERA5 from January to December, 1993–2020) to explore the atmospheric drivers linked to the strongest and weakest Ross Gyre circulation periods. Finally, we analyzed linear spatial trends in OSC and subsurface thermohaline properties to assess whether long-term variations in the Ross Gyre circulation strength are associated with the observed changes in water masses over the West Antarctic off-shelf and continental shelf regions. Statistical significance was assessed from the corresponding *p-values* of the regression slope, and trends were considered significant at the 95% confidence level (p-*value* < 0.05).

4.2.3 Results and Discussion

4.2.3.1 Representation of West Antarctic water masses in GLORYS12v1

The main thermohaline structure reproduced by GLORYS12v1 is broadly consistent with the hydrographic observations (**Figure 21b–c**), including the low-salinity Antarctic Surface Water, the Winter Water temperature minimum, and the subsurface temperature maximum associated with CDW. However, important biases remain. In

GLORYS12v1, surface and intermediate waters occupy a narrower and more homogeneous range in Θ-S_A distributions than in the observations [**Figure 21b–c**], indicating an overly smoothed water-mass structure, consistent with the GLORYS12v1 assessment of Drévillon et al. [2022]. This pattern is also consistent with known limitations in the representation of sea-ice-related processes, including polynya-driven brine rejection [Lellouche *et al.,* 2018].

In addition, GLORYS12v1 does not reproduce the observed high-salinity tail of Dense Shelf Water above 34.8 g kg^{-1}, indicating a weak representation of the saline end-member (**Figure 21b–c**). This limitation is likely related to unresolved dense-water overflows, smoothed bathymetry, and the absence of explicit ice-shelf cavity processes, all of which affect the formation and export of dense waters contributing to Antarctic Bottom Water [Kerr *et al.,* 2009; Renner *et al.,* 2009; Stewart *et al.,* 2019; Oelerich *et al.,* 2022; Noro *et al.,* 2025].

4.2.3.2 Seasozonal and interannual Ross Gyre variability and its drivers

The time-mean barotropic streamfunction reveals a well-defined cyclonic Ross Gyre occupying the southwestern Pacific sector of the Southern Ocean (**Figure 21a**). Over the study period, the gyre exhibits a mean circulation strength of approximately –14 ± 1.7 Sv. This estimate lies within the lower range of previous studies, which report transports varying from roughly –15 to –45 Sv [Chu & Fan, 2007; Mazloff *et al.,* 2010; Nakayama *et al.,* 2014; Wang *et al.,* 2024]. These differences primarily reflect the various methods used to define gyre boundaries and circulation strength. For example, studies reporting larger transports, such as Wang et al. [2024], which reported a gyre circulation strength of –45 Sv between 2011 and 2016, defined the gyre circulation strength as the lateral transport across a meridional section extending from the gyre center to its southern boundary, with the gyre boundaries identified from the maximum closed barotropic streamfunction contour. In contrast, Prend et al. [2024] quantified the gyre circulation strength using the area-averaged barotropic streamfunction within the −8 Sv contour over the 2013–2018 period. By adopting the same area-averaging method, our estimate is dynamically consistent and directly comparable with the ~ −16 Sv reported by Prend et al. [2024].

The gyre exhibits a detectable annual cycle, characterised by stronger circulation during austral autumn (–14.42 ± 2.23 Sv; **Figure 22a**), with maximum circulation

strength in May reaching –14.92 ± 2.83 Sv (**Figure 22a**), and weaker conditions in summer (–13.25 ± 1.40 Sv; **Figure 22a**), with minimum strength in December reaching –12.78 ± 1.12 Sv (**Figure 22a**). Overall, this corresponds to ~14% reduction in gyre circulation strength from autumn to summer. Variations in gyre circulation strength are accompanied by coherent changes in gyre area, indicating that seasonal circulation intensification is associated with an eastward expansion of the gyre's eastern boundary with expansion during autumn, with a maximum area of 2.05 ± 0.70 x 10^6 km^2 in May (**Figure 22b**), and contraction in summer, with a minimum area of 1.60 ± 0.45 x 10^6 km^2 in December (**Figure 22b**).

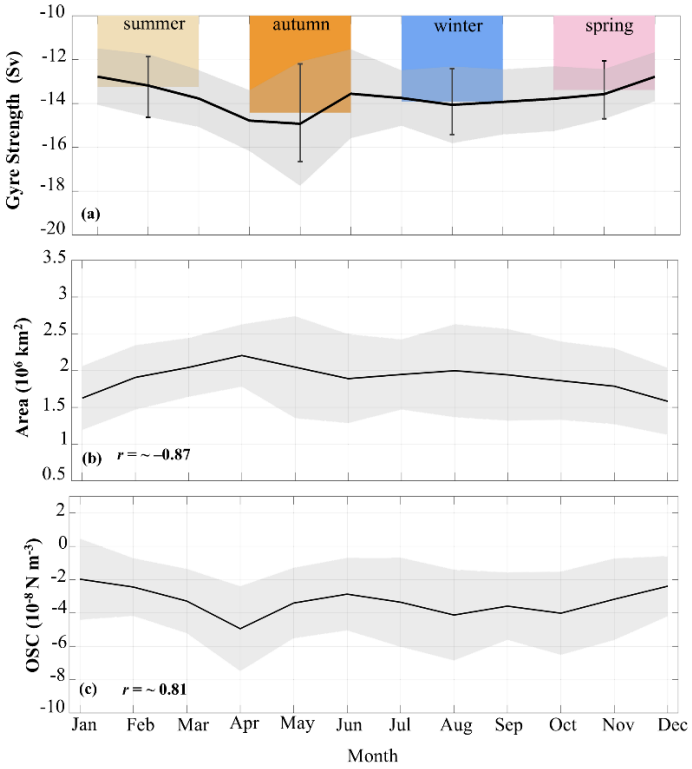


Figure 22: Seasonal variability of the Ross Gyre properties and atmospheric forcing during 1993–2020. (a) Gyre circulation strength, **(b)** gyre area, and **(c)** ocean surface stress curl (OSC). In panel **(a)**, bars show the seasonal mean gyre circulation strength for December–February (summer), March–May (autumn), June–August (winter), and September–November (spring), with error bars indicating the standard deviation of the values within each season. Shaded areas represent the monthly climatological standard deviation. The correlation coefficient (*r*) between gyre circulation strength and the variable shown in each panel is indicated. All correlations are significant at the 95% confidence level (*p-value* < 0.05).

Our results contrast with those of Dotto et al. [2018], who reported a pronounced semiannual cycle in the Ross Gyre circulation strength derived from satellite altimetry. This discrepancy likely reflects a combination of differences in the circulation strength

metrics and methods employed, the analyzed time periods, and the intrinsic limitations of the datasets used. The satellite sea surface height primarily captures the geostrophic response of the surface ocean to atmospheric forcing. In contrast, the barotropic streamfunction represents the vertically integrated circulation, including deep baroclinic structure and bottom velocities that substantially contribute to the total gyre circulation [Wang *et al.,* 2024]. Temporally, the 28-year GLORYS12v1 record used here also filters part of the short-term variability, providing a distinct statistical baseline relative to the five-year observational period analyzed by Dotto et al. [2018]. In addition, differences between observational satellite altimetry and reanalysis products may further contribute to the contrasting seasonal signals, since the simulated circulation in GLORYS12v1 depends on prescribed atmospheric forcing and model parameterizations, including sea-ice–ocean momentum transfer schemes [Lellouche *et al.,* 2018].

Beyond the seasonal cycle, the Ross Gyre exhibits pronounced interannual variability (Figure 3a). Periods of intensified circulation coincide with larger gyre areas and enhanced cyclonic OSC, suggesting a strong dynamical linkage between atmospheric forcing and the gyre variability. Specifically, during strong circulation periods, when the circulation anomaly exceeds −1 standard deviation, the mean gyre circulation strength anomaly reaches −1.60 ± 0.50 Sv (**Figure 23a**), 0.28 ± 0.21 × 10^6 km^2 for gyre area (**Figure 23b**), and –2.51 ± 2.30 × 10^{-8} N m^{-3} for OSC (**Figure 23c**). Conversely, during weak circulation periods, which exceed +1 standard deviation, the reverse; reaching 1.50 ± 0.30 Sv, −0.54 ± 0.27 × 10^6 km^2, and 2.20 ± 2.40 × 10^{-8} N m^{-3} for the gyre circulation strength, gyre area, and OSC, respectively (**Figure 23a–c**). These relationships are further supported by the significant correlations between gyre circulation strength and OSC (r = 0.56, *p-value* < 0.05) and between gyre circulation strength and gyre area (r = –0.72, *p-value* < 0.05), consistent with the interpretation that enhanced cyclonic vorticity input strengthens the gyre circulation and promotes an eastward expansion of its eastern boundary [*e.g.,* Gouretski, 1999; Dotto *et al.,* 2018; Prend *et al.,* 2024]. Here, we encompass more periods of both stronger and weaker Ross Gyre circulation events than previous studies [*e.g.,* Dotto *et al.,* 2018; Prend *et al.,* 2024], indicating that these relationships are statistically more robust and less sensitive to short-term variability.

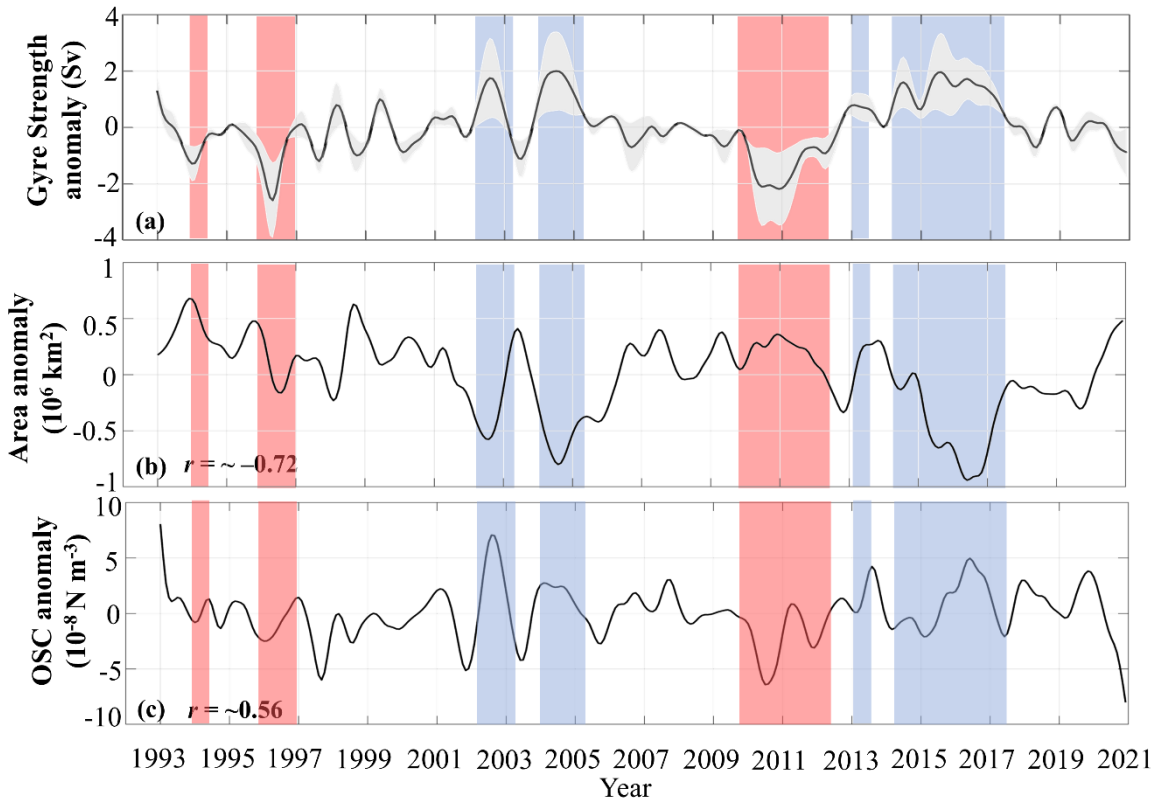


Figure 23: Interannual variability of Ross Gyre properties from GLORYS12v1 (1993-2020): (a) Gyre circulation strength anomaly. The gray shaded area in **(a)** represents the standard deviation., **(b)** gyre area anomaly, and **(c)** ocean surface stress curl (OSC) anomaly. The correlation coefficient (*r*) between gyre circulation strength and each variable is indicated in the corresponding panel. All correlations are significant at the 95% confidence level ($p < 0.05$). Red and blue rectangles denote strong and weak gyre periods, respectively, defined as periods when gyre circulation strength anomalies exceed ±1 standard deviation relative to the detrended mean, and used for the composite analysis.

We also evaluated the potential influence of surface buoyancy flux on the Ross Gyre circulation variability. However, no statistically significant relationship was found between the gyre circulation strength and surface buoyancy flux anomalies over the continental shelf ($r = 0.26$; **Supplementary Figure 7**). This confirms that, on seasonal to interannual scales, wind-driven vorticity input is the primary driver of the depth-integrated circulation in this sector.

Previous studies have proposed components of this dynamical linkage, although mostly based on temporally limited records [*e.g.,* Dotto *et al.,* 2018; Prend *et al.,* 2024]. For example, Dotto et al. [2018] identified the coupling between OSC and surface gyre circulation strength using a five-year satellite altimetry record, while Prend et al. [2024] demonstrated through Lagrangian analyses that an expanded Ross Gyre can steer CDW

towards the Amundsen-Bellingshausen Seas. However, it remained unclear whether this atmospheric forcing pathway could sustain long-term thermohaline changes in the off-shelf CDW reservoir.

By integrating atmospheric forcing, gyre variability, and subsurface thermohaline properties over the 1993–2020 period, our results provide evidence that the coupling between cyclonic OSC, gyre spin-up, and off-shelf CDW warming represents a robust multidecadal feature of the regional circulation. These results indicate that OSC-driven Ross Gyre variability exerts a persistent control on the volume and heat content of the off-shelf CDW reservoir. Together, these results demonstrate that the Ross Gyre variability serves as a large-scale preconditioning mechanism for the off-shelf CDW reservoir via persistent OSC-driven changes in circulation.

4.2.3.3 Off-shelf thermohaline response to the gyre circulation strengthening

Our composite analyses evidence that changes in the Ross Gyre circulation strength and area are associated with significant variations in subsurface thermohaline properties in the Amundsen-Bellingshausen off-shelf region (**Figure 24**). During periods of intensified circulation and gyre expansion, the off-shelf areas exhibit widespread warming (**Figure 24a**) and salinification (**Figure 24d**). These positive anomalies indicate an enhanced CDW presence, consistent with increased lateral heat and salt advection from the Pacific sector, driven by a stronger Ross Gyre. Conversely, weakened gyre periods are associated with cooler (**Figure 24b**) and fresher (**Figure 24e**) subsurface conditions, indicating a reduction of the CDW reservoir. The robustness associated with temperature and salinity anomalies was evaluated using the Monte Carlo permutation test, which indicates that the observed differences, with off-shelf area-averaged anomalies of 0.06 ± 0.03 ºC and 0.13 ± 0.004 g kg^{-1} (**Figures 24c and f**), exceed the 95% confidence interval across large portions of the off-shelf region. Together with the spatial coherence of the anomalies (**Figure 24**), these results indicate that the thermohaline contrasts between strong and weak gyre periods are robust features of the reanalysis.

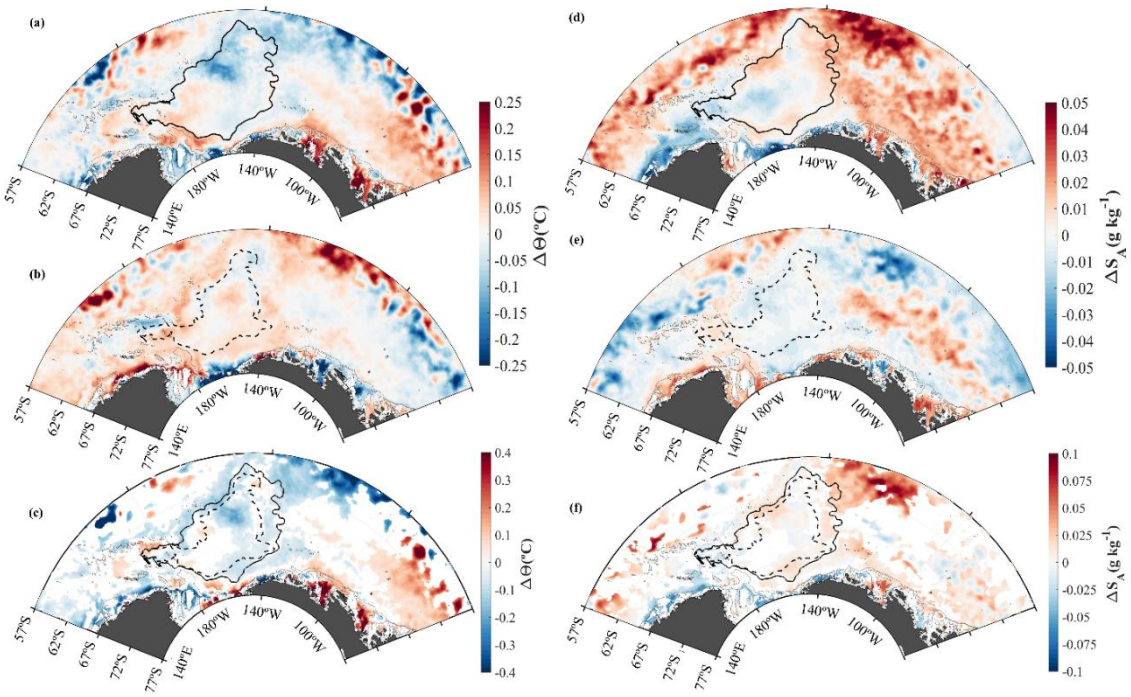


Figure 24: Subsurface thermohaline anomalies off West Antarctica associated with the Ross Gyre variability. (a) Conservative temperature (Θ) anomalies, during strong Ross Gyre periods and the Ross Gyre boundary are evidenced by the solid black line. **(b)** Same as in **(a)**, but during weak Ross Gyre periods, the Ross Gyre boundary is shown as a dashed black line. **(c)** Difference (D) in Θ between strong and weak Ross Gyre periods. **(d)-(f)** Same as in **(a)-(c)**, respectively, but for absolute salinity, S_A. Blank areas in panels **(c)** and **(f)** indicate differences that are not significant according to the Monte Carlo permutation test. Thin gray contours represent the 500 and 1,500 m isobaths from the RTopo-2 dataset [Schaffer *et al.,* 2016].

The variability of off-shelf subsurface properties is also tightly coupled to atmospheric forcing. Periods of stronger gyre circulation are consistently associated with lower sea level pressure over the West Antarctica region (**Figure 25a**), accompanied by more cyclonic OSC over the gyre (**Figure 25a**). This atmospheric configuration contributes to Ekman divergence, which injects cyclonic vorticity and spins up the gyre and enhances the eastward redistribution of CDW. While previous studies have proposed this link based on shorter records [*e.g.,* Dotto *et al.,* 2018; Nakayama *et al.,* 2018; Prend *et al.,* 2024], our 28-year analysis demonstrates that the coupling between OSC, gyre circulation strength, and off-shelf heat content is robust on multidecadal timescales.

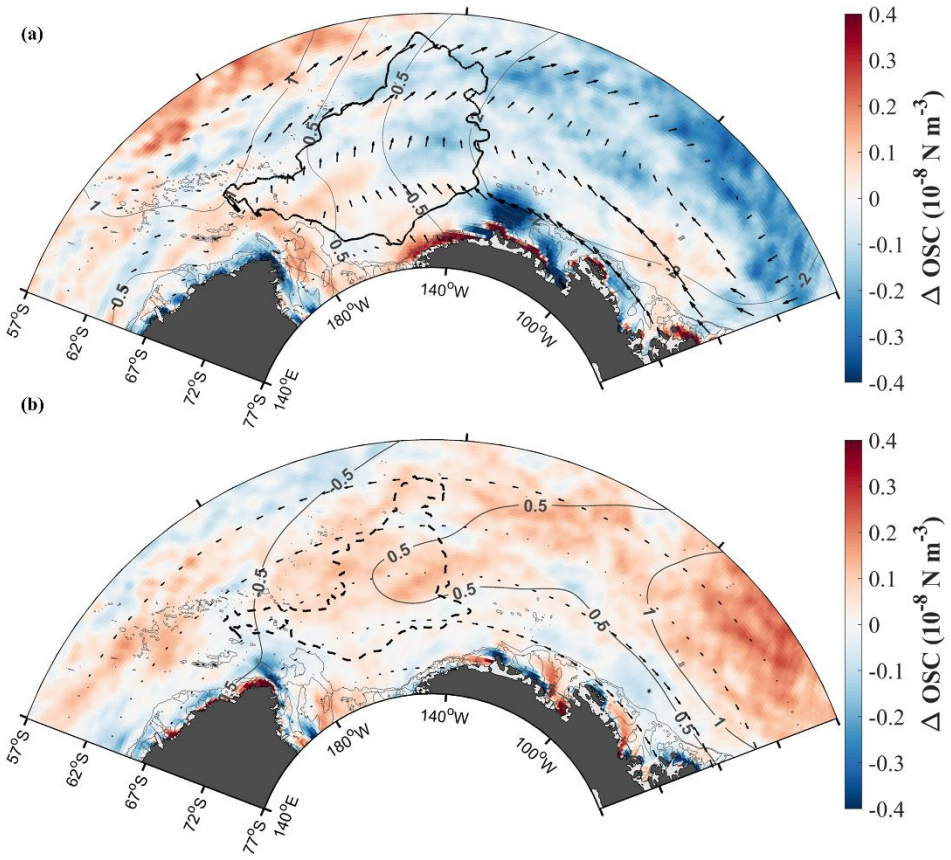


Figure 25: Atmospheric anomalies associated with Ross Gyre variability. (a) Sea level pressure (gray contours), the winds (black arrows) and ocean surface stress curl (OSC, shaded colors) anomalies (D) associated with strong Ross Gyre periods shown as a solid black line, **(b)** Same as in **(a)**, but for weak Ross Gyre periods shown as a dashed black line. Thin gray contours represent the 500 and 1,500 m isobaths from the RTopo-2 dataset [Schaffer *et al.*, 2016].

The intensified cyclonic wind forcing during strong Ross Gyre circulation periods may favour enhanced CDW Ekman-driven upwelling. This interpretation is supported by the small shoaling of the CDW core (~30 m; **Supplementary Figure 8**), which may warm the subsurface waters over the region. However, vertical heaving alone cannot explain changes in intrinsic water-mass properties. Our vertical section analysis (**Figure 26**) reveals a coherent subsurface warming signal occurring approximately along constant density surfaces, particularly between the σ_θ = 27.5 and 28 kg m^{-3} isopycnals. This warming along isopycnals suggests that, in addition to local upwelling, intensified gyre circulation may also contribute to the lateral redistribution of warmer CDW toward the Amundsen-Bellingshausen Seas. Together, these results indicate that off-shelf CDW variability during strong gyre circulation periods likely reflects a combined response involving both OSC-driven vertical exchange and lateral redistribution of subsurface

heat, consistent with previous studies which evidenced lateral heat transport modulated by the Ross Gyre [*e.g.,* Nakayama *et al.,* 2018; Prend *et al.,* 2024].

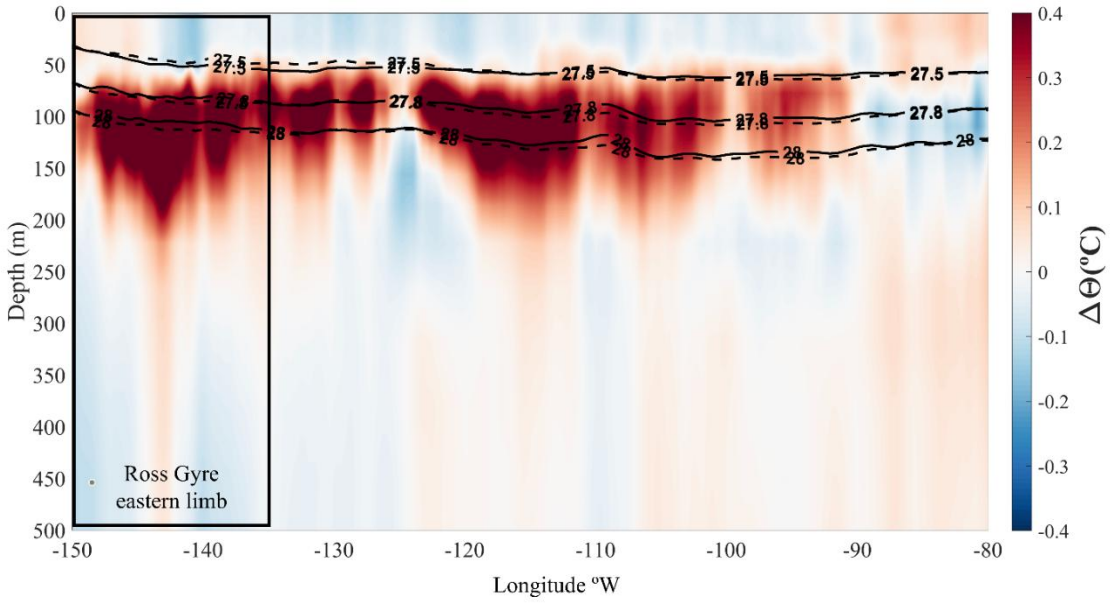


Figure 26: Cross-gyre section's composite difference in subsurface conservative temperature (ΔΘ). Θ of strong Ross Gyre period minus Θ of weak Ross Gyre periods along the cross-gyre section extending from the eastern boundary of the Ross Gyre toward the Amundsen-Bellingshausen Seas (see **Figure 1a**). Solid black contours indicate potential density anomalies (σ_θ) for stronger Ross Gyre periods, while dashed black countours indicate weaker Ross Gyre periods.

The sea level pressure anomalies observed during strong gyre circulation periods (**Figure 25a**) reflect a regional deepening characteristic of an intensified Amundsen Sea Low - ASL [Hosking *et al.,* 2013; Turner *et al.,* 2015]. Given the strong correlation identified here between cyclonic OSC and the Ross Gyre circulation strength (**Figure 22c**), such broad atmospheric changes [*i.e.,* more frequent deepening and intensification of ASL, reflecting stronger westerlies; Wang *et al.,* 2024] could lead to more occurrences of strong gyre circulation periods [*e.g.,* Hosking *et al.,* 2013]. That is supported by our trend analysis, which revealed progressively more cyclonic OSC (**Figure 27c**), suggesting an increase in the intensity and/or persistence of strong Ross Gyre circulation periods over the 1993-2020 period. This atmospheric–oceanic configuration may contribute to the progressive off-shelf warming (**Figure 27a**) and salinification (**Figure 27b**) identified in our linear trends. Consequently, the Ross Gyre likely modulates the off-shelf heat reservoir available to the Amundsen–Bellingshausen Seas, with potential downstream implications for ice-shelf basal melting. However, the extent to which this

gyre-driven off-shelf variability directly affects enhanced shelf heat transport remains uncertain, as cross-shelf exchange depends strongly on local shelf break dynamics [*e.g.*, Azaneu *et al.*, 2023; Dotto *et al.*, 2019, 2020; Nakayama *et al.*, 2018; Oelerich *et al.*, 2022; Wåhlin *et al.*, 2011, 2013; Kim *et al.*, 2017].

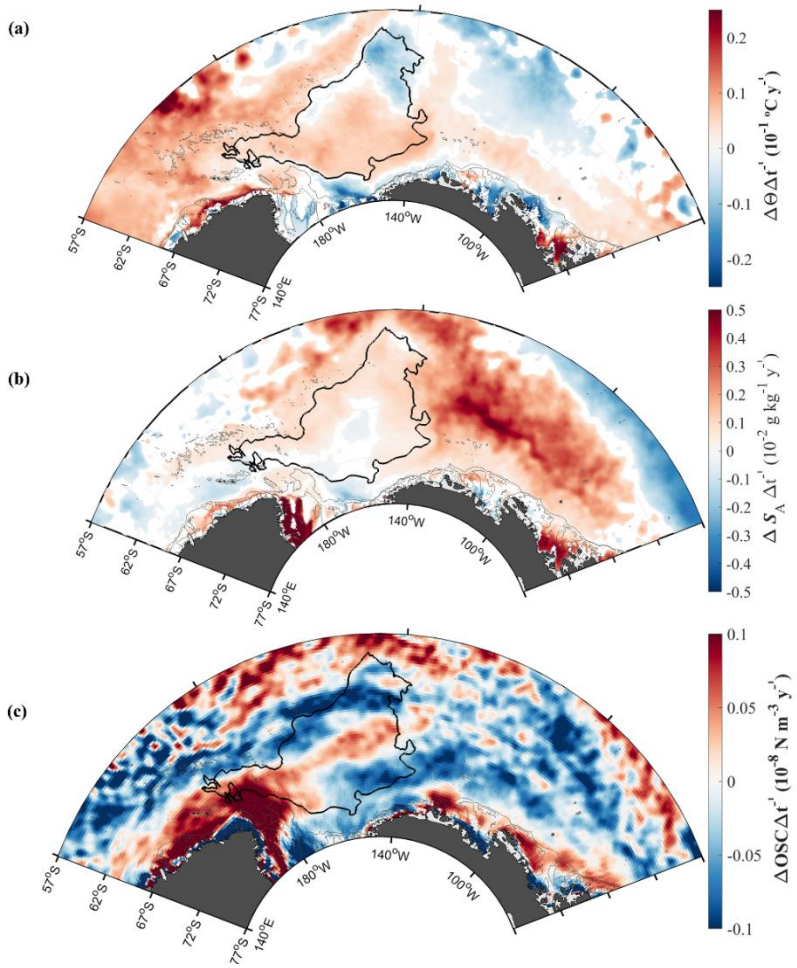


Figure 27: Temporal subsurface thermohaline properties trends with grid cells masked where not significant and atmospheric conditions forcing trends over the West Antarctica region. (a) conservative temperature (Θ), **(b)** subsurface absolute salinity (S_A) and **(c)** ocean surface stress curl (OSC) trends over the West Antarctica region. The solid black line indicates the time-mean Ross Gyre position. Thin grey contours represent the 500 m and 1,500 m isobaths from the R–Topo2 dataset [Schaffer *et al.*, 2016].

4.2.3.4 Implications for the continental shelf

Our results demonstrate that off-shelf heat storage and its transport onto the continental shelf should not be interpreted as dynamically equivalent processes. Although stronger Ross Gyre periods systematically enhance the off-shelf heat and salt reservoir in the Amundsen-Bellingshausen Seas (**Figure 24**), these thermohaline anomalies are not

uniformly advected onto the continental shelf. Instead, the continental shelf response differs substantially between the Amundsen and Bellingshausen sectors, indicating that off-shelf heat preconditioning and cross-shelf heat intrusions are dynamically distinct processes. Rather than being directly controlled by large-scale Ross Gyre variability, the advection of CDW onto the shelf appears to depend primarily on regional atmosphere-ocean interactions and shelf break processes that regulate cross-shelf exchange [*e.g.,* Azaneu *et al.,* 2023; Dotto *et al.,* 2019, 2020; Nakayama *et al.,* 2018; Oelerich *et al.,* 2022; Wåhlin *et al.,* 2011, 2013; Kim *et al.,* 2017].

To exemplify this, linear trend analyses further reveal contrasting regional tendencies between the Amundsen and Bellingshausen Seas, demonstrating the dichotomy between the two areas and the off-shelf regime. Notably, the off-shelf warming and increase in salinity during strong gyre periods did not translate into uniform shelf responses (**Figure 27**). On the Amundsen Sea shelf, subsurface waters display statistically significant cooling (**Figure 27a**) and freshening (**Figure 27b**). In contrast, the Bellingshausen Sea shelf shows significant warming (**Figure 27a**) and salinification (**Figure 27b**). These opposing trends suggest that local atmosphere-ice-ocean interactions and shelf break processes exert stronger control on heat and salt intrusions to the shelf than off-shelf gyre-driven variability. This interpretation is reinforced by the persistence of Amundsen shelf cooling and freshening even during periods of enhanced cyclonic OSC and stronger Ross Gyre circulation (**Figure 27c**).

The long-term cooling trend on the Amundsen Sea continental shelf observed here is accompanied by a weakening of subsurface warm anomalies after 2014 (**Figures 28a**). At the same time, near the entrance to Pine Island Trough East at Section 1 (**Figure 21a**), the thermocline associated with isopycnals exhibits a deepening trend of –5.3 m yr^{-1} (*p-value* < 0.01; **Figure 28c**), indicating reduced access of CDW-derived heat to the shelf. These changes are consistent with wind-driven changes at the Amundsen shelf break, where trends in OSC associated with increasingly westward winds [Dotto *et al.,* 2020] likely suppress the upward supply of CDW and promote greater retention of colder surface-derived waters, including Winter Water and Glacial Melt Water. Together, these changes imply weaker cross-shelf heat transport from the off-shelf CDW reservoir, consistent with reduced basal melting. This interpretation aligns with Christie et al. [2023], who linked the slowdown in grounding-line retreat and ice-shelf thinning during the early 2010s to an atmospheric forcing regime that limited warm-water access to the

shelf. Therefore, the persistence of cooling and freshening over the Amundsen shelf despite enhanced off-shelf CDW heat availability suggests that off-shelf heat content alone does not determine the transport of heat to the continental shelf. Instead, local shelf break dynamics likely exert more control on cross-shelf heat transport than the off-shelf heat reservoir itself.

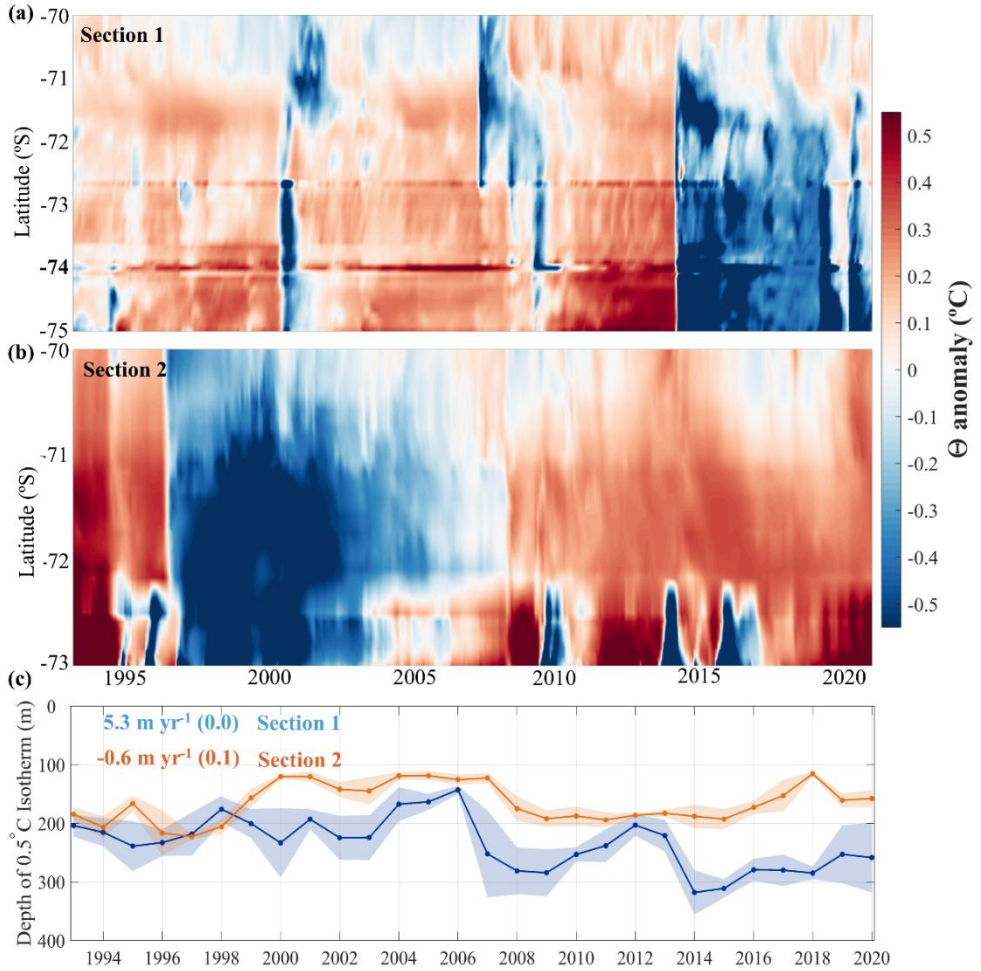


Figure 28: Variability of subsurface temperature and thermocline depth: (a, b) Hovmöller diagrams of subsurface conservative temperature anomalies (Θ) along cross-shelf sections 1 (Amundsen Sea) and 2 (Bellingshausen Sea), respectively (see **Figure 21a**). **(c)** Interannual variability of the mean thermocline depth along the continental shelf, including linear trends and corresponding *p-values* for each section. Shaded areas represent the standard deviation.

In contrast, the Bellingshausen Sea shelf exhibits hydrographic changes more consistent with transport of off-shelf subsurface anomalies onto the continental shelf. At Section 2 (**Figure 21a**), the thermocline associated with isopycnals shows a weak and not significant shoaling trend of ~ –0.6 m yr^{-1} (*p-value* = 0.1; **Figure 28c**), favouring a more direct influence of warm and saline subsurface waters on the shelf (**Figures 27a-b, 28b**

and Supplementary Figure 9b). This interpretation is further supported by the observed continental shelf warming and salinification, which is consistent with the configuration described by Christie et al. [2023], in which the Bellingshausen Sea remained under a more sustained influence of CDW than the Amundsen Sea during the 2010s. In this region, this process may be facilitated by the weak or absent Antarctic Slope Front [Thompson *et al.,* 2018] and by the closer proximity of the Southern ACC Front to the shelf break (**Figure 21a**), which would enhance the likelihood of cross-shelf CDW intrusions, potentially supported by mesoscale eddy activity [Couto *et al.,* 2017; Martinson & McKee, 2012; Moffat *et al.,* 2009]. This mechanism is also consistent with the continued dynamic thinning detected by satellite observations in the Bellingshausen sector since ~2010 [Christie *et al.,* 2023]. Together, these results indicate that the off-shelf Ross Gyre-related thermohaline anomalies do not exhibit a simple or spatially uniform synchronous expression on the continental shelf in GLORYS12v1. This suggests that Ross Gyre variability primarily preconditions the off-shelf heat reservoir, whereas the advection of that signal onto the shelf depends on regional shelf break processes.

Although GLORYS12v1 reproduces the large-scale thermohaline structure of the West Antarctic continental shelf reasonably well [*e.g.,* Damini *et al.,* under review], its limitations must be acknowledged when interpreting cross-shelf heat transport. The GLORYS12v1 does not fully resolve narrow bathymetric features such as submarine glacial troughs, which act as gateways for CDW intrusions [Oelerich *et al.,* 2022], nor does it explicitly resolve submesoscale eddy activity that facilitates shelf break exchange [Couto *et al.,* 2017; Martinson & McKee, 2012]. These limitations may lead to an underestimation of cross-shelf heat transport. However, they do not affect the robust modulation of the off-shelf heat reservoir by Ross Gyre variability demonstrated here. Rather than invalidating our results, they reinforce the interpretation that shelf break processes are strongly controlled by topography and small-scale dynamics, which regulate whether off-shelf heat anomalies can access the continental shelf.

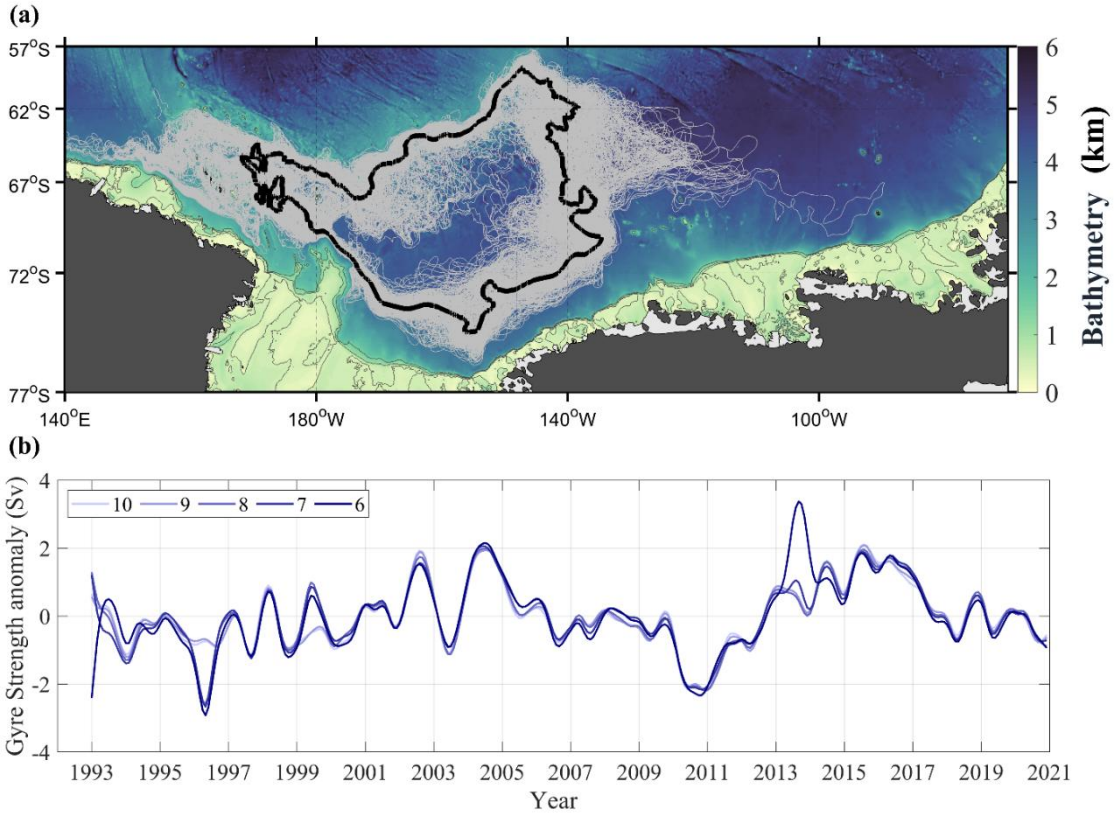
Here, we demonstrate that variability in the thermohaline properties of subsurface waters off-shelf is not intrinsically coupled to the changes observed on the continental shelf. Instead, the transport of off-shelf signals onto the shelf depends on dynamic shelf break processes. Variations in thermocline depth associated with local coastal wind forcing can intermittently suppress CDW access to the continental shelf, thereby decoupling off-shelf and continental shelf variability [Azaneu *et al.,* 2023; Dotto *et al.,*

2019, 2020; Nakayama *et al.,* 2018; Oelerich *et al.,* 2022; Wåhlin *et al.,* 2011, 2013; Kim *et al.,* 2017]. This perspective complements Gómez-Valdivia et al. [2023], who projected future continental shelf warming associated with a strengthening Ross Gyre regime. Our results indicate that off-shelf heat content alone is insufficient to predict continental shelf warming, as heat intrusions depend on shelf break exchange processes. Future projections will therefore benefit from higher-resolution models capable of resolving the small-scale processes and bathymetric troughs that govern cross-shelf heat transport.

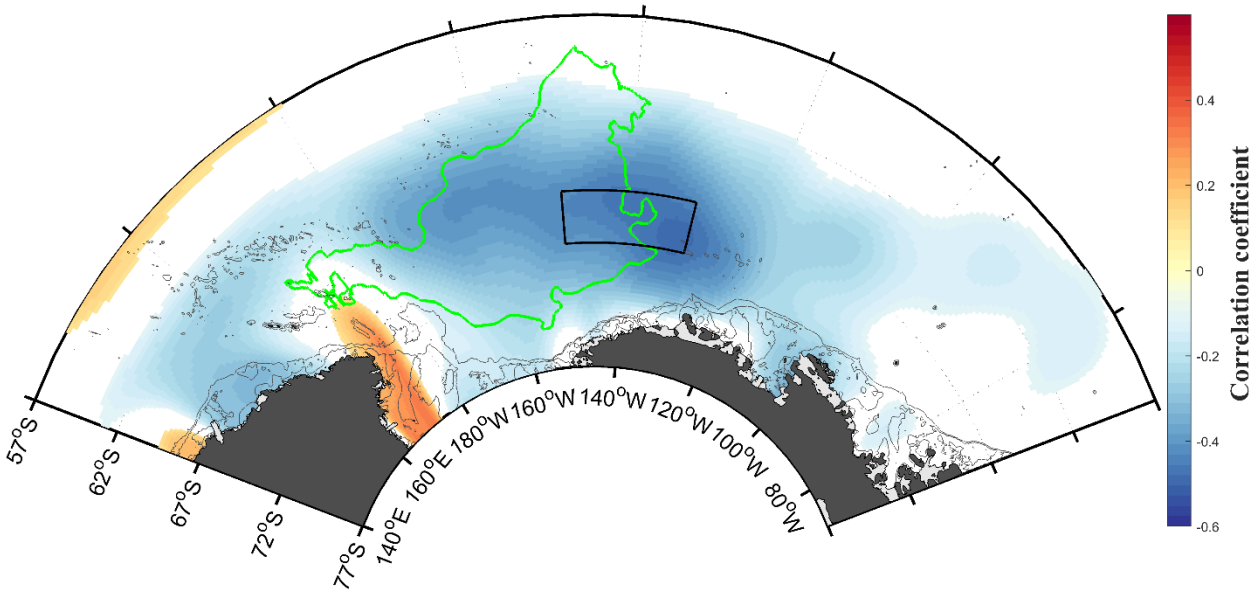
4.2.4 Concluding remarks

This study shows that the Ross Gyre variability is closely associated with cyclonic OSC variability and plays an important role in modulating the off-shelf CDW heat reservoir in the Pacific sector of West Antarctica. Using the GLORYS12v1 reanalysis, we identified a clear seasonal and interannual variability in the gyre circulation strength and area, accompanied by coherent changes in off-shelf subsurface heat and salt content. Our results further reveal that the intensification of the Ross Gyre circulation, combined with Ekman-driven upwelling, contributes to the subsurface CDW reservoir over the West Antarctica off-shelf region. Despite the enhanced off-shelf heat reservoir during strong gyre periods, these thermohaline anomalies are not uniformly advected onto the continental shelf. For example, the Amundsen shelf exhibits cooling and freshening even during periods of off-shelf warming. Together, these results suggest a dynamical decoupling between off-shelf CDW preconditioning and cross-shelf heat transport. In this sense, the Ross Gyre acts primarily as a large-scale preconditioning driver of the off-shelf heat reservoir, while regional shelf break processes likely exert a stronger influence on heat transport onto the continental shelf. Nevertheless, the long-term trends discussed here are based on the GLORYS12v1 reanalysis and should be interpreted considering the intrinsic limitations of the product. Future assessments of ocean-driven ice-sheet variability should therefore account for the combined influence of large-scale gyre variability and regional shelf break dynamics controlling CDW access to the continental shelf. Moreover, high-resolution coupled ice-ocean models that explicitly resolve troughs and shelf-break eddies will be essential to better quantify how gyre preconditioning interacts with local dynamics under continued climate change.

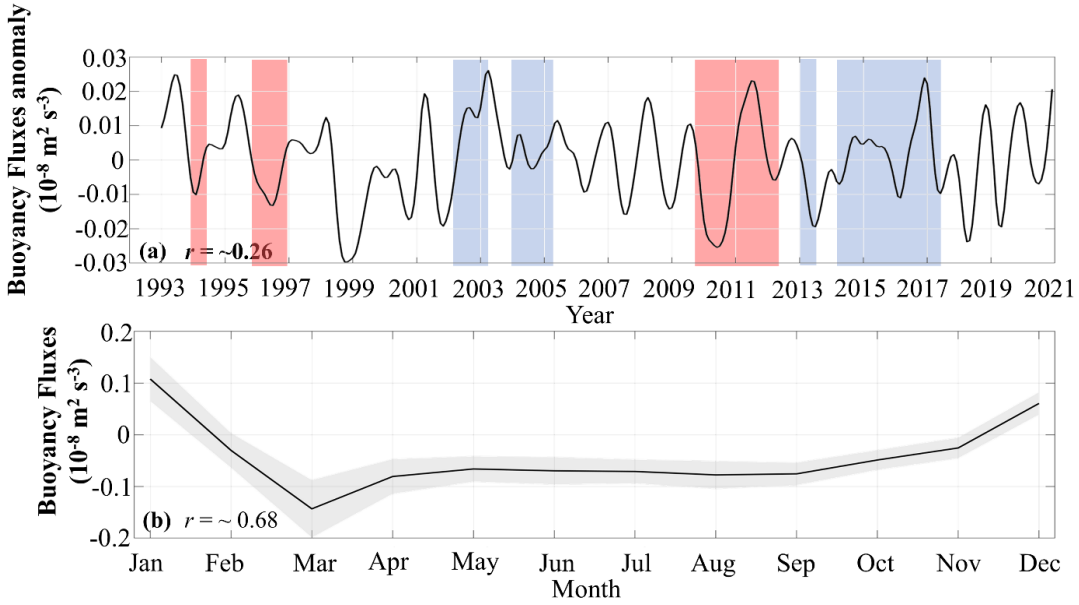
4.2.5 Supplementary information



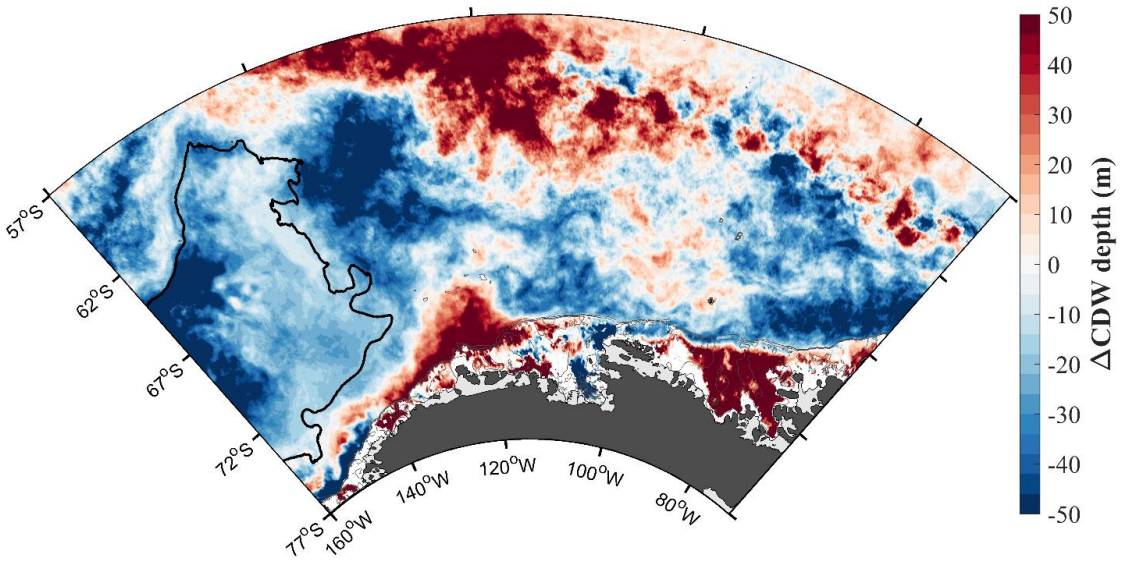
Supplementary Figure 5: Ross Gyre position and time series of gyre strength defined using the barotropic streamfunction. (a) Time-mean Ross Gyre boundary defined by the −8 Sv barotropic streamfunction closed contour (black) and all monthly −8 Sv closed contours (gray) during 1993–2020. **(b)** Ross Gyre strength time series computed using five different streamfunction contours. Although the absolute transport values vary with the selected contour, all estimates remain highly correlated with the −8 Sv-based metric ($r > 0.9$).



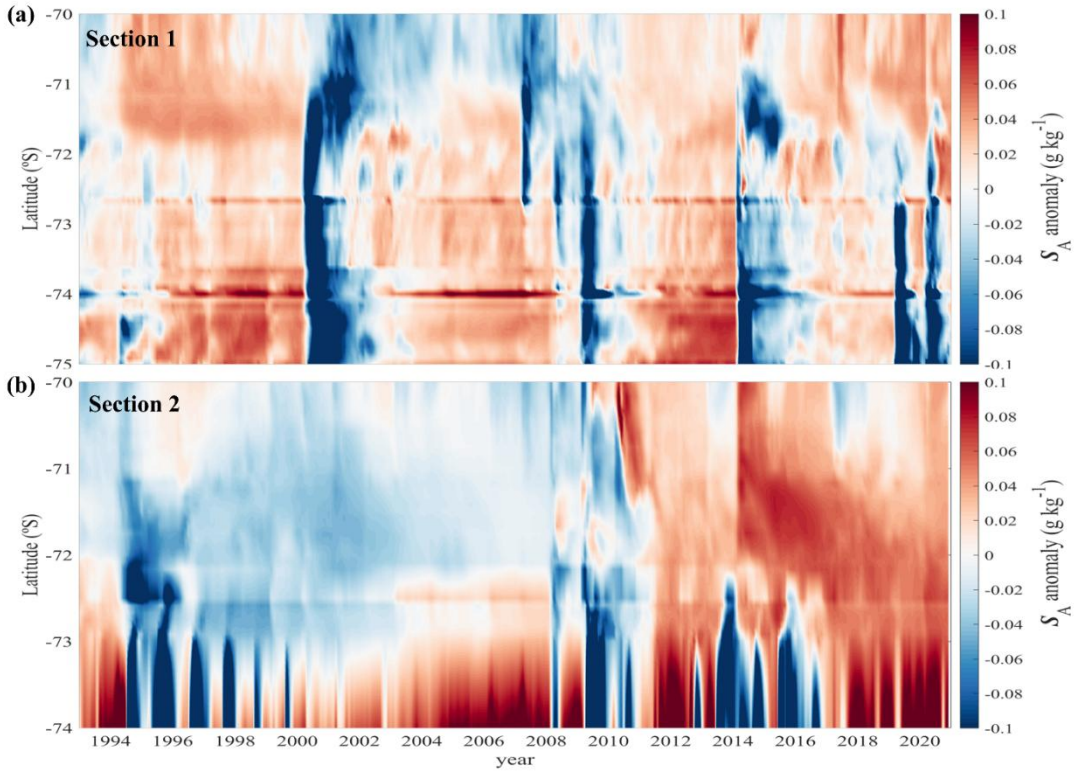
Supplementary Figure 6: Correlation coefficient between the gyre strength, defined as the mean value of the barotropic streamfunction within the −8 Sverdrup contour, and ocean surface stress curl in each grid cell. The green contour indicates the mean gyre boundary. Blank areas denote regions where the correlation is not statistically significant. The black box marks the region of highest correlation, interpreted here as the area that most strongly forces the gyre. The ocean surface stress curl averaged over this region is shown in **Figures 23c and 24c**.



Supplementary Figure 7: Interannual and seasonal variability of Buoyancy fluxes. **(a)** Interannual buoyancy fluxes time-series averaged at the continental shelves off Ross Sea. Red and blue rectangles denote strong and weak gyre periods, respectively, defined as periods when gyre strength anomalies exceed ±1 standard deviation relative to the detrended mean, and used for the composite analysis. **(b)** Seasonal buoyancy fluxes time-series averaged at the continental shelves off Ross Sea. The correlation coefficient between gyre strength and buoyancy fluxes interannual and seasonal, corresponding panel.



Supplementary Figure 8: Composite difference (Δ) of the core of CDW layer depth between strong and weaker Ross Gyre periods. Positive (negative) anomalies indicate downwelling (upwelling) of the warm CDW layer during intensified gyre circulation. The solid black line shows Ross Gyre's time-mean position. Thin grey contours represent the 500 m and 1,500 m isobaths from the R-Topo2 dataset [Schaffer *et al.*, 2016].



Supplementary Figure 9: Hovmöller diagrams of subsurface thermohaline variability and thermocline depth along the Amundsen and Bellingshausen shelf sections: (a) Absolute Salinity, S_A (g kg^{-1}), along Section 1 in the Amundsen Sea; **(b)** same as in **(a)**, but along Section 2 in the Bellingshausen.

4.3 Circulação de verão e transporte de massas d'água no estreito de Bransfield, Antártica: avaliação da resposta aos efeitos combinados do SAM e do ENSO

O manuscrito, de autoria de Brendon Yuri Damini, André L. Brum, Rob A. Hall, Tiago S. Dotto, José Luiz L. Azevedo, Karen J. Heywood, Mauricio M. Mata, Carlos A. E. Garcia e Rodrigo Kerr, intitulado "Summer circulation and water masses transport in Bransfield Strait, Antarctica: An evaluation of their response to combined effects of Southern Annular Mode and El Niño–Southern Oscillation", foi publicado no periódico *Deep-Sea Research Part I* (Damini *et al.*, 2025 – disponível em https://doi.org/10.1016/j.dsr.2025.104516). Em síntese, o estudo caracteriza o padrão de circulação ciclônica no estreito de Bransfield durante o verão, destacando a atuação da BC em direção nordeste ao longo das Ilhas Shetland do Sul até a Ilha Elefante, e da Corrente Costeira Antártica em direção sudoeste, entrando na região próxima de 62,40°S e 55,00°W. Os resultados, a partir de dados do GLORYS12v1 e de altimetria, mostram que parte da BC deixa a bacia leste entre as ilhas Rei George e Clarence, além de evidenciar uma recirculação ao redor das Ilhas Shetland do Sul. O estudo também fornece a primeira estimativa robusta, de longo período, do transporte de TBW entre as ilhas Rei George e Elefante, evidenciando mais uma rota de fornecimento dessa massa de água para a BC. Além disso, os resultados revelam que a intensidade desse transporte está associada à variabilidade dos modos climáticos de grande escala, sendo modulada pela ação combinada do Modo Anular do Sul e do *El Niño*–Oscilação Sul, expressa pelo índice combinado SEI. Em anos com condições negativas de SEI, o transporte médio de TBW para o interior do estreito é de 0,10 Sv, enquanto em anos com condições positivas esse transporte aumenta para 0,31 Sv. Esses achados contribuem para o entendimento dos mecanismos que controlam a circulação regional e suas implicações sobre as propriedades físicas e biogeoquímicas do estreito de Bransfield. As seções principais do manuscrito são apresentadas a seguir.

4.3.1 Introduction

Bransfield Strait is a semi–closed region in the northern Antarctic Peninsula, situated between the South Shetland Islands and Antarctic Peninsula (**Figure 29**). It is

considered a key area for studying the impacts of climate change due to its transitional environment connecting waters from the cold shelf regime of the northwestern Weddell Sea with the relatively warm oceanic regime of the Bellingshausen Sea [*e.g.,* Wilson *et al.,*1999; Gordon *et al.,*2000; Heywood *et al.,*2004; Dotto *et al.,*2016; Kerr *et al.,*2018a; Damini *et al.,*2022].

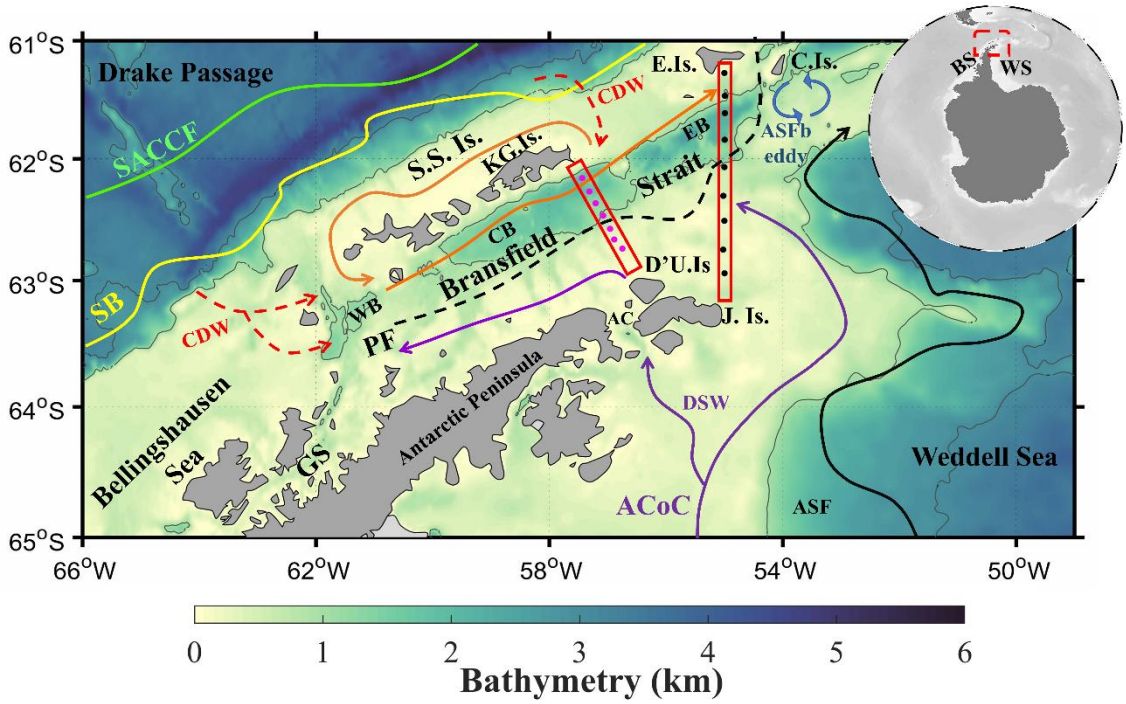


Figure 29: Schematic representation of the mean circulation at the Northern Antarctic Peninsula. The red (purple) arrows represent the pathways of the Circumpolar Deep Water (Dense Shelf Water) entering Bransfield Strait. The green and yellow lines indicate the mean locations of the Southern Antarctic Circumpolar Current Front (SACCF) and Southern Boundary of Antarctic Circumpolar Current (SB), respectively. Light blue arrows indicate Antarctic Slope Front bifurcation (ASFb) eddy. The orange arrows depict Bransfield Current and its recirculation around the South Shetland Islands (S.S.Is.). The black line represents the mean location of the Antarctic Slope Front (ASF). The red rectangles bounding the magenta and black dots depict hydrographic Sections 1 and 2, respectively. The black dashed line represents the Peninsula Front (PF). The acronyms stand for: Antarctic Channel (AC), Antarctic Coastal Current (ACoC), Joinville Island (J.Is.), D'Urville Island (D'U.Is.), Elephant Island (E. Is.), Clarence Island (C. Is.), Bellingshausen Sea (BS), Drake Passage (DP), Weddell Sea (WS), Western Basin (WB), Central Basin (CB), Eastern Basin (EB), and Gerlache Strait (GS). The thin gray lines indicate the 0.10 km and 0.30 km isobaths provided by *https://www.scar.org/science/ibcso/ibcso/*. The inset panel depicts the region study. Modified from Damini *et al.,* [2022].

In this context, several authors have reported significant changes in Bransfield Strait, particularly in the physical and biogeochemical of the water masses in the region

[*e.g.,* Dotto *et al.,*2016; Avelina *et al.,*2020; Ferreira *et al.,*2020; Damini *et al.,*2022; Santos-Andrade *et al.,*2023]. For instance, cooling, freshening, and lightening have been documented from the 1960s to 2000s [*e.g.,* Wilson *et al.,*1999; Azaneu *et al.,*2013; Dotto *et al.,*2016; Ruiz Barlett *et al.,*2018; Damini *et al.,*2022], likely contributing to the dilution of total alkalinity and dissolved inorganic carbon concentration reported from 2000 to 2010 [Santos-Andrade *et al.,*2023]. However, since the 2010s, Bransfield Strait experienced signals of warming and salinification, which led to an increase in total alkalinity and dissolved inorganic carbon concentration [Dotto *et al.,*2016; Damini *et al.,*2022; Santos-Andrade *et al.,*2023]. This variability in water masses properties influences biological activity, such as phytoplankton succession [Mendes *et al.,*2018; Costa *et al.,*2020], and consequently affects the sea-air CO_2 exchanges in the region [Ito *et al.,*2018].

The circulation within Bransfield Strait comprises two main surface–subsurface currents: a northeastward jet, the Bransfield Current, which transports waters from the Bellingshausen Sea mixed with Circumpolar Deep Water – CDW (hereafter referred to as Transitional Zonal Water with Bellingshausen Sea influence – TBW) along the southern slope of the South Shetland Island; and the southwestward jet, the Antarctic Coastal Current, a coastally–trapped current which borders the northern slope of the Northern Antarctic Peninsula and advects Weddell Sea sourced waters (hereafter referred to as Transitional Zonal Water with Weddell Sea influence – TWW) [Fig. 1; *e.g.,* Hofmann *et al.,*1996; von Gyldenfeldt *et al.,*2002; Heywood *et al.,*2004; Sangrà *et al.,*2011, 2017; Collares *et al.,*2018; van Caspel *et al.,*2018]. These boundary current jets are separated along Bransfield Strait by a surface thermal front known as the Peninsula Front (marked by the black dashed line in **Figure 29**). This shallow mesoscale structure is considered a crucial factor affecting regional circulation, with its position modulated by the variability of water masses in Bransfield Strait [Sangrà *et al.,*2011, 2017].

CDW is characterized by relatively warm, saline, low-oxygen, and nutrient and carbon–rich intermediate waters advected by the Antarctic Circumpolar Current [ACC; Martinson & McKee, 2012]. Along the western Antarctic Peninsula continental shelf, CDW upwells to within 150–300 m of surface and mixes with waters from the Bellingshausen Sea, forming the TBW [Orsi et al 1995], which subsequently intrudes into Bransfield Strait [Gordon *et al.,*2000]. The primary pathways for TBW intrusions into Bransfield Strait are: (i) between the South Shetland Islands, south of the western basin

[Wessel & Smith, 1996], (ii) south of Drake Passage between King George and Elephant Islands [Hofmann *et al.,*1996], and (iii) through Gerlache Strait [Niller *et al.,*1991].

TWW is characterized by relatively cold and saline shelf waters advected by the Antarctic Coastal Current from the Weddell Sea into Bransfield Strait via the Antarctic Sound and at the north of Joinville Island [Gordon *et al.,*2000; Sangrà *et al.,*2011, 2017; Collares *et al.,*2018]. Once it reaches Bransfield Strait, TWW sinks through several canyons along the continental shelf [Lopez *et al.,*1999]. Furthermore, the topographic features of Bransfield Strait facilitate the partitioning of the flow into three deep basins (western, central, and eastern) separated by relatively shallow sills. These sills help preserve the thermohaline properties of TWW in the deeper layer [Wilson *et al.,*1999], in its purest form in the central basin [Dotto *et al.,*2016; Damini *et al.,*2022]. This makes Bransfield Strait an ideal proxy region for studying the structure, variability, and trends of Weddell Sea shelf waters [Dotto *et al.,*2016], an essential source of Antarctic Bottom Water [Kerr *et al.,*2018b].

The ACC plays a critical role in advecting CDW onto the Antarctic continental shelf, contributing to the formation of TBW, which is subsequently transported into Bransfield Strait. The ACC transport is concentrated in a series of well–defined fronts (*i.e.,* Subantarctic Front, Polar Front, and Southern ACC Front – SACCF). Each of these fronts has distinct temperature and salinity gradients and their positions are influenced by wind pattern variability and associated climate modes [*i.e.,* Southern Annular Mode – SAM and El Niño–Southern Oscillation – ENSO; Marshall *et al.,*2003; Renner *et al.,*2012]. In recent decades, the ACC fronts have migrated poleward [*e.g.,* Yamazaki *et al.,*2021], which resulted in an increase in eddy kinetic energy [*e.g.,* Hogg *et al.,* 2015; Martínez-Moreno *et al.,* 2022]. This poleward migration could lead to greater CDW inflow onto the Antarctic continental shelf, such as Bransfield Strait [*e.g.,* Dotto *et al.,*2016; Damini *et al.,*2022; Ruiz Barllet *et al.,* 2018] and/or could also promote the formation of eddies shed by the ACC towards the West Antarctic Peninsula [Martinson & McKee, 2012; Couto *et al.,*2017]. Moreover, the enhancement of CDW transport in these areas contributes to greater ice–mass loss due to the basal melt of ice shelves [Cook *et al.,*2016], leading to an increase in freshwater input to the ocean [Rott *et al.,*2018].

Observations have shown that the positive phase of SAM (SAM+) leads to an intensification and poleward shift of the westerly winds over the Southern Ocean [*e.g.,*

Thompson & Solomon, 2002], causing a poleward shift of SACCF [*e.g.,* Yamazaki *et al.,*2021]. This is believed to intensify the intrusion of TBW [Ruiz Barlett *et al.,*2018] while weakening the inflow of TWW [Dotto *et al.,*2016; Damini *et al.,*2022] into Bransfield Strait. Conversely, the negative phase of SAM (SAM–) leads to a decrease and equatorward shift of the westerly winds over the Southern Ocean, causing an equatorward shift of SACCF, which intensifies the intrusion of TWW and weakens the inflow of TBW into Bransfield Strait [Marshal *et al.,*2003; Renner *et al.,*2012; Dotto *et al.,*2016; Damini *et al.,*2022]. Previous studies showed that the positive phase of ENSO (ENSO+) and negative phase of ENSO (ENSO–) induce similar circulation patterns to SAM– and SAM+, respectively [*e.g.,* Yuan, 2004, 2018; Loeb *et al.,*2010; Ruiz Barlett *et al.,*2018]. Therefore, when both modes are in phase, *i.e.,* during ENSO– and SAM+ or ENSO+ and SAM–, TBW advection into Bransfield Strait is intensified or weakened, respectively [*e.g.,* Damini *et al.,*2022].

Although Bransfield Strait plays a crucial role in water mass exchange between the Bellingshausen and Weddell Seas [*e.g.,* Gordon *et al.,*2000; Thompson *et al.,*2009], few studies have focused on its long–term circulation system and the temporal variability of water masses transport rates through this circulation system [Veny *et al.,*2022; Wang *et al.,*2022; Gordey *et al.,*2024]. This study re–examines the austral summer surface–subsurface circulation in Bransfield Strait using a long–term and high-quality hydrographic dataset spanning 2003 to 2019, provided by the Brazilian High Latitude Oceanography Group [GOAL; Mata *et al.,*2018]. The analysis also incorporates altimetry data and the global eddy-resolving ocean reanalysis product GLORYS12v1 [Jean-Michel *et al.,*2021]. In particular, we focus on the volume transport rates and temporal variability of water masses in the region under the combined effects of SAM and ENSO climate modes. Understanding the circulation in this dynamic region is crucial as it directly affects the physical processes, the distribution of biogeochemical properties and, consequently, the local biota and ecosystem connections.

4.3.2 Data and Methods

4.3.2.1 Hydrographic data

The hydrographic measurements were obtained during austral summers from 2003 to 2019 (**Figure 30**). During that period, two hydrographic sections in Bransfield

Strait were occupied 17 times with Conductivity-Temperature-Depth (CTD) profiles with 1 dbar of vertical resolution (**Figure 29**). Section 1 was located between King George and D'Urville Islands (indicated by a red rectangle bounding the magenta dots in **Figure 29**), while Section 2 was situated between Elephant and Joinville Islands (a red rectangle bounding the black dots in **Figure 29**). The conservative temperature (Θ, ^{o}C) and absolute salinity (S_A, g kg^{-1}) were computed using the International Thermodynamic Equation of Seawater – 2010 (TEOS – 10) [McDougall *et al.*,2009]. The reader is referred to Dotto *et al.*, [2021] for more details about the GOAL hydrographic measurements used here.

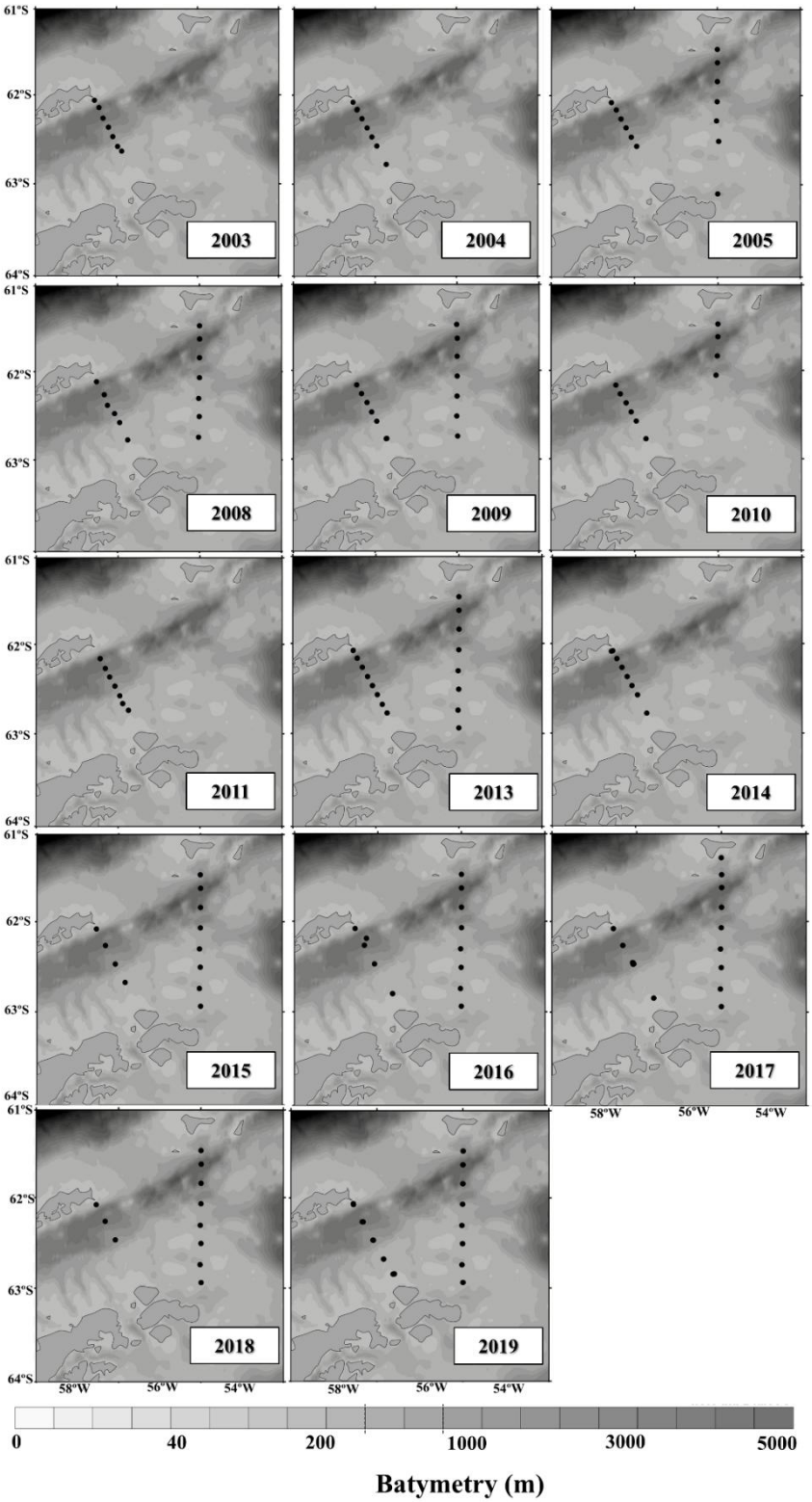


Figure 30: Hydrographic CTD measurements positions across the two repetitive sections over 2003–2019.

4.3.2.2 Geostrophic velocities estimates by hydrographic data

Cross–section geostrophic ocean current velocities were computed, referencing the shear to a level of no motion at 500 m, following other studies carried out in this

region [*e.g.,* Grelowski *et al.,*1986; Gomis *et al.,*2002; Sangrà *et al.,*2011, 2017]. It seems that 500 m could be a good choice for the reference level, as only small areas of these sections extend beyond this depth. Additionally, the slope of the isopycnals at depths greater than 500 m is less pronounced (**Figure 31**), suggesting minimal contribution from deep layers to the upper geostrophic velocities. This choice therefore reduces the uncertainty associated with the selection of the no motion level. Furthermore, one of the main currents, the Bransfield Current, located along the edge of the South Shetland Islands is essentially confined to the upper 500 m (**Figure 32**). Mukhametyanov *et al.,* [2022], tested different reference levels to calculate volume transports in the Bransfield Strait and compared their results with those obtained using a lowered current profiler. They reported that the 500 m reference level accounts for more than half of the lowered current profiler transport.

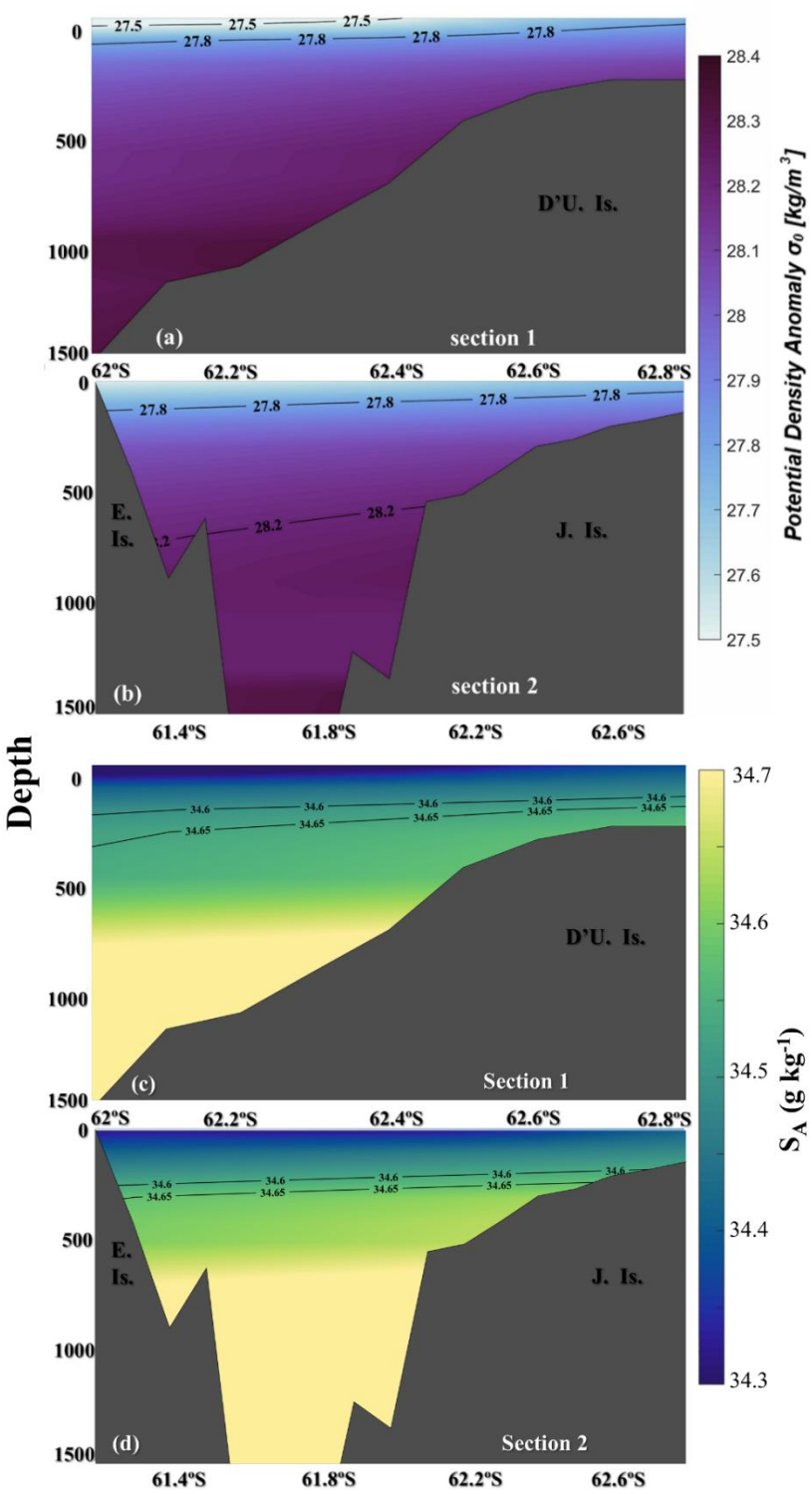


Figure 31: Time–averaged (2003–2019) of potential density anomaly (σθ in kg m^{-3}) and Absolute Salinity (S_A g kg^{-1}) within Bransfield Strait system **(a)** and **(c)** for Section 1, between King George and D' Urville Island (D' U. Is.), and **(b)** and **(d)** for Section 2 between Elephant (E. Is.) and Joinvile Islands (J. Is.).

The hydrographic properties (*i.e.,* Θ and S_A) and geostrophic velocities along the cross-sections were gridded onto 0.05º of latitude spanning from the first to the last measurement profiles along each year's section. Each grid was 2–D interpolated using a

radial basis function with a linear weighting, and the smoothing factor related to the magnitude of signal noise, set to 0.1. The radial basis function interpolation method was chosen for its flexibility in adapting to the spatial structure of the data, making it particularly effective for irregular or sparse datasets. We decided to apply an interpolation method to allow us to calculate the time–average over the entire period since we have spatial data gaps in certain years.

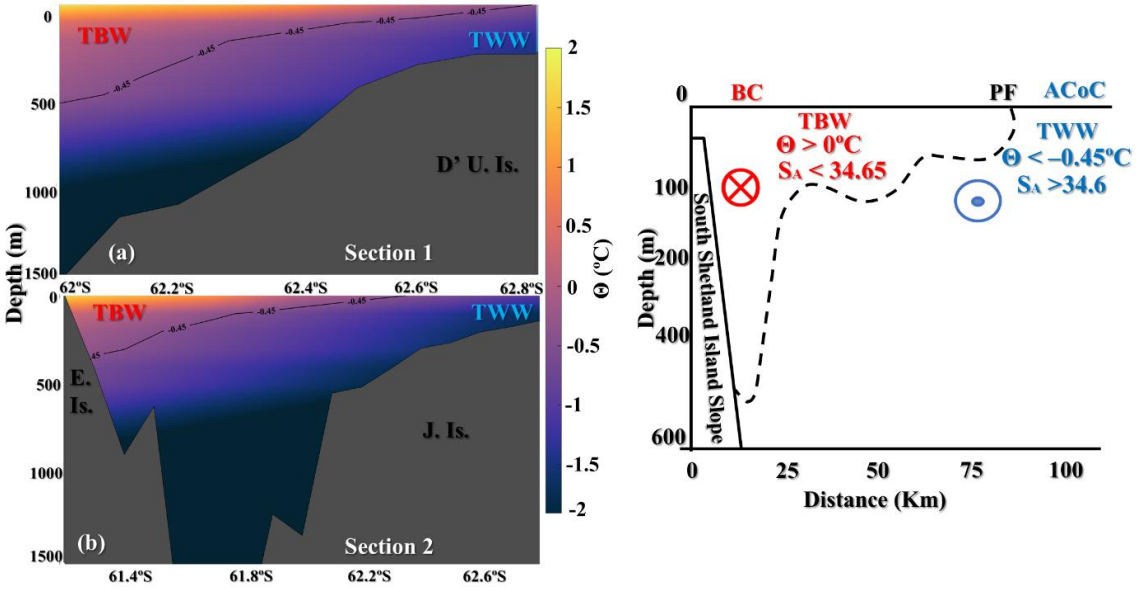


Figure 32: Time–averaged (2003–2019) of conservative temperature (Θ in ºC) within Bransfield Strait system for **(a)** Section 1, between King George and D' Urville Island, and **(b)** Section 2 between Elephant and Joinvile Islands. Scheme modified from Sangrà *et al.,* [2011] of the main components of the Bransfield Strait system along the section crossing of the strait (South Shetland Islands to Antarctic Peninsula) is depicted in **(c)**. The red ⊗ indicates a flow into the page (*i.e.,* northeastward flow), while the blue circle indicates a flow leaving the page (*i.e.,* southwestward flow). The acronyms stand for: Antarctic Coastal Current (ACoC), Bransfield Current (BC), Transitional Zonal Water with Bellingshausen influence (TBW), Transitional Zonal Water with Weddell influence (TWW), and Peninsula Front (PF). The topographic feature along the sections is shown in black and is based on IBCSO v1.0 data (https://www.scar.org/science/ibcso/ibcso/).

4.3.2.3 Surface geostrophic circulation by satellite altimetry

The surface geostrophic circulation in the study area is derived from the Global Ocean Gridded L4 Sea Surface Heights and Derived Variables Reprocessed dataset (DOI:10.48670/moi-00145), accessible through the Copernicus Marine Environment Monitoring Service (CMEMS; data.marine.copernicus.eu). The surface geostrophic

velocities derived from this dataset have a spatial resolution of 0.25º and were used for comparison with geostrophic velocities calculated from hydrography. Additionally, relative vorticity was calculated $\zeta_z = \partial v/\partial x - \partial u/\partial y$, where u and v are zonal and meridional components of the current velocity field, respectively.

4.3.2.4. Water mass transport calculation by GLORYS12v1 output

GLORYS12v1 is a global eddy-resolving physical ocean and sea ice reanalysis with 1/12º horizontal resolution and 50 standard vertical levels. It covers the period from 1993 to the present, is based on the Nucleos for European Modelling of the Ocean platform (NEMO), and is atmospherically forced with ERA–Interim (https://www.ecmwf.int/en/forecasts/dataset/ecmwf-reanalysis-interim). Quality assessments have shown that GLORYS12v1 effectively captures the main interannual climate variability signals for the ocean and sea ice [Jean-Michel *et al.*,2021]. Additionally, it effectively captures the low-frequency variability of the sea ice extent in the Arctic and Antarctic Oceans [Jean-Michel *et al.*,2021]. The GLORYS12v1 bathymetry is based on ETOPO1 for the deep ocean and GEBCO8 for the coast and continental shelf but does not include ice shelf cavities [Jean-Michel *et al.*,2021].

We select thermohaline properties and velocity field (*i.e.,* with barotropic and baroclinic components) output from GLORYS12v1, corresponding to the same months as the hydrographic measurements. After that, we computed the Θ and S_A from GLORYS12v1 using the same methodology applied to the hydrographic dataset. Then, summer averages (January–March) of Θ, S_A and velocity were calculated. These averaged fields were used to estimate the volume transport of water masses (Sv; 1 Sv = 10^6 m^3 s^{-1}) across the mean positions of the two sections previously analyzed using hydrographic measurements. To achieve this, velocities perpendicular to each section were computed. Water mass transport across each section was computed by area–integrating the velocities within their respective layers, defined by Θ and S_A: Transitional Zonal Water with Bellingshausen influence (TBW, $\Theta > 0$ °C and $S_A < 34.65$ S_A, g kg^{-1}) and Transitional Zonal Water with Weddell influence (TWW, $\Theta < -0.45$°C and $S_A > 34.60$ S_A, g kg^{-1}), following criteria established in previous studies [*e.g.,* Huneke *et al.*,2016; Morozov *et al.*,2021; Gordey *et al.*,2024]. To further investigate water mass transport variability in the northern Antarctic Peninsula, we computed the average thickness of CDW layer, defined by $\Theta > 0$ °C and 34.60 g $kg^{-1} < S_A > 34.92$ g kg^{-1}. This analysis reveals the

vertical distribution of CDW and its influence on regional water mass circulation. It is worth mentioning that the use of higher-resolution models would likely lead to more accurate transport estimations, besides providing a better representation of small- and mesoscale processes. Such processes facilitate the upwelling of CDW onto the continental shelf [*e.g.,* Moffat *et al.,* 2009; Boeira Dias *et al.,* 2023] and could affects the TBW transports into the Bransfield Strait. For instance, Ong *et al.,* [2024], showed that eddy activity in cross-slope exchanges is significantly enhanced in models with resolutions higher than 1/20°.

The summer–averaged hydrographic measurements spanning the full study period (2003–2019) were utilized to validate GLORYS12v1 output. To achieve this, we gridded the hydrographic measurements onto the same grid of the reanalysis. Furthermore, for both datasets, the averaged thermohaline properties profile of the two analyzed sections were calculated to evaluate the difference between the datasets.

4.3.2.5. Ancillary data sets

The wind patterns around the Antarctic Peninsula, and consequently the circulation of Bransfield Strait (*i.e.,* intrusion of TBW and TWW in the region), are influenced by both ENSO and SAM [*e.g.,* Dotto *et al.,*2016; Ruiz Barlett *et al.,*2018; Damini *et al.,*2022]. In this study, we seek to understand the combined effects of summer SAM (https://legacy.bas.ac.uk/met/gjma/sam.html) and summer ENSO (https://origin.cpc.ncep.noaa.gov/products/analysis_monitoring/ensostuff/ONI_v5.php) on winds in the Antarctic Peninsula and their subsequent impact on Bransfield Strait's circulation. Therefore, we employed the summer SEI index (https://zenodo.org/records/7500163; **Figure 33**) to account for the combined effects of the SAM and ENSO indices. In summary, the indices SEI+ (values > 0.50) and SEI– (values < –0.50) represent combinations of SAM+ with ENSO– and SAM– with ENSO+ periods, respectively [for more details, please see Llanillo *et al.,*2023]. The average positions of SAACF during SEI+ and SEI– years conditions were derived from Argo float temperature profiles from 2004 to 2019 (https://sio-argo.ucsd.edu/RG_Climatology.html) using the 1.80 ºC isotherm at 500 m [Orsi *et al.,*1995].

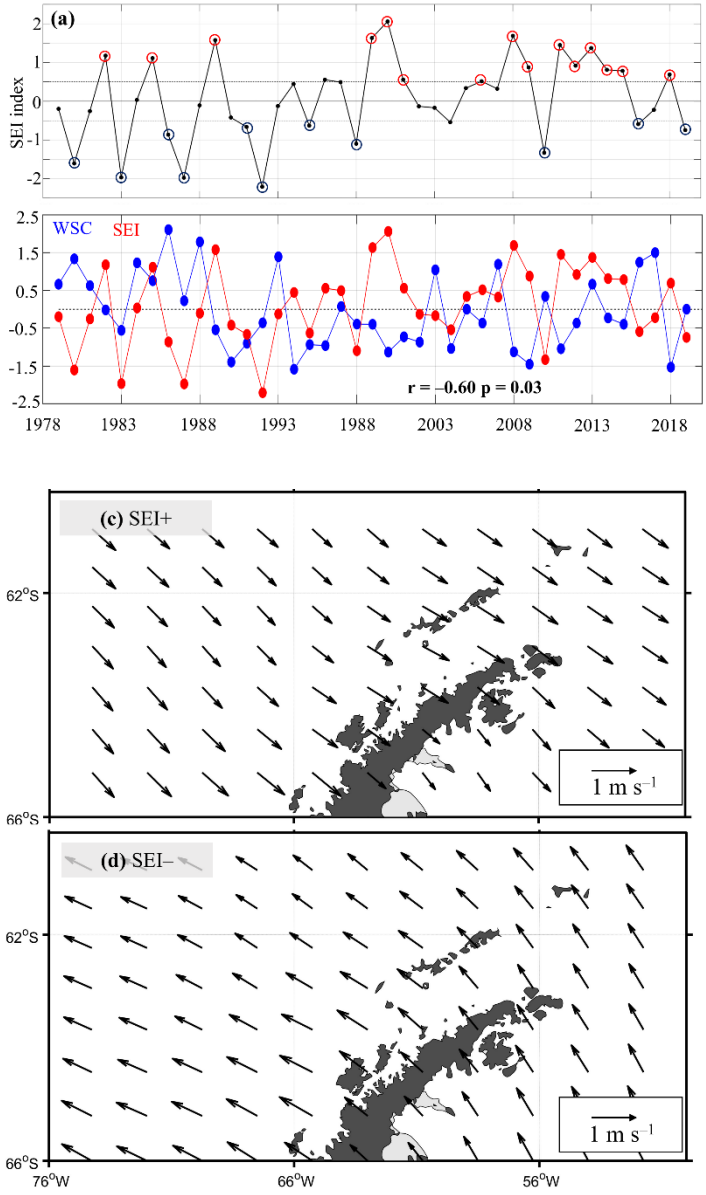


Figure 33: (a) Temporal evolution of the Southern Annular Mode-El Niño-Southern Oscillation (SEI) indices during austral summer periods (January–March) from 1979 to 2019. The red circles represent the SEI+ years, while the blue circles indicate the SEI– years. **(b)** The correlations between the normalized and detrended summer wind stress curl (WSC) over the northern Antarctic Peninsula and the summer SEI indices are presented, with the Spearman's correlation coefficient (r) and p-value (p) indicating the coefficient and statistical significance of the relationship, respectively. The summertime (January–march) composite maps of the anomaly of 10–m wind vector (black arrows), where **(c)** represents the average of yearly wind anomaly patterns during SEI + periods, and **(d)** represents the average of yearly wind anomaly patterns during SEI– periods. The yearly anomaly wind pattern was calculated from the time-average over the full period (1979-2019) minus each year's wind pattern.

Following Veny *et al.*,[2024], the average of the summertime (January–March) wind stress curl and Ekman vertical velocity were calculated from monthly averaged wind

velocity from the European Centre for Medium–Range Weather Forecast Reanalysis – Interim [ERA – Interim; https://www.ecmwf.int/en/forecasts/dataset/ecmwf-reanalysis-interim; Dee *et al.,*2011], which has a horizontal resolution of 0.70 x 0.70º over the period 1979 to 2019. Anomalies of wind stress curl was calculated by subtracting the time–average over the full period (January–March, 2003–2019) from the average of each SEI period analyzed (*i.e.,* SEI+ and SEI–). In addition, the Spearman's correlations between the normalized and detrended wind stress curl over the northern Antarctica Peninsula and SEI indices were tested from 1979 to 2019.

4.3.3 Results and Discussion

4.3.3.1 The Bransfield Strait Circulation System in the Central and the Eastern Basin

4.3.3.1.1 Subsurface circulation derived from hydrography

Bransfield Strait's circulation is characterized by a cyclonic circulation pattern consisting of two major inflows, namely the Bransfield Current and Antarctic Coastal Current, as depicted in the annual velocities (**Figures 34 and 35**) as well as time–averaged velocity field (*i.e.,* mean of 14 years to section 1 and mean of 10 years to section 2; **Figure 36a–d**). The Bransfield Current, a northeastward flow, moves along the southern slope of the South Shetland Islands towards Elephant Island. The core of this flow has a time–averaged velocity of 10 ± 4 cm s^{-1} at the surface layer in Section 1, and 14 ± 2 cm s^{-1} at 100 m depth in Section 2 (**Figures 36a–d**). The velocities decrease towards the bottom at each section (**Figures 36a–b**). In contrast, the Antarctic Coastal Current is a southwestward flow along the northern slope of the northern Antarctic Peninsula. This flow reaches an average velocity of –5 ± 4 cm s^{-1} and –7 ± 2 cm s^{-1} at 100 m of depth in Sections 1 and 2, respectively (**Figures 36a–d**).

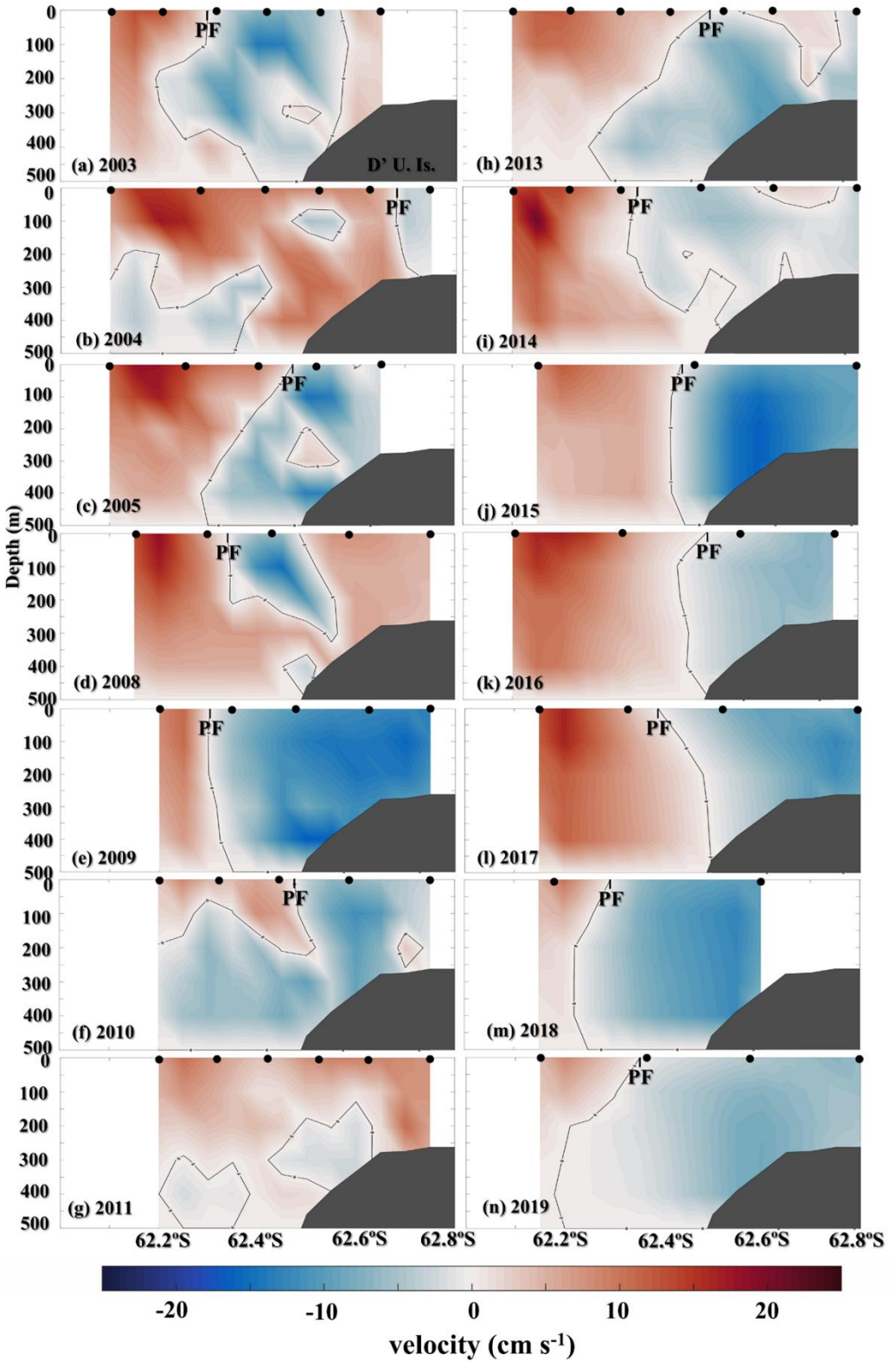


Figure 34: Annual cross–section geostrophic velocities at Section 1, between King George and D' Urville Islands (D' U. Is). Positive velocities correspond to Bransfield Current, while negative values indicate Antarctic Coastal Current. The thin black lines indicate the 0 m s^{-1} isolines of velocity. The position of the Peninsula Front (PF) is indicated by the black line on each panel. Black dots indicate the locations of the geostrophic current profiles. Topographic features along the sections are shown in black and are based on

IBCSO v1.0 data (https://www.scar.org/science/ibcso/ibcso/).

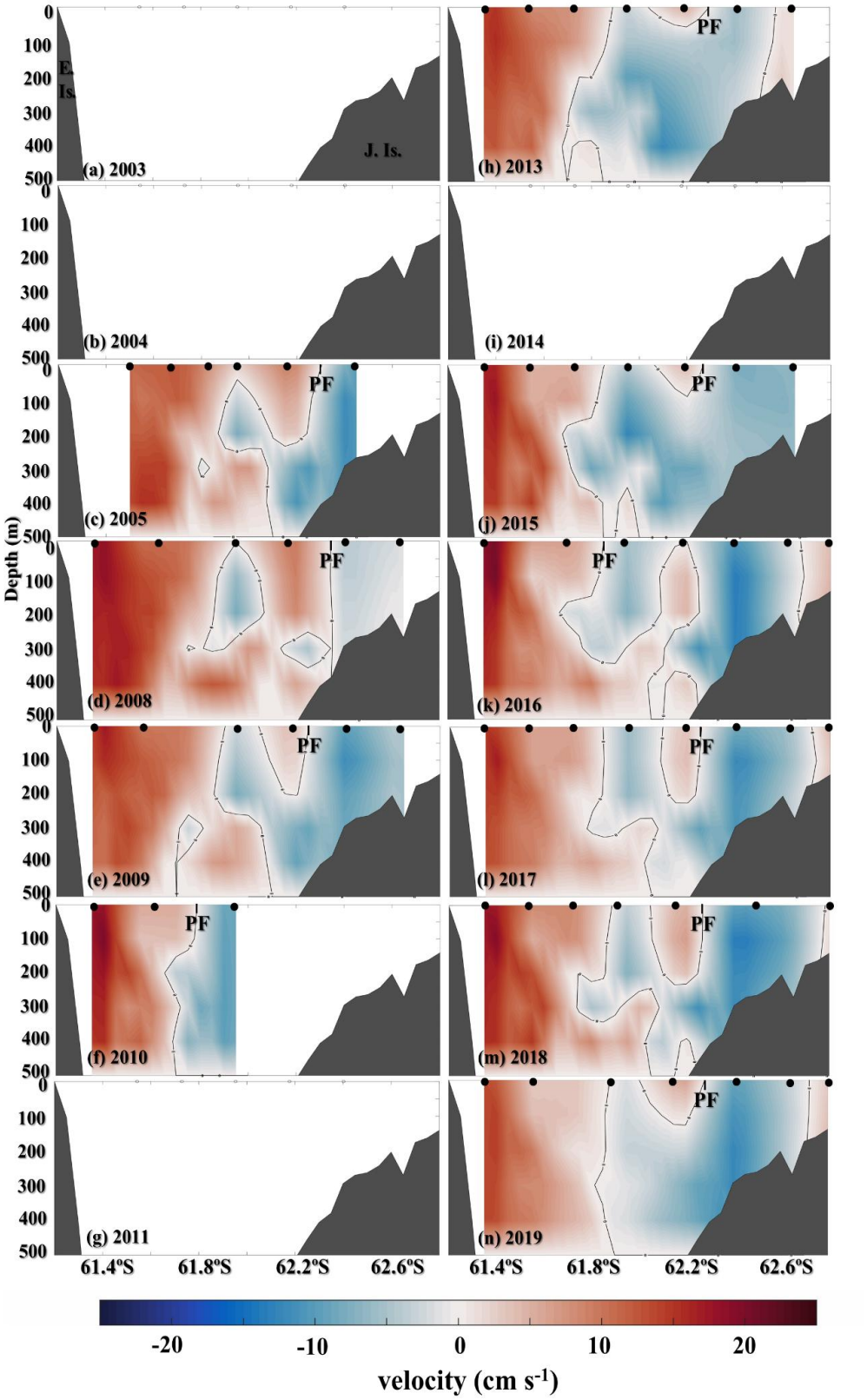


Figure 35: As **Figure 34** but for section 2, between Elephant (E. Is.) and Joinville Islands (J. Is).

At the surface, the boundary between the Bransfield Current and the Antarctic Coastal Current depicts the Peninsula Front (black lines in **Figures 34, 35** and **36**). Previous studies, based on summertime hydrographic measurements, have used different isotherms to characterize the location of the Peninsula Front at the surface, ranging from –0.7˚C to 1˚C [*e.g.,* Sangrà *et al.,*2011, 2017; Huneke *et al.,*2016; Gordey *et al.,*2024]. Due to the variety of definitions of the Peninsula Front, we opted to define it as the contour line where alongshore surface geostrophic velocities are zero, which marks the switch in the ocean current direction. In addition, using GLORYS12v1 outputs (which have no data spatial-temporal gaps during summer–period of this study), we evaluated the long–term mean position of the Peninsula Front and found close agreement in its averaged position based on the 0.5 ˚C isotherm and the zero-velocity definition (**Figure 37**).

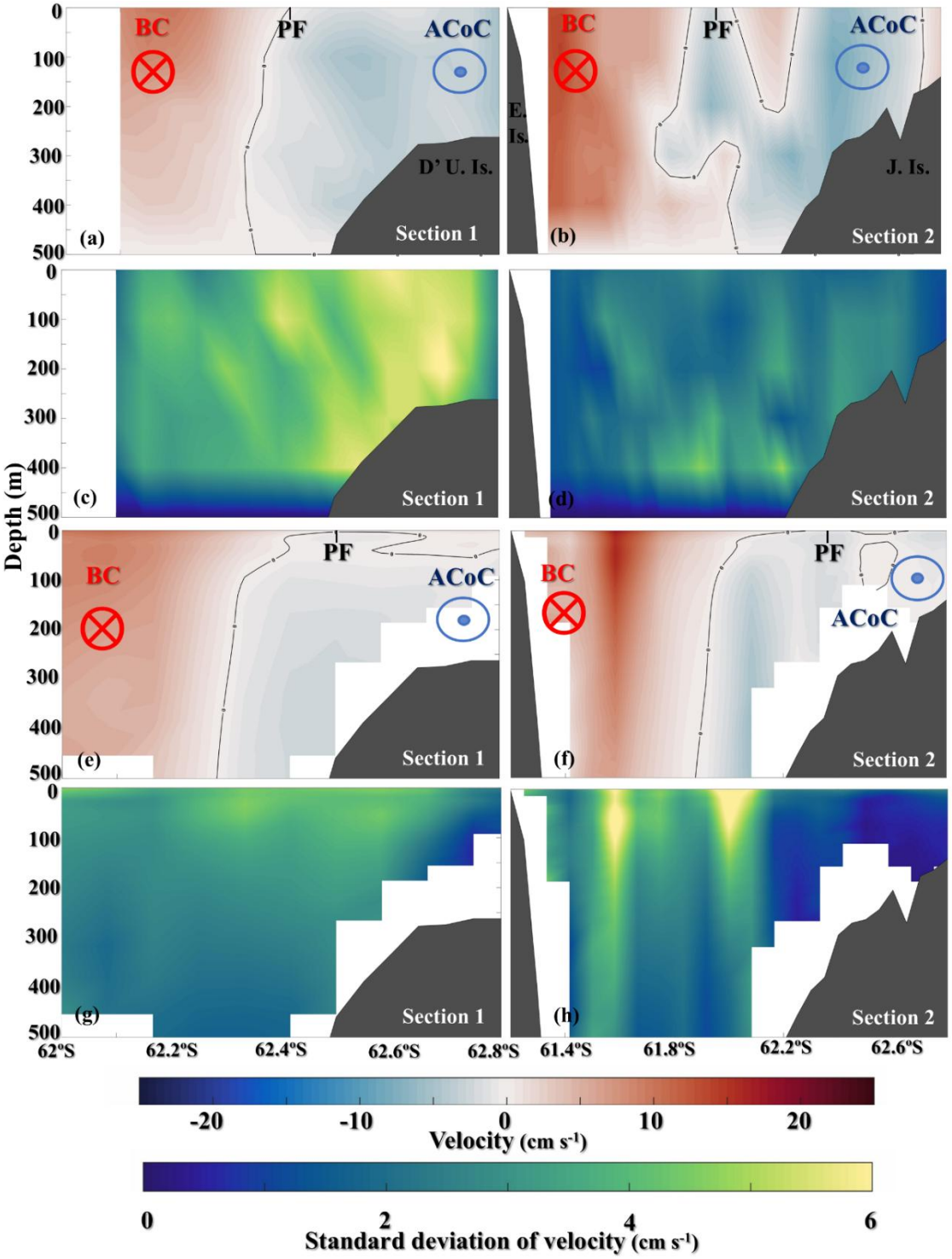


Figure 36: Time–averaged (2003–2019) of vertical cross–sections **(a)** of geostrophic velocities estimate from hydrographic measurements for the summertime (January–March) at Section 1, between King George and D' Urville Islands (D' U. Is.), and **(b)** Section 2, between Elephant (E. Is.) and Joinville Islands (J. Is.). Positive cross–sections velocities correspond to the Bransfield Current (BC), while negative values indicate the Antarctic Coastal Current (ACoC). The standard deviations of the geostrophic velocity time–averaged based hydrographic measurements are shown in panels **(c)** and **(d)** for sections 1 and 2, respectively. Similarly, the time–average of vertical cross–sections of velocities derived from GLORYS12v1 reanalysis

product for the same period (*i.e.,* January–March, 2003–2019) at **(e)** Section 1 and **(f)** Section 2. The corresponding standard deviations of the GLORYS's velocity time–averaged are shown in panels **(g)** and **(h)** for section 1 and 2, respectively. The red ⊗ indicates a flow into the page (*i.e.,* northeastward flow), while the blue circle indicates a flow leaving the page (*i.e.,* southwestward flow). The thin black lines indicate the 0 isolines of velocity. The position of the Peninsula Front (PF) is indicated by the black line on each panel. The topographic feature along the sections is shown in black and is based on IBCSO v1.0 data (https://www.scar.org/science/ibcso/ibcso/).

The annual geostrophic velocity distributions (**Figures 34 and 35**) revealed interannual displacement of the Peninsula Front across the hydrographic sections. This displacement suggests temporal variability in the relative contributions of the Bransfield Current and the Antarctic Coastal Current as also shown by temporal variability in the hydrographic properties (*i.e.,* Θ and S_A; **Figures 37 and Supplementary Figures 10, 11, 12 and 13**) during the analyzed period. For instance, in certain years (*e.g.,* 2010, 2016 and 2019), a greater contribution of TWW was inferred from lower Θ of the water column found along the sections (**Supplementary Figures 10 and 11**). This situation is facilitated by the increased intensity of the Antarctic Coastal Current, which was accompanied by a northward displacement of the Peninsula Front.

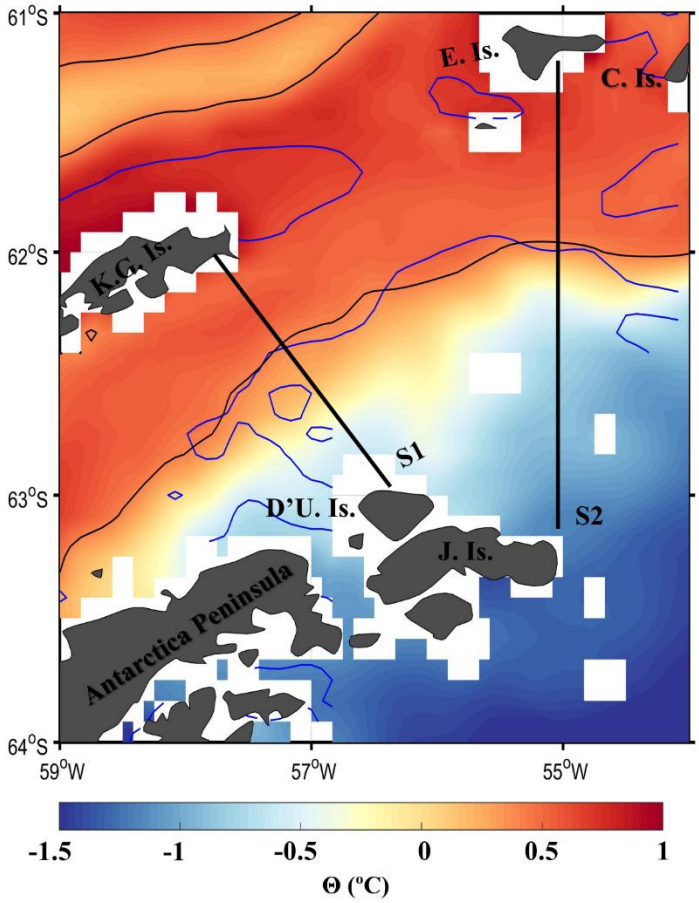


Figure 37: Surface (~50 m) horizontal distribution of averaged conservative temperature – Θ showing the close match between the 0 cm s-1 isoline (blue) and 0.5 ºC isotherm (dark gray) depicting the Peninsula Front. The thick black lines represent the positions of hydrographic sections 1 (S1) and 2 (S2) analyzed in this study. The acronyms stand for D'Urville Island (D'U.Is.), Clarence Island (C. Is.), Elephant Island (E. Is.), and Joinville Island (J.Is.).

Thus, as reported in previous studies, the geostrophic estimates from hydrographic measurements along these two repeated sections revealed that the cyclonic circulation pattern in Bransfield Strait is primarily composed of surface–subsurface currents (*i.e.,* the Bransfield and Antarctic Coastal Currents). Our further results suggest that the high interannual variability observed in hydrographic properties (*i.e.,* Θ and S_A; **Supplementary Figures 10, 11, 12 and 13**) is associated with changes in the intensification of these currents (**Figures 34 and 35**), as they are responsible for the advection of TBW and TWW within Bransfield Strait, respectively. For instance, years with a greater contribution of TWW within Bransfield Strait were associated with more intense of the Antarctic Coastal Current during those periods. Despite the cyclonic defined by these currents being well captured by geostrophic estimation from hydrographic measurements, we emphasize that the geostrophic approximation tends to

underestimate compared to instantaneous directly-measured velocities (e.g. shipboard Acoustic Doppler Current Profiler observations) because (i) the latter also captures the influence of tides, inertial oscillations and wind–driven currents [Trasviña-Castro *et al.,*2011]; and (ii) the assumption of no motion at 500 m does not capture the barotropic component. Additionally, we emphasize that velocity fields are dependent on the spacing of stations. As such, cumulative volume transport estimates provide a more robust metric for discussion and comparison with previous studies, as they are not affected by variability in CTD station spacing occupation. However, given the presence of data gaps in certain years (**Figure 30**), we opted to calculate yearly water mass transports using velocities derived from the GLORYS12v1 output. This approach ensures consistency and continuity in volume transport estimates throughout the study period.

Overall, unlike previous studies that relied primarily on data from one or two oceanographic cruises [*e.g.,* Sangrà *et al.,* 2011, 2017; Gordey *et al.,* 2024], this study is based on 17 years of observations, enabling a detailed analysis of long–term surface and subsurface circulation patterns in the Bransfield Strait, including the Bransfield Current and Antarctic Coastal Current. Thus, providing robust evidence of interannual variability in the intensity of these currents and consequently their influence on the hydrographic properties.

4.3.3.1.2 Surface circulation derived from altimetry

We also analyze the surface geostrophic velocities derived from satellite altimetry, enabling the assessment of differences between the geostrophic velocity structure estimated from hydrographic measurements and the geostrophic velocity field derived from satellite estimates. Additionally, the altimetry estimates provide a broader perspective on geostrophic circulation, allowing the study of the velocity field across the entire region. Thus, by examining the time–averaged (January–March, 2003–2019) surface geostrophic velocities derived from satellite altimetry (**Figure 38**) we could observe the Bransfield Strait circulation patterns (*i.e.,* Bransfield Current and Antarctic Coastal Current) similar to the geostrophic velocity estimates from the hydrographic measurements (**Figures 34, 35** and **36a–b**). The Bransfield Current is a coastal jet flowing northeastward along the southern slope of the South Shetland Islands extending towards Elephant Island (**Figure 38**). Previous studies have suggested that the Bransfield Current could extend as far as Elephant Island [*e.g.,* López *et al.,*1999; Zhou *et al.,*2002, 2006;

Thompson *et al.*,2009; Sángrà *et al.*,2011, 2017; Damini *et al.*,2023; Costa *et al.*,2023]. For instance, Thompson *et al.*, [2009] observed, from drifter trajectories, a continuation of the Bransfield Current near Clarence Island. Here we provide clear evidence from altimetry measurements to support these reports since we could observe the northeastward flow near Clarence Island, with time–averaged velocities of ~13 cm s^{-1} in Section 1 and ~16 cm s^{-1} in Section 2. The altimetry estimates (**Figure 38**) also corroborate previous studies regarding the dynamics of the Bransfield Current, showing that (i) part of the current leaves the eastern basin through the gap between King George and Clarence Islands, recirculating around the South Shetland Islands [López et al, 1999; Sangrà et al, 2011, 2017; Veny et al, 2024]; and (ii) part of the current in eastern Bransfield Strait basin is supplied by the intrusion of waters through the gap between King George and Elephant Islands [Hoffmann *et al.*,1996; López *et al.*,1999; Wilson *et al.*,1999; Loeb *et al.*,2009, 2010; Sanchez *et al.*,2019]. The Antarctic Coastal Current, a Northern Antarctic Peninsula slope–trapped current, is weaker with time–mean velocities of approximately –2 cm s^{-1} in both Sections 1 and 2 (**Figure 38**). The altimetry estimates indicate that the Antarctic Coastal Current enters Bransfield Strait at approximately 62.40ºS and 55.00ºW (**Figure 38**) in agreement with previous analysis of hydrographic sections [Heywood *et al.*,2004], moorings observations [von Gyldenfeldt *et al.*,2002] and trajectories of drifters [Thompson *et al.*,2009].

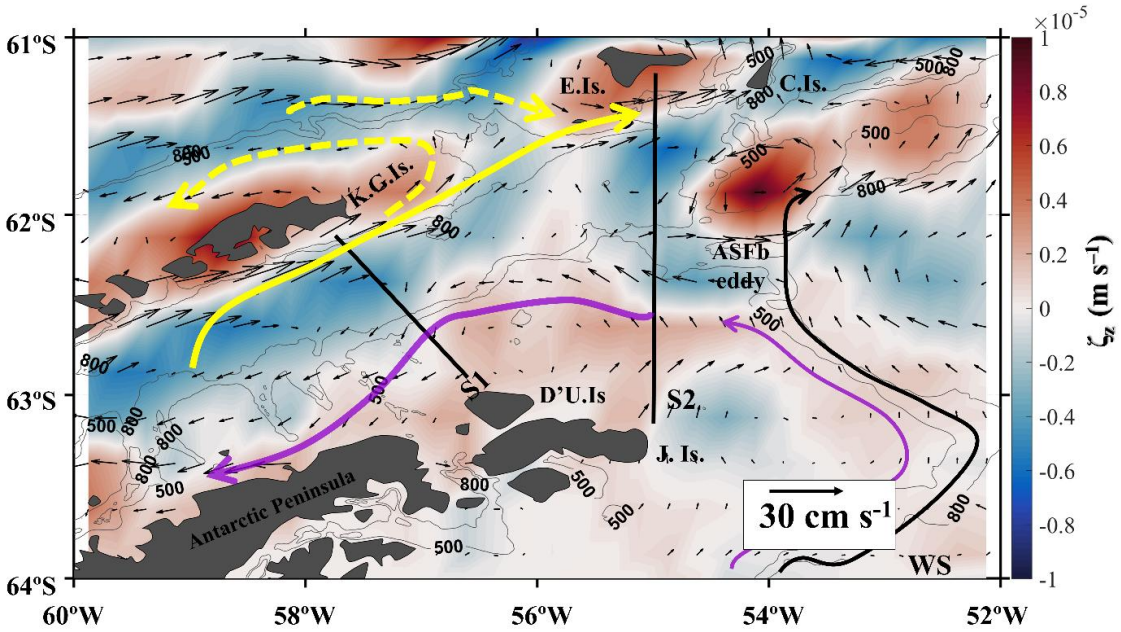


Figure 38: Time–averaged (January–March, 2003–2019) of relative vorticity (ζz; colour) and surface geostrophic velocity (vectors) in the Northern Antarctica Peninsula derived from altimetry. The black lines

represent the mean position of the hydrographic Section 1 (S1) and Section 2 (S2) analyzed in this study. The yellow and purple arrows represent Bransfield Current and Antarctic Coastal Current, respectively. The black arrow depicts Antarctic Slope Front and ASFb eddy represents the Antarctic Slope Front bifurcation eddy. The acronyms stand for: D'Urville Island (D'U.Is.), Clarence Island (C. Is.), Elephant Island (E. Is.), and Joinville Island (J.Is.).The thin gray lines indicate the 500 m and 800 m isobaths based on IBCSO v1.0 data (https://www.scar.org/science/ibcso/ibcso/).

The 17–year summer–mean surface circulation derived from altimetry reveals the persistent presence of the Antarctic Slope Front bifurcation (ASF) eddy (**Figure 38**; Thompson *et al.,*2009; Damini *et al.,*2023) trapped within the 500–800 m isobaths. The strong horizontal velocity shear associated with the Antarctic Slope Front meandering likely forms and maintains the ASFb above the topography due to potential vorticity conservation [Thompson *et al.,*2009; Damini *et al.,*2023]. The presence of the ASFb eddy in the 17–year average velocity field supports its persistent presence in the region, as previously demonstrated by Thompson *et al.,* [2009] using historical surface drifter data spanning from 1989 to 2005. Additionally, some studies have shown that ASFb eddy play a crucial role in regulating sea–air CO_2 exchanges, acting as a major region for CO_2 outgassing in the Bransfield Strait [Damini *et al.,*2023; Kerr *et al.,*2025]. Therefore, indicating the importance of future studies focusing on temporal investigations of this mesoscale structure.

Our satellite altimetry analysis provides robust evidence (with 17–year average velocity field) of key circulation features in the Bransfield Strait, including the Bransfield and Antarctic Coastal Currents, also ASFb eddy. Hence, corroborating previous studies based on moorings and drifter measurements. These observations reinforce the findings from hydrographic measurements, while the extended spatial coverage provided by altimetry broadens our understanding of the regional circulation. The next section will explore the implications of these circulation patterns for regional water masses transport (*i.e.,* TBW and TWW) within the Bransfield Strait and their variability.

4.3.3.2 Water mass transport from the GLORYS12v1

Few studies have focused on the interannual variability of water mass transports within the Bransfield Strait and its drivers [*e.g.,* Veny *et al.,*2022]. This study investigates the interannual summer variability of TBW and TWW transport across two sections analysed using hydrographic measurements and GLORYS12v1 outputs. Before

calculating these transports, we first validate GLORYS12v1 by comparing its outputs against hydrographic properties and geostrophic transport estimates derived from hydrographic measurements along the two sections examined in this study, thus ensuring the reliability of the reanalysis product.

4.3.3.2.1 Reanalysis validation

A time–averaged (January–March, 2003–2019) comparison of the Θ and S_A mean profile from the two sections derived from GLORYS12v1 outputs and available hydrographic measurements, reveals some discrepancies. For instance, the Θ suggest a warm bias across most of the vertical structure (**Figure 39a**), while the S_A profiles highlight a salty bias throughout much of the vertical S_A structure (**Figure 39b**). Despite these biases, GLORYS12v1 shows consistency in representing the main water masses advected by Bransfield Current and Antarctic Coastal Current (*i.e.,* TBW and TWW, respectively; **Figure 40**).

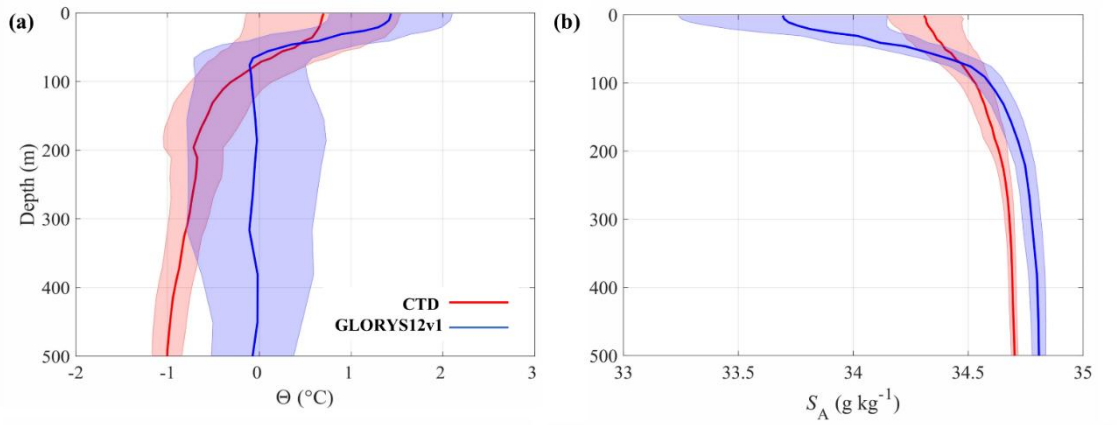


Figure 39: Time–averaged (January–March, 2003–2019) of the mean profile of **(a)** Θ and **(b)** S_A from the two sections by CTD dataset (in red) and GLORYS12v1 output (in blue), with the shaded area representing the standard deviation.

In addition, an analysis of the time–averaged cross–section velocities derived from the hydrographic measurements and GLORYS12v1 outputs indicates that both sections exhibited a cyclonic ocean circulation pattern (*i.e.,* formed by the Bransfield Current and the Antarctic Coastal Current), consistent with our results estimates from hydrographic measurements (**Figures 34 and 35**). However, the GLORYS12v1 showed some discrepancies: (i) the Bransfield Current showed more intense in the GLORYS12v1 compared to hydrographic measurements, reaching a time–averaged velocity of 11 ± 4

cm s^{-1} and 18 ± 6 cm s^{-1} at the surface layer in Sections 1 and 2, respectively (**Figure 36e–h**); and (ii) the Antarctic Coastal Current showed weaker in GLORYS12v1 compared to estimates from hydrographic measurements, reaching a time–averaged velocity of –3 ± 2 cm s^{-1} at 453 m depth in Sections 1 and –6 ± 3 cm s^{-1} at 380 m depth in Sections 2 (**Figure 36e–h**).

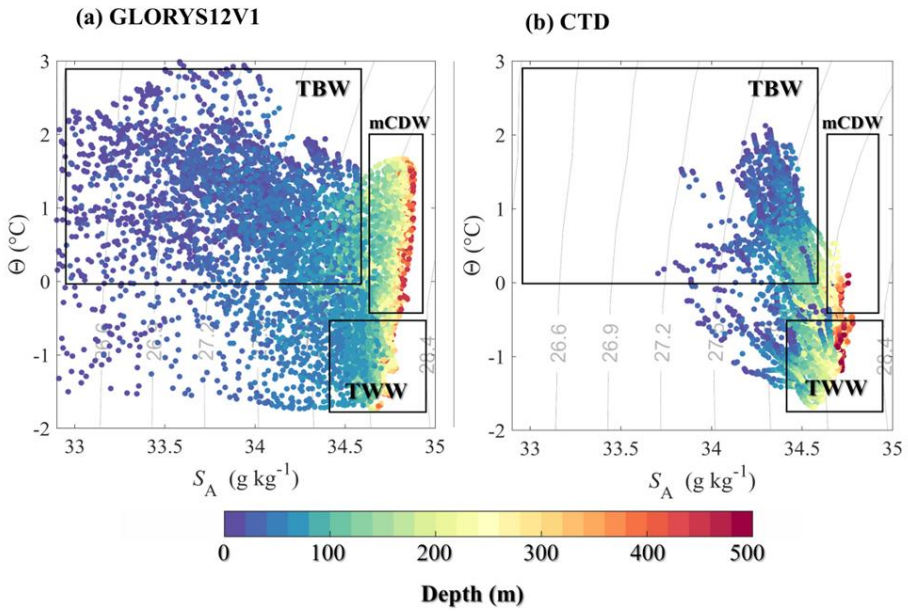


Figure 40: Summer–averaged (January–March) conservative temperature (Θ in ºC) – absolute salinity (S_A in g Kg^{-1}) diagrams up to 500 m depth for the two analyzed sections in the Bransfield Strait over the entire study period (2003–2019) for **(a)** GLORYS12v1 reanalysis and **(b)** CTD. The depth is indicated by the colours. The water masses indicated are: Transitional Zonal Water with Bellingshausen influence (TBW), Transitional Zonal Water with Weddell influence (TWW), and modifed Circumpolar Deep Water (mCDW). The boundaries of water masses indicated by black rectangles are based on [Huneke *et al.*,2016; Morozov *et al.*,2021; Gordey *et al.*,2024].

Since our focus is on study the variability of surface–subsurface currents (*i.e.*, Bransfield Current and Antarctic Coastal Current), we calculated time–averaged (January–March, 2003–2019) of the depth-integrated (50–500 m) velocity field with the hydrographic properties (Θ and S_A) averaged over depth (50–500 m) from GLORYS12v1. Thus, it reduces the high discrepancies observed in GLORYS12v1 at the surface (above 50 m; **Figure 39**) while allowing us to identify the circulation features in the Bransfield Strait, including the Bransfield Current and Antarctic Coastal Current, as well as the ASFb eddy. Our results show the influence of TBW (**Figure 42**) through a flow reaching ~ 0.50 ºC and ~ 34.45 g kg^{-1} at both sections (**Figure 42**). This flow is

advected at ~ 12 cm s^{-1} by the Bransfield Current along the South Shetland Islands as far as Elephant Island (**Figure 42c**). This finding corroborates the altimetry estimates, which also evidenced that flow extends to Elephant Island (**Figure 38**). Additionally, as seen in the altimetry measurements (**Figure 38**), there are distinct flows at the gap between King George and Elephant Islands, with an inflow near Elephant Island and an outflow near King George Islands (**Figure 42**). Conversely, as observed on time–averaged on the cross–section velocities (**Figure 36e–f**), an underestimation of the Antarctic Coastal Current within Bransfield Strait was observed in time–averaged of the depth–averaged field of properties (**Figure 42**). This discrepancy could be attributed to limitations in the bathymetry used in GLORYS12v1. Given the predominantly barotropic nature of this current [*e.g.,* von Gyldenfeldt *et al.,*2002; Heywood *et al.,*2004], the Antarctic Coastal Current is particularly sensitive to local bathymetry. GLORYS12v1's bathymetry underestimates the depth of troughs in the region (**Figure 41**), potentially acting as a topography barrier and reducing the flow of the Antarctic Coastal Current into Bransfield Strait, thus affecting the circulation pattern of the region. Oelerich *et al.,* [2022] reported similar findings in the Bellingshausen Sea, where GLORYS12v1 bathymetry restricts heat transport onto the continental shelf. Moreover, GLORYS12v1 does not capture the influence of the ASFb eddy, which is formed by the interaction between currents associated with the Antarctic Slope Front with the region's bathymetry. This likely stems from the underrepresentation of these currents or limitations in the reanalysis's bathymetry, which may not resolve the eddy's formation or trapping.

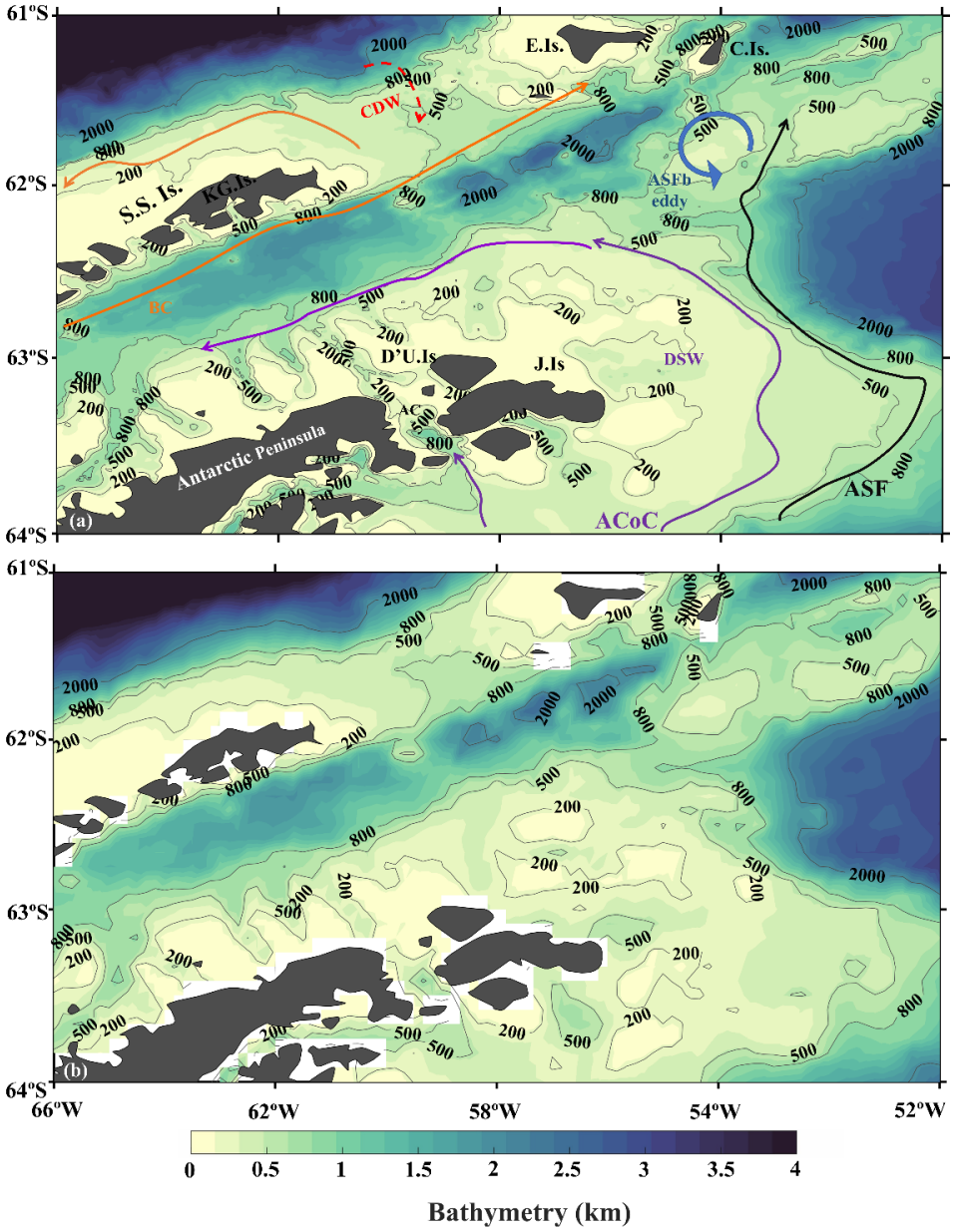


Figure 41: Bathymetry of the Northern Antarctica Peninsula extracted from **(a)** IBCSO v1.0; and **(b)** GLORYS12v1. The thin gray lines indicate the 200 m, 500 m, 800 m, and 2000 m isobaths. The red (purple) arrows represent the pathways of the Circumpolar Deep Water (Dense Shelf Water, via Antarctic Coastal Current – ACoC) entering Bransfield Strait. The orange arrows depict Bransfield Current and its recirculation around the South Shetland Islands (S.S.Is.). Light blue arrows indicate the position of Antarctic Slope Front bifurcation (ASFb) eddy. The black line represents the mean location of Antarctic Slope Front (ASF). The acronyms stand for: D'Urville Island (D'U.Is.), Clarence Island (C. Is.), Elephant Island (E. Is.), and Joinville Island (J.Is.).

The GLORYS12v1 demonstrated consistency with both altimetry and hydrographic measurements, underscoring its utility in capturing key features of the Bransfield Strait, including the cyclonic circulation formed by the Bransfield and Antarctic Coastal Currents, as well as the main water masses (*i.e.,* TBW and TWW)

transported by these currents, with the majority of their transport occurring within the upper 500 m (**Figure 40**). However, we suggest that inaccuracies in the model's bathymetry contribute to the observed underestimation of the Antarctic Coastal Current and limit its ability to fully resolve the ASFb eddy. Although these limitations warrant cautious interpretation, GLORYS12v1 remains a valuable tool to investigate water mass transport variability and the mechanisms driving this variability, particularly the influence of climate modes such as SAM and ENSO, which play a major role in modulating the regional dynamics and influence the biogeochemistry of the northern Antarctic Peninsula [*e.g.,* Dotto *et al.,*2016; Avelina *et al.,*2020; Damini *et al.,*2022; Monteiro *et al.,*2023; Kerr *et al.,*2025].

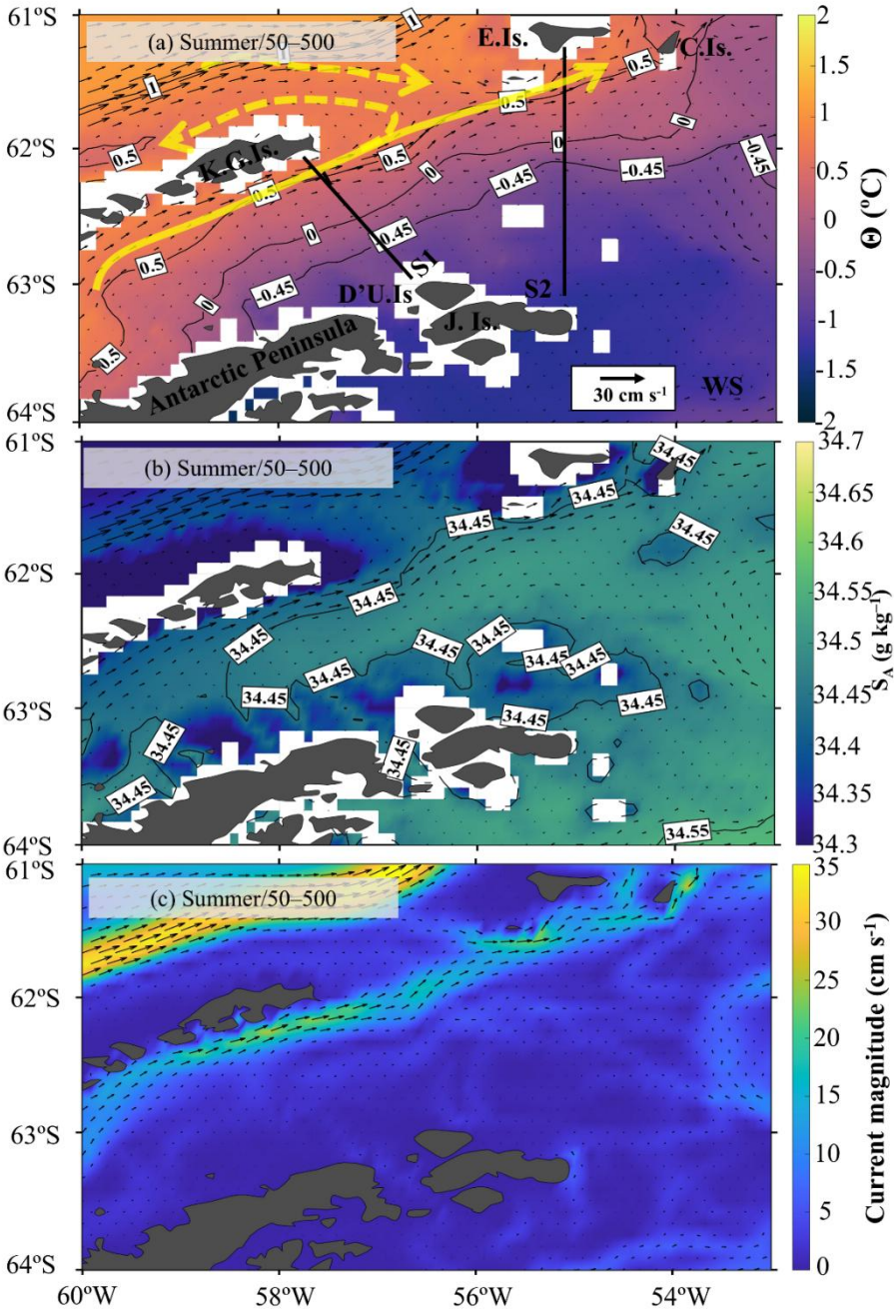


Figure 42: Time–mean of depth-integrated (50–500 m) velocity field (January–March, 2003–2019) with hydrographic properties averaged over the same depth range as the background field (colour) in the Northern Antarctic Peninsula, derived from GLORYS12v1 for **(a)** conservative temperature (Θ in ºC); **(b)** absolute salinity (S_A in g kg^{-1}) and **(c)** the current magnitude (cm s^{-1}) calculated as $\sqrt{u^2 + v^2}$ where u and v are the zonal and meridional velocity components, respectively. The black lines indicate the mean of positions of hydrographic sections 1 (S1) and 2 (S2) analyzed in this study. The yellow arrows represent the Bransfield Current. The acronyms stand for D'Urville Island (D'U.Is.), Clarence Island (C. Is.), Elephant Island (E. Is.), and Joinville Island (J.Is.).

4.3.3.2.2 Water masses transport and their variability

Here, we remind the reader that this study aims to investigate the summer variability of surface–subsurface currents within Bransfield Strait. In addition, as observed in the vertical resolution of velocities from GLORYS12v1 outputs (**Figure 43**), the troughs in Bransfield Strait represented by GLORYS12v1's bathymetry are shallower compared to available regional bathymetry datasets (*e.g.,* IBCSO; **Figure 41**). Consequently, GLORYS12v1 contains only a few regions with depths greater than 500 m that include velocities outputs. Thus, we calculate the volume of water mass transports following their hydrographic properties (**see section 2.4**) up to 500 m depth. By the time–average (January–March, 2003–2019) of TBW volume transport via Bransfield Current estimated from GLORYS12v1 is 0.34 ± 0.24 Sv in Section 1 and 0.53 ± 0.34 Sv in Section 2 (**Figure 44**). Assuming mass conservation, we infer an intrusion of TBW into the eastern basin of Bransfield Strait through the gap between King George and Elephant Islands, with a time–average of 0.23 ± 0.20 Sv (**Figure 44**). This intrusion is likely fed by CDW upwelling to depths of 150–300 m as ACC reaches Drake Passage [Orsi *et al.,*1995]. Our findings suggest this upwelling is driven by a pronounced negative wind stress curl in the region (**Figure 44**), which generates surface water divergence and brings CDW to shallow depths (~190 m; **Supplementary Figure 14a**) via Ekman suction. After TBW enters the eastern basin of Bransfield Strait, this water flows eastward, driven by Bransfield Current towards the Powell Basin. Additionally, our results agree with previous studies, which reported geostrophic estimates (50–500 m) of summertime (January–March) volume transport ranging between 0.38 and 1 Sv for the Bransfield Current along the South Shetland Islands, [López *et al.,*1999; Sangrà *et al.,*2011]. On the other hand, despite GLORYS12v1 underestimates the Antarctic Coastal Current (**Figure 36e–f**), we found a time–average of TWW volume transport of approximately –0.09 ± 0.11 Sv and –0.02 ± 0.11 Sv through Sections 1 and 2, respectively (**Figure 44**). Sangrà *et al.,* [2011], reported summertime (January–March) geostrophic estimates (0–500 m) of volume transport from two cruises of around –0.20 ± 0.10 Sv for the Antarctic Coastal Current near D' Urville Island.

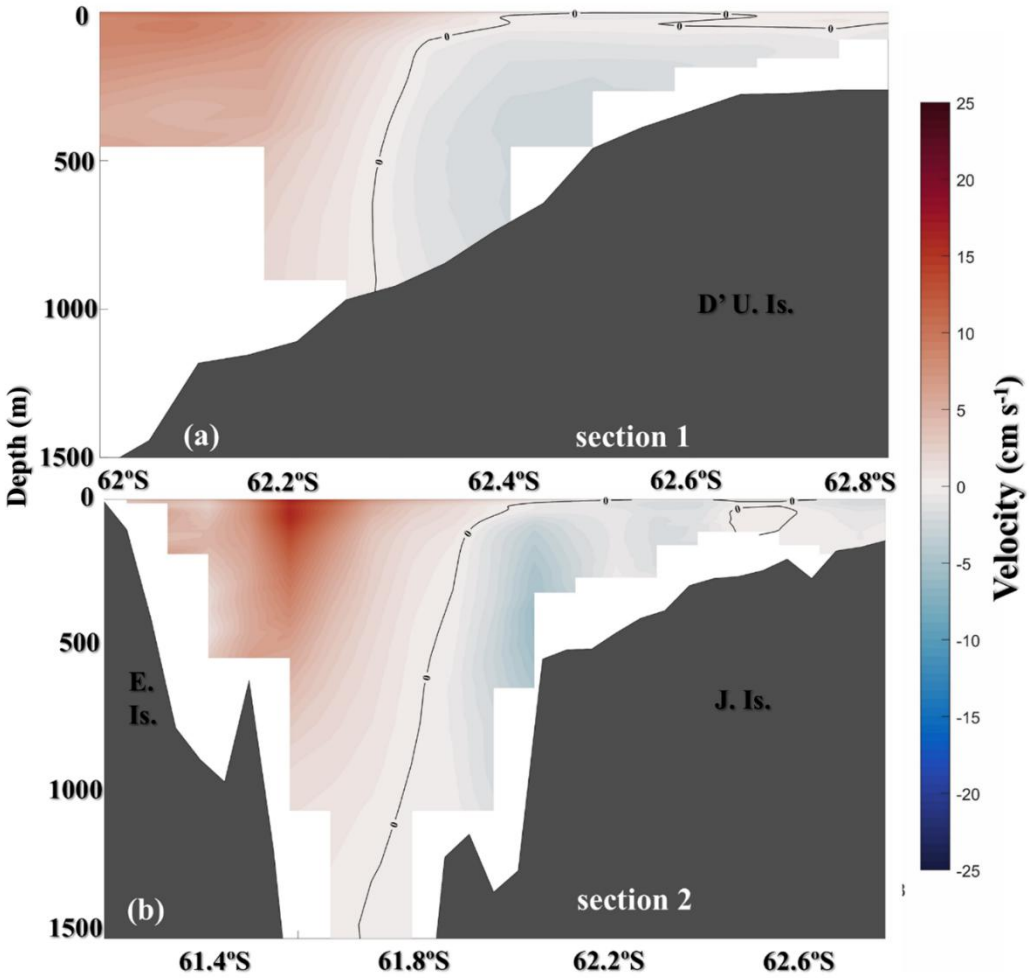


Figure 43: Time–average of vertical cross–sections of velocities derived from GLORYS12v1 reanalysis product for the same period (*i.e.,* January–March, 2003–2019) at **(a)** Section 1 (between King George Island and D' Urville Island – D' U. Is.) and **(b)** Section 2 (between Elephant Island – E. I.s and Joinville Island

Overall, our results provide a valuable estimate for the intrusion of TBW into the Bransfield Strait through the gap between King George and Elephant Islands. This intrusion is influenced by the local wind patterns of the region, further emphasizing the dynamic of the region's circulation and the importance of understanding these interannual variability in the context of global climate change. Additionally, the good representation of TBW in GLORYS12v1 reanalysis output (**Figure 40**) and the effective representation of the Bransfield Current through velocity fields (**Figures 36e–f and 42**) suggest that the reanalysis can reliably capture the variability in TBW volume transport via the Bransfield Current. However, due to the reanalysis's bathymetry inaccuracies, an underestimation of the Antarctic Coastal Current limits the GLORYS's ability to fully resolve the TWW transport, resulting in low TWW volume transport values (**Figure 44**). Consequently, we could only evaluate the variability of TBW transport associated with the summer SEI

indices.

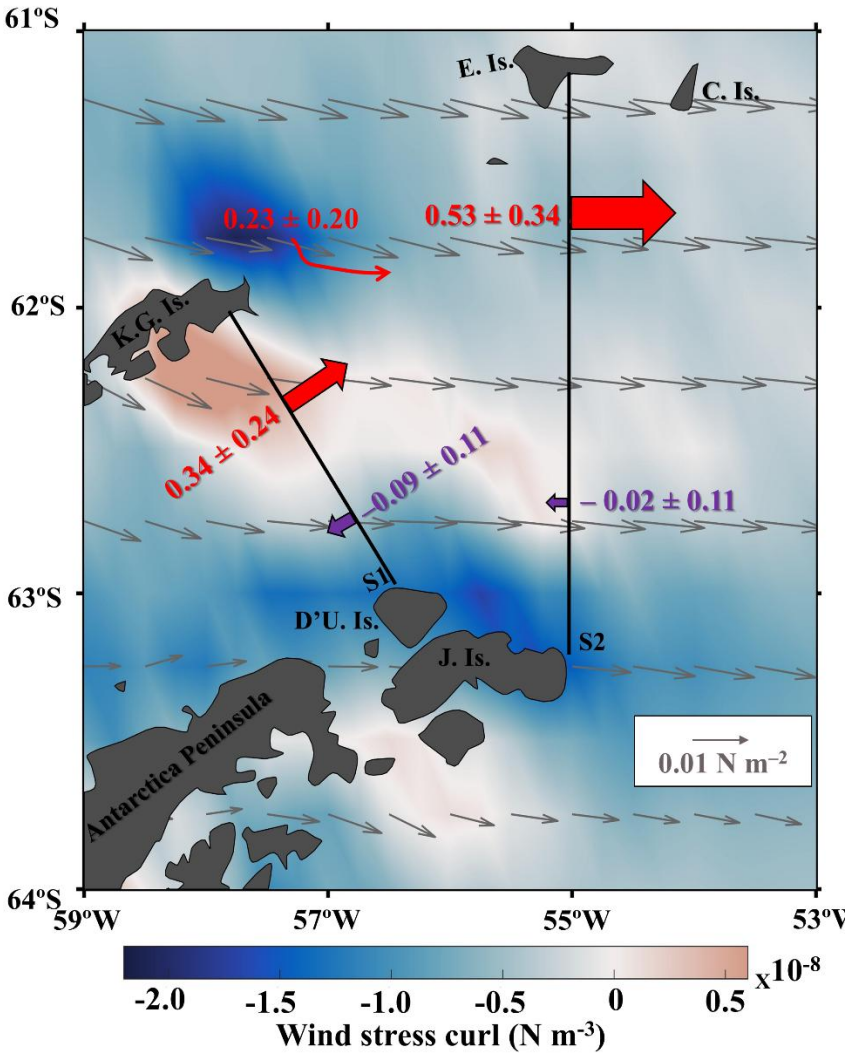


Figure 44: Surface horizontal distribution of time–averaged (January–March, 2003–2019) wind stress curl (colour–coded), with purple and red solid arrows representing the time-averaged volume transport (Sv) of Transitional Zonal Water with Weddell influence (TWW) and Transitional Zonal Water with Bellingshausen influence (TBW), respectively. The mean position of Sections 1 (S1) and 2 (S2) are depicted as black solid lines. Additionally, the length of the arrows indicates the magnitude of these transports. The grey vectors depict the wind stress. The acronyms stand for: D'Urville Island (D'U.Is.), Clarence Island (C. Is.), Elephant Island (E. Is.), and Joinville Island (J.Is.).

We highlight that the use of the SEI index provides a more comprehensive understanding of how SAM and ENSO jointly modulate wind–driven circulation dynamics in the region. For instance, Llanillo *et al.,* [2023] reported a stronger correlation when considering the SEI index rather than individual climate modes to explain the variability of intrusions of the Warm Deep Water (modified CDW in the Weddell Sea)

onto the continental shelf. Furthermore, using monthly averaged wind velocity (Jan–March, 2003–2019) provides by ERA–Interim we calculated wind speed by $|V| = \sqrt{u^2 + v^2}$ (where u and v are the zonal and meridional wind velocity components, respectively) for each summer climate mode period, such as ENSO+ (2004, 2005, 2010, 2015, 2016), ENSO–+ (2006, 2008, 2009, 2011, 2012, 2018, 2019), SAM+ (2005, 2008, 2009, 2012, 2013, 2014, 2015, 2016, 2018, 2019), SAM– (2003, 2010, 2017), SEI+ (2006, 2008, 2009, 2011, 2012, 2013, 2015, 2018) and SEI– (2004, 2005, 2010, 2016, 2019) over the northern Antarctic Peninsula (~61–66ºS and 66–52ºW). Our results indicate that SEI periods lead to more intense winds, with an average wind speed of 3.15 ± 0.53 m s^{-1} during SEI+ phases and 3.74 ± 0.89 m s^{-1} during SEI– phases. In comparison, SAM+ (SAM–) periods showed an average wind speed of 2.86 ± 0.50 m s^{-1} (3.00 ± 0.81 m s^{-1}), while ENSO+ (ENSO–) periods exhibited an average wind speed of 2.75 ± 0.52 m s^{-1} (3.00 ± 0.55 m s^{-1}). Thus, underscoring the importance of considering both climate modes in the dynamic circulation studies in the Antarctic regions. The Spearman's correlations between the normalized and detrended Wind Stress Curl and SEI indices were tested from 2003 to 2019 and showed a significant anti–correlation ($r = -0.60$ at the >95% statistical significance level; **Figure 33b**). This result is in line with previous studies that demonstrate the important role of SAM and ENSO climate modes in driving wind variability in the region [*e.g.,* Miguel Andres-Martin *et al.,*2024].

For the time–average of summers of SEI+ conditions (**Figures 45a and 33a**), stronger northwesterly winds along the northern Antarctic Peninsula were observed (**Figure 33b**), which, through Ekman transport, drives the SACCF closer to the Peninsula (**Figure 45a**). These observations align with previous studies that have reported a poleward shift of SACCF under similar wind patterns [*e.g.,* Marshall *et al.,*2003; Loeb *et al.,*2009, 2010; Renner *et al.,*2012]. Additionally, this wind regime induces a pronounced negative wind stress curl over the Antarctica Peninsula, as evidenced by positive wind stress curl anomalies (*i.e.,* since that the wind stress curl in the Antarctic Peninsula region is predominantly negative, SEI+ periods exhibit more negative wind stress curl conditions compared to the overall temporal average; **Figure 45a**). This shallow CDW (**Supplementary Figure 14b**) might then be mixed with waters from the Bellingshausen Sea, forming TBW, which is subsequently transported into the Bransfield Strait through the gap between King George Island and Elephant Island (**Supplementary Figure 15a**). This TBW intrusion process is supported by an increase in TBW transport from 0.36 ±

0.20 Sv in Section 1 to 0.71 ± 0.28 Sv in Section 2 during the average of SEI+ periods (**Figure 45a**), and assuming mass conservation, we infer TBW volume transport through the gap between King George Island and Elephant Island of 0.31 ± 0.16 Sv (**Figure 45a**). Our findings are coherent with the changes in hydrographic (freshening and lightening) and biogeochemical (dilution of total alkalinity and dissolved inorganic carbon) parameters as reported by Dotto *et al.,* [2016], Damini *et al.,* [2022] and Santos-Andrade *et al.,* [2023]. These authors hypothesized that changes observed in Bransfield Strait are related to an increase in TBW volume transport into Bransfield Strait associated with the intensification of westerly winds associated with climate modes (*i.e.,* SAM and ENSO events). Here we provide evidence from GLORYS12v1 to support that hypothesis.

For the time–average of summers of SEI– conditions (**Figures 45b** and **33a**), weaker northwesterly winds and some southeasterly winds were observed (**Figure 33c**), through Ekman transport cause the SACCF to shift further away from the Antarctic Peninsula (**Figure 45b**). These observations also corroborate previous findings on the SACCF northward shifts under comparable wind patterns [*e.g.,* Marshall *et al.,*2003; Loeb *et al.,*2009, 2010; Renner *et al.,*2012]. This wind pattern induces a weaker negative wind stress curl over the Antarctica Peninsula, evidenced by negative values on the wind stress curl anomaly (*i.e.,* SEI– periods exhibit less negative wind stress curl conditions compared to the overall temporal average **Figure 45b**). The weaker wind stress curl over the Antarctica Peninsula (**Figure 45b**) leads to reduced Ekman transport of surface waters and reduced CDW upwelling (**Supplementary Figure 14c**), which consequently decreases TBW advection into the Bransfield Strait (**Supplementary Figure 15b**). This is consistent with the lower TBW volume transport observed during SEI– periods compared with SEI+ periods, with values of 0.27 ± 0.25 Sv in Section 1 and 0.33 ± 0.28 Sv in Section 2 (**Figure 45b**). Assuming mass conservation, we infer a TBW volume transport of 0.10 ± 0.03 Sv through the gap between King George and Elephant Islands during SEI+ summers. This represents a reduction of approximately 30% of TBW accessing the eastern Bransfield Strait through this gap during SEI– periods, compared to SEI+ periods (**Figure 45b**). Therefore, our results evidenced the interplay between TBW transport and climate modes (*i.e.,* SEI index), emphasizing the sensitivity of Bransfield Strait circulation to atmospheric forces.

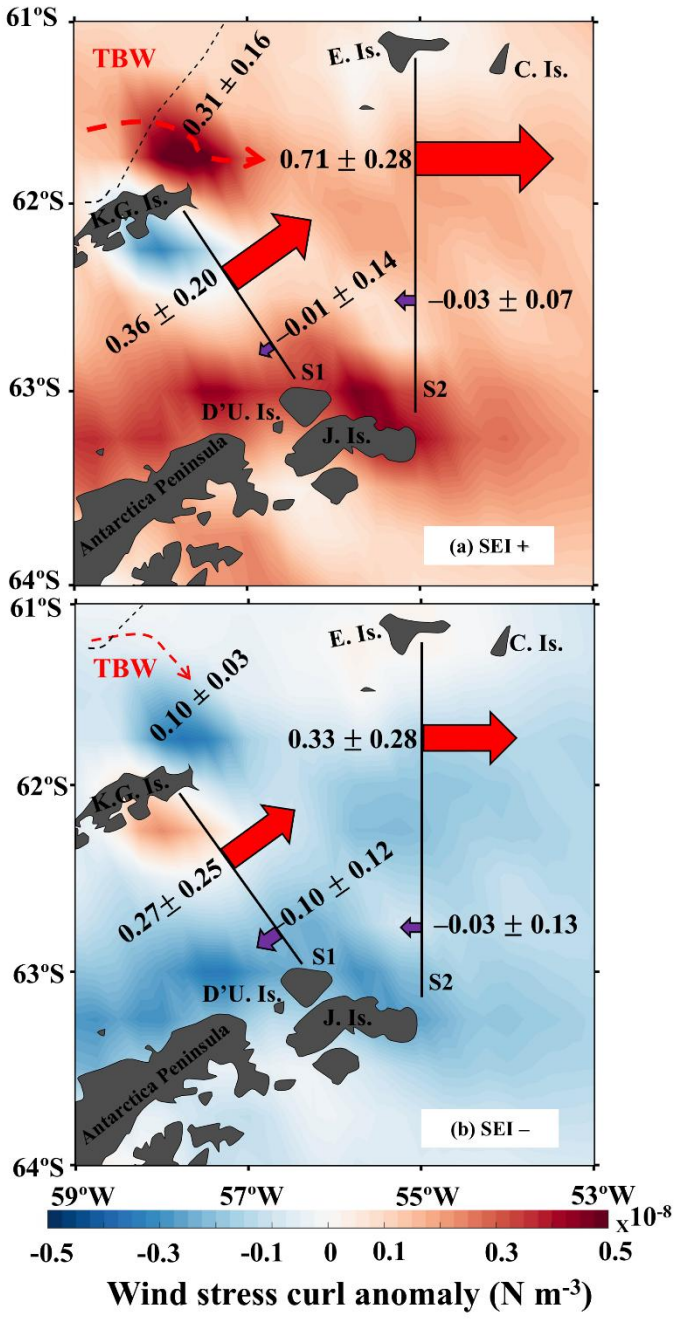


Figure 45: Surface horizontal distribution of averaged wind stress curl anomaly (colour–coded) of (a) SEI+ phase summers (*i.e.,* 2006, 2008, 2009, 2011, 2012, 2013, 2014, 2015, and 2018) and (b) SEI– phase summers (*i.e.,* 2010, 2016, and 2019). The purple and red solid arrows represent the time-averaged volume transport (Sv) of Transitional Zonal Water with Weddell influence (TWW) and Transitional Zonal Water with Bellingshausen influence (TBW), respectively, and their widths indicate the magnitude of these transports. The time-averaged of the TBW and TWW transports and the standard deviation of time-averaged are indicated by numbers. Southern Antarctic Circumpolar Current Front (SACCF) is represented by a black dashed line in both maps, while the mean position of Sections 1 (S1) and 2 (S2) are denoted by black solid lines. The acronyms stand for: D'Urville Island (D'U.Is.), Clarence Island (C. Is.), Elephant Island (E. Is.), and Joinville Island (J.Is.).

We highlight those additional factors in the Bransfield Strait, potentially unresolved by the resolution of GLORYS12v1 (*e.g.,* underestimation of the currents due to inaccuracies of topography) may influence the interannual variability of TBW transport into Bransfield Strait (**Figure 41**). For instance, unidentified processes may have intensified TBW outflow along the 500 m isobath near King George Island in 2004, 2007, and 2017 (**Supplementary Figure 16a**). In addition, the absence of eddies representation because of GLORYS12v1's resolution could affect the variability of TBW transport into Bransfield Strait as well. Those structures (*i.e.,* eddies) facilitate the upwelling of CDW onto the continental shelf [*e.g.,* Moffat *et al.,*2009; Boeira Dias *et al.,*2023], contributing to the formation of TBW, which is subsequently transported into the Bransfield Strait. Despite these limitations, our results confirm a strong relationship between SEI influence on wind stress curl and TBW transport (**Figures 45 and Supplementary Figures 15, 16 and 17**), indicating that GLORYS12v1 provides a reliable basis for studying ocean dynamics in Bransfield Strait. Nevertheless, further studies using higher-resolution models or additional observational data are necessary to fully understand local dynamics.

A poleward shift of the SACCF has been observed associated with climate modes [*e.g.,* ENSO and SAM; Yuan, 2004; Loeb *et al.,*2009, 2010]. Here, we observed this shift for the average of SEI+ summers (**Figure 45a**). This shift has significant implications for the circulation and characteristics of Bransfield Strait. For example, poleward movement of SACCF during SAM+ and/or ENSO– periods could bring warm, nutrient–rich CDW, which mixes with iron-rich coastal waters, enhancing primary production [*e.g.,* Loeb *et al.,*2009, 2010]. This process could lead to an increase in the consumption of organic matter in the region and contribute to the formation of a CO_2 sink area [da Cunha *et al.,*2018; Avelina *et al.,*2020]. Our GLORYS12v1 analysis provides evidence of this CDW upwelling to shallow depth (**Supplementary Figure 14**) and supports these studies. Additionally, a tendency for more frequent SAM+ and ENSO– periods in future has been reported in previous studies based on climate model projections [*e.g.,* Cai *et al.,*2015; Fogt & Marshall, 2020], that could potentially lead a more frequent of that combined event occurs (referred to here as SEI+). And consequently, leading to a greater intrusion of CDW into Bransfield Strait. These observations underscore the importance of comprehensively understanding regional circulation patterns and their driving mechanisms in a climate–sensitive polar environment.

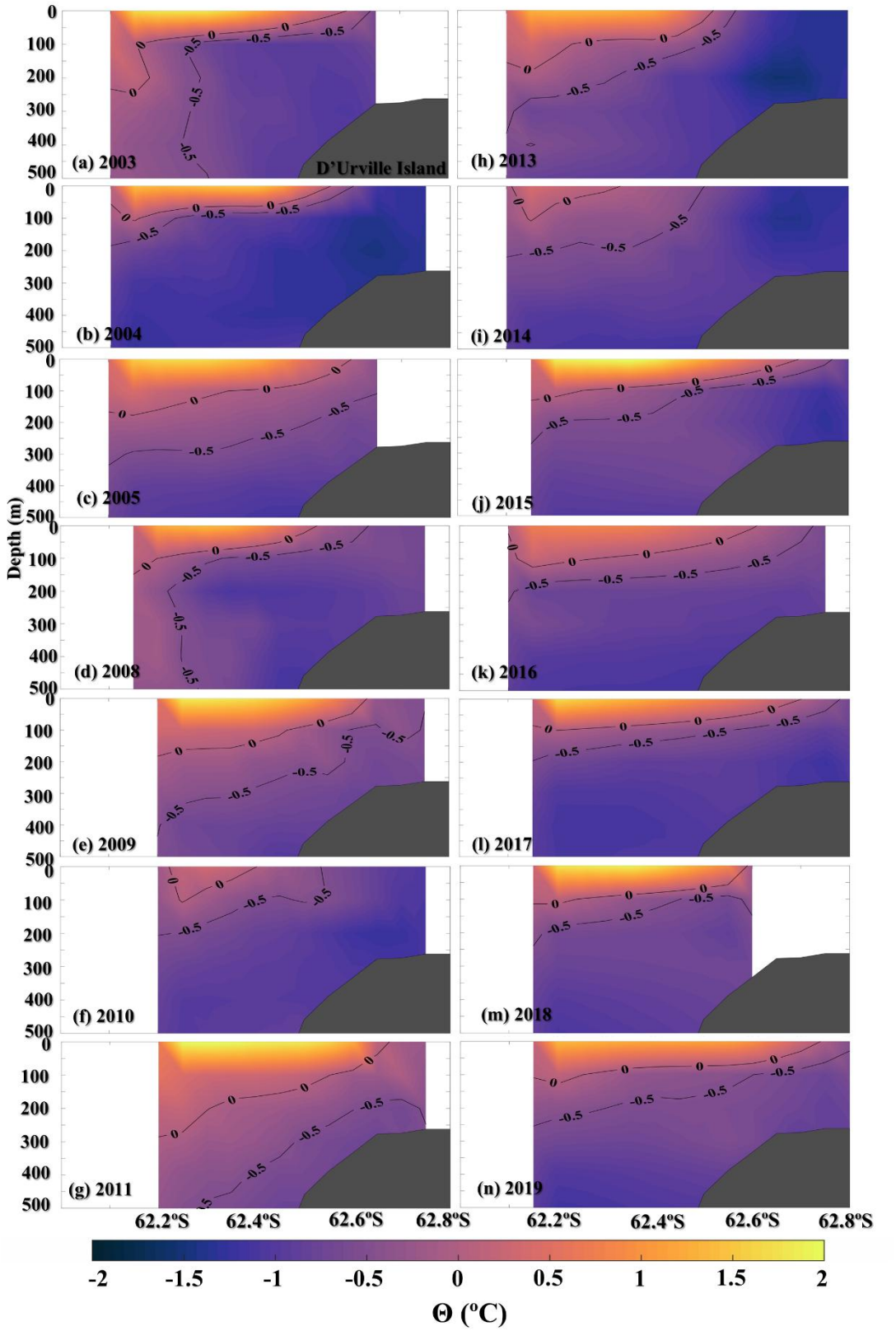
4.3.4 Summary and conclusions

Here, we reported the first comprehensive long–term assessment of summer circulation within Bransfield Strait between 2003 and 2019, integrating high–quality hydrographic measurements, satellite altimetry, and the output of an eddy-permitting ocean reanalysis (GLORYS12v1). The geostrophic estimates from hydrographic measurements along the two repetitive sections used in this study show that the cyclonic circulation pattern in Bransfield Strait is primarily composed of the Bransfield and Antarctic Coastal Currents. Furthermore, our results reveal that the high interannual variability of hydrographic properties observed in the region is associated with changes in the intensification of these currents, which are responsible for the advection of TBW and TWW within Bransfield Strait. Both altimetry and reanalysis agree with the previous studies [*e.g.,* López *et al.,*1999; Gordon *et al.,*2000; Loeb *et al.,*2009, 2010; Veny *et al.,*2024] highlighting the intrusion of TBW between King George and Elephant Islands feeding the Bransfield Current. The velocity fields from the GLORYS12v1 showed reasonable agreement with observations. For instance, the reanalysis accurately represents the influence of TBW and Bransfield Current system, highlighting the need for further efforts to address the representation of Weddell Sea currents, such as Antarctic Coastal Current and currents associated with Antarctic Slope Front, and their impact on the northern Antarctic Peninsula region. Our study suggests that, although absolute values may have some discrepancies, GLORYS12v1 provides a reliable basis for studying ocean dynamics in the northern Antarctic Peninsula.

Furthermore, by using GLORYS12v1 output we quantified the long–term TBW intrusions through the gap between King George and Elephant Islands, a key aspect of our study. We estimate a time–average rate of 0.23 ± 0.20 Sv from 2003 to 2019, providing the first robust estimate of this process over an extended period. While previous studies [*e.g.,* López *et al.,* 1999; Gordon *et al.,* 2000; Loeb *et al.,* 2009, 2010; Veny *et al.,* 2024] have documented TBW intrusions into the Bransfield Strait, our study advances these findings by quantifying their magnitude and variability, indicating the wind forcing modulation by combined effects of SAM and ENSO. The averaged SEI+ summer conditions induce a pronounced negative wind stress curl over Antarctica Peninsula, resulting in ~ 30% increase in the inflow of TBW through the gap between King George and Elephant Islands. The long–term trends associated with the projected southward

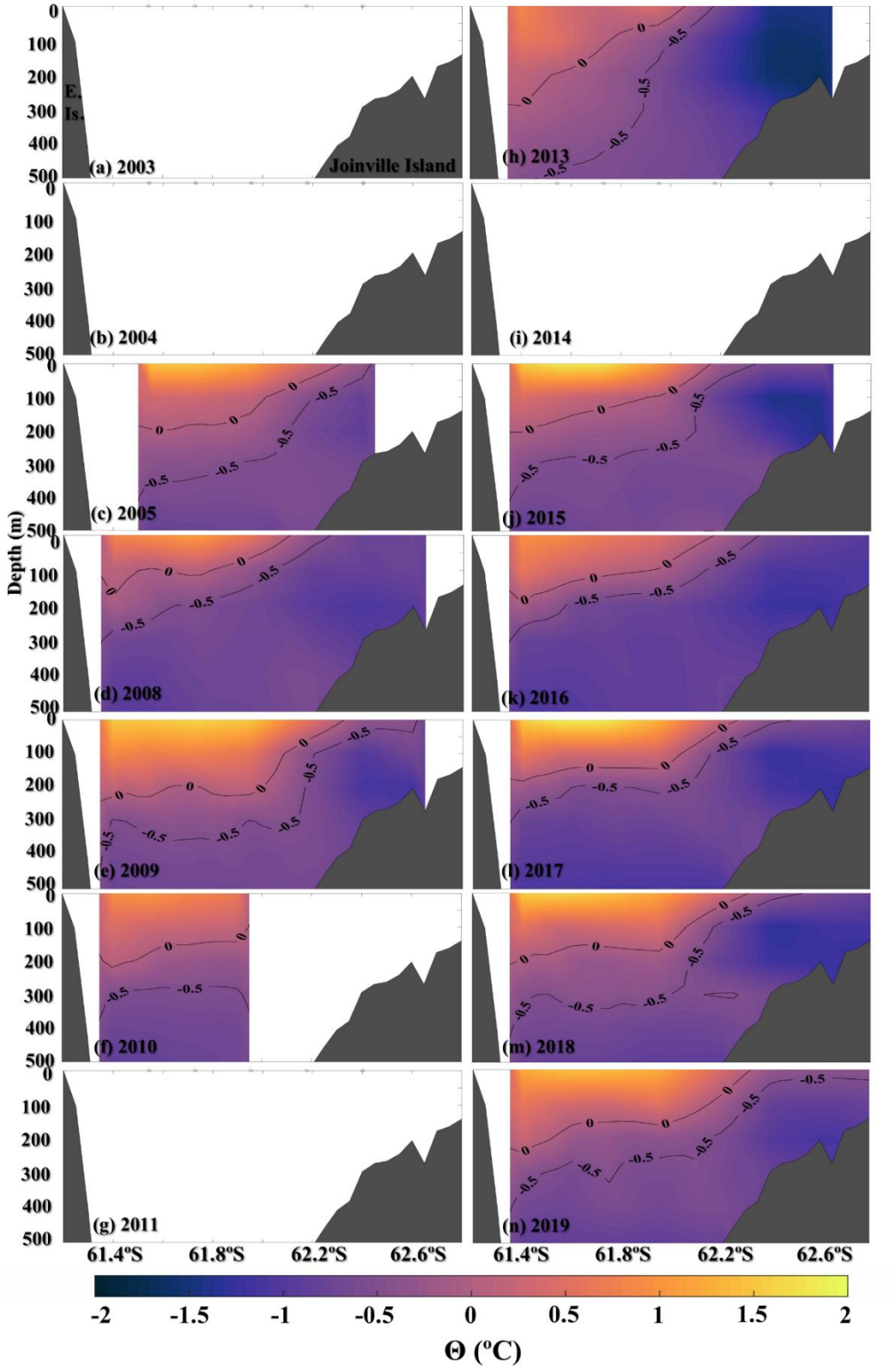
migration of the winds and ACC could favor more intrusion of TBW into the region. This would alter both physical and biogeochemical properties in the northern Antarctic Peninsula, with potential impacts on carbon sequestration and instability of regional glaciers. Given these potential impacts, ongoing hydrographic observations and assessing high–resolution ocean circulation models [*e.g.,* Regional Ocean Modeling System – ROMS; Wang *et al.,*2022] are essential for further understanding of the regional circulation and its influence on water mass transport and biogeochemical processes.

4.3.5 Supplementary information

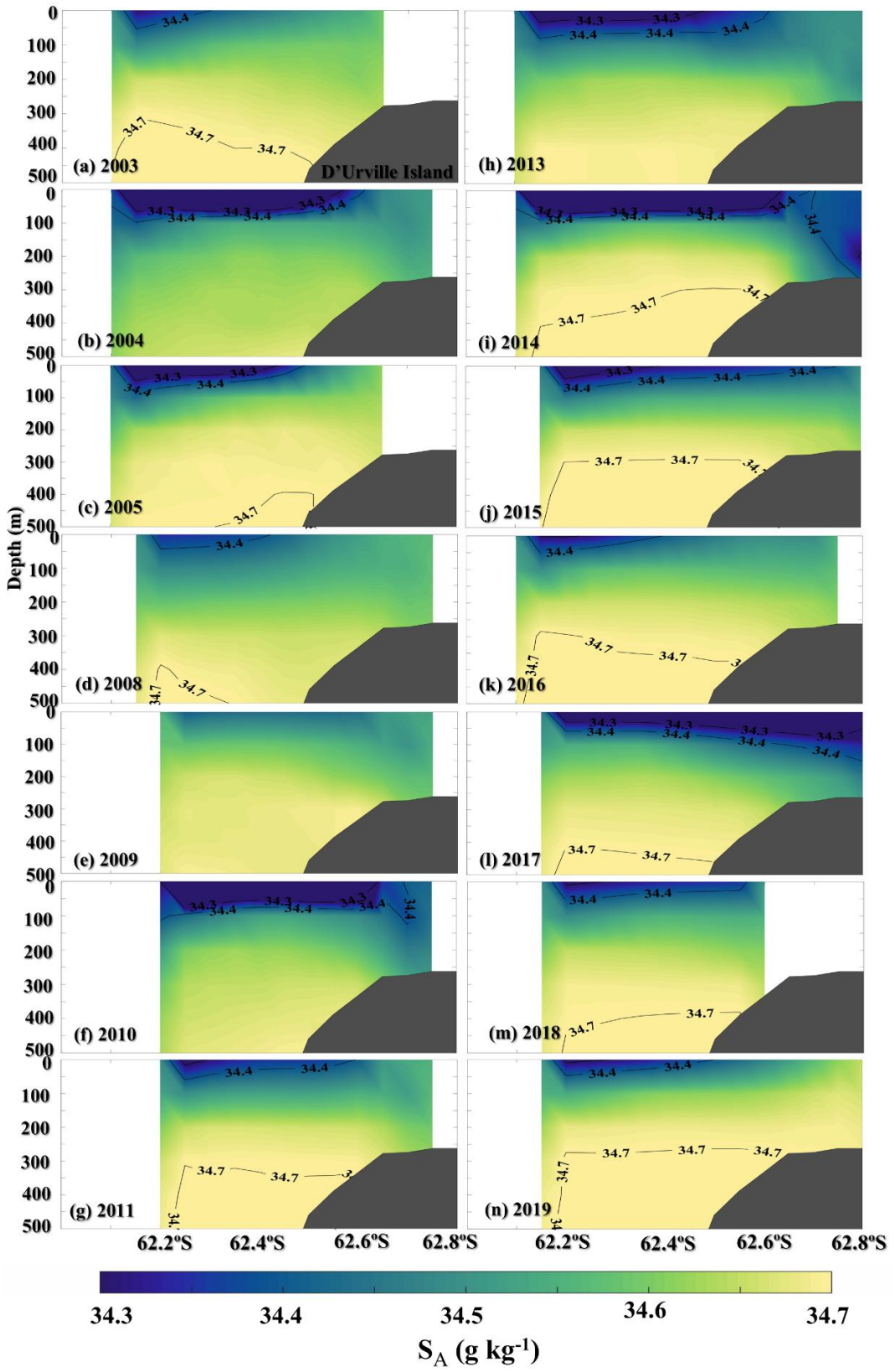


Supplementary Figure 10: Annual cross–section conservative temperature in Section 1 (Θ in ºC), between King George and D' Urville Islands. The thin black lines indicate the –0.5 and 0 isolines. The topographic

feature along the sections is shown in black and is based on IBCSO v1.0 data (https://www.scar.org/science/ibcso/ibcso/).

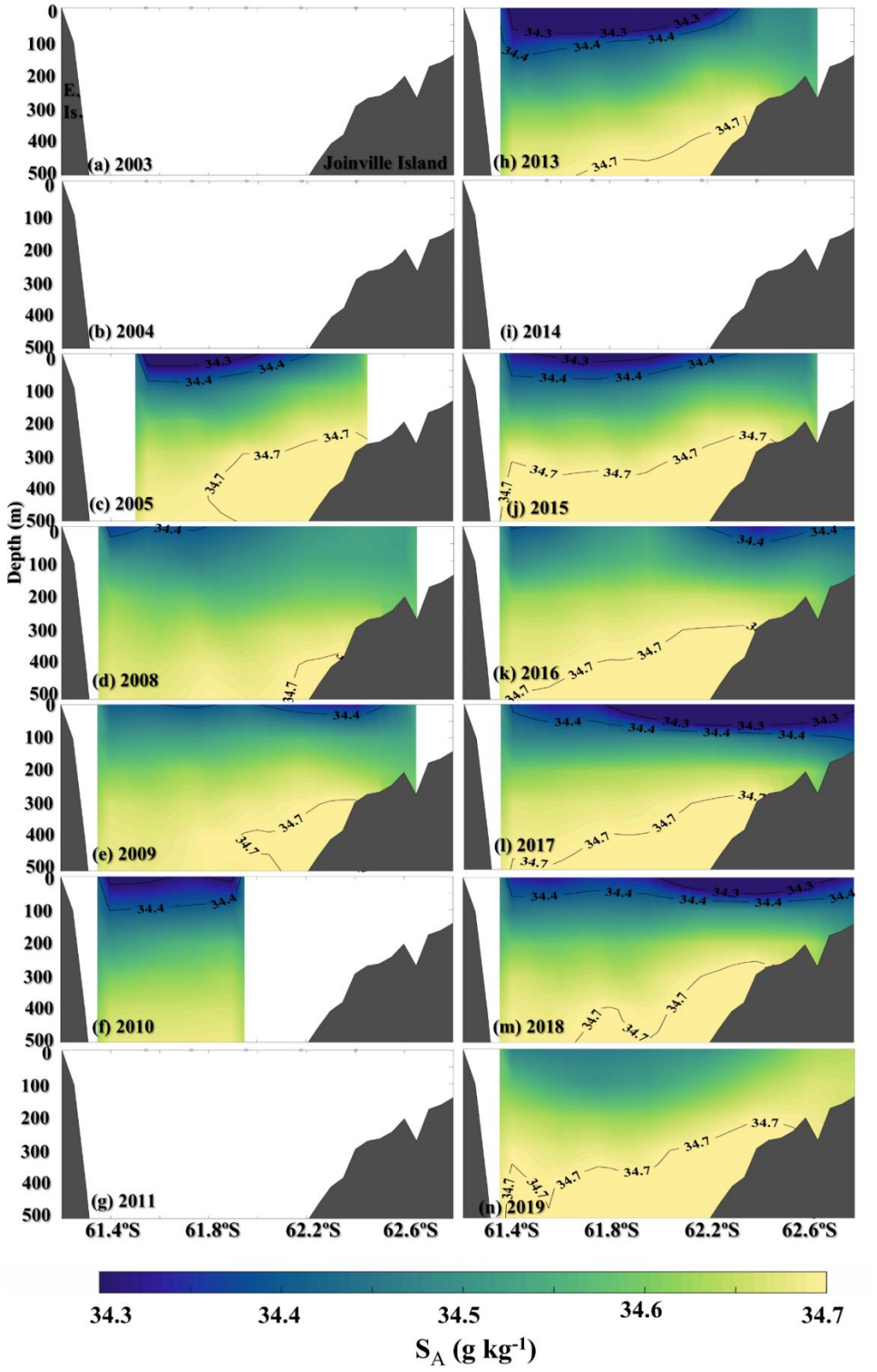


Supplementary Figure 11: As **Supplementary Figure S10** but for section 2, between Elephant (E.Is.) and Joinville Islands.

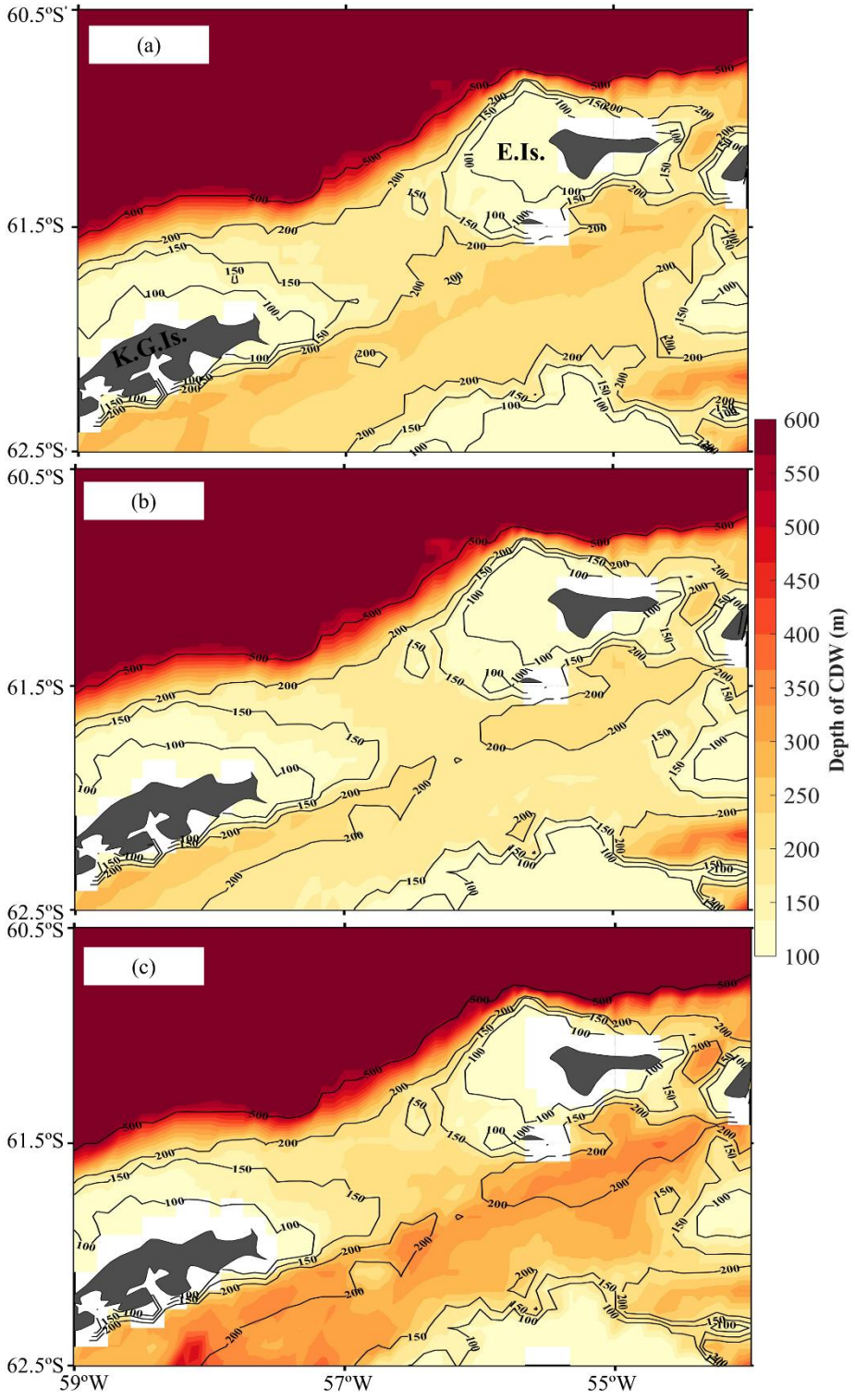


Supplementary Figure 12: Annual cross–section absolute salinity in Section 1 (S_A in g kg^{-1}), between King George and D' Urville Islands. The thin black lines indicate the 34.3, 34.4 and 34.7 isolines. The topographic feature along the sections is shown in black and is based on IBCSO v1.0 data

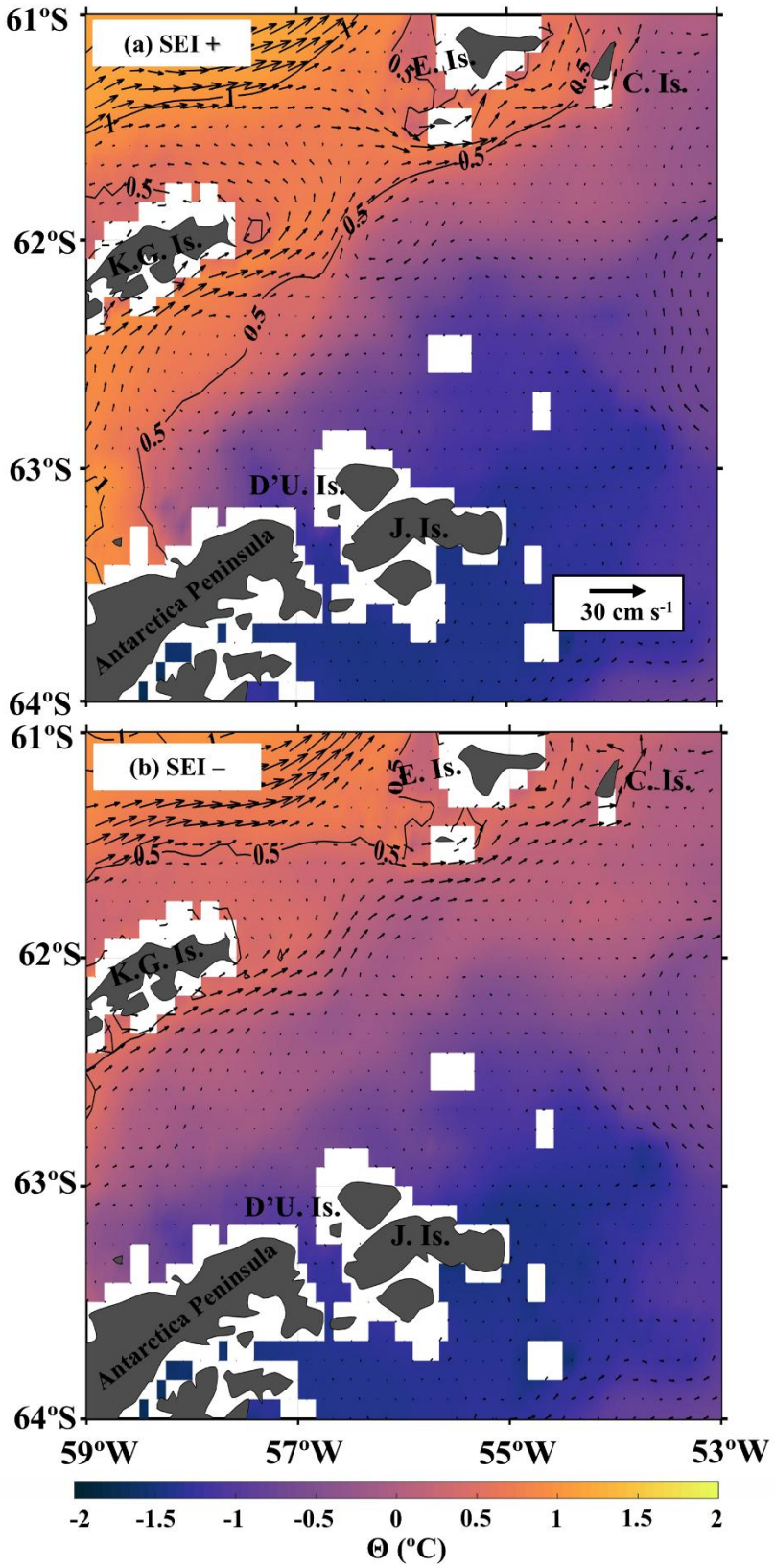
(https://www.scar.org/science/ibcso/ibcso/).



Supplementary Figure 13: As **Supplementary Figure 12** but for section 2, between Elephant (E. Is.) and Joinville Islands.

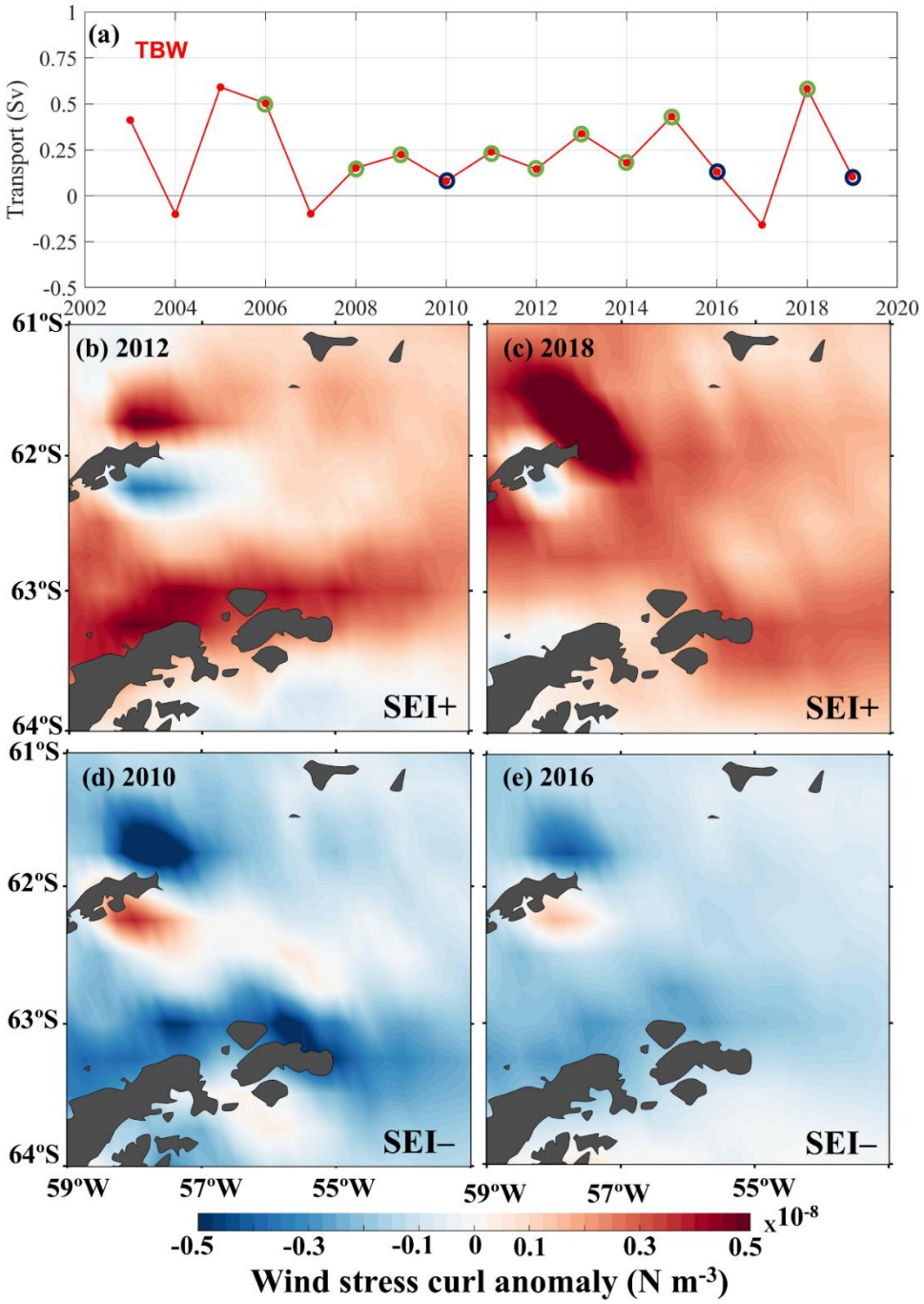


Supplementary Figure 14: Distribution of average Circumpolar Deep Water (CDW) thickness layer (colour) during **(a)** the entire study period (2003-2019), **(b)** positive Southern Annular Mode–El Niño–Southern Oscillation Index (SEI+) phases (*i.e.,* 2008, 2009, 2011, 2013, 2014, 2015, and 2018) and **(c)** negative SEI (SEI–) phases (*i.e.,* 2004, 2010, 2016, and 2019. Elephant and King George Islands are labelled as E. Is., and K.G. Is., respectively.

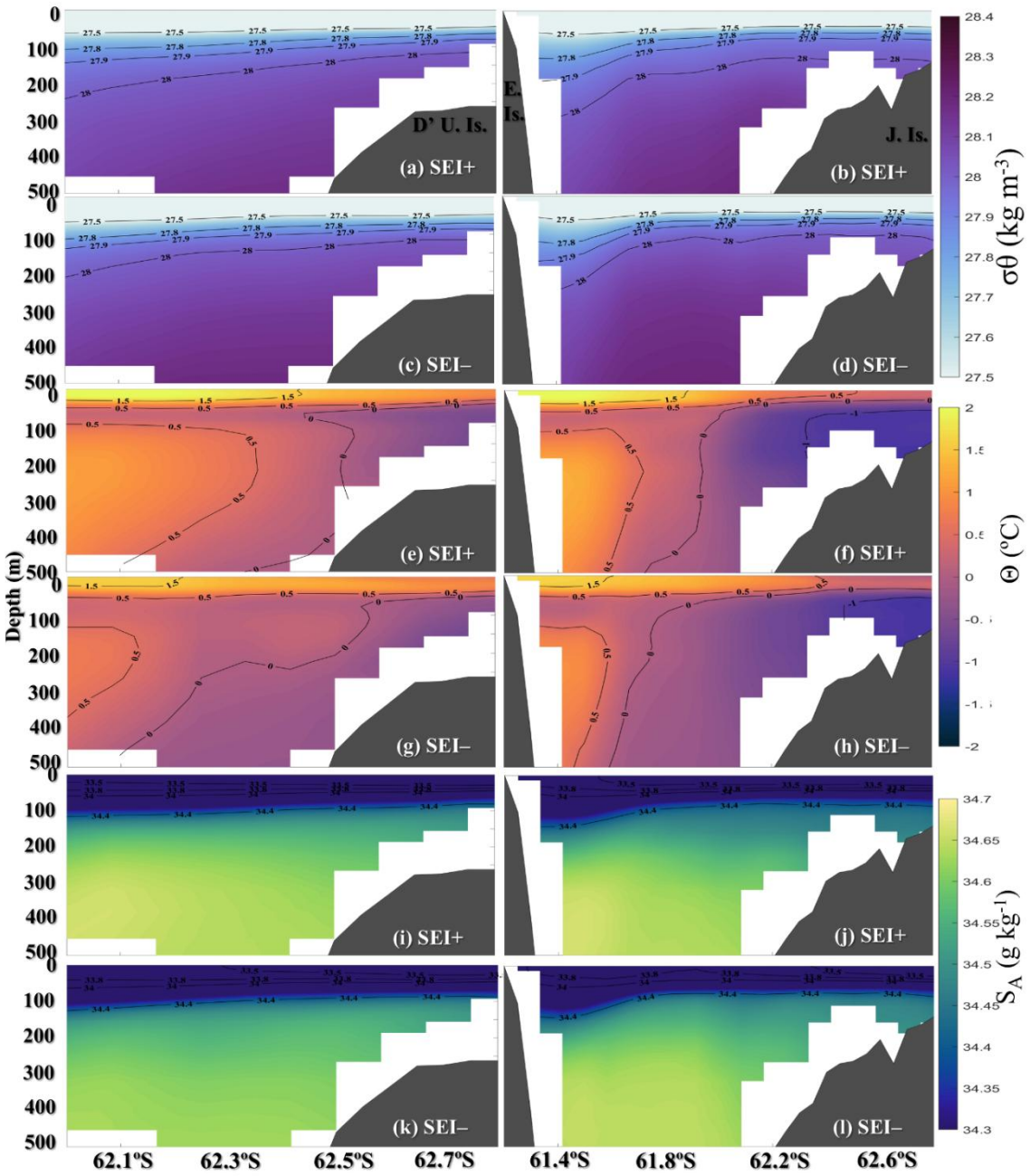


Supplementary Figure 15: Depth–averaged (50–500 m) of conservative temperature – Θ (colour–coded) and the depth–integrated (50–500 m) geostrophic velocity (vectors) of (a) SEI+ phase summers (*i.e.,* 2006, 2008, 2009, 2011, 2012, 2013, 2014, 2015, and 2018) and (b) SEI–phase summers (*i.e.,* 2010, 2016, and

2019). The acronyms stand for: D' Urville Island (D'U.Is.), Clarence Island (C. Is.), Elephant Island (E. Is.), and Joinville Island (J.Is.).



Supplementary Figure 16: (a) Time–series of Transitional Zonal Water with Bellingshausen influence (TBW) transports. The green circles represent the SEI+ years, while the blue circles indicate the SEI– years. Positive (negative) values indicate TBW inflow (outflow) to Bransfield Strait Panels **(b)** and **(c)** show the surface horizontal distribution of the wind stress curl anomaly (colour–coded) during positive SEI phase (*i.e.,* 2012 and 2018, respectively), while panels **(d)** and **(f)** represent negative SEI phase (*i.e.,* 2010 and 2016, respectively). The years were selected to represent a year of highest and lowest TBW intrusion for each SEI period (*e.g.,* SEI+ and SEI–).



Supplementary Figure 17: Potential density anomaly (σθ, in kg m⁻³), conservative temperature (Θ ºC) and absolute salinity (S_A g kg⁻1) within the Bransfield Strait system at sections 1 (between Elephant Island – E. Is. and Joinville Islands – J. Is.) and 2 (between King George and D' Urville Island – D'U. Is.). Panels (a), (b), (e), (f), (i), and (j) represent the time-averaged conditions during SEI+ phase summers (2006, 2008, 2009, 2011, 2012, 2013, 2014, 2015, and 2018), while panels (c), (d), (g), (h), (k) and (i) represent the time-averaged conditions during SEI– phase summers (2010, 2016, and 2019).

Capítulo V: Sumário e conclusões

A seguir, serão destacados os principais pontos de discussão e conclusões gerados nessa tese. Primeiramente, esses destaques serão apresentados individualmente para cada artigo desta tese e, posteriormente, a tese será concluída com as considerações finais e o impacto à sociedade.

5.1 Variabilidade interdecenal das propriedades termohalinas da CDW no verão ao longo do oeste da Antártica e forçantes associadas

A CDW na região ao largo da plataforma continental do oeste da Antártica apresentou aquecimento e salinização interdecadais entre 1990 e 2010, com uma intensificação acentuada após 2010. A robustez desse cenário é reforçada pela concordância qualitativa e quantitativa entre os dados hidrográficos e a reanálise GLORYS. Os resultados reportados aqui refutaram a hipótese central desta tese, de que a variabilidade da CDW seria controlada principalmente pela modulação da posição dos sistemas frontais da ACC impulsionada pelos ventos de oeste, pois indicaram que o aquecimento da CDW ao largo da plataforma continental não decorre majoritariamente de um deslocamento meridional da SACCF. Embora a SACCF tenha migrado para o sul durante a década de 2010, a decomposição dos sinais termalinos revelou que essa contribuição foi secundária, respondendo por apenas 10% da variação observada. O componente predominante (90%) vincula-se a processos advectivos ao longo de isopicnais, interpretados como o efeito combinado de dois fatores: o aumento do transporte zonal de calor, associado ao fortalecimento do Giro de Ross, e o incremento

das trocas meridionais através da ACC, impulsionadas pela atividade de mesoescala e difusão isopicnal.

Assim, o trabalho sustenta que a margem oeste antártica integra um contexto amplo de aquecimento subsuperficial do oceano Austral, mas evidencia que os mecanismos locais diferem daqueles propostos para o leste do continente. Tais mudanças nas propriedades da CDW estão ligadas a forçantes atmosféricas de grande escala, especificamente à intensificação e ao deslocamento dos ventos de oeste para os polos, somados ao fortalecimento e ao aprofundamento da ASL, que reorganizaram a circulação regional. Dessa forma, o primeiro objetivo desta tese é cumprido ao isolar e quantificar o impacto real da migração frontal das frentes da ACC na alteração termohalina da CDW.

Por fim, verificou-se que o aquecimento ao largo da plataforma continental não ocorre de forma homogênea sobre a plataforma continental. Enquanto as intrusões de águas quentes foram favorecidas no oeste do mar de Amundsen e leste do mar de Bellingshausen, um resfriamento no leste de Amundsen e oeste de Bellingshausen foi observado. Essa diferença sugere que a intrusão de CDW é decisivamente modulada por processos locais na quebra de plataforma, tais como ventos, inclinação de isopicnais, a subcorrente do mar de Amundsen e a retenção de Água de Inverno (*Winter Water*). Tal constatação demonstra que a variabilidade na região ao largo da plataforma continental e a resposta da plataforma continental não apresentam um acoplamento linear.

5.2 Variabilidade interanual do Giro de Ross e seu papel na modulação das propriedades da CDW na região ao largo da plataforma continental no setor Amundsen–Bellingshausen

O segundo artigo desta tese investigou como a variabilidade sazonal e interanual do Giro de Ross modula o reservatório de calor da CDW na região ao largo da plataforma continental do oeste da Antártica, e como esse sinal se propaga para a plataforma continental. Com base na reanálise GLORYS12v1 (1993–2020), o estudo revelou que o Giro de Ross possui um ciclo sazonal bem definido e forte variabilidade interanual. Ao analisar uma série de 28 anos, este trabalho avança em relação a pesquisas de curto prazo, demonstrando que a correlação entre o fortalecimento do giro e as alterações nas propriedades da CDW é uma característica persistente em escala multidecenal, e não apenas um fenômeno esporádico.

Um dos principais achados foi a identificação do forçamento atmosférico dominante sobre o sistema. A intensidade e a área do giro mostraram-se fortemente vinculadas ao rotacional da tensão do cisalhamento total superficial oceânico, tanto no ciclo sazonal quanto nas anomalias interanuais. Em contrapartida, os fluxos de flutuabilidade na superfície não apresentaram relação estatística significativa. Isso indica que o Giro de Ross responde prioritariamente à injeção de momentum devido ao incremento de vorticidade ciclônica forçada pelo vento na região, e não a ajustes estéricos. Tal resultado consolida a interpretação de que a dinâmica do giro é controlada, sobretudo, pelo campo de ventos.

Além disso, foi observado que fases de intensificação do Giro de Ross coincidem com sua expansão espacial e com a presença de águas subsuperficiais mais quentes e salinas na margem continental profunda. Assim, o giro atua como um modulador do conteúdo de calor ao largo da plataforma continental, precondicionando o reservatório de CDW que, potencialmente, alimenta a plataforma continental. Contudo, a resposta das águas sobre a plataforma não ocorre de forma síncrona ou linear em relação ao regime ao largo da plataforma continental. Em vez de uma propagação direta, os resultados indicam um contraste regional marcante: a plataforma do mar de Amundsen apresentou tendências de resfriamento, dessalinização e aprofundamento da termoclina, sugerindo menor acesso ao calor da CDW. Já a plataforma do mar de Bellingshausen exibiu aquecimento, salinização e soerguimento da termoclina. Essa diferença reforça que, embora o Giro de Ross gerencie o reservatório de calor ao largo da plataforma continental, a transferência efetiva de calor através da quebra de plataforma é mediada por processos locais, como ventos costeiros, batimetria e atividade de mesoescala. Com a identificação dessa dinâmica e da dependência do giro em relação ao rotacional da tensão do cisalhamento total superficial oceânico, cumpre-se o segundo objetivo, estabelecendo de forma robusta como o Giro de Ross atua como o principal modulador do conteúdo de calor na região ao largo da plataforma continental, a qual precede a intrusão na plataforma continental.

5.3 Circulação de verão e transporte de massas de água no estreito de Bransfield, Antártica

Neste capítulo da tese, foi caracterizada, a circulação de verão no estreito de Bransfield em longo prazo, integrando dados hidrográficos (2003–2019), altimetria de satélite e a reanálise oceânica GLORYS. Os resultados confirmam uma circulação

regional ciclônica, estruturada por duas correntes principais: a BC, que flui para o nordeste ao longo das ilhas Shetland do Sul, e a ACoC, que escoa para sudoeste acompanhando a Península Antártica.

Observou-se que parte da BC deixa a bacia leste pela passagem entre as ilhas King George e Clarence, recirculando as ilhas Shetland do Sul, enquanto outra fração é alimentada por intrusões provenientes da passagem entre as ilhas King George e Elephant. A convergência entre estimativas hidrográficas, altimétricas e de reanálise conferiu consistência à identificação da entrada da ACoC em aproximadamente 62,40°S e 55,00°W. Além disso, o estudo evidencia que a variabilidade interanual das propriedades termalinas no estreito é ditada pela intensidade relativa dessas correntes, que controlam a advecção de TBW e da TWW.

A utilização do GLORYS permitiu quantificar o transporte de TBW em 0,34 ± 0,24 Sv (Seção 1) e 0,53 ± 0,34 Sv (Seção 2), implicando uma intrusão média de 0,23 ± 0,20 Sv para a bacia leste. Assim, a tese converte uma hipótese qualitativa recorrente na literatura em uma estimativa quantitativa, consolidando essa passagem entre as ilhas Shetland do Sul e a ilha Elephant como uma via crítica para a entrada de águas com influência de Bellingshausen e da CDW (*i.e.,* TBW) no estreito. Além disso, essa tese demonstrou que a intrusão de TBW por essa passagem é sensível ao modo climático SEI. Em fases de SEI+, os ventos favorecem o deslocamento da SACCF em direção à Península, intensificando o curl negativo do estresse do vento e a sucção de Ekman. Esse mecanismo potencializa a ressurgência de CDW rasa, favorecendo a formação e intrusão de TBW no estreito (0,31 ± 0,16 Sv). Inversamente, sob condições SEI−, a redução da ressurgência limita esse transporte a 0,10 ± 0,03 Sv. Assim, a circulação de verão no estreito de Bransfield não é um sistema isolado, mas uma resposta direta à modulação atmosférica de larga escala. A obtenção dessas taxas de transporte inéditas e a correlação estabelecida com o índice SEI atestam o cumprimento do terceiro objetivo, fornecendo a base física e quantitativa para a compreensão da variabilidade no transporte de CDW na Península Antártica.

5.4 Considerações Finais

Esta tese demonstra que a variabilidade das propriedades da CDW e de massas d'água derivadas dela, ao redor do oeste da Antártica e no norte da Península Antártica,

resulta da interação entre forçantes atmosféricas de grande escala e processos oceanográficos regionais que controlam a redistribuição e a transferência de calor. Em conjunto, os resultados mostram que a circulação de larga escala reorganiza o conteúdo de calor disponível ao redor da Antártica, mas que a sua expressão sobre a plataforma continental e em bacias costeiras não ocorre de forma automática, linear ou espacialmente uniforme. A principal contribuição conceitual desta tese é, portanto, evidenciar que a região ao largo da plataforma continental e a plataforma continental não devem ser tratadas como um sistema diretamente acoplado, pois a transferência efetiva de calor para as margens antárticas depende de mecanismos locais e regionais que modulam ou até bloqueiam esse sinal.

No setor Amundsen–Bellingshausen, a tese mostra que o aquecimento interdecenal da CDW na região ao largo da plataforma continental foi dominado principalmente por processos advectivos ao longo de isopicnais, associados ao fortalecimento do Giro de Ross e ao aumento das trocas de calor transversais à ACC, enquanto o deslocamento meridional da SACCF exerceu contribuição secundária. Em escalas sazonais e interanuais, verificou-se ainda que a variabilidade do Giro de Ross é controlada sobretudo pelo rotacional da tensão do cisalhamento total superficial oceânico, reforçando seu papel como modulador do reservatório subsuperficial de calor ao largo da plataforma. No entanto, esse reservatório ao largo da plataforma continental mais quente e salino não se traduz em uma resposta síncrona sobre a plataforma continental. A plataforma do mar de Amundsen apresentou resfriamento, dessalinização e aprofundamento da termoclina, enquanto a do mar de Bellingshausen mostrou aquecimento, salinificação e elevação da termoclina, evidenciando que a transferência de calor para a plataforma depende da interação entre ventos costeiros, estrutura frontal local, profundidade da termoclina, batimetria e processos de quebra da plataforma.

No norte da Península Antártica, a tese mostra que a circulação de verão e o transporte de massas d'água no estreito de Bransfield também respondem à variabilidade atmosférica de grande escala, especialmente aos efeitos combinados de SAM e ENSO, que modulam os ventos regionais, a posição da SACCF e a intrusão de águas com influência do mar de Bellingshausen. Assim, embora os três artigos abordem contextos oceanográficos distintos, todos convergem para a mesma interpretação: a variabilidade de larga escala precondiciona a redistribuição do calor ao redor da Antártica, enquanto sua transferência efetiva para plataformas continentais, margens glaciais e bacias

costeiras é controlada por mecanismos regionais e locais. De forma mais ampla, os resultados ressaltam a necessidade de projetar esses mecanismos sob cenários futuros, avaliando como a intensificação e o deslocamento para o sul dos ventos de oeste, bem como a maior recorrência de configurações atmosféricas favoráveis, poderão alterar a redistribuição da CDW, a intrusão de calor sobre a plataforma e, consequentemente, a estabilidade das geleiras e plataformas de gelo do oeste da Antártica.

5.5 Impactos na sociedade

Do ponto de vista científico e social, os resultados desta tese são relevantes porque mostram que mudanças na circulação oceânica e atmosférica ao redor do oeste da Antártica podem alterar a disponibilidade e a transferência de calor para as plataformas de gelo, com consequências potenciais para a estabilidade da camada de gelo e para a elevação do nível do mar. Embora esses processos atuem em regiões remotas, seus efeitos podem se propagar globalmente, aumentando a vulnerabilidade de zonas costeiras, infraestrutura urbana, portos e populações expostas a inundações e erosão costeira. Em um sentido mais amplo, aprimorar a compreensão desses mecanismos também é importante para reduzir incertezas sobre os processos climáticos de grande escala que podem influenciar a frequência, a intensidade e os impactos de eventos extremos que têm se tornado cada vez mais evidentes nos últimos anos. Nesse contexto, esta tese também fornece subsídios para o aprimoramento dos modelos utilizados no estudo do oceano Austral, ao identificar os mecanismos que conectam a circulação de grande escala, a variabilidade atmosférica e os processos regionais na quebra da plataforma à redistribuição de calor ao largo da plataforma continental e à sua potencial intrusão sobre a plataforma continental. Esse avanço é particularmente importante porque uma representação mais realista da interação entre oceano e gelo é essencial para compreender as causas do derretimento basal das plataformas de gelo, avaliar a resposta futura das margens glaciais antárticas e produzir projeções mais robustas da contribuição da Antártica para a elevação do nível do mar. Assim, compreender os mecanismos que regulam o aquecimento da CDW, sua variabilidade ao largo da plataforma continental e sua transferência para a plataforma continental não é apenas uma questão de oceanografia física local, mas um passo necessário para reduzir incertezas sobre impactos climáticos futuros que podem afetar diretamente a sociedade.

Capítulo VI: Agradecimentos

This study is part of the activities of the Brazilian High Latitude Oceanography Group (GOAL) within the Brazilian Antarctic Program (PROANTAR). GOAL has been funded and/or has received logistical support from the Brazilian Ministry of the Environment (MMA), the Brazilian Ministry of Science, Technology, and Innovation (MCTI), the National Council for Scientific and Technological Development (CNPq), the Brazilian Navy, the Inter-ministerial Secretariat for Sea Resources (SECIRM), the National Institute of Science and Technology of the Cryosphere (INCT CRIOSFERA; CNPq Grant Nos. 573720/2008-8, 465680/2014-3, and 408461/2024-1), and the Research Support Foundation of the State of Rio Grande do Sul (FAPERGS; Grant No. 17/2551-000518-0). This work was conducted within the framework of multiple GOAL projects (including CNPq Grant Nos. 550370/2002-1, 520189/2006-0, 556848/2009-8, 565040/2010-3, 405869/2013-4, 407889/2013-2, 442628/2018-8, 442637/2018-7, 440859/2023-9, and 440865/2023-9), as well as the activities of the CARBON Team (www.carbonteam.furg.br). Additional support was provided by the Coordination for the Improvement of Higher Education Personnel (CAPES) through the “Ciências do Mar” program (Grant No. 23038.001421/2014-30). CAPES also provided access to scientific literature through the “Periódicos CAPES” portal and support via the Graduate Program

in Oceanology. This study also contributes to the TARSAN project, part of the International Thwaites Glacier Collaboration (ITGC), with support from the National Science Foundation (NSF; Grant 1929991) and the Natural Environment Research Council (NERC; Grant NE/S006419/1). Logistical support was provided by the NSF U.S. Antarctic Program and the NERC British Antarctic Survey (ITGC Contribution No. ITGC-159). Brendon Yuri Damini acknowledges financial support from CAPES through PhD scholarships (Grant Nos. 88887.719848/2022-00 and 88881.982653/2024-01). Tiago S. Dotto was supported by the NERC National Capability Programme AtlantiS (NE/Y005589/1). Karen J. Heywood and Rob A. Hall were supported by NERC (Grant Nos. NE/P021395/1, NE/S006419/1, and NE/W007045/1). Alberto C. Naveira Garabato acknowledges support from U.K. Research and Innovation through guarantee funding for a European Research Council Advanced Grant (EP/X025136/1). Rodrigo Kerr and Mauricio M. Mata acknowledge research fellowships from CNPq (Grant Nos. 309978/2021-1 and 312569/2021-1). Ilana Wainer was supported by Fundação de Amparo à Pesquisa do Estado de São Paulo (FAPESP) 2020/14356-5; 2024/00949-5 and by CNPq/INCT: 408461/2024-1. Marina Noro was supported CNPq: 141102/2022-5]. The authors thank the officers and crew of the Brazilian Navy polar vessel Almirante Maximiano, as well as all scientists and technicians involved in the cruises, for their essential support during data collection and processing. We also acknowledge the constructive comments provided by anonymous reviewers, which significantly improved the quality of this work. All datasets used in this study are properly cited and available as indicated in the respective chapters.

Chapter V: Summary and Conclusions

Following this, the main discussion points and conclusions generated in this thesis are highlighted. First, these key findings are presented individually for each article included in the thesis, and subsequently, the thesis is concluded with final remarks and social impacts.

5.1 Interdecadal variability of CDW thermohaline properties in summer along West Antarctica and associated forcings

This thesis demonstrated that CDW in the off-shelf region of West Antarctica underwent interdecadal warming and salinification between the 1990s and the 2010s, with a marked intensification after 2010. The robustness of this pattern is reinforced by the qualitative agreement between the hydrographic data and the GLORYS reanalysis. The results reported here refuted the central hypothesis of this thesis, that the variability of the CDW would be controlled mainly by the modulation of the position of the ACC frontal systems driven by westerly winds, as they indicated that the warming of the off-shelf CDW does not result primarily from a meridional displacement of the SACCF. Although the SACCF migrated southward during the 2010s, the decomposition of the thermohaline signals revealed that this contribution was secondary, accounting for only 10% of the

observed variation. The dominant component (90%) is linked to advective processes along isopycnals, interpreted as the combined effect of two factors: enhanced zonal heat transport associated with Ross Gyre strengthening and increased meridional exchanges across the ACC, driven by mesoscale activity and isopycnal diffusion.

Thus, this work supports the view that the West Antarctica is embedded within a circumpolar context of subsurface warming in the Southern Ocean, while showing that the local mechanisms differ from those proposed for the eastern sector of the continent. These changes in CDW properties are linked to large-scale atmospheric forcing, specifically the intensification and poleward shift of the westerlies, together with the strengthening and deepening of the ASL, which reorganized the regional circulation. Thus, the first objective of this thesis is achieved by isolating and quantifying the real impact of frontal migration of ACC fronts on the thermohaline alteration of CDW.

Finally, it was found that off-shelf warming does not occur uniformly across the continental shelf. While warm-water intrusions were allowed in the western Amundsen Sea and eastern Bellingshausen Sea, cooling was observed in the eastern Amundsen and western Bellingshausen sectors. This difference suggests that CDW intrusion is decisively modulated by local shelf-break processes, such as coastal winds, isopycnal slope, the Amundsen Sea Undercurrent, and the retention of Winter Water. This finding demonstrates that off-shelf variability and the continental shelf response are not linearly coupled.

5.2 Interannual variability of the Ross Gyre and its role in modulating CDW properties in the off-shelf Amundsen–Bellingshausen sector

The second article of this thesis examined how seasonal and interannual variability in the Ross Gyre modulates the off-shelf CDW heat reservoir in West

Antarctica, and the extent to which this signal extends onto the continental shelf. Based on the GLORYS12v1 reanalysis (1993–2020), the study revealed that the Ross Gyre exhibits a well-defined seasonal cycle and strong interannual variability. By analysing a 28-year record, this work advances beyond short-term studies by showing that the correlation between gyre strengthening and changes in CDW properties is a persistent multidecadal feature rather than merely an episodic phenomenon.

One of the main findings was the identification of the dominant atmospheric forcing acting to modulation the system. The gyre strength and area were found to be strongly linked to ocean surface stress curl, both in the seasonal cycle and in the interannual anomalies. In contrast, surface heat and freshwater fluxes (buoyancy fluxes) showed no statistically significant relationship. This indicates that the Ross Gyre responds primarily to wind-driven cyclonic vorticity input rather than to steric adjustments. This result reinforces the interpretation that gyre dynamics are controlled mainly by the wind field.

In addition, periods of Ross Gyre intensification were found to coincide with gyre expansion and with warmer, saltier subsurface waters along the deep continental margin. The gyre therefore acts as a modulator of the off-shelf heat content, preconditioning the CDW reservoir that potentially feeds the continental shelf. However, the shelf-water response does not occur synchronously or linearly with the off-shelf regime. Rather than a direct propagation, the results reveal a marked regional contrast: whereas the Amundsen Sea shelf showed cooling, freshening, and thermocline deepening, suggesting reduced access to CDW heat, the Bellingshausen Sea shelf exhibited warming, salinification, and thermocline shoaling. This contrast reinforces the idea that, although the Ross Gyre manages the off-shelf reservoir, the effective transfer of heat across the shelf break is mediated by local processes, such as coastal winds, bathymetry, and mesoscale activity.

By identifying this dynamic and the dependence of the gyre on the total ocean stress curl surface, the second objective is achieved, establishing how the Ross Gyre acts as the main modulator of the heat content over the off-shelf that precedes intrusion onto the continental shelf.

5.3 Summer circulation and water-mass transport in Bransfield Strait, Antarctica

In this chapter of the thesis, the long-term summer circulation in Bransfield Strait was characterized by integrating hydrographic data (2003–2019), satellite altimetry, and the GLORYS ocean reanalysis. The results confirm a regional cyclonic circulation structured by two main currents: the BC, which flows northeastward along the South Shetland Islands, and the ACoC, which flows southwestward along the Antarctic Peninsula.

It was observed that part of the BC leaves the eastern basin through the passage between King George and Clarence Islands, recirculating around the South Shetland Islands, while another fraction is fed by intrusions entering through the passage between King George and Elephant Island. The convergence between hydrographic, altimetric, and reanalysis estimates lends consistency to the identification of the ACoC inflow at approximately 62.40°S and 55.00°W. In addition, the study shows that the interannual variability of thermohaline properties within the strait is governed by the relative intensity of these currents, which control the advection of TBW and TWW.

The use of GLORYS allowed the quantification of TBW transport as 0.34 ± 0.24 Sv (Section 1) and 0.53 ± 0.34 Sv (Section 2), implying a mean intrusion of 0.23 ± 0.20 Sv into the eastern basin. In this way, the thesis transforms a recurring qualitative hypothesis in the literature into a quantitative estimate, establishing the passage between

the South Shetland Islands and Elephant Island as a critical pathway for the entry of waters influenced by the Bellingshausen Sea and CDW into the Bransfield Strait. Moreover, this thesis demonstrated that TBW intrusion through this passage is sensitive to the SEI climate mode. During SEI+ phases, winds favour the displacement of the SACCF toward the Peninsula, intensifying negative wind-stress curl and Ekman suction. This mechanism enhances the upwelling of shallow CDW, allowing the formation and intrusion of TBW into the strait (0.31 ± 0.16 Sv). Conversely, under SEI− conditions, reduced upwelling limits this transport to 0.10 ± 0.03 Sv. Thus, summer circulation in Bransfield Strait is not an isolated system, but rather a direct response to large-scale atmospheric modulation. Obtaining these transport rates, together with their correlation with the SEI index, demonstrates the achievement of the third objective by providing the physical and quantitative basis needed to understand the variability in CDW transport toward the Antarctic Peninsula.

5.4 Final Remarks

This thesis demonstrates that the variability of CDW properties, and of water masses derived from it, around West Antarctica and the northern Antarctic Peninsula results from the interaction between large-scale atmospheric forcing and regional oceanographic processes that govern heat redistribution and transfer. Taken together, the results show that large-scale circulation reorganizes the heat content available around Antarctica, but its expression on the continental shelf and in coastal basins does not occur in an automatic, linear, or spatially uniform way. The main conceptual contribution of this thesis is therefore to show that the off-shelf ocean and the continental shelf should not be treated as a directly coupled system, because the effective transfer of heat toward the Antarctic margins depends on local and regional mechanisms that can modulate, delay, or even inhibit that signal.

In the Amundsen–Bellingshausen sector, the thesis shows that interdecadal off-shelf CDW warming was dominated primarily by advective processes along isopycnals, associated with Ross Gyre strengthening and enhanced cross-ACC heat exchange, whereas the meridional displacement of the SACCF made a secondary contribution. On seasonal to interannual timescales, Ross Gyre variability was also found to be controlled mainly by ocean surface stress curl, reinforcing its role as a modulator of the subsurface heat reservoir offshore of the continental shelf. Yet this warmer and saltier off-shelf reservoir does not translate into a synchronous response on the continental shelf. The Amundsen Sea shelf exhibited cooling, freshening, and thermocline deepening, whereas the Bellingshausen Sea shelf showed warming, salinification, and thermocline shoaling, indicating that heat transfer onto the shelf depends on the interaction between coastal winds, local frontal structure, thermocline depth, bathymetry, and shelf-break processes.

In the northern Antarctic Peninsula, the thesis shows that summer circulation and water-mass transport in Bransfield Strait also respond to large-scale atmospheric variability, especially to the combined effects of the SAM and the ENSO, which modulate regional winds, the position of the SACCF, and the intrusion of Bellingshausen-influenced waters into the region. Thus, although the three articles address distinct oceanographic settings, they all converge on the same interpretation: large-scale variability preconditions heat redistribution around Antarctica, whereas its effective transfer to continental shelves, glacial margins, and coastal basins is controlled by regional and local mechanisms. More broadly, these findings highlight the need to project these mechanisms under future scenarios, assessing how the intensification and poleward shift of the westerlies, together with the increased recurrence of favorable atmospheric configurations, may alter CDW redistribution, shelf heat intrusion, and, consequently, the stability of West Antarctic glaciers and ice shelves.

5.5 Social Impacts

From both scientific and social perspectives, the results of this thesis are relevant because they show that changes in oceanic and atmospheric circulation around West Antarctica can alter the availability and transfer of heat to ice shelves, with potential consequences for ice-sheet stability and sea-level rise. Although these processes act in remote regions, their effects can propagate globally, increasing the vulnerability of coastal zones, urban infrastructure, ports, and populations exposed to flooding and coastal erosion. In a broader sense, improving our understanding of these mechanisms is also important for reducing uncertainties about the large-scale climate processes that can influence the frequency, intensity, and impacts of extreme events that have become increasingly evident in recent years. In this context, this thesis also provides support for improving the models used to study the Southern Ocean by identifying the mechanisms that connect large-scale circulation, atmospheric variability, and regional shelf-break processes to off-shelf heat redistribution and its potential intrusion onto the continental shelf. This advance is particularly important because a more realistic representation of ocean–ice interactions is essential for understanding the causes of basal ice-shelf melting, assessing the future response of Antarctic glacial margins, and producing more robust projections of Antarctica's contribution to sea-level rise. Thus, understanding the mechanisms that regulate CDW warming, its off-shelf variability, and its transfer onto the continental shelf is not merely a matter of local physical oceanography, but a necessary step toward reducing uncertainties about future climate impacts that may directly affect society.

Capítulo VII: Referências Bibliográficas

Andres-Martin M, Azorin-Molina C, Serrano E, et al. (2024) Near-surface wind speed trends and variability over the Antarctic Peninsula, 1979–2022. Atmos. Res. 309, 107568. https://doi.org/10.1016/J.ATMOSRES.2024.107568

Armitage TWK, Bacon S, Kwok R (2018) Arctic Sea Level and Surface Circulation Response to the Arctic Oscillation. Geophys. Res. Lett. 45, 6576–6584. https://doi.org/10.1029/2018GL078386

Arneborg L, Wahlin AK, Björk G, et al. (2012) Persistent inflow of warm water onto the central Amundsen shelf. Nat. Geosci. 5, 876–880. https://doi.org/10.1038/ngeo1644

Auger M, Morrow R, Kestenare E, et al. (2021) Southern Ocean in-situ temperature trends over 25 years emerge from interannual variability. Nature Communications 2021 12:1 12, 514-. https://doi.org/10.1038/s41467-020-20781-1

Avelina R, Cotrim da Cunha L, Farias CDO, et al. (2020) Contrasting dissolved organic carbon concentrations in the Bransfield strait, Northern Antarctic peninsula: Insights into ENSO and SAM effects. Journal of Marine Systems 103457. https://doi.org/10.1016/j.jmarsys.2020.103457

Azaneu M, Kerr R, Mata MM, et al. (2013) Trends in the deep Southern Ocean (1958-2010): Implications for Antarctic Bottom Water properties and volume export. J. Geophys. Res. Oceans 118, 4213–4227. https://doi.org/10.1002/jgrc.20303

Azaneu M, Webber B, Heywood KJ, et al. (2023) Influence of Shelf Break Processes on the Transport of Warm Waters Onto the Eastern Amundsen Sea Continental Shelf. J. Geophys. Res. Oceans 128, e2022JC019535. https://doi.org/10.1029/2022JC019535

Billany W, Swart S, Hermes J, et al. (2010) Variability of the Southern Ocean fronts at the Greenwich Meridian. Journal of Marine Systems 82, 304–310. https://doi.org/10.1016/J.JMARSYS.2010.06.005

Böning CW, Dispert A, Visbeck M, et al. (2008) The response of the Antarctic Circumpolar Current to recent climate change. Nat. Geosci. 1, 864–869. https://doi.org/10.1038/ngeo362

Cai W, Santoso A, Wang G, et al. (2015) ENSO and greenhouse warming. Nature Climate Change 2015 5:9 5, 849–859. https://doi.org/10.1038/nclimate2743

Castagno P, Falco P, Dinniman MS, et al. (2017) Temporal variability of the Circumpolar Deep Water inflow onto the Ross Sea continental shelf. Journal of Marine Systems 166, 37–49. https://doi.org/10.1016/J.JMARSYS.2016.05.006

Chapman CC, Lea MA, Meyer A, et al. (2020) Defining Southern Ocean fronts and their influence on biological and physical processes in a changing climate. Nature Climate Change 2020 10:3 10, 209–219. https://doi.org/10.1038/s41558-020-0705-4

Christie FDW, Steig EJ, Gourmelen N, et al. (2023) Inter-decadal climate variability induces differential ice response along Pacific-facing West Antarctica. Nature Communications 2023 14:1 14, 93-. https://doi.org/10.1038/s41467-022-35471-3

Chu PC, Fan C (2007) An inverse model for calculation of global volume transport from wind and hydrographic data. Journal of Marine Systems 65, 376–399. https://doi.org/10.1016/J.JMARSYS.2005.06.010

Clem KR, Fogt RL (2015) South Pacific circulation changes and their connection to the tropics and regional Antarctic warming in austral spring, 1979-2012. J. Geophys. Res. 120, 2773–2792. https://doi.org/10.1002/2014JD022940

Clem KR, Renwick JA, McGregor J, et al. (2017) Large-Scale Forcing of the Amundsen Sea Low and Its Influence on Sea Ice and West Antarctic Temperature. J. Clim. 30, 8405–

8424. https://doi.org/10.1175/JCLI-D-16-0891.1

Cochran JR, Tinto KJ, Bell RE (2020) Detailed Bathymetry of the Continental Shelf Beneath the Getz Ice Shelf, West Antarctica. J. Geophys. Res. Earth Surf. 125, e2019JF005493. https://doi.org/10.1029/2019JF005493

Collares LL, Mata MM, Kerr R, et al. (2018) Iceberg drift and ocean circulation in the northwestern Weddell Sea, Antarctica. Deep Sea Research Part II: Topical Studies in Oceanography 149, 10–24. https://doi.org/10.1016/j.dsr2.2018.02.014

Cook AJ, Holland PR, Meredith MP, et al. (2016) Ocean forcing of glacier retreat in the western Antarctic Peninsula 353

Costa RR, Ferreira A, de Souza MS, et al. (2023) Physical-biological drivers modulating phytoplankton seasonal succession along the Northern Antarctic Peninsula. Environ. Res. 231, 116273. https://doi.org/10.1016/J.ENVRES.2023.116273

Costa RR, Mendes CRB, Tavano VM, et al. (2020) Dynamics of an intense diatom bloom in the Northern Antarctic Peninsula, February 2016. Limnol. Oceanogr. https://doi.org/10.1002/lno.11437

Cotrim da Cunha L, Hamacher C, Farias CDO, et al. (2018) Contrasting end-summer distribution of organic carbon along the Gerlache Strait, Northern Antarctic Peninsula: Bio-physical interactions. Deep Sea Research Part II: Topical Studies in Oceanography 149, 206–217. https://doi.org/10.1016/j.dsr2.2018.03.003

Couto N, Martinson DG, Kohut J, et al. (2017) Distribution of Upper Circumpolar Deep Water on the warming continental shelf of the West Antarctic Peninsula. J. Geophys. Res. Oceans 122, 5306–5315. https://doi.org/10.1002/2017JC012840

Cowley, R., Killick, R. E., Boyer, T., Gouretski, V., Reseghetti, F., Kizu, S., et al. (2021). International quality-controlled ocean database (IQuOD) v0.1: The temperature uncertainty specification. Frontiers in Marine Science, 8, 689695. https://doi.org/10.3389/fmars.2021.689695

Czaja A, Hausmann U, Czaja A, et al. (2009) Observations of Entry and Exit of Potential Vorticity at the Sea Surface. J. Phys. Oceanogr. 39, 2280–2294.

https://doi.org/10.1175/2009JPO4024.1

Damini BY, Brum AL, Hall RA, et al. (2025) Summer circulation and water masses transport in Bransfield Strait, Antarctica: An evaluation of their response to combined effects of Southern Annular Mode and El Niño–Southern Oscillation. Deep Sea Research Part I: Oceanographic Research Papers 222, 104516. https://doi.org/10.1016/J.DSR.2025.104516

Damini BY, Kerr R, Dotto TS, et al. (2022) Long-term changes on the Bransfield Strait deep water masses: Variability, drivers and connections with the northwestern Weddell Sea. Deep Sea Research Part I: Oceanographic Research Papers 179, 103667. https://doi.org/10.1016/j.dsr.2021.103667

de Verdière AC, Verdière AC de (1989) On the interaction of wind and buoyancy driven gyres. J. Mar. Res. 47

Dee DP, Uppala SM, Simmons AJ, et al. (2011) The ERA-Interim reanalysis: Configuration and performance of the data assimilation system. Quarterly Journal of the Royal Meteorological Society 137, 553–597. https://doi.org/10.1002/QJ.828

Drévillon *et al.,* M. Drévillon, E. Fernandez, J. Lellouche., 2022. Product user manual for the global ocean physical multi year product GLOBAL_MULTIYEAR_PHY_001_030, 10.48670/moi-00021

Dias FB, England MH, Morrison AK, et al. (2025) Seasonal variability of ocean heat transport and ice-shelf basal melt around Antarctica. Cryosphere 19, 5231–5258. https://doi.org/10.5194/TC-19-5231-2025

Dinniman MS, Klinck JM, Smith WO, et al. (2011) Deep-Sea Research II A model study of Circumpolar Deep Water on the West Antarctic Peninsula and Ross Sea continental shelves. Deep-Sea Research Part II 58, 1508–1523. https://doi.org/10.1016/j.dsr2.2010.11.013

Dong X, Wang Y, Shugui HOU, et al. (2020) Robustness of the Recent Global Atmospheric Reanalyses for Antarctic Near-Surface Wind Speed Climatology. J. Clim. 33, 4027–4043. https://doi.org/10.1175/JCLI-D-19-0648.1

Dotto TS, Garabato ACN, Bacon S, et al. (2019) Wind-Driven Processes Controlling Oceanic Heat Delivery to the Amundsen Sea, Antarctica. J. Phys. Oceanogr. 49, 2829–2849. https://doi.org/10.1175/JPO-D-19-0064.1

Dotto TS, Kerr R, Mata MM, et al. (2016) Multidecadal freshening and lightening in the deep waters of the Bransfield Strait, Antarctica. J. Geophys. Res. Oceans 121, 3741–3756. https://doi.org/10.1002/2015JC011228

Dotto TS, Mata MM, Kerr R, et al. (2021) A novel hydrographic gridded data set for the northern Antarctic Peninsula. Earth Syst. Sci. Data 13, 671–696. https://doi.org/10.5194/ESSD-13-671-2021

Dotto TS, Naveira Garabato A, Bacon S, et al. (2018) Variability of the Ross Gyre, Southern Ocean: Drivers and Responses Revealed by Satellite Altimetry. Geophys. Res. Lett. 45, 6195–6204. https://doi.org/10.1029/2018GL078607

Dotto TS, Naveira Garabato AC, Wåhlin AK, et al. (2020) Control of the Oceanic Heat Content of the Getz-Dotson Trough, Antarctica, by the Amundsen Sea Low. J. Geophys. Res. Oceans 125, e2020JC016113. https://doi.org/10.1029/2020JC016113

Dufour CO, Griffies SM, de Souza GF, et al. (2015) Role of Mesoscale Eddies in Cross-Frontal Transport of Heat and Biogeochemical Tracers in the Southern Ocean. J. Phys. Oceanogr. 45, 3057–3081. https://doi.org/10.1175/JPO-D-14-0240.1

Dutrieux P, Stewart C, Jenkins A, et al. (2014) Basal terraces on melting ice shelves. Geophys. Res. Lett. 41, 5506–5513. https://doi.org/10.1002/2014GL060618

Fahrbach E, Rohardt G, Krause G (1992) The Antarctic coastal current in the southeastern Weddell Sea. Polar Biol. 12, 171–182. https://doi.org/10.1007/BF00238257

Ferrari R, Nikurashin M (2010) Suppression of Eddy Diffusivity across Jets in the Southern Ocean. J. Phys. Oceanogr. 40, 1501–1519. https://doi.org/10.1175/2010JPO4278.1

Ferreira A, Costa RR, Dotto TS, et al. (2020) Changes in Phytoplankton Communities Along the Northern Antarctic Peninsula: Causes, Impacts and Research Priorities. Front. Mar. Sci. 7. https://doi.org/10.3389/fmars.2020.576254

Flexas MM, Thompson AF, Schodlok MP, et al. (2022) Antarctic Peninsula warming triggers

enhanced basal melt rates throughout West Antarctica. Sci. Adv. 8. https://doi.org/10.1126/SCIADV.ABJ9134

Fogt RL, Jones JM, Renwick J, et al. (2012) Seasonal Zonal Asymmetries in the Southern Annular Mode and Their Impact on Regional Temperature Anomalies. J. Clim. 25, 6253–6270. https://doi.org/10.1175/JCLI-D-11-00474.1

Fogt RL, Marshall GJ (2020) The Southern Annular Mode: Variability, trends, and climate impacts across the Southern Hemisphere. Wiley Interdiscip. Rev. Clim. Change 11, 1–24. https://doi.org/10.1002/wcc.652

Frederikse T, Landerer F, Caron L, et al. (2020) The causes of sea-level rise since 1900. Nature 2020 584:7821 584, 393–397. https://doi.org/10.1038/s41586-020-2591-3

Friedlingstein P, Sullivan MO, Jones MW, et al. (2020) Global Carbon Budget 2020 2020, 3269–3340

Frölicher TL, Sarmiento JL, Paynter DJ, et al. (2015) Dominance of the Southern Ocean in Anthropogenic Carbon and Heat Uptake in CMIP5 Models. J. Clim. 28, 862–886. https://doi.org/10.1175/JCLI-D-14-00117.1

García MA, López O, Sospedra J, et al. (1994) Mesoscale variability in the Bransfield Strait region (Antarctica) during Austral summer. Ann. Geophys. 12, 856–867. https://doi.org/10.1007/s00585-994-0856-z

García MA, Castro CG, Ríos AF, et al. (2002) Water masses and distribution of physico-chemical properties in the Western Bransfield Strait and Gerlache Strait during Austral summer 1995/96. Deep. Sea. Res. 2. Top. Stud. Oceanogr. 49, 585–602. https://doi.org/10.1016/S0967-0645(01)00113-8

Gille ST (2014) Meridional displacement of the Antarctic Circumpolar Current. Philosophical Transactions of the Royal Society A: Mathematical, Physical and Engineering Sciences 372. https://doi.org/10.1098/RSTA.2013.0273

Gille ST (2008) Decadal-Scale Temperature Trends in the Southern Hemisphere Ocean. J. Clim. 21, 4749–4765. https://doi.org/10.1175/2008JCLI2131.1

Gille ST (2002) Warming of the Southern Ocean since the 1950s. Science (1979). 295, 1275–

1277. https://doi.org/10.1126/SCIENCE.1065863/SUPPL_FILE/1065863S1_THUMB.GIF

Gille ST, McKee DC, Martinson DG (2016) Temporal changes in the Antarctic circumpolar current: Implications for the Antarctic continental shelves. Oceanography 29, 96–105. https://doi.org/10.5670/OCEANOG.2016.102

Good, S.A., Martin, M.J., Rayner, N.A., 2013. EN4: Quality controlled ocean temperature and salinity profiles and monthly objective analyses with uncertainty estimates. J. Geophys. Res. Oceans 118, 6704–6716. https://doi.org/10.1002/2013JC009067

Gómez-Valdivia F, Holland PR, Siahaan A, et al. (2023) Projected West Antarctic Ocean Warming Caused by an Expansion of the Ross Gyre. Geophys. Res. Lett. 50, e2023GL102978. https://doi.org/10.1029/2023GL102978

Gomis, D., García, M.A., L´opez, O., Pascual, A., 2002. Quasi-geostrophic 3D circulation and mass transport in the western Bransfield Strait during Austral summer 1995/96. Deep Sea Res. Part II Top. Stud. Oceanogr. 49, 603–621. https://doi.org/10.1016/ S0967-0645(01)00114-X

Gordey AS, Frey DI, Drozd ID, et al. (2024) Spatial variability of water mass transports in the Bransfield Strait based on direct current measurements. Deep Sea Research Part I: Oceanographic Research Papers 207, 104284. https://doi.org/10.1016/J.DSR.2024.104284

Gordon AL, Mensch M, Zhaoqian D, et al. (2000) Deep and bottom water of the Bransfield Strait eastern and central basins. J. Geophys. Res. Oceans 105, 11337–11346. https://doi.org/10.1029/2000JC900030

Goyal R, Sen Gupta A, Jucker M, et al. (2021) Historical and Projected Changes in the Southern Hemisphere Surface Westerlies. Geophys. Res. Lett. 48, e2020GL090849. https://doi.org/10.1029/2020GL090849

Greene CA, Blankenship DD, Gwyther DE, et al. (2017) Wind causes Totten Ice Shelf melt and acceleration. Sci. Adv. 3. https://doi.org/10.1126/SCIADV.1701681

Grelowski A, Majewick A, Pastuszak M (1986) Mesoscale hydrodynamic processes in the

region of Bransfield Strait and the southern part of Drake Passage during B I O M A S S - S I B E X 1983 / 84 *. Pol. Polar Res. 7, 353–369

Gruber N, Clement D, Carter BR, et al. (2019) The oceanic sink for anthropogenic CO 2 from 1994 to 2007. Science (1979). 363, 1193–1199. https://doi.org/10.1126/science.aau5153

Hattermann T, Nicholls KW, Hellmer HH, et al. (2021) Observed interannual changes beneath Filchner-Ronne Ice Shelf linked to large-scale atmospheric circulation. Nature Communications 2021 12:1 12, 2961-. https://doi.org/10.1038/s41467-021-23131-x

Herraiz-Borreguero L, Naveira Garabato AC (2022) Poleward shift of Circumpolar Deep Water threatens the East Antarctic Ice Sheet. Nature Climate Change 2022 12:8 12, 728–734. https://doi.org/10.1038/s41558-022-01424-3

Hersbach H, Bell B, Berrisford P, et al. (2020) The ERA5 global reanalysis. Quarterly Journal of the Royal Meteorological Society 146, 1999–2049. https://doi.org/10.1002/QJ.3803

Heywood KJ, Garabato ACN, Stevens DP, et al. (2004) On the fate of the Antarctic Slope Front and the origin of the Weddell Front 109, 1–13. https://doi.org/10.1029/2003JC002053

Hofmann EE, Klinck JM, Lascara CM, et al. (1996) Water mass distribution and circulation west of the Antarctic Peninsula and including Bransfield Strait. pp. 61–80. https://doi.org/10.1029/AR070p0061

Hogg AMC, Meredith MP, Chambers DP, et al. (2015) Recent trends in the Southern Ocean eddy field. J. Geophys. Res. Oceans 120, 257–267. https://doi.org/10.1002/2014JC010470

Hosking JS, Orr A, Marshall GJ, et al. (2013) The Influence of the Amundsen–Bellingshausen Seas Low on the Climate of West Antarctica and Its Representation in Coupled Climate Model Simulations. J. Clim. 26, 6633–6648. https://doi.org/10.1175/JCLI-D-12-00813.1

Huguenin MF, Holmes RM, Spence P, et al. (2024) Subsurface Warming of the West Antarctic Continental Shelf Linked to El Niño-Southern Oscillation. Geophys. Res. Lett. 51, e2023GL104518. https://doi.org/10.1029/2023GL104518

Huneke WGC, Huhn O, Schröeder M (2016) Water masses in the Bransfield Strait and

adjacent seas, austral summer 2013. Polar Biol. 39, 789–798. https://doi.org/10.1007/S00300-016-1936-8/FIGURES/7

Ito RG, Tavano VM, Borges Mendes CR, et al. (2018) Sea-air CO2 fluxes and pCO2 variability in the Northern Antarctic Peninsula during three summer periods (2008–2010). Deep. Sea. Res. 2. Top. Stud. Oceanogr. 149, 84–98. https://doi.org/10.1016/j.dsr2.2017.09.004

Jackett, D.R., McDougall, T.J., Jackett, D.R., McDougall, T.J., 1997. A Neutral Density Variable for the World's Oceans. J. Phys. Oceanogr. 27, 237–263. https://doi.org/10.1175/1520-0485(1997)027

Jacobs SS, Jenkins A, Giulivi CF, et al. (2011) Stronger ocean circulation and increased melting under Pine Island Glacier ice shelf. Nature Geoscience 2011 4:8 4, 519–523. https://doi.org/10.1038/ngeo1188

Jean-Michel L, Eric G, Romain BB, et al. (2021) The Copernicus Global 1/12° Oceanic and Sea Ice GLORYS12 Reanalysis. Front. Earth Sci. (Lausanne). 9, 698876. https://doi.org/10.3389/FEART.2021.698876/FULL

Jenkins, A., Dutrieux, P., Jacobs, S., Steig, E. J., Gudmundsson, G. H., Smith, J., & Heywood, K. J. (2016). Decadal ocean forcing and Antarctic ice sheet response: Lessons from the Amundsen Sea. Oceanography, 29(4), 106–117. https://doi.org/10.5670/oceanog.2016.103

Jenkins A, Shoosmith D, Dutrieux P, et al. (2018) West Antarctic Ice Sheet retreat in the Amundsen Sea driven by decadal oceanic variability. Nature Geoscience 2018 11:10 11, 733–738. https://doi.org/10.1038/s41561-018-0207-4

Kerr R, Dotto TS, Mata MM, et al. (2018a) Three decades of deep water mass investigation in the Weddell Sea (1984–2014): Temporal variability and changes. Deep. Sea. Res. 2. Top. Stud. Oceanogr. 149, 70–83. https://doi.org/10.1016/j.dsr2.2017.12.002

Kerr R, Mata MM, Mendes CRB, et al. (2018b) Northern Antarctic Peninsula: a marine climate hotspot of rapid changes on ecosystems and ocean dynamics. Deep. Sea. Res. 2. Top. Stud. Oceanogr. 149, 4–9. https://doi.org/10.1016/j.dsr2.2018.05.006

Kerr R, Monteiro T, Batista MS, et al. (2025) Physical-biological processes regulating summer sea-air CO2 exchanges along the Drake Passage and northern Antarctic Peninsula. Mar. Chem. 269, 104497. https://doi.org/10.1016/J.MARCHEM.2025.104497

Kim TW, Ha HK, Wåhlin AK, et al. (2017) Is Ekman pumping responsible for the seasonal variation of warm circumpolar deep water in the Amundsen Sea? Cont. Shelf Res. 132, 38–48. https://doi.org/10.1016/J.CSR.2016.09.005

Kim YS, Orsi AH (2014) On the Variability of Antarctic Circumpolar Current Fronts Inferred from 1992–2011 Altimetry. J. Phys. Oceanogr. 44, 3054–3071. https://doi.org/10.1175/JPO-D-13-0217.1

Kusahara K, Tatebe H, Hajima T, et al. (2023) Antarctic Sea Ice Holds the Fate of Antarctic Ice-Shelf Basal Melting in a Warming Climate. J. Clim. 36, 713–743. https://doi.org/10.1175/JCLI-D-22-0079.1

Lellouche JM, Greiner E, Le Galloudec O, et al. (2018) Recent updates to the Copernicus Marine Service global ocean monitoring and forecasting real-time 1g 12° high-resolution system. Ocean Science 14, 1093–1126. https://doi.org/10.5194/OS-14-1093-2018

Llanillo PJ, Kanzow T, Janout MA, et al. (2023) The Deep-Water Plume in the Northwestern Weddell Sea, Antarctica: Mean State, Seasonal Cycle and Interannual Variability Influenced by Climate Modes. J. Geophys. Res. Oceans 128, e2022JC019375. https://doi.org/10.1029/2022JC019375

Loeb V, Hofmann EE, Klinck JM, et al. (2010) Deep-Sea Research II Hydrographic control of the marine ecosystem in the South Shetland-Elephant Island and Bransfield Strait region. Deep-Sea Research Part II 57, 519–542. https://doi.org/10.1016/j.dsr2.2009.10.004

Loeb VJ, Hofmann EE, Klinck JM, et al. (2009) ENSO and variability of the Antarctic Peninsula pelagic marine ecosystem 21, 135–148. https://doi.org/10.1017/S0954102008001636

Lopez O, Garcia MA, Gomis D, et al. (1999) Hydrographic and hydrodynamic characteristics aof the eastern basin of the Bransfiled Strait. Deep Sea Research Part I: Oceanographic Research Papers 46

Marshall GJ (2003) Trends in the Southern Annular Mode from observations and reanalyses. J. Clim. 16, 4134–4143. https://doi.org/10.1175/1520-0442(2003)016<4134:TITSAM>2.0.CO;2

Madec and the NEMO Team, 2008 G. Madec, The NEMO Team NEMO Ocean Engine. Note Du Pôle De Modélisation France: Institut Pierre-Simon Laplace (IPSL), 1288–1619 (2008)

Martínez-Marrero A, Stegner A, Rodríguez-Santana A, et al. (2011) The Bransfield current system. Deep Sea Research Part I: Oceanographic Research Papers 58, 390–402. https://doi.org/10.1016/j.dsr.2011.01.011

Martínez-Moreno J, Hogg AMC, England MH, et al. (2021) Global changes in oceanic mesoscale currents over the satellite altimetry record. Nature Climate Change 2021 11:5 11, 397–403. https://doi.org/10.1038/s41558-021-01006-9

Martinson DG, Mckee DC (2012) Transport of warm Upper Circumpolar Deep Water onto the western Antarctic Peninsula continental shelf 433–442. https://doi.org/10.5194/os-8-433-2012

Mata MM, Tavano VM, Garcia CAE (2018) 15 years sailing with the Brazilian High Latitude Oceanography Group (GOAL). Deep Sea Research Part II: Topical Studies in Oceanography 149, 1–3. https://doi.org/10.1016/j.dsr2.2018.05.007

Mazloff Matthew R, Heimbach P, Wunsch C (2010) An eddy-permitting Southern Ocean state estimate. J. Phys. Oceanogr. 40, 880–899. https://doi.org/10.1175/2009JPO4236.1

Mazloff Matthew R., Heimbach P, Wunsch C, et al. (2010) An Eddy-Permitting Southern Ocean State Estimate. J. Phys. Oceanogr. 40, 880–899. https://doi.org/10.1175/2009JPO4236.1

McDougall TJ, Barker PM (2011) Getting started with TEOS-10 and the Gibbs Seawater (GSW). Scor/Iapso Wg127 28

Mckee DC, Martinson DG, Schofield O (2019) Origin and Attenuation of Mesoscale Structure in Circumpolar Deep Water Intrusions to an Antarctic Shelf. J. Phys. Oceanogr. 49, 1293–1318. https://doi.org/10.1175/JPO-D-18-0133.1

Meijers AJS, Bindoff NL, Rintoul SR (2011) Frontal movements and property fluxes: Contributions to heat and freshwater trends in the Southern Ocean. J. Geophys. Res. Oceans 116, 8024. https://doi.org/10.1029/2010JC006832

Mendes CRB, Tavano VM, Kerr R, et al. (2018) Impact of sea ice on the structure of phytoplankton communities in the northern Antarctic Peninsula. Deep Sea Research Part II: Topical Studies in Oceanography 149, 111–123. https://doi.org/10.1016/j.dsr2.2017.12.003

Meneghello G, Marshall J, Campin JM, et al. (2018) The Ice-Ocean Governor: Ice-Ocean Stress Feedback Limits Beaufort Gyre Spin-Up. Geophys. Res. Lett. 45, 11,293-11,299. https://doi.org/10.1029/2018GL080171

Meredith MP (2022) Carbon storage shifts around Antarctica. Nature Communications 2022 13:1 13, 3400-. https://doi.org/10.1038/s41467-022-31152-3

Meredith MP (2016) Understanding the structure of changes in the Southern Ocean eddy field. Geophys. Res. Lett. 43, 5829–5832. https://doi.org/10.1002/2016GL069677

Mizobata K, Hirano D, Kusahara K, et al. (2025) Ocean Response Along the East Antarctic Coastal Margin to the Southern Annular Mode. Geophys. Res. Lett. 52, e2024GL112914. https://doi.org/10.1029/2024GL112914

Mishonov, A. V, Boyer, T.P., Baranova, O.K., Bouchard, C.N., Cross, S.L., Garcia, H.E., Locarnini, R.A., Paver, C.R., Reagan, J.R., Wang, Z., Seidov, D., Grodsky, A.I., Beauchamp, J.G., Raimondo, G.M., Spinrad, R.W., Volz, S., Administrator, A., 2024. World Ocean Database 2023. https://doi.org/10.25923/Z885-H264

Moffat C, Owens B, Beardsley RC (2009) On the characteristics of Circumpolar Deep Water intrusions to the west Antarctic Peninsula Continental Shelf. J. Geophys. Res. Oceans 114. https://doi.org/10.1029/2008JC004955

Monteiro T, Henley SF, Pollery RCG, et al. (2023) Spatiotemporal variability of dissolved inorganic macronutrients along the northern Antarctic Peninsula (1996–2019). Limnol. Oceanogr. 68, 2305–2326. https://doi.org/10.1002/LNO.12424

Morozov EG, Frey DI, Krechik VA, et al. (2021) Water Masses, Currents, and Phytoplankton

in the Bransfield Strait in January 2020 55–64. https://doi.org/10.1007/978-3-030-78927-5_4

Morrison AK, England MH, Hogg AMC, et al. (2023) Weddell Sea Control of Ocean Temperature Variability on the Western Antarctic Peninsula. Geophys. Res. Lett. 50, e2023GL103018. https://doi.org/10.1029/2023GL103018

Morrison AK, Hogg AM, England MH, et al. (2020) Warm Circumpolar Deep Water transport toward Antarctica driven by local dense water export in canyons

Mukhametyanov RZ, Frei DI, Morozov EG (2022) Currents in the Bransfield Strait Based on Geostrophic Calculations and Data of Instrumental Measurements. Izvestiya, Atmospheric and Oceanic Physics 2022 58:5 58, 500–506. https://doi.org/10.1134/S0001433822050061

Nakayama Y, Menemenlis D, Zhang H, et al. (2018) Origin of Circumpolar Deep Water intruding onto the Amundsen and Bellingshausen Sea continental shelves. Nature Communications 2018 9:1 9, 3403-. https://doi.org/10.1038/s41467-018-05813-1

Nakayama Y, Schröder M, Hellmer HH (2013) From circumpolar deep water to the glacial meltwater plume on the eastern Amundsen Shelf. Deep Sea Research Part I: Oceanographic Research Papers 77, 50–62. https://doi.org/10.1016/J.DSR.2013.04.001

Nakayama Y, Timmermann R, Rodehacke CB, et al. (2014) Modeling the spreading of glacial meltwater from the Amundsen and Bellingshausen Seas. Geophys. Res. Lett. 41, 7942–7949. https://doi.org/10.1002/2014GL061600

Naughten, K. A., Holland, P. R., & De Rydt, J. 2023. Unavoidable future increase in West Antarctic ice-shelf melting over the twenty-first century. Nature Climate Change, 13(11), 1222–1228. https://doi.org/10.1038/s41558-023-01818-x

Neme J, England MH, Hogg AMC (2021) Seasonal and Interannual Variability of the Weddell Gyre From a High-Resolution Global Ocean-Sea Ice Simulation During 1958–2018. J. Geophys. Res. Oceans 126, e2021JC017662. https://doi.org/10.1029/2021JC017662

Niller PP, Amos A, Hu JH (1991) Water masses and 200 m relative geostrophic circulation in the western Bransfield Strait region. Deep Sea Research Part A, Oceanographic Research

Papers 38, 943–959. https://doi.org/10.1016/0198-0149(91)90091-S

Noro M, Dotto TS, Tonelli M, et al. (2025) Variability of the Weddell Sea deep waters in GLORYS12v1 reanalysis. Deep Sea Research Part I: Oceanographic Research Papers 225, 104599. https://doi.org/10.1016/J.DSR.2025.104599

Nost OA, Biuw M, Tverberg V, et al. (2011) Eddy overturning of the Antarctic Slope Front controls glacial melting in the Eastern Weddell Sea. J. Geophys. Res. Oceans 116. https://doi.org/10.1029/2011JC006965

O'Connor GK, Nakayama Y, Steig EJ, et al. (2025) Enhanced West Antarctic ice loss triggered by polynya response to meridional winds. Nature Geoscience 2025 18:9 18, 840–847. https://doi.org/10.1038/s41561-025-01757-6

Oelerich R, Heywood KJ, Damerell GM, et al. (2022) Wind-Induced Variability of Warm Water on the Southern Bellingshausen Sea Continental Shelf. J. Geophys. Res. Oceans 127, e2022JC018636. https://doi.org/10.1029/2022JC018636

Ong EQY, Doddridge E, Constantinou NC, et al. (2024) Intrinsically Episodic Antarctic Shelf Intrusions of Circumpolar Deep Water via Canyons. J. Phys. Oceanogr. 54, 1195–1210. https://doi.org/10.1175/JPO-D-23-0067.1

Orsi AH, Whitworth T, Nowlin WD (1995) On the meridional extent and fronts of the Antarctic Circumpolar Current. Deep-Sea Research Part I 42, 641–673. https://doi.org/10.1016/0967-0637(95)00021-W

Paolo FS, Padman L, Fricker HA, et al. (2018) Response of Pacific-sector Antarctic ice shelves to the El Niño/Southern Oscillation. Nat. Geosci. 11, 121. https://doi.org/10.1038/S41561-017-0033-0

Park YH, Park T, Kim TW, et al. (2019) Observations of the Antarctic Circumpolar Current Over the Udintsev Fracture Zone, the Narrowest Choke Point in the Southern Ocean. J. Geophys. Res. Oceans 124, 4511–4528. https://doi.org/10.1029/2019JC015024

Peterson RG, White WB (1998) Slow oceanic teleconnections linking the Antarctic Circumpolar Wave with the tropical El Niño-Southern Oscillation. J. Geophys. Res. Oceans 103, 24573–24583. https://doi.org/10.1029/98JC01947

Prend CJ, MacGilchrist GA, Manucharyan GE, et al. (2024) Ross Gyre variability modulates oceanic heat supply toward the West Antarctic continental shelf. Communications Earth & Environment 2024 5:1 5, 47-. https://doi.org/10.1038/s43247-024-01207-y

Raphael MN, Marshall GJ, Turner J, et al. (2016) The Amundsen Sea Low: Variability, Change, and Impact on Antarctic Climate. Bull. Am. Meteorol. Soc. 97, 111–121. https://doi.org/10.1175/BAMS-D-14-00018.1

Renner AHH, Heywood KJ, Thorpe SE (2009) Validation of three global ocean models in the Weddell Sea. Ocean Model. (Oxf). 30, 1–15. https://doi.org/10.1016/j.ocemod.2009.05.007

Residual-Mean Solutions for the Antarctic Circumpolar Current and Its Associated Overturning Circulation in: Journal of Physical Oceanography Volume 33 Issue 11 (2003) [WWW Document] (n.d.). URL https://journals.ametsoc.org/view/journals/phoc/33/11/1520-0485_2003_033_2341_rsftac_2.0.co_2.xml

Ribeiro N, Morrison AK, Rintoul SR, et al. (2025) Wind-Driven Variability of Modified Circumpolar Deep Water Intrusions Into Vincennes Bay, East Antarctica. J. Geophys. Res. Oceans 130, e2025JC022843. https://doi.org/10.1029/2025JC022843

Rignot E, Mouginot J, Scheuchl B, et al. (2019) Four decades of Antarctic ice sheet mass balance from 1979–2017. Proc. Natl. Acad. Sci. U. S. A. 116, 1095–1103. https://doi.org/10.1073/pnas.1812883116

Rintoul SR, Sokolov S (2001) Baroclinic transport variability of the Antarctic Circumpolar Current south of Australia (WOCE repeat section SR3). J. Geophys. Res. Oceans 106, 2815–2832. https://doi.org/10.1029/2000JC900107

Riser, S. C., Ren, L., & Wong, A. (2015). Salinity in Argo: A modern view of a changing ocean. Oceanography, 21(1), 56–67. https://doi.org/10.5670/oceanog.2008.67

Roach CJ, Speer K (2019) Exchange of Water Between the Ross Gyre and ACC Assessed by Lagrangian Particle Tracking. J. Geophys. Res. Oceans 124, 4631–4643. https://doi.org/10.1029/2018JC014845

Roquet, F., Charrassin, J.-B., Marchand, S., Boehme, L., Fedak, M., Reverdin, G., & Guinet, C. (2011). Delayed-mode calibration of hydrographic data obtained from animal-borne satellite relay data loggers. Journal of Atmospheric and Oceanic Technology, 28(6), 787–801. https://doi.org/10.1175/2010JTECHO801.1

Rott H, Abdel Jaber W, Wuite J, et al. (2018a) Changing pattern of ice flow and mass balance for glaciers discharging into the Larsen A and B embayments, Antarctic Peninsula, 2011 to 2016. Cryosphere 12, 1273–1291. https://doi.org/10.5194/TC-12-1273-2018

Rott H, Abdel Jaber W, Wuite J, et al. (2018b) Changing pattern of ice flow and mass balance for glaciers discharging into the Larsen A and B embayments, Antarctic Peninsula, 2011 to 2016. Cryosphere 12, 1273–1291. https://doi.org/10.5194/tc-12-1273-2018

Ruiz Barlett EM, Tosonotto G V., Piola AR, et al. (2018) On the temporal variability of intermediate and deep waters in the Western Basin of the Bransfield Strait. Deep Sea Research Part II: Topical Studies in Oceanography 149, 31–46. https://doi.org/10.1016/j.dsr2.2017.12.010

Sallée JB (2018) Southern ocean warming. Oceanography 31, 52–62. https://doi.org/10.5670/OCEANOG.2018.215

Sanchez N, Reiss CS, Holm-Hansen O, et al. (2019) Weddell-Scotia Confluence Effect on the Iron Distribution in Waters Surrounding the South Shetland (Antarctic Peninsula) and South Orkney (Scotia Sea) Islands During the Austral Summer in 2007 and 2008. Front. Mar. Sci. 6, 1–16. https://doi.org/10.3389/fmars.2019.00771

Sangrá, P., Gordo, C., Hern´andez-Arencibia, M., Marrero-Díaz, ´A., Rodríguez- Santana, A., Stegner, A., Martínez-Marrero, A., Pelegrí, J.L., Pichon, T., (2011). The Bransfield current system. Deep Sea Res. Oceanogr. Res. Pap. 58, 390–402. https:// doi.org/10.1016/j.dsr.2011.01.011

Sangrà P, Stegner A, Hernández-Arencibia M, et al. (2017) The Bransfield Gravity Current. Deep. Sea. Res. 1. Oceanogr. Res. Pap. 119, 1–15. https://doi.org/10.1016/j.dsr.2016.11.003

Santos-Andrade M, Kerr R, Orselli IBM, et al. (2023) Drivers of Marine CO2-Carbonate Chemistry in the Northern Antarctic Peninsula. Global Biogeochem. Cycles 37,

e2022GB007518. https://doi.org/10.1029/2022GB007518

Savidge DK, Amft JA (2009) Circulation on the West Antarctic Peninsula derived from 6 years of shipboard ADCP transects. Deep Sea Research Part I: Oceanographic Research Papers 56, 1633–1655. https://doi.org/10.1016/J.DSR.2009.05.011

Schaffer J, Timmermann R, Erik Arndt J, et al. (2016) A global, high-resolution data set of ice sheet topography, cavity geometry, and ocean bathymetry. Earth Syst. Sci. Data 8, 543–557. https://doi.org/10.5194/ESSD-8-543-2016

Schiavon G, Gille ST, Oliveira FSC (2025) Response of Antarctic Circumpolar Current Jets to Southern Hemisphere Westerly Shifts During the 21st Century. J. Geophys. Res. Oceans 130, e2025JC022897. https://doi.org/10.1029/2025JC022897

Schmidtko S, Heywood KJ, Thompson AF, et al. (2014) Multidecadal warming of Antarctic waters. Science (1979). 346, 1227–1231. https://doi.org/10.1126/SCIENCE.1256117

Schulze Chretien LM, Thompson AF, Flexas MM, et al. (2021) The Shelf Circulation of the Bellingshausen Sea. J. Geophys. Res. Oceans 126, e2020JC016871. https://doi.org/10.1029/2020JC016871

Sheehan PMF, Heywood KJ, Thompson AF, et al. (2023) Sources and Pathways of Glacial Meltwater in the Bellingshausen Sea, Antarctica. Geophys. Res. Lett. 50, e2023GL102785. https://doi.org/10.1029/2023GL102785

Shepherd A, Wingham D, Wallis D, et al. (2010) Recent loss of floating ice and the consequent sea level contribution. Geophys. Res. Lett. 37. https://doi.org/10.1029/2010GL042496

Si Y, Stewart AL, Eisenman I (2023). Heat transport across the Antarctic Slope Front controlled by cross-slope salinity gradients. Sci. Adv. 9. https://doi.org/10.1126/SCIADV.ADD7049

Siegelman, L., Roquet, F., Mensah, V., Rivière, P., Pauthenet, E., Picard, B., & Guinet, C. (2019). Correction and accuracy of High- and low-resolution CTD data from animal-borne instruments. Journal of Atmospheric and Oceanic Technology, 36(5), 745–760. https://doi.org/10.1175/JTECH-D-18-0170.1

Silvano A, Holland PR, Naughten KA, et al. (2022) Baroclinic Ocean Response to Climate

Forcing Regulates Decadal Variability of Ice-Shelf Melting in the Amundsen Sea. Geophys. Res. Lett. 49, e2022GL100646. https://doi.org/10.1029/2022GL100646

Silvano A, Rintoul SR, Peña-Molino B, et al. (2018) Freshening by glacial meltwater enhances melting of ice shelves and reduces formation of Antarctic Bottom Water. Sci. Adv. 4. https://doi.org/10.1126/sciadv.aap9467

Sokolov S, Rintoul SR (2009a) Circumpolar structure and distribution of the Antarctic Circumpolar Current fronts: 2. Variability and relationship to sea surface height. J. Geophys. Res. Oceans 114. https://doi.org/10.1029/2008JC005248

Sokolov S, Rintoul SR (2009b) Circumpolar structure and distribution of the antarctic circumpolar current fronts: 1. Mean98 circumpolar paths. J. Geophys. Res. Oceans 114, 11018. https://doi.org/10.1029/2008JC005108

Sokolov S, Rintoul SR (2007) On the relationship between fronts of the Antarctic Circumpolar Current and surface chlorophyll concentrations in the Southern Ocean. J. Geophys. Res. Oceans 112. https://doi.org/10.1029/2006JC004072

Schubert, R., Thompson, A. F., Speer, K., Schulze Chretien, L., & Bebieva, Y. (2021a). The Antarctic Coastal Current in the Bellingshausen Sea. Cryosphere, 15(9), 4179–4199. https://doi.org/10.5194/TC-15-4179-2021

Schubert, R., Thompson, A. F., Speer, K., Schulze Chretien, L., & Bebieva, Y. (2021b). The Antarctic Coastal Current in the Bellingshausen Sea. Cryosphere, 15(9), 4179–4199. https://doi.org/10.5194/TC-15-4179-2021

Stewart AL, Klocker A, Menemenlis D, et al. (2019) Acceleration and Overturning of the Antarctic Slope Current by Winds, Eddies, and Tides. J. Phys. Oceanogr. 49, 2043–2074. https://doi.org/10.1175/JPO-D-18-0221.1

Talley LD, Pickard GL, Emery WJ, et al. (2011) Descriptive Physical Oceanography, 6th ed. Elsevier

Thompson AF, Garabato ACN, Thompson AF, et al. (2014a) Equilibration of the Antarctic Circumpolar Current by Standing Meanders. J. Phys. Oceanogr. 44, 1811–1828. https://doi.org/10.1175/JPO-D-13-0163.1

Thompson AF, Heywood KJ, Schmidtko S, et al. (2014b) Eddy transport as a key component of the Antarctic overturning circulation. Nature Geoscience 2014 7:12 7, 879–884. https://doi.org/10.1038/ngeo2289

Thompson AF, Heywood KJ, Thorpe SE, et al. (2009) Surface Circulation at the Tip of the Antarctic Peninsula from Drifters. J. Phys. Oceanogr. 39, 3–26. https://doi.org/10.1175/2008JPO3995.1

Thompson AF, Speer KG, Schulze Chretien LM (2020) Genesis of the Antarctic Slope Current in West Antarctica. Geophys. Res. Lett. 47. https://doi.org/10.1029/2020GL087802

Thompson AF, Stewart AL, Spence P, et al. (2018) The Antarctic Slope Current in a Changing Climate. Reviews of Geophysics 56, 741–770. https://doi.org/10.1029/2018RG000624

Thompson DWJ, Solomon S (2002) Interpretation of recent Southern Hemisphere climate change. Science (1979). 296, 895–899. https://doi.org/10.1126/science.1069270

Tokarczyk R (1987) Classification of water masses in the Bransfield Strait and southern part of the Drake Passage using a method of statistical multidimensional analysis. Pol. Polar Res. 8, 333–366

Trasviña A, Heywood KJ, Renner AHH, et al. (2011) The impact of high-frequency current variability on dispersion off the eastern Antarctic Peninsula. J. Geophys. Res. Oceans 116. https://doi.org/10.1029/2011JC007003

Turner J, Hosking JS, Bracegirdle TJ, et al. (2015) Recent changes in Antarctic Subject Areas: Philosophical Transaction of The Royal Society A 373, 1–12

Turner J, Orr A, Gudmundsson GH, et al. (2017) Atmosphere-ocean-ice interactions in the Amundsen Sea Embayment, West Antarctica. Reviews of Geophysics 55, 235–276. https://doi.org/10.1002/2016RG000532

van Caspel M, Hellmer HH, Mata MM, et al. (2018) On the ventilation of Bransfield Strait deep basins. Deep. Sea. Res. 2. Top. Stud. Oceanogr. 149, 25–30. https://doi.org/10.1016/j.dsr2.2017.09.006

van Caspel M, Schröder M, Huhn O, et al. (2015) Precursors of Antarctic Bottom Water formed on the continental shelf off Larsen Ice Shelf. Deep. Sea. Res. 1. Oceanogr. Res.

Pap. 99, 1–9. https://doi.org/10.1016/j.dsr.2015.01.004

Veny M, Aguiar-González B, Marrero-Díaz Á, et al. (2024) Biophysical coupling of seasonal chlorophyll-a bloom variations and phytoplankton assemblages across the Peninsula Front in the Bransfield Strait. Ocean Science 20, 389–415. https://doi.org/10.5194/OS-20-389-2024

Veny M, Aguiar-González B, Marrero-Díaz Á, et al. (2022) Seasonal circulation and volume transport of the Bransfield Current. PrOce 204, 102795. https://doi.org/10.1016/J.POCEAN.2022.102795

Von Gyldenfeldt AB, Fahrbach E, García MA, et al. (2002) Flow variability at the tip of the Antarctic Peninsula. Deep Sea Research Part II: Topical Studies in Oceanography 49, 4743–4766. https://doi.org/10.1016/S0967-0645(02)00157-1

Walker DP, Jenkins A, Assmann KM, et al. (2013) Oceanographic observations at the shelf break of the Amundsen Sea, Antarctica. J. Geophys. Res. Oceans 118, 2906–2918. https://doi.org/10.1002/JGRC.20212

Wang X, Moffat C, Dinniman MS, et al. (2022) Variability and Dynamics of Along-Shore Exchange on the West Antarctic Peninsula (WAP) Continental Shelf. J. Geophys. Res. Oceans 127, e2021JC017645. https://doi.org/10.1029/2021JC017645

Wang Y, Chassignet EP, Speer K (2024) On the dynamics of the Ross Gyre: the relative importance of wind, buoyancy, eddies, and the Antarctic Circumpolar Current. Front. Mar. Sci. 11, 1465808. https://doi.org/10.3389/FMARS.2024.1465808/TEXT

Webber BGM, Heywood KJ, Stevens DP, et al. (2019) The Impact of Overturning and Horizontal Circulation in Pine Island Trough on Ice Shelf Melt in the Eastern Amundsen Sea. J. Phys. Oceanogr. 49, 63–83. https://doi.org/10.1175/JPO-D-17-0213.1

Webber BGM, Heywood KJ, Stevens DP, et al. (2017) Mechanisms driving variability in the ocean forcing of Pine Island Glacier. Nature Communications 2017 8:1 8, 14507-. https://doi.org/10.1038/ncomms14507

Wessel P, Smith WHF (1996) A global, self-consistent, hierarchical, high-resolution shoreline database. J. Geophys. Res. Solid Earth 101, 8741–8743.

https://doi.org/10.1029/96JB00104

Wilson C, Klinkhammer GP, Chin CS (1999) Hydrography within the Central and East Basins of the Bransfield Strait, Antarctica. J. Phys. Oceanogr. 29, 465–479. https://doi.org/10.1175/1520-0485(1999)029<0465:HWTCAE>2.0.CO;2

Yamazaki K, Aoki S, Katsumata K, et al. (2021) Multidecadal poleward shift of the southern boundary of the Antarctic Circumpolar Current off East Antarctica. Sci. Adv 7, 8755–8766

Yamazaki K, Aoki S, Mizobata K (2023) Diffusion of Circumpolar Deep Water Towards Antarctica. J. Geophys. Res. Oceans 128, e2022JC019422. https://doi.org/10.1029/2022JC019422

Yamazaki K, Aoki S, Shimada K, et al. (2020) Structure of the Subpolar Gyre in the Australian-Antarctic Basin Derived From Argo Floats. J. Geophys. Res. Oceans 125, e2019JC015406. https://doi.org/10.1029/2019JC015406

Yuan X (2004) ENSO-related impacts on Antarctic sea ice: a synthesis of phenomenon and mechanisms. Antarct. Sci. 16, 415–425. https://doi.org/10.1017/S0954102004002238

Yuan X, Kaplan MR, Cane MA (2018) The interconnected global climate system-a review of tropical-polar teleconnections. J. Clim. 31, 5765–5792. https://doi.org/10.1175/JCLI-D-16-0637.1

Yuri Damini B, Rodrigo Costa R, Dotto TS, et al. (2023) Antarctica Slope Front bifurcation eddy: A stationary feature influencing CO2 dynamics in the northern Antarctic Peninsula. Prog. Oceanogr. 212, 102985. https://doi.org/10.1016/J.POCEAN.2023.102985

Zhang Y, Chambers D, Liang X (2021) Regional Trends in Southern Ocean Eddy Kinetic Energy. J. Geophys. Res. Oceans 126, e2020JC016973. https://doi.org/10.1029/2020JC016973

Zhou M, Niiler PP, Hu JH (2002) Surface currents in the Bransfield and Gerlache Straits, Antarctica. Deep. Sea. Res. 1. Oceanogr. Res. Pap. 49, 267–280. https://doi.org/10.1016/S0967-0637(01)00062-0

Zhou M, Niiler PP, Zhu Y, et al. (2006) The western boundary current in the Bransfield Strait,

Antarctica. Deep. Sea. Res. 1. Oceanogr. Res. Pap. 53, 1244–1252. https://doi.org/10.1016/j.dsr.2006.04.003

Zu Y, Gao L, Guo G, et al. (2022) Changes of Circumpolar Deep Water between 2006 and 2020 in the south-west Indian Ocean, East Antarctica. Deep Sea Research Part II: Topical Studies in Oceanography 197, 105043. https://doi.org/10.1016/J.DSR2.2022.105043

Yamazaki, A., (2022) Poleward transport of Circumpolar Deep Water off East Antarctica. https://doi.org/10.14943/DOCTORAL.K14766

Yamazaki, K., Aoki, S., & Mizobata, K. (2023). Diffusion of Circumpolar Deep Water Towards Antarctica. Journal of Geophysical Research: Oceans, 128(2), e2022JC019422. https://doi.org/10.1029/2022JC019422

Yamazaki, K. et al. (2024). Revisiting circulation and water masses over theEast Antarctic margin (80–150° E). Progress in Oceanography,103285. https://doi.org/10.1016/j.pocean.2024.103285